Applied Science Dept.

JOURNAL OF THE AERONAUTICAL SCIENCES

INSTITUTE OF THE AERONAUTICAL SCIENCES

ST. LOUIS PUBLIC LIBRARY JAN 8 1957

VOLUME 24 — 1957 JANUARY, 1957 NUMBER 1

CONTENTS

On the Use of Interfering Flow Fields for the Reduction of Drag at Supersonic Speeds.. ANTONIO FERRI AND JOSEPH H. CLARKE 1

An Experimental Study of the Response of Simple Panels to Intense Acoustic Loading.. LESLIE W. LASSITER, ROBERT W. HESS, AND HARVEY H. HUBBARD 19

Stagnation Point of a Blunt Body in Hypersonic Flow.. TING-YI LI AND RICHARD E. GEIGER 25

Unsteady Flow Around Thin Wings at High Mach Numbers.. MÅRTEN T. LANDAHL 33

A Simple Method of Matric Structural Analysis.. BERTRAM KLEIN 39

An Experimental Investigation of Leading-Edge Shock-Wave - Boundary-Layer Interaction at Mach 5.8.. JAMES M. KENDALL, JR. 47

An Investigation of Effects of Certain Types of Structural Nonlinearities on Wing and Control Surface Flutter.. DONALD S. WOOLSTON, HARRY L. RUNYAN, AND ROBERT E. ANDREWS 57

Readers' Forum.. 64

A717733

PUBLIC LIBRARY ST LOUIS MO

Published by
INSTITUTE OF THE AERONAUTICAL SCIENCES, INC.

JOURNAL OF THE AERONAUTICAL SCIENCES

Editor: W. R. SEARS
Director, Graduate School of Aeronautical Engineering, Cornell University

Associate Editor: ROBERT R. DEXTER *Managing Editor:* RITA J. TURINO
Editorial Assistant: CAROLINE TAYLOR

Editorial Committee

Aerodynamics and Fluid Mechanics
Holt Ashley
H. Julian Allen
Dean R. Chapman
Francis H. Clauser
Hugh L. Dryden
John C. Evvard
Antonio Ferri
Alexander Flax
Wallace D. Hayes
R. T. Jones
Carl Kaplan
H. W. Liepmann
C. C. Lin
H. F. Ludloff
Harold Luskin
Clark B. Millikan
C. D. Perkins
H. J. E. Reid
George S. Schairer
G. B. Schubauer
John Stack
Theodore Theodorsen
Arthur N. Tifford
Th. von Kármán

Flight Testing
R. R. Gilruth
Melvin N. Gough
W. L. Howland
W. F. Milliken, Jr.

Rotating Wing Aircraft
F. B. Gustafson
K. H. Hohenemser
Bartram Kelley
R. B. Maloy
Ralph McClarren
R. H. Miller
R. H. Prewitt
Igor I. Sikorsky

Structures
John E. Duberg
N. J. Hoff
Samuel Levy
J. F. McBrearty
W. Ramberg
E. E. Sechler
F. R. Shanley
C. R. Strang
S. Timoshenko

Meteorology
C. F. Brooks
D. M. Little
F. W. Reichelderfer
K. C. Spengler

Vibration and Flutter
Lee Arnold
M. A. Biot
R. L. Bisplinghoff
Harold A. Cheilek
I. E. Garrick
Martin Goland

Aircraft Design
W. E. Beall
E. H. Heinemann
Hall L. Hibbard
Richard Hutton
C. L. Johnson
A. A. Kartveli
E. G. Stout
F. K. Teichmann

Electronics
Welcome W. Bender
K. C. Black
M. V. Kiebert, Jr.
David S. Little
S. B. Rogers
Paul Rosenberg
L. M. Sherer

Physiologic Problems
H. G. Armstrong
Louis H. Bauer
Robert J. Benford
W. Randolph Lovelace, II
Ross A. MacFarland

Flight Propulsion
William Bollay
George W. Brady
R. P. Kroon
Frank E. Marble
Abe Silverstein
Martin Summerfield
E. S. Taylor

Instruments
Alan G. Binnie
Charles H. Colvin
Frank R. Cook
C. S. Draper
S. G. Eskin
C. F. Savage
R. C. Sylvander

SUBSCRIPTION RATES

JOURNAL OF THE AERONAUTICAL SCIENCES, Published Monthly. United States and Possessions: 1 Year, $15.00; Single Copies, $1.50. Foreign Countries Including Canada (American Currency Rates): 1 Year, $16.00; Single Copies, $1.50.
AERONAUTICAL ENGINEERING REVIEW, Published Monthly. United States and Possessions: 1 Year, $3.00; Single Copies, $0.50. Foreign Countries Including Canada (American Currency Rates): 1 Year, $3.50; Single Copies, $0.50.
Notices of change of address should be sent to the Institute at least 30 days prior to actual change of address.
Manuscripts for publication, proofs, and all correspondence should be addressed to the Editorial Office of the JOURNAL.
Publication Office, 20th and Northampton Sts., Easton, Pa. Correspondence regarding subscriptions may be addressed to the Editorial Office of the JOURNAL OF THE AERONAUTICAL SCIENCES, 2 East 64th Street, New York 21, N.Y.

© *Copyright, 1957, by the Institute of the Aeronautical Sciences, Inc.*

Entered as Second-Class Matter at the Post Office, Easton, Pa., May 1, 1937. Acceptance for mailing at a special rate of Postage provided for in the Act of August 24, 1912. Authorized April 29, 1937.

Ref 629.1
Shelved w. 050

JOURNAL OF THE AERONAUTICAL SCIENCES

VOLUME 24 JANUARY, 1957 NUMBER 1

On the Use of Interfering Flow Fields for the Reduction of Drag at Supersonic Speeds†

ANTONIO FERRI* AND JOSEPH H. CLARKE**

Polytechnic Institute of Brooklyn

SUMMARY

A general outline is given of possibilities for favorable wave interference between supersonic aircraft components. The interference between a three-dimensional wing with swept leading edges and a small reflecting surface in biplane arrangement is discussed in terms of linearized flow theory. Relationships are developed which facilitate the determination of the interference drag of a large class of such three-dimensional configurations without the need for determination of the flow field. The method is applied to several biplane configurations of practical interest. It is shown that the pressure drag of the wing can be greatly reduced or that the volume near the root section of the wing can be considerably increased without penalty in pressure drag. The three-dimensional biplane is then discussed from the practical point of view.

SYMBOLS

A = area of integration
B = $(M_1^2 - 1)^{1/2}$
C_D = drag coefficient based on plan-form area of wing
C_{Di} = interference drag coefficient based on plan-form area of wing
c_p = pressure coefficient
c = chord at root section
D = drag
D_i = interference drag
d = dimension shown in Fig. 9; see Eq. (30)
f = quantity proportional to intensity of source distribution
h = distance between planes of wing and plate
k = tangent of sweepback angle of associated edge
M = Mach Number
M_1 = Mach Number of undisturbed stream
n = k/B
R = dimensionless distance in Fig. 10
r = dimensionless distance in Figs. 14 and 18
r = radial coordinate in cylindrical coordinate system
S = area of integration
S_p = area of reflecting plate plan form
S_w = area of wing plan form
s = distance shown in Fig. 9; see Eq. (29)
s = length of arc
T = ratio defined by Eq. (47)
u = x component of perturbation velocity
V_1 = velocity of undisturbed stream
v_r = r component of perturbation velocity
w = z component of perturbation velocity
x = streamwise Cartesian coordinate
y = lateral Cartesian coordinate
z = normal Cartesian coordinate
α = oblique coordinate used in Appendix; see Fig. 8(a)
β = oblique coordinate used in Appendix; see Fig. 8(a)
γ = variable used in Appendix
ζ = normal Cartesian coordinate
η = lateral Cartesian coordinate
ϑ = cylindrical angular coordinate
λ = inclination of surface with respect to plane of wing in plane of constant y
μ = Mach angle
ξ = streamwise Cartesian coordinate
ρ_1 = density of undisturbed stream
τ = maximum thickness at root section relative to chord
φ = perturbation velocity potential

Received May 7, 1956.

† This research was supported by the United States Air Force through the Air Force Office of Scientific Research, Air Research and Development Command, under Contract AF 18(600)-694, Project No. R-352-30-11. The authors are indebted to Anthony Casaccio for his assistance with the calculations. The present paper is a modified form of *On The Use of Interference Effects for Shock Drag Reduction at Supersonic Speeds* by Antonio Ferri and Joseph H. Clarke, Confidential PIBAL Report No. 258, July, 1954. It substantially consists of those portions of the latter which were declassified on October 13, 1955.

* Professor of Aerodynamics and Director of Aerodynamics Laboratory.

** Assistant Professor of Aeronautical Engineering.

ST LOUIS PUBLIC LIBRARY NOV 18 1959

INTRODUCTION

THE TOTAL DRAG produced by the motion of a body at supersonic speeds is considered to be composed of (1) the friction and form drag directly related to viscous effects near the surface of the body, (2) the vortex drag due to the lift distribution, and (3) the wave drag due to the lift distribution and to the distribution of the thickness or volume of the body. In the nonviscous theory of supersonic flow it is the last two that appear as a variation of momentum at infinity. All types of drag are sensibly affected by the interference

effects resulting from the presence of more than one body in the stream, and it has been known for some time that wave drag can be notably reduced by judicious use of interference effects. It was shown in 1935 that the wave drag due to thickness of a two-dimensional profile can be eliminated by the introduction of either another wing or a reflecting surface, these being designed to establish a wave pattern in which no waves are propagated away from the system.[1] The first configuration is usually referred to as the Busemann biplane.

The purpose of this report is, first, to outline different types of favorable wave interference in three-dimensional systems and, second, to discuss in some detail the use of interference of the biplane type for the reduction of wave drag due to thickness of three-dimensional swept wings.

Favorable Wave Interference in Supersonic Flow

In supersonic flow, shock waves are produced either as the envelope of compression waves or by discontinuities in the shape of stream surfaces imposed by the presence of the body in the flow field. The presence of shock waves produces an increase in the entropy of the stream and, therefore, a loss in momentum corresponding to wave drag. In the first approximation the loss of momentum per unit area through a given stream tube extending from minus infinity to plus infinity is proportional to the product of the entropy increase and the free-stream pressure. When a body travels at supersonic speeds both compression and expansion waves are produced by the motion. The compression waves are normally cancelled by the expansion waves at large distances from the body but, in the general case, the compression waves will form an envelope before being cancelled by the expansion waves and thereby produce drag. In order to reduce entropy losses the cancellation of shock or compression waves by means of either interfering expansion waves or interfering surfaces must be accomplished as close as possible to the body.

If the interference is analyzed in terms of small perturbation theory, these nonlinear features of the wave pattern disappear, and the momentum losses appear differently. Let the system be enclosed in a control surface consisting of a right circular cylinder whose axis is parallel to the direction of motion; then let the lateral curved surface and the downstream end face recede to infinity (see reference 2 for proper limiting procedures). By application of the momentum theorem to this control surface, the following expression is obtained for the wave drag:

$$D = -\rho_1 \int\int_S uv_r r d\vartheta dx \qquad (1)$$

The integration is extended over the infinite lateral surface S of the cylinder. It is also found that the cylindrical velocity perturbation components are mutually related by the expression[2]

$$u = -(v_r/B)$$

on the cylinder. No contribution to the wave drag appears on the downstream end face of the control surface. In the case of lifting systems, however, a contribution to the drag from this surface does arise which is, in fact, the vortex drag of the system. It is remarked that the problem of minimizing the wave drag of a system is not, in general, compatible with the problem of minimizing its vortex drag, so that the sum of the two forms of drag is the quantity to be subjected to minimization in a general treatment of arbitrary lifting systems.

In terms of the linearized theory, favorable wave interference in a given system is obtained when measures are adopted which decrease the magnitudes of the disturbances reaching the remote lateral curved surface S, thereby diminishing the value of the integral in Eq. (1). Two general methods for accomplishing this end present themselves. These are discussed below.

The first type of favorable wave interference is achieved as follows. An interference flow field, which is induced by a modification of the primary surface or by a suitably chosen complementary surface in the system, is superposed upon the flow field induced by the primary surface of the system. The second surface is designed so that the primary induction reaching the remote control surface is attenuated by the interference induction. Then deviations of the pressure from the free-stream value throughout the flow field are, on the average, reduced; variations in area of individual stream tubes are correspondingly suppressed. Because no one-to-one correspondence exists between points on the surface of the system and points on the remote control surface as in two-dimensional flow, care must be exercised that attenuative overlapping of primary and interference induction over one part of the control surface is not offset by reinforcement of the two flow fields over a second part of the control surface. That is, the induction due to the primary system at a given point on the remote surface can be reduced, say to zero, by producing a suitable interference disturbance somewhere on the surface of the system. No assurance exists, however, that this interfering flow field will combine with the primary flow field to produce similar attenuation of induction at other points on the control surface. These favorably interfering flow fields are established by designing, positioning, and contouring the several components which constitute the aircraft—e.g., wing, body, tail, and inlet—such that they are complementary, the flow fields of each dovetailing to produce minimal total induction on the remote cylinder. These geometric modifications are limited by the geometric, aerodynamic, and other practical restraints imposed on the system. The total volume and lift of the system might well be prescribed; the structural integrity must be maintained; important nonlinear and viscous effects attendant upon undulatory fuselage contouring, for example, must be considered. Restraints such as prescribed volume and lift are important to a formal analysis in order to rule out, for example, the trivial result that the wave drag is a

NOV 5 1959

minimum when there is superposed upon the primary system its negative. It is apparent that the entire configuration must be designed as an entity if the possibility of important drag reductions by favorable wave interference is to be fully realized.

This favorable interference is perhaps more conveniently envisaged in terms of a direct determination of the drag by pressure integration over the surface of the system. (Strictly speaking, the pressure integration gives the sum of wave drag and vortex drag.) Then favorable interference between two components is established when the flow field induced by each imparts thrust to the other. It is clear that this interference is a function of the design, of the relative position, and of the contours of the two components. The drag of the two components is given by the sum of the integrals over each surface of the self-induced pressure and of the interference pressure. It is quite possible for the sum of these four terms to be less than the self-induced drag of either component.

A second type of favorable interference is also possible. Disturbances originating from the primary surfaces are intercepted by interference surfaces before they arrive at the remote control surface. These disturbances may be cancelled on the interference surface or reflected back to the primary surface where they are then cancelled. No induction at infinity due to these disturbances then appears. With interference of this type, complete elimination of the wave drag due to thickness is possible in principle. In terms of pressure distributions over the system, the effect of this type of interference is to balance the high pressure distributed over the upstream projected area of the system with high pressure distributed over the downstream projected area.

Drag reduction by means of the first type of favorable interference recently has received considerable attention. Stimulated by the implications of the transonic area rule[3] and utilizing the concept of the equivalent source position,[4] a number of investigators[5, 6, 7] have made systematic mathematical studies of favorable wave interference at supersonic speeds by considering the effectiveness at the remote control surface of planar and linear distributions of disturbances representing wing-body combinations. Fuselage contouring is proposed which attenuates wing-body disturbances at infinity. Wing-body combinations which exhibit minimum drag under prescribed restraints are discussed. Experiments indicate that the significant drag reductions predicted by the theory are often possible, although the theoretical findings are subject to considerable practical interpretation.

Other investigators have observed that considerable favorable interference of this type between aircraft components can be realized by considering directly the nature of the pressure field induced by each component on adjacent solid boundaries. Attempts are made to orient and contour the surfaces of components appearing in a given system so that each component receives a thrust contribution from the pressure fields

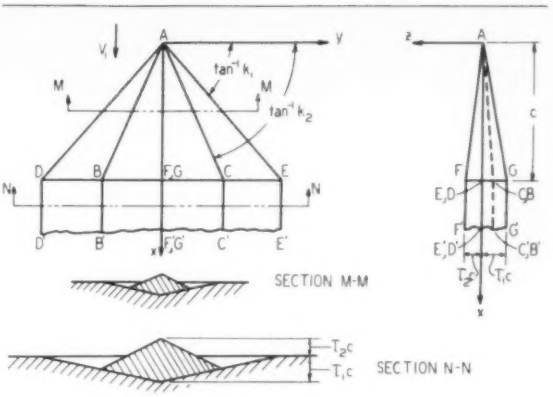

FIG. 1. Canopy configuration.

induced by other components. These engineering considerations, which are predicated on the direct rather than the indirect formulation of drag, provide a relatively simple approach to wave drag reduction in which practical restraints are prominent but from which absolute optima are not usually forthcoming.

As an elementary example, consider a protuberance consisting of the triangular pyramid ABFC which is followed by a semi-infinite right triangular prism (see Fig. 1). The protuberance rests on the infinite x-y plane in an axial supersonic stream as shown in Fig. 1. The protuberance might represent, for example, an aircraft canopy mounted on a circular cylindrical fuselage of very large radius. It is proposed to contour the x-y plane in the neighborhood of the canopy in order to establish a favorable interference. Suppose that a recess or indentation is produced in the plane whose shape is again described by a triangular pyramid followed by a semi-infinite right triangular prism. The canopy then rests in the recess as shown in Fig. 1. If the surface inclinations are regarded to be sufficiently winglike, the geometry is represented in terms of linearized wing theory (see for example, reference 8) by a uniform distribution of sources over ABC and a uniform distribution of sinks over ABD and ACE. If the height of the point F above the x-y plane is $\tau_2 c$ and if the depth of the point G below the x-y plane is $\tau_1 c$, then the inclination in the planes parallel to the x-z plane of surfaces ABF and ACF is τ_2 and the like inclination of surfaces ABD and ACE is $-\tau_1$. The surfaces downstream of the line $x = c$ exhibit no such inclination and thus require no source distributions. The sweep of the leading edges of the canopy is given by $n_2 \equiv k_2/B > 1$ and of the recess by $n_1 \equiv k_1/B$. The drag of the system, supported on the exposed surfaces of the pyramids only, is readily calculated. It is evident that the pressure field induced by the exposed recess is of opposite sign to that induced by the canopy and that a favorable interference has been established between the two. On the other hand, the selfinduced drag of the recess is positive. With a suitably chosen recess, the drag of the system can be reduced to a value below that of the isolated canopy.

From the computed drag of the system the optimum

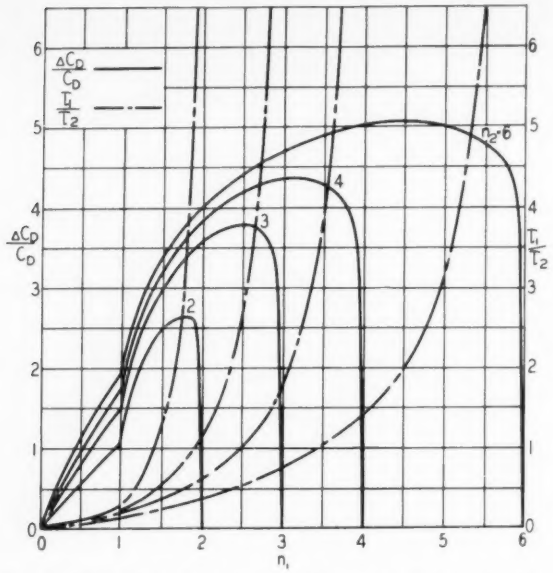

FIG. 2. Relative drag reduction of canopy configuration for optimum inclination of indentation; c, n_2, and τ_2 prescribed.

values of the recess parameters n_1 and τ_1 have been computed for two cases. First regard the values of n_2, τ_2, and c as prescribed; then the height of the point F on the canopy above the x-y plane is fixed. The minimum drag of the system for optimum value of τ_1 may be obtained in terms of n_1 by differentiation. In Fig. 2 is presented the relative drag reduction as a function of n_1 for various values of the canopy sweep parameter n_2. The quantity C_D represents the drag of the isolated canopy for the same values of n_2, τ_2, and c. The quantity ΔC_D is defined as the drag of the isolated canopy minus the minimum drag of the system. The corresponding optimum ratio τ_1/τ_2 is also plotted versus n_1 for various values of n_2 in the same Figure. The optimum value of n_1 for the prescribed n_2 may be noted from the stationary point on each curve for $\Delta C_D/C_D$. This value of n_1 is only slightly less than the corresponding value of n_2. It is seen that the maximum value of $\Delta C_D/C_D$ increases with increasing n_2 whereas the associated value of τ_1/τ_2 decreases with increasing n_2. The maximum value of $\Delta C_D/C_D$ is about $^1/_2$ when $n_2 = 6$. When the recess is optimum for a given canopy, it is seen from Fig. 2 that τ_1 is several times τ_2. But, because n_1 is only slightly less than n_2, most of the recess is covered by the canopy and the actual indentation depth is much less than $\tau_1 c$.

Suppose now that n_2, $(\tau_1 + \tau_2)$, and c are prescribed; in this case the total height of the canopy $(\tau_1 + \tau_2)c$ is fixed (this is the length FG in Fig. 1) but the canopy is permitted to sink into the recess without constraint. The calculations just described for the first case may be repeated for this case. In Fig. 3 is presented $\Delta C_D \div C_D$ versus n_1 for several values of n_2 and the optimum value of $\tau_1/(\tau_1 + \tau_2)$ versus n_1 for the same values of n_2. For given n_2 and for $n_1 < n_2$, it may be seen that the drag reductions tend to be large and that the protuberance extends above the x-y plane. When $n_1 = n_2$, the drag of the system is zero and $\tau_1 = (\tau_1 + \tau_2)$. We thus arrive at the trivial result wherein the protuberance is completely submerged in the recess and the x-y plane is completely free of disturbance. This simple problem illustrates on the one hand that large drag reductions can be obtained by use of favorable interference and on the other hand that care must be exercised to impose realistic restraints on geometric modifications.

A classical example of the second type of interference is the two-dimensional Busemann biplane.[1] The configuration, consisting of two symmetrically arranged wings, is illustrated in Fig. 4 in the nonlinear instance and in Fig. 5 in the linear instance. The waves produced at the leading edge of each wing are reflected from the opposite wing, as shown in the figures, and are then cancelled on the back of the original wing. The wave drag of the system (to the second approximation) is zero because no waves are propagated to infinity. The pressure distribution on each wing is symmetric. An axially symmetric counterpart, consisting of a body enveloped by a cowling (see Fig. 6), was proposed in reference 9 and analyzed in reference 10.

It is of interest for later application to discuss further the nature of the linearized flow field in Fig. 5. The disturbances produced by the surface AB are transmitted unchanged to the flow in the region between parallel waves AE and BF. If the surface EF has the same inclination as AB, no reflections of the waves AE and BF occur. The pressure forces on the two surfaces are equal and opposite so that their resultant is a pure couple. The surfaces DE and BC bear a similar relationship, supporting a couple equal and opposite to the first. It is evident that the flow field in the region ABCNTA is unaltered if the stream surface TN is replaced by a flat reflecting plate of zero thickness and if the upper wing is subsequently removed. Then the waves AT and BN, produced by the surface AB, are reflected from the plate TN as waves of the opposite

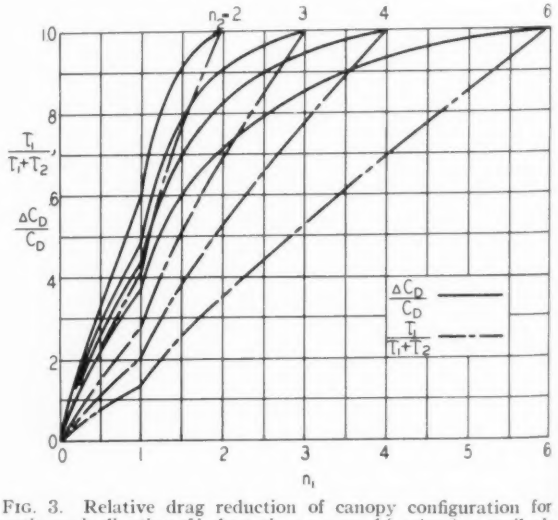

FIG. 3. Relative drag reduction of canopy configuration for optimum inclination of indentation; c, n_2, and $(\tau_1 + \tau_2)$ prescribed.

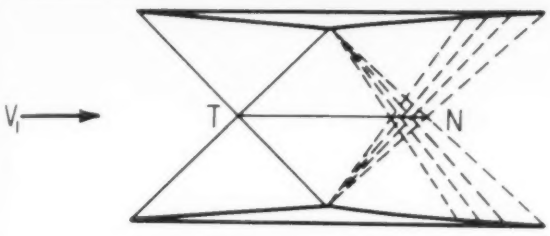

FIG. 4. Nonlinear Busemann biplane.

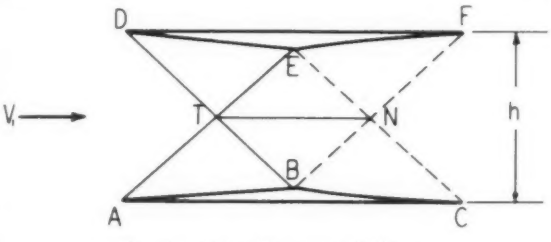

FIG. 5. Linear Busemann biplane.

family. There is produced along the surface BC a pressure disturbance of the same sign and a deviation of opposite sign as that existing along surface AB. Since the inclination of BC is equal and opposite to that of AB, no reflections of the waves TB and NC occur. The axial pressure forces on the surfaces AB and BC balance each other and their resultant normal force balances the resultant normal force supported by the plate.

The remainder of the present report is concerned with analogous favorable interference between three-dimensional swept wings and reflecting surfaces in biplane arrangement. Reflecting surfaces will be proposed which reduce the wave drag due to thickness of the given wing. The necessity of dealing with the reflection of three-dimensional waves makes an analysis of the problem considerably more involved than the analogous two-dimensional treatment.

Determination of the Interference Effects Between Three-Dimensional Surfaces

The interference between a wing and a reflecting surface were analyzed in reference 1 for the case of two-dimensional supersonic flow. In reference 11 two identical wings of rectangular plan form oriented in the Busemann relationship were analyzed by linear theory to determine the tip effects due to finite aspect ratio. The more general case of a three-dimensional wing of variable chord interacting with a reflecting surface can also be analyzed by means of linearized wing theory.

Consider, for example, the biplane configuration shown in Fig. 7. Let the geometric angle of attack of both wing and reflecting surface be zero. Suppose for simplicity of discussion that all edges of each plan form are supersonic and that a source-sink distribution, of intensity proportional to the local slope $\partial z/\partial x$ of the surface, is used to represent each wing, considered isolated, in the usual manner. The pertinent velocity and pressure field may then be calculated from the well-known relations

$$\varphi(x, y, z) = -\iint_{\tau} \frac{f(\xi, \eta)d\xi d\eta}{\sqrt{(x-\xi)^2 - B^2(y-\eta)^2 - B^2(z-\zeta)^2}} \tag{2}$$

$$u(x, y, z) = \partial\varphi/\partial x \tag{3}$$

$$w(x, y, z) = \partial\varphi/\partial z \tag{4}$$

$$c_p = -2u/V_1 \tag{5}$$

where the integration is to be extended over the planar regions τ which appear inside the fore Mach cone from the point $P(x, y, z)$.

The distribution of w in the plane of the reflecting surface due to the wing may be found from these relations. An additional distribution of sources must be added in the region of the reflecting surface to cancel this upwash and thereby to maintain the boundary shape, the source intensity at each point being proportional to the value of w at the same point. The pressure distribution over the reflecting surface, due to the source distributions in this surface and in the forewing, may then be calculated. Similarly, the distribution of downwash over the back of the wing due to the complete source distribution in the reflecting surface is to be computed. An additional source distribution must be added on the upper wing surface to cancel this downwash. The pressure distribution over the wing may then be computed, and can be considered in two parts: the pressure distribution induced by the sources representing the isolated wing, and the pressure distribution

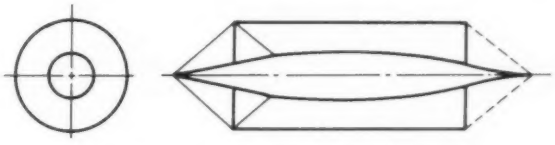

FIG. 6. Body of revolution enveloped by cowling.

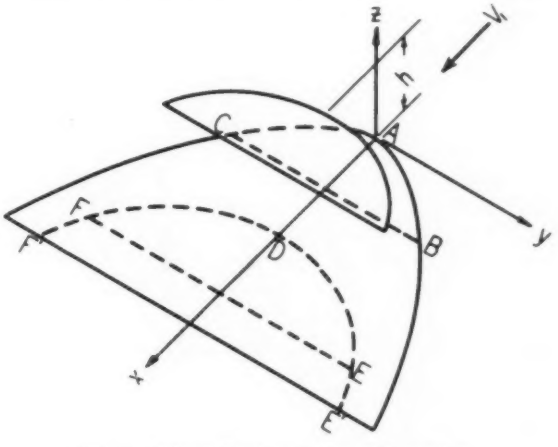

FIG. 7. Wing-reflecting surface configuration.

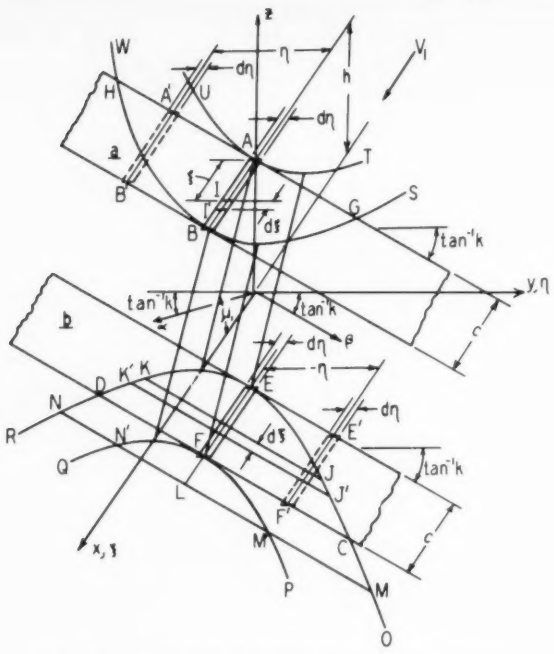

FIG. 8(a). Flow field of elemental source distributions.

induced by both the complete distribution of sources representing the reflecting surface and the interference sources in the afterwing. The first leads to the drag of the isolated wing and the second to the interference drag of the wing. If the wing lies in a region influenced by the flow behind the trailing edge of the reflecting surface, then the influence of this wake on the wing must also be considered.

This tedious procedure is unlikely to suggest the criteria by means of which superior configurations—i.e., those giving substantial favorable interference, might be proposed. It would appear that integral relationships, providing information on the total amount of upwash and on the total pressure force without recourse to determination of the flow field, would implement the development and analysis of suitable wing-reflecting surface configurations.

Such relations are in fact suggested by an examination of the linearized flow field of the two-dimensional Busemann biplane which is illustrated in Fig. 5. As previously discussed, the drag of the system is zero because the disturbances produced by the surface DE are transmitted to the surface BC, along which there results a balancing thrust and, collaterally, the closure of the lower wing without reflection (surfaces AB and EF have a similar relationship). For generality we superpose a spanwise component to the undisturbed stream shown in Fig. 5; according to simple sweep theory the spanwise velocity remains everywhere the same and the perturbation flow field is unchanged. Let k be the tangent of the resulting sweepback angle. We then consider further the relationship between the complementary surfaces DE and BC with the aid of Fig. 8(a). The surface a is the half of the chord plane DF in Fig. 5 which supports the inclination DE, and the surface b is the half of the chord plane AC in Fig. 5 which supports the inclination BC. The streamwise chord of surfaces a and b is denoted by c in the Figure. Surfaces a and b are supplied in Fig. 8(a) for the purposes of reference and orientation. The inclination DE in Fig. 5 is represented in Fig. 8(a) by distributing over the lower face of the surface a a source distribution of constant intensity proportional to f.

Identify on b a streamwise element of area EF whose chord is c and whose elemental width is $d\eta$. For convenience the leading and trailing edges of this element (and of similar elements to follow) are taken parallel to the y axis; the discrepancies are of higher order. The fore Mach cones from points E and F result in the hyperbolic traces TAU and SBW, respectively, in the plane $z = h$. These hyperbolas are tangent to the leading and trailing edges of plane a at points A and B, respectively. The perturbation velocity field established over the element EF (and, indeed, everywhere in the region between the plane of the leading edges of a and b and the plane of the trailing edges of a and b) by the constant inclination existing over the lower surface of a follows immediately from two-dimensional flow considerations as

$$u = -\pi f B\sqrt{1 - n^2} \tag{6}$$

$$w = -\pi f \tag{7}$$

in terms of the wind axes shown. Here n is defined as the ratio of k to B. These perturbations are induced by disturbances appearing in the region GBH of the plane a. We can then form the two area integrals over the elemental area EF

$$\int_{EF} u_{GBH}\, dA = -\pi f c d\eta\, B\sqrt{1 - n^2} \tag{8}$$

$$\int_{EF} w_{GBH}\, dA = -\pi f c d\eta \tag{9}$$

Let the region of plane a between points G and H be subdivided into a lateral array of streamwise elemental areas such as AB and A′B′, each having the elemental width $d\eta$. Each area supports a uniform source distribution. The induction over EF, given by Eqs. (6) and (7), can be regarded as the summation of the contributions of each of these elemental distributions, since at least part of each influences EF. The regions of the plane $z = 0$ influenced by the points A and B of the elemental source AB are defined by the hyberbolic traces OER and PFQ of their respective Mach cones; these are tangent to the leading and trailing edges of b at points E and F, respectively. The element AB influences the plane b in the region CED. The element A′B′, whose lateral distance from AB is η, produces a similar pair of hyperbolas which are displaced laterally a distance η and longitudinally a distance $k\eta$ from the first pair. Let E′F′ be an element of area displaced from element EF by a lateral distance $(-\eta)$ and a longitudinal distance $(-k\eta)$. Because the physical phenomena depend on only rela-

tive distances and not on the absolute coordinates, the induction over E′F′ due to AB is the same as the induction over EF due to A′B′. Suppose, as before, that the region of plane b between points C and D is subdivided into a lateral array of streamwise elemental areas like EF and E′F′. Then, by summation of like effects, the integral of the induction over all the elements of area which compose the region CED due to the elemental source distribution AB is equal to the integral of induction over the elemental area EF due to the array of elemental source distributions composing the region GBH. Thus,

$$\int_{\text{CED}} u_{\text{AB}}\, dA = \int_{\text{EF}} u_{\text{GBH}}\, dA \tag{10}$$

$$\int_{\text{CED}} w_{\text{AB}}\, dA = \int_{\text{EF}} w_{\text{GBH}}\, dA \tag{11}$$

But the right-hand members of Eqs. (10) and (11) are given by Eqs. (8) and (9), respectively. We therefore obtain the relations

$$\int_{\text{CED}} u_{\text{AB}}\, dA = -\pi f c d\eta / B\sqrt{1 - n^2} \tag{12}$$

$$\int_{\text{CED}} w_{\text{AB}} dA = -\pi f c d\eta \tag{13}$$

which give the integral of induction over region CED due to the elemental source distribution AB, whose intensity is given by f, whose chord is given by c, and whose width is $d\eta$.

Consider a point L located on the streamwise axis of the elemental area EF at an arbitrary distance downstream of the point F. Construct a line segment through point L parallel to the edges of surface b such that it extends from one branch of the hyperbola OER to the other branch. It is evident from two-dimensional considerations that the induction of L due to the above-mentioned lateral array of elemental source distributions extending from point G to point H on surface a is zero. From the same argument applied above, it follows that the line integral of the induction due to elemental source distribution AB along the line segment through L is zero. That is,

$$\int_{\text{N}}^{\text{M}} u_{\text{AB}}\, ds = 0 \tag{14}$$

$$\int_{\text{N}}^{\text{M}} w_{\text{AB}}\, ds = 0 \tag{15}$$

It follows from Eqs. (14) and (15) that the area integral of induction due to element AB is zero over any region circumscribed by the two branches of hyperbola OER, by the line segment CD, and by any line parallel to CD which is downstream of CD.

Consider a point I on the element AB whose distance downstream from point A is ξ. Consider an associated point I′ whose distance downstream from point A is $(\xi + d\xi)$. Let KJ and K′J′ be line segments parallel to CD which are tangent to the hyperbolic traces in the x-y plane from points I and I', respectively. Apply the theorems expressed in Eqs. (12) and (13) to obtain the integral of induction over region J′EK′ due to element AI′. Subtract from this the integral of induction over region JEK due to the element AI. This difference gives the integral of induction over the elemental area JJ′K′K due to the elemental source distribution AI′. Noting that the induction due to element AI′ is the same as that due to element AB in this region, and dividing by the elemental length $d\xi$, one finds

$$\int_{\text{K}}^{\text{J}} u_{\text{AB}}\, dy = -\pi f d\eta / B\sqrt{1 - n^2} \tag{16}$$

$$\int_{\text{K}}^{\text{J}} w_{\text{AB}}\, dy = -\pi f d\eta \tag{17}$$

It is seen that the line integrals are independent of the distance ξ; thus the value of the integral of induction along all oblique line segments like KJ which are within region CED is the same. Because Eqs. (16) and (17) supply information on the distribution of induction due to the element AB in the region CED, they supplement Eqs. (12) and (13).

The relations derived provide information on the induction due to a source distribution, whose constant intensity is proportional to f, over the elemental area $cd\eta$. It is clear that this disturbance can be regarded as a line source of constant linear intensity proportional to $fd\eta$, provided that the distance h is finite. Therefore, the relations derived still hold if the element AB is rotated about its streamwise axis to an arbitrary position. Moreover, the distance c may be made arbitrarily small. The above relations can now be recast in a readily applicable form with the aid of Fig. 8(b). Consider a rectangular element of area $d\xi d\omega$ on some surface supporting a source distribution. Let

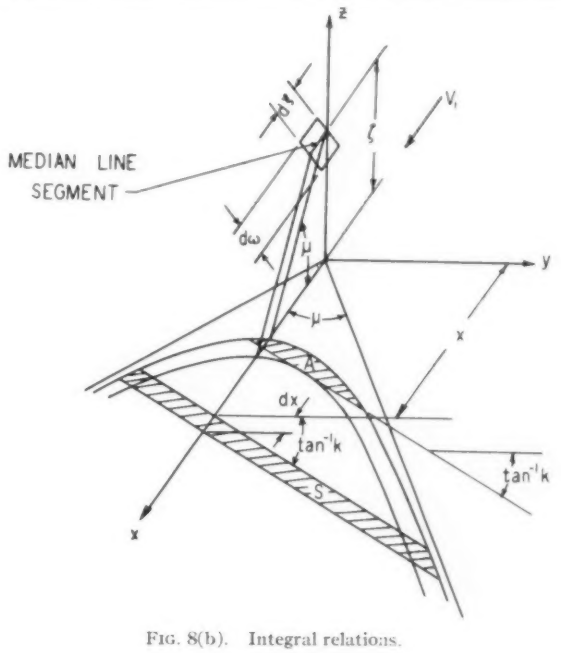

FIG. 8(b). Integral relations.

the lateral edges of the element be streamwise. Let δu and δw be the x and z components, respectively, of the perturbation velocity induced in the x-y plane by the elementary source distribution f supported by the element of area. Then Eqs. (12), (13), (14), and (15) may be written

$$\int_A \delta u \, dA = -\pi f \, d\xi \, d\omega \, B\sqrt{1 - n^2} \tag{18}$$

$$\int_A \delta w \, dA = \mp \pi f \, d\xi \, d\omega \tag{19}$$

$$\int_S \delta u \, dS = 0 \tag{20}$$

$$\int_S \delta w \, dS = 0 \tag{21}$$

where $n = k/B$, where the areas A and S are related to the hyperbolas and oblique line segments as shown in Fig. 8(b), and where the minus sign applies in Eq. (19) when $\zeta > 0$ and the plus sign applies when $\zeta < 0$. An analytical derivation of these integral relations is given in the Appendix.

For certain classes of configurations, Eqs. (18) through (21) can be used to determine the total lift or drag and the integral of the downwash induced by a system of disturbances without computing the flow field of these disturbances.* In the present paper they will be used for the analysis of the interference between the parallel surfaces of three-dimensional biplanes. Because only unswept trailing edges will be considered, the value of the parameter n will henceforth be zero.

Consider the evaluation of the drag of the previously discussed wing-reflecting surface configuration illustrated in Fig. 7 by means of the integral relations just developed. In addition to the aforementioned characteristics of the configuration, assume that the reflecting surface is a flat plate. Suppose that the preliminary step requiring the representation of the isolated wing by a distribution of sources and the calculation of its drag has been accomplished and that the interference drag is to be computed. Let the distribution of sources on the wing which influence the reflecting plate be ABC. The integral of the upwash from region ABC over the plan form of the reflecting plate may be computed from Eq. (19), taken with the plus sign, and from Eq. (21), provided that the two hyperbolic traces (which sensibly merge) in the plane of the reflecting surface from each elemental source in region ABC intersect the plan-form boundary of the plate only along a straight trailing edge. We assume that the leading and trailing edges of the plate in Fig. 7 conform with this requirement. Thus the shape of the plate is given by the curved envelope of hyperbolas emanating from points on the leading edge of the region ABC (coinciding with the leading edge of the wing) and by the straight line which comprises the envelope of hyperbolas emanating from points on the straight line BC. It is further assumed here that the trailing edge of the plate (and, consequently, line BC) is unswept. The leading edge of the plate is seen to extend forward to the undisturbed flow; it may, of course, be extended farther upstream with no effect. In order to satisfy the boundary conditions, a distribution of sources is to be added over the plan form of the plate which cancels this upwash with downwash, point by point. By superposition of the effect of each elemental source in region ABC, given by Eqs. (19) and (21), it follows that

$$\pi \int_{\text{plate}} f \, dS = -\int_{\text{plate}} w_{\text{plate}} \, dS = \int_{\text{plate}} w_{\text{ABC}} \, dS = \pi \int_{\text{ABC}} f \, dS \tag{22}$$

Let the region DEF in the plane of the wing be constructed from the envelopes of hyperbolas originating from points on the periphery of the plate in the manner described above. Let DE′F′ be the entire region of the wing influenced by the plate. The integral of the downwash induced by the plate on the afterwing may be determined as above, providing again that the pair of hyperbolas associated with each elemental source in the plate intersect the plan-form boundary of the wing only along a straight trailing edge, which is here also assumed unswept. Then the total source strength in the plane of the wing necessary to cancel this downwash is

$$\int_{\text{DEF}} f \, dS = \int_{\text{plate}} f \, dS \tag{23}$$

If the line EF falls downstream of the trailing edge of the wing, only that part of the plate influencing the afterwing should be considered in the present calculation. If the wake of the plate is not to influence the wing and if, concurrently, the full effect of the plate on the wing is to be obtained, then the plane of the trailing edges of plate and wing must be inclined at the angle μ to the x axis so that EF coincides with E′F′. Such an orientation is henceforth assumed.

The integral over DEF of u due to the plate source distribution may be obtained by superposition of the effects of each elemental source in the plate given by Eqs. (18) and (20). Just as above,

* Those relations above which give the integral of the pressure, as well as some additional information on the center of pressure, are briefly indicated in reference 12 for the case $n = 0$. Although no applications are presented, the possibility of the application of those integral relations to cruciform wing arrangements is mentioned. Proofs are not presented in reference 12, but the author indicates that the relations he gives are generalizations of similar relations which are derived in reference 13. The latter expressions give the value of the integral of source-induced pressure over the plane which contains the elemental source, as well as the corresponding center of pressure. They are used in reference 13 to compute the lift and center of pressure of planar wings; several interesting planar systems with both swept and unswept trailing edges are considered. The different point of view presented herein provides information on the integral of downwash as well as pressure and facilitates repeated application of the relations in multiple reflection problems for the purpose of the calculation of drag.

$$\int_{DEF} u_{plate}\, dS = -(\pi/B)\int_{plate} f\, dS \qquad (24)$$

In order to find the corresponding integral effect due to the sources in the afterwing, Eqs. (18) and (20) are used for the degenerate case where the distance ζ in Fig. 8(b) is zero. Thus,

$$\int_{DEF} u_{DEF}\, dS = -(\pi/B)\int_{DEF} f\, dS \qquad (25)$$

The value of the integral of u on the wing due to the complete interference is found by combining Eqs. (22), (23), (24), and (25) to obtain

$$\int_{DEF} u\, dS = -2(\pi/B)\int_{ABC} f\, dS \qquad (26)$$

The interference drag is defined by the formula

$$D_i/(\rho_1 V_1^2/2) = -(2/V_1)\int_{DEF} \lambda u\, dS \qquad (27)$$

If the inclination λ is considered constant over region DEF, Eqs. (26) and (27) then give, for the interference drag of the wing,

$$D_i/(\rho_1 V_1^2/2) = (4\pi\lambda/BV_1)\int_{ABC} f\, dS \qquad (28)$$

where λ is generally negative over DEF. The drag of the reflecting plate, having no inclination, is necessarily zero. With the specified geometric restrictions, the interference is evidently quasi-two-dimensional; it is seen that the interference drag may be readily calculated. The integral relations also indicate, by inspection, that no lift is introduced into these systems when the plate is added.

It is possible to generalize somewhat the restriction that λ be constant over DEF. With use of Eqs. (18)–(21), only the lateral distribution of the induction from each elemental source is unknown. By applying the above procedure to three successive lateral elemental strips in region ABC, in the plate, and in region DEF—each separated by the distance Bh in the x direction—the interference drag may still be computed for the case where $\lambda = \lambda(x)$ in the region DEF of the wing.

The reflecting plate thickness need not have been considered as zero. A distribution of sources representing its thickness may be added but, if its drag is to be computed with the integral relations, the restrictions on λ must be satisfied. Even if the thickness distribution does not fulfill these restrictions, the interference drag of the wing can still be computed with the method discussed. The drag due to this plate thickness could be offset by appropriately recessing the afterwing, if convenient. Alternatively, a stream surface slightly above the reflecting plate in the configuration under discussion may be selected as the lower face of a reflecting surface producing the same effect on the wing as the flat plate. A suitable distribution of singularities must first be assigned to the exterior plate face. This consideration has been discussed in a preceding paragraph in reference to the two-dimensional problem.

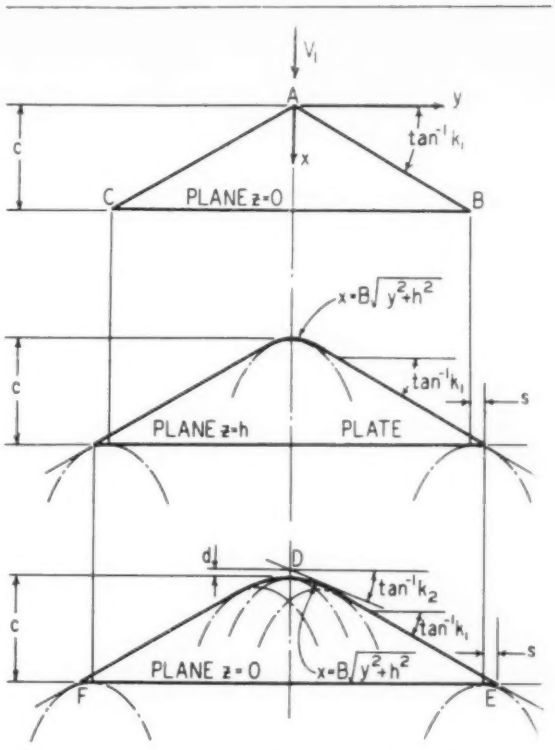

FIG. 9. Interaction regions when region ABC is triangular.

Some applications of the method discussed to the determination of the interference drag of wings and reflecting plates in combination are given in the following section. The configurations considered are variations of Fig. 2. The plates are assumed to have zero thickness; the geometric angles of attack of the wings and plates are likewise zero. The size and orientation of the plate used with each wing are governed by the size of suitable interaction regions ABC and DEF exhibited by the wing considered. In the following examples, the plate will be so selected that line EF coincides with the trailing edge of the wing and region ABC contains sources but not sinks. In Fig. 9, the shapes of the three interaction regions discussed above are shown for the case where the region ABC is triangular. It is seen that the chord of each region is the same. The dimensions s and d, needed for calculations, are found from the geometry to be

$$s = (h/n_1)(1 - \sqrt{1 - n_1^2}) \qquad (29)$$

$$d = 2Bh(1 - \sqrt{1 - n_2^2}) \qquad (30)$$

DRAG OF SOME THREE-DIMENSIONAL BIPLANES

Pentagonal Wing

Consider the sweptback, tapered wing of pentagonal plan form which is shown in Fig. 10. Spanwise sections are dissimilar and the relative thickness dimin-

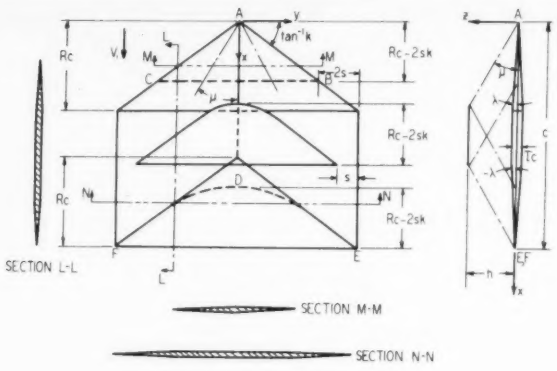

FIG. 10. Pentagonal wing.

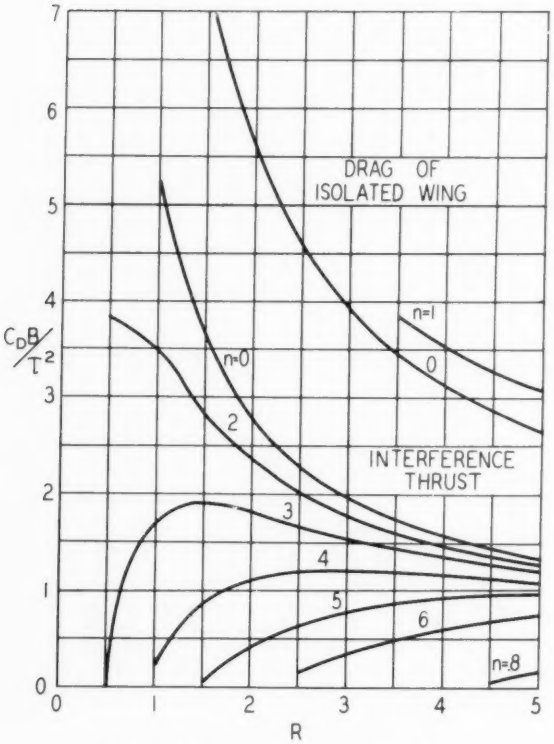

FIG. 11. Symmetric pentagonal wing.

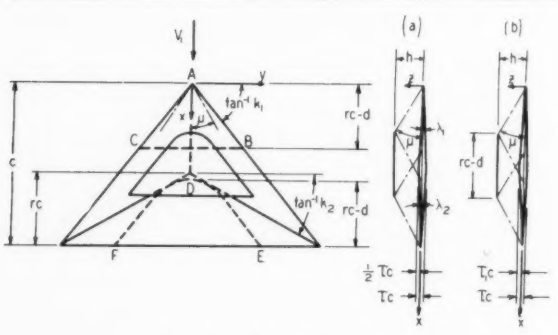

FIG. 14. Triangular wing.

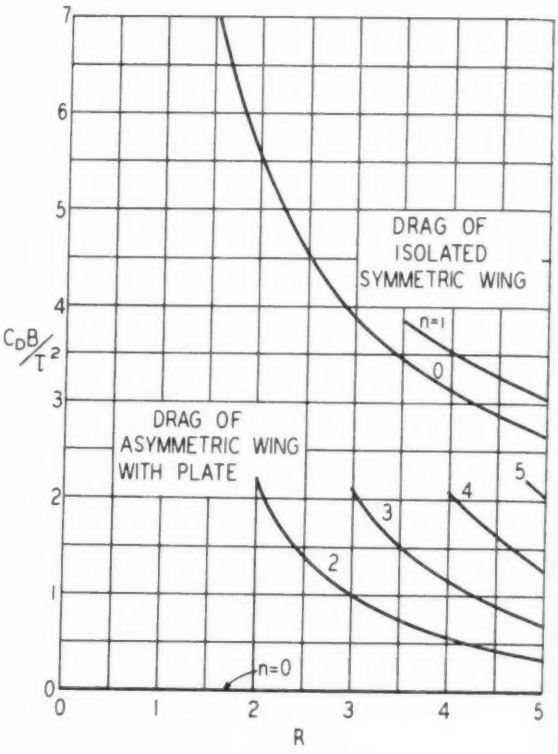

FIG. 12. Pentagonal wing.

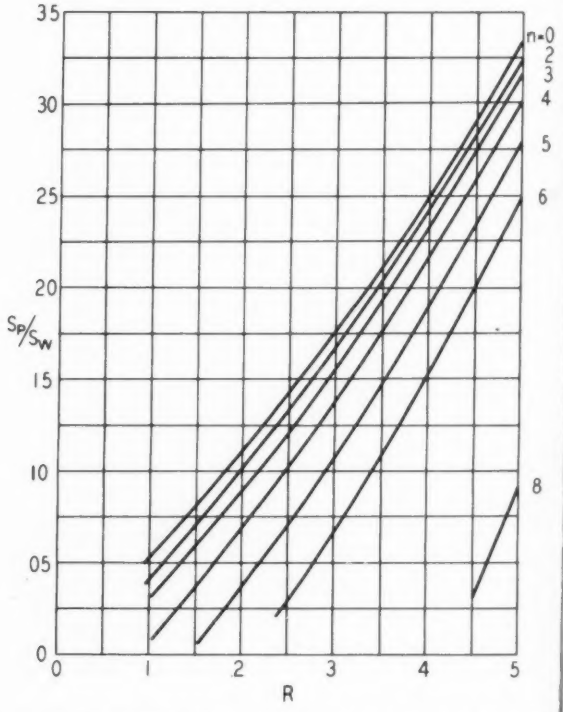

FIG. 13. Pentagonal wing: ratio of plate area to wing area.

ishes along the span, vanishing at the tip. The geometry of the wing is defined by the parameters R, n, c, and τ, where τ is the relative thickness at the root section. The drag may be computed by standard methods of linearized theory and is given in reference 14. The drag parameter $C_D B/\tau^2$ is plotted vs. R for $n = 0, 1$ in Fig. 11 for the case of symmetric distribution of thickness and zero angle of attack.

A reflecting plate for this wing, designed in accord with the discussion of the preceding section, would be triangular in plan form with rounded apex; it could, of course, be extended farther into the undisturbed flow without affecting the interaction. The plate and the other two interaction regions, ABC and DEF, are indicated in Fig. 10. In this example, the plate is so oriented to the wing that EF coincides with the wing trailing edge. In addition, the plate is so sized that DEF is just circumscribed by the triangle of the after-wing plan form. These two assumptions give the maximum interaction amenable to calculation by the method discussed in the last section. The shape and orientation of each of the three interaction elements are thereby specified. The configuration is suggested by two-dimensional considerations applied for the limiting case of n tending to zero. In this case all of the disturbances produced on the plate side of the forewing are intercepted by the plate and reflected back to fully close the wing and balance the fore drag on the plate side. From the diagram

$$h = [(1 - R)c + 2sk]/2B \tag{31}$$

From Eqs. (29) and (31),

$$s = (1 - R)\,(c/2B)\,(1 - \sqrt{1 - n^2})/n\sqrt{1 - n^2} \tag{32}$$

From Fig. 10,

$$\int_{ABC} f\,dS = (V_1\lambda/\pi k)\,(Rc - 2sk)^2 \tag{33}$$

where $\lambda = \partial z/\partial x$ is the constant inclination in region ABC. From Eqs. (28), (32), and (33) the interference drag for the symmetric wing is found to be

$$C_{D_i} B/\tau^2 = -[1/R(2 - R)]\,[1 - (1 - R) \times (1 - \sqrt{1 - n^2})/R\sqrt{1 - n^2}]^2 \tag{34}$$

where

$$C_{D_i} \equiv D_i/(\rho_1 V_1^2/2)S_w$$

$$S_w = (Rc^2/k)\,(2 - R)$$

$$\lambda = \tau/2R$$

Eq. (34) holds when the quantity in the bracket is non-negative. The lateral spreading of disturbances as they pass successively from region ABC to the plate to region DEF (which is characterized by the parameter s) can become so large that the region ABC shrinks to a point for a fixed value of the span of region DEF. This condition occurs when the values of n and R are such that the quantity in the bracket of Eq. (34) vanishes, and corresponds to

$$Rc - 2sk = 0 \tag{35}$$

in Fig. 10.

The interference thrust, given by the negative of Eq. (34), is plotted vs. R, for various values of n, in Fig. 11. The total drag of the configuration for specified value of n is given by the difference of the two curves. If a plate is used on both sides of the symmetric wing, the total thrust is twice the value shown in Fig. 11. In the two-dimensional case, for which $n = 0$, the cancellation of the wing drag on the side of the plate is complete, as is to be expected for this configuration. When n is in the neighborhood of 0.2 or 0.3, the reduction in drag is still of the same order; the thrust obtained with this configuration is very close to the two-dimensional value.

Consider now the same configuration excepting that all the thickness is regarded to be distributed over only the plate side of the wing, the value of τ being unaltered. The opposite side is assumed to be flat and uninclined. In the computation of the isolated wing drag, the interaction between the two faces of the wing at the tips must be considered. Using the methods of reference 15, the contribution of the tips to the drag of the isolated wing may be computed and is given in reference 14. The total drag coefficient of the asymmetric isolated wing is found by adding to this tip drag coefficient twice the value of the drag coefficient of the symmetric isolated wing. It is found that the contribution of the tip drag to the total is virtually negligible ($n \lesssim R$). The interference drag coefficient is four times that value given by Eq. (34). In Fig. 12, the total drag of the asymmetric wing with plate is compared to the drag of the isolated symmetric wing having the same total thickness. This basis of comparison is a conservative one because, for given values of n, R, and τ, the drag of the isolated wing is a minimum when the thickness is symmetrically distributed. In the two-dimensional instance, corresponding to $n = 0$, the cancellation of the drag of the asymmetric wing by the plate is complete. When n is in the neighborhood of 0.2 or 0.3 and R of order 0.5, the drag is still much less than that of the isolated symmetric wing. For example, if $n = 0.3$ and $R = 0.5$, the drag of the configuration is about 25 per cent of the drag of the isolated symmetric wing or $12^1/_2$ per cent of the drag of the isolated asymmetric wing. The range $0 \lesssim n \lesssim 0.3$, in which interference of the biplane type is seen to be most effective, is particularly appropriate to the higher Mach Number regime.

The ratio of plate area to wing area S_p/S_w is plotted vs. R for several values of n in Fig. 13. It is seen that the plate area is only about 30 per cent of the wing area with good interference.

Triangular Wing

The second problem considered is that of the interaction between a wing with triangular plan form and a suitable reflecting plate (see Fig. 14). The wing has diamond profiles which are geometrically similar and is characterized by the parameters r, n_1, c, and τ when the profiles are regarded as symmetric; the case of

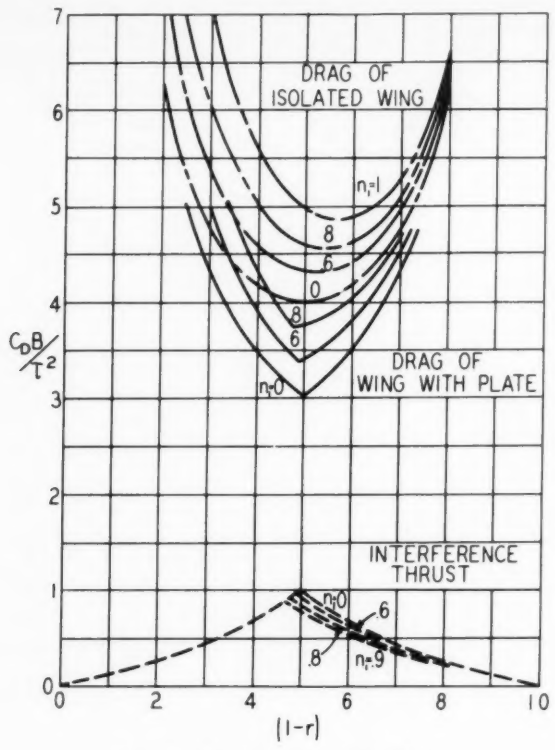

FIG. 15. Symmetric triangular wing.

supersonic leading edges—i.e., $n_1 < 1$—is of interest here. Again the drag is readily calculated by linearized methods[8, 16] and is shown plotted vs. $(1 - r)$ for several values of n_1 in Fig. 15 for the case of a symmetric thickness distribution.

The design and orientation of the reflecting plate is dictated by considerations similar to the preceding example. In the case of small r, the size and shape of the afterwing region having constant inclination governs the size of the interaction elements. For maximum interference under this restriction, the region DEF will be inscribed in the triangle whose altitude is rc and whose base is the wing trailing edge. The size and orientation of the three interaction regions are thereby determined, their chord being $(rc - d)$. From Fig. 14(a), and Eq. (30),

$$h = [(1 - r)c + d]/2B \tag{36}$$

$$d = c(1 - r)\,(1 - \sqrt{1 - r^2n_1^2})/\sqrt{1 - r^2n_1^2} \tag{37}$$

From Fig. 14,

$$\int_{ABC} f\,dS = (V_1\lambda_1/\pi k_1)\,(rc - d)^2 \tag{38}$$

From Eqs. (28), (37), and (38), the interference drag for the symmetric wing is found to be

$$C_{D_i}B/\tau^2 = -(r/1 - r)\,[1 - (1 - r/r) \times (1 - \sqrt{1 - r^2n_1^2})/\sqrt{1 - r^2n_1^2}]^2 \tag{39}$$

when the quantity in the bracket is non-negative. Here the drag coefficient is based on the wing area

$$S_w = c^2/k_1 \tag{40}$$

and the relations

$$\lambda_1 = \tau/2(1 - r) \qquad \lambda_2 = -\tau/2r \tag{41}$$

have been used. Eq. (39) holds as long as the afterwing governs; from Fig. 14 this condition may be written

$$(rc - d) \gtrless (1 - r)c \tag{42}$$

or

$$[1 - (1 - r/r) \times (1 - \sqrt{1 - r^2n_1^2})/\sqrt{1 - r^2n_1^2}] \gtrless (1 - r/r) \tag{43}$$

If the upstream interaction region is to contain only compressive disturbances, then, for values of n_1 and r not satisfying Eq. (43), the forewing governs the size of the three interaction elements. The region ABC is then selected so as to be inscribed in the triangle formed by the leading edge of the wing and the line $x = (1 - r)c$. The line EF is still selected to be coincident with the trailing edge of the wing. There is then obtained

$$h = rc/2B \tag{44}$$

$$\int_{ABC} f\,dS = (V_1\lambda_1/\pi k_1)\,(1 - r)^2c^2 \tag{45}$$

and

$$C_{D_i}B/\tau^2 = -(1 - r)/r \tag{46}$$

Eq. (46) applies to the symmetric wing when Eq. (43) holds with the inequality sign reversed.

The plate thrust, given by the negative of Eqs. (39) and (46), is plotted vs. $(1 - r)$ for several values of n_1 in Fig. 15 and may be compared to the drag of the isolated symmetric wing. The total drag of the biplane configuration is also given. By using a reflecting plate on both sides of the wing, the reduction in drag could be doubled. Fig. 15 shows that the relative wave drag reductions are not nearly as large as in the case of the pentagon wing. That the triangular wing is not particularly suited for use with a reflecting plate may be seen from an application of two-dimensional methods to the limiting case of n_1 tending to zero and $(1 - r) = 0.5$. Only one-half of the compressive disturbances from the forewing on the plate side are intercepted and reflected back to the afterwing by the plate. Thus the plate eliminates only one-half of the two-dimensional drag of the plate side of the wing. This observation is borne out by Fig. 15. A similar discussion applies when n_1 is non-zero.

The ratio of reflecting plate area to wing area is shown in Fig. 16 and is seen to be quite small. If $(1 - r) = 0.5$ and $n_1 = 0.3$, it may be seen from Figs. 15 and 16 that the wave drag reduction obtained with one plate is about 23 per cent of the drag of the isolated symmetric wing, whereas the area of the reflecting plate is about 26 per cent of the wing area.

Due to the asymmetry of the configuration when only one plate is used, a symmetric distribution of wing thickness does not give the minimum configuration drag for given values of n_1, r, and τ. The minimum drag

corresponds to a profile having more than half of the total thickness on the plate side. Let τ_1 be the constant relative thickness on the plate side of the wing and $(\tau - \tau_1)$ be the relative thickness on the other side, where τ represents the total relative thickness [see Fig. 14(b)]. The interference drag is given by Eqs. (39) and (46) with τ replaced by $2\tau_1$. The total drag of the configuration, written in terms of τ_1 and $(\tau - \tau_1)$ with the aid of references 16 or 8, may be minimized with respect to variations of τ_1/τ. The total configuration drag, for optimum τ_1/τ, is plotted vs. $(1 - r)$ for several values of n_1 in Fig. 17. These results are compared to the drag of the symmetric isolated wing in this Figure. The optimum ratio of τ_1/τ is also shown. By comparing Figs. 15 and 17, it may be seen that the configuration drag is somewhat reduced by the redistribution of the thickness. If $(1 - r) = 0.5$ and $n_1 = 0.3$, the drag reduction in the asymmetric case is about 30 per cent of the drag of the isolated symmetric wing. It may be pointed out that the size and orientation of the plate remains unchanged by the redistribution of thickness.

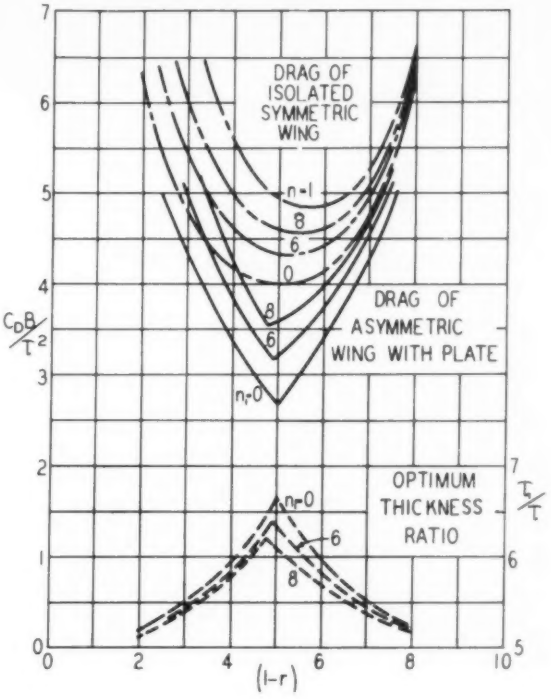

FIG. 17. Triangular wing.

Triangular Wing with Pentagonal Protuberance

One can design the reflecting plate large enough to intercept a major part of the disturbances originating from the forewing. A smaller reflecting plate, designed to intercept only disturbances produced near a possibly thick root section, can also be envisaged. Consider a symmetric triangular wing to which there is added a pentagonal protuberance on one side in the vicinity of the root section. There results a wing with a variable spanwise distribution of relative thickness. The protuberance might be regarded as a storage volume. Such a configuration, obtained by geometric superposition of the wings discussed in the first two examples, is shown in Fig. 18. It is assumed that $n_1 < 1$. If τ_I represents the relative thickness of the symmetric basic wing and if τ_{II} represents twice the maximum relative thickness of the protuberance on one side of the wing (see Fig. 18), then the wing is geometrically characterized by the parameters r, n_1, c, τ_1, and T, where

$$T = \tau_{II}/\tau_1 \tag{47}$$

The isolated drag of the protuberance side of the wing has been computed and is given in reference 14. The drag of the opposite side may be found in references 16 or 8. The complete drag of the isolated wing is plotted vs. $(1 - r)$ for several values of n_1 in Figs. 19, 20, and 21, which correspond to values of T of 0.5, 1.0, and 2.0, respectively. Also shown in each Figure for comparison is the drag of the isolated wing without the protuberance.

The size, shape, and orientation of the reflecting plate is identical with the first example, providing that the chord c is the same in each case. Then the distances h and s are given by Eqs. (31) and (32), respectively, wherein R is replaced by r, k by k_1, and n by n_1. From Fig. 18,

$$\int_{ABC} f\,dS = \Gamma_1(\lambda_1 + \lambda_3)\,(rc - 2sk_1)^2/\pi k_1 \tag{48}$$

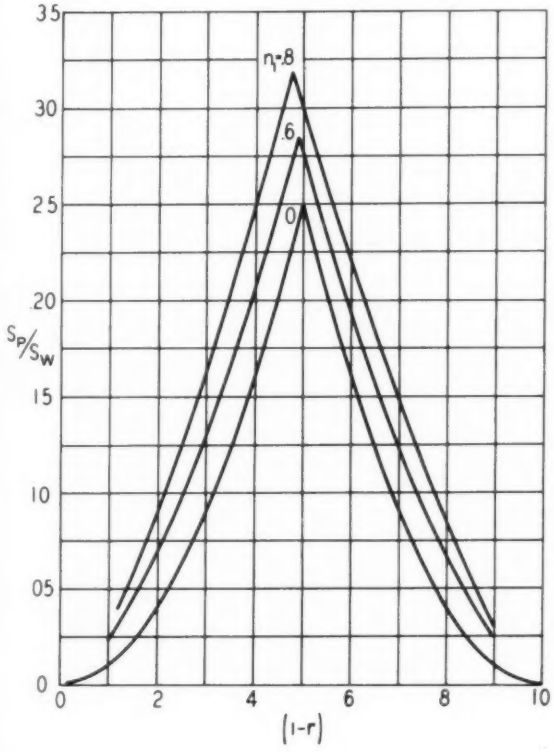

FIG. 16. Triangular wing: ratio of plate area to wing area.

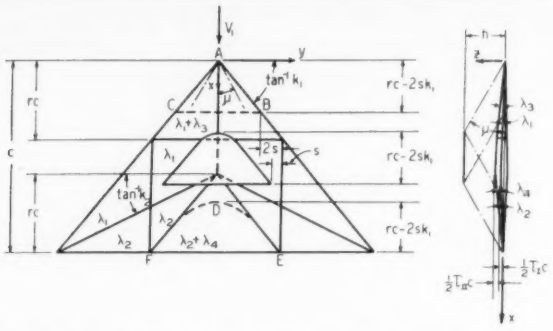

FIG. 18. Triangular wing with pentagonal protuberance.

With use of Eq. (28), there results for the interference drag

$$C_{D_i}B/\tau_1^2 = -(1 + T)\,[r/(1 - r)] \times [1 + T(1 - r)/r]\,[1 - (1 - r) \times (1 - \sqrt{1 - n_1^2})/r\sqrt{1 - n_1^2}]^2 \quad (49)$$

providing the squared quantity in brackets is non-negative.

The interference thrust, given by the negative of Eq. (49), is plotted vs. $(1 - r)$ for several values of n_1 in Figs. 19, 20, and 21, these curves being drawn for values of T of 0.5, 1.0, and 2.0, respectively. Also shown in these Figures is the total drag of the wing with the plate. These curves may be compared to those previously cited in the Figures which describe the isolated wing and the isolated wing without protuberance. For the case $n_1 = 0$ it may be seen, by comparing the three Figures, that the drag of the biplane is independent of T for all values of $(1 - r)$. This result is to be expected from two-dimensional considerations. If $n_1 = 0.3$ and $(1 - r) = 0.5$, the Figures show that the drag of the biplane increases only slightly as T is increased successively from 0.5 to 1.0 and then to 2.0, whereas the drag of the isolated wing increases a great deal when T is increased in the same way. When $n_1 = 0.3$, $(1 - r) = 0.5$, and $T = 0.5$ or 1.0, the plate thrust overbalances the drag increment attendant upon the addition of the protuberance to the wing; when $T = 2.0$, the two opposing effects virtually balance. Fig. 12, after minor adjustment of the ordinate and abscissa, can be regarded as the limiting case $T \gg 1$. Fig. 15 does not, however, correspond to the case $T = 0$, because the reflecting plate in the second example is larger than in the third.

It is apparent that the thickness of the wing in the vicinity of the root may be significantly increased with little or no penalty in drag. Moreover, the reflecting plate required is quite small. The ratio of plate area to wing area S_p/S_w is plotted vs. r in Fig. 22. When $n_1 = 0.3$ and $r = 0.5$, $S_p/S_w = 0.236$; if r is decreased to 0.4, S_p/S_w falls to 0.147. Figs. 19, 20, and 21 show that the increase in biplane drag when r is decreased from 0.5 to 0.4, for given n_1 and T, is not large.

Practicality of the Three-Dimensional Biplane

The virtual absence of the thickness drag of the symmetric two-dimensional Busemann biplane (see Fig. 5) has been known since 1935,[1] but a number of undesirable features appear to limit the usefulness of this configuration. Among these are numbered the sensitivity of the favorable interference to variations of the Mach Number from the design value and the possibility of choking in the internal passage. The maximum practical contraction ratio between the two wings is limited, as in the case of inlets, by the requirement that the configuration start at, say, the design Mach Number[17]; this limits the thickness of the wings. Furthermore, the elimination of the monoplane thickness drag is offset by an increase in other forms of drag when the symmetric biplane is substituted for the monoplane, providing that the two systems are compared for equal lift. The following comparison is presented in reference 18. The two-dimensional profile at an angle of attack supports wave drag due to thickness, wave drag due to lift, and skin-friction drag; each form of drag is normally of the same order. If the thickness is suitably redistributed and a second wing is added to form a symmetric biplane, then the thickness drag is eliminated, the drag due to lift is unaltered, but the skin friction is roughly doubled because the wetted area has been doubled. If the chord of each wing is halved and the angle of attack of each is doubled to preserve the same lift, then this biplane exhibits no thickness drag, twice the induced drag of the original monoplane, and roughly the same skin-friction drag as the monoplane. If, for example, the three forms of drag of the original monoplane are all equal, then neither biplane cited offers an aerodynamic advantage over the monoplane.

This assessment of the symmetric lifting two-dimensional biplane is misleading, however, because it considers only triangular profiles. A more efficient lifting two-dimensional biplane results when trapezoidal profiles, such as appear in Fig. 10 for $R < 0.5$, are adopted, This modification allows some lift to be produced efficiently in the internal passage of symmetric thickness arrangements. Furthermore, a reflecting plate or other smaller wing can be substituted for the second symmetric wing, the former not conforming to the central streamline of the symmetric thickness arrangement. The chord of these auxiliary surfaces need be only a fraction of the chord of the basic trapezoidal wing. The proposed configurations readily excel the monoplane on the basis of the comparison of total drags used in reference 18 and repeated above.

In the case of the three-dimensional biplane configurations herein considered, the possibility of eliminating most of the thickness drag of the isolated wing has been shown to remain. This provides the opportunity to increase the wing thickness and storage volume, especially near the root section, without a large drag penalty. But the three-dimensional biplane also exhibits the same undesirable sensitivity of the favor-

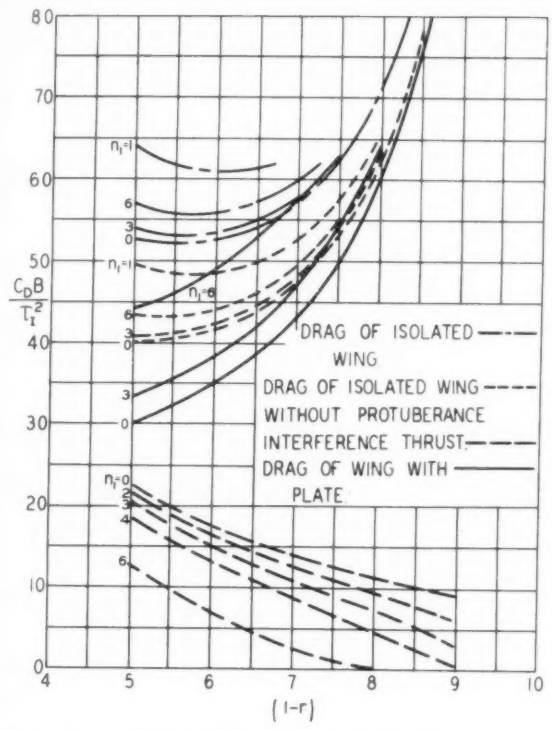

FIG. 19. Triangular wing with pentagonal protuberance, $T = 0.5$.

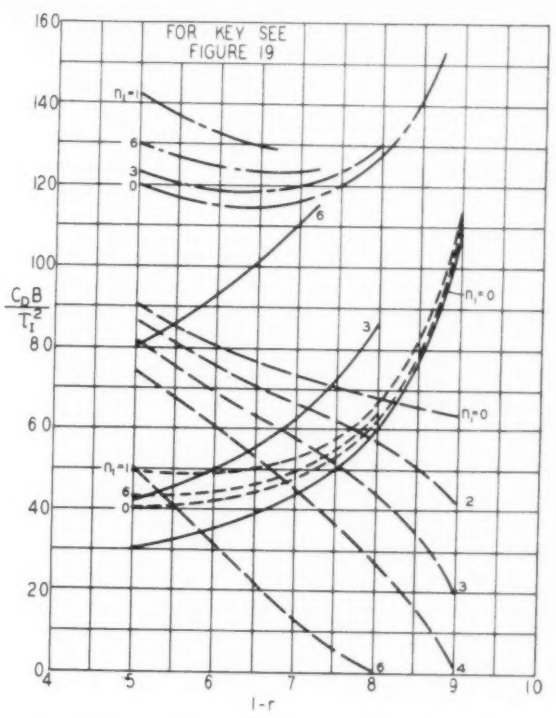

FIG. 21. Triangular wing with pentagonal protuberance, $T = 2.0$

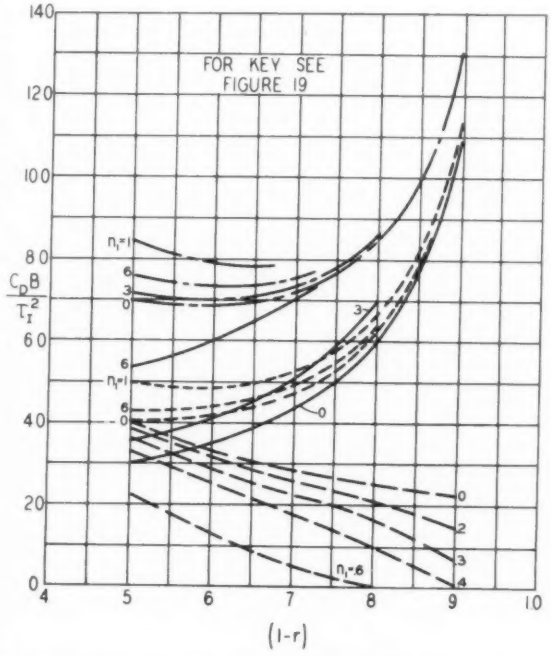

FIG. 20. Triangular wing with pentagonal protuberance, $T = 1.0$.

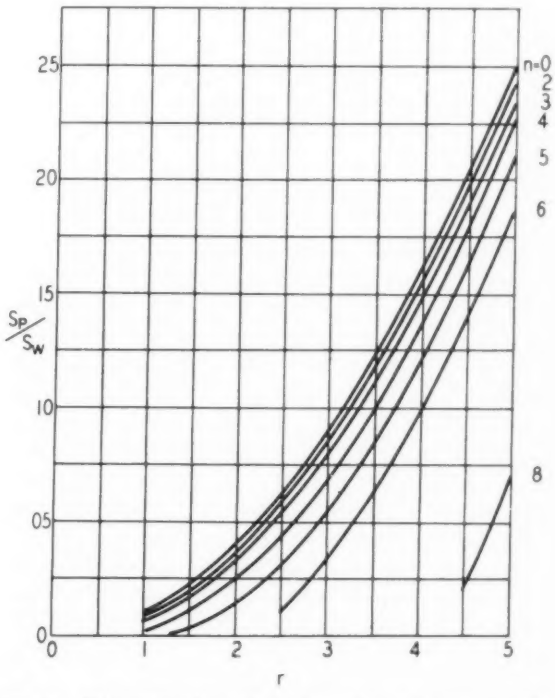

FIG. 22. Triangular wing with pentagonal protuberance: ratio of plate area to wing area.

able interference to variations of the stream Mach Number from the design value which is characteristic of the two-dimensional biplane. This effect is a subject for further research. The geometric limitations which are imposed by the contingency of choking in the two-dimensional configurations are largely eliminated in the case of the three-dimensional swept biplanes discussed because spanwise flow is unrestricted. Therefore, large thickness distributions in the vicinity of the wing root may be used collaterally with a small gap. The reflecting plate is relatively small, the ratio S_p/S_w falling in the range 15–30 per cent for the cases discussed, so that the increase in skin friction or drag due to lift which attends the reduction of thickness drag when the biplane is substituted for the isolated wing need not be severe in the case of suitable lifting configurations. This point is illustrated by considering the configuration illustrated in Fig. 10 for the limiting case where n tends toward zero. For equal angles of attack, for equal chords, and for all values of R, the lift and pressure drag of this configuration are the same as the lift and drag due to lift, respectively, of the isolated symmetric pentagon wing. Thus the thickness drag of the latter is, in effect, eliminated without changing the induced drag; the increase in wetted area and, hence, skin friction, is only 33 per cent when $R = 0.5$. When n is non-zero, it can still be expected that the lifting biplane will exhibit substantially less total drag than the isolated symmetric wing generating the same lift, whether the comparison be made on the basis of equal chord or equal wetted area. It is believed that a consideration of plate thickness does not substantially change these conclusions. Lifting three-dimensional biplanes will be considered by the authors in a subsequent publication.

Conclusions

A general outline has been given of possibilities for favorable interference between supersonic aircraft components. The interference between a three-dimensional wing and a small reflecting surface in biplane arrangement has been discussed in terms of linearized flow theory. Relationships have been developed which permit the analysis of such biplane configurations without the need for determination of the flow field. These relations apply in the linear approximation to a large class of such configurations. The method has been applied to several biplane arrangements of practical interest. It has been shown that the pressure drag of the wing can be greatly reduced or that the volume near the root section of the wing can be considerably increased without penalty in pressure drag. The biplane has been discussed from the engineering point of view, on the basis of which it appears that the configuration might be a practical one for some applications, particularly in the higher Mach Number range.

Appendix—Analytic Derivation of the Integral Relations

Consider an elemental area AB in the plane $z = h$ whose streamwise length is c, whose elemental width is $d\eta$, and whose orientation with respect to the coordinate system is as shown in Fig. 8(a). Let this area support a source distribution of constant intensity proportional to f. The trace in the plane $z = 0$ of the downstream Mach cone with apex at point $A(0, 0, h)$ is given by

$$x = B\sqrt{y^2 + h^2} \tag{A-1}$$

Similarly, the Mach cone with apex at the point $B(c, 0, h)$ produces the trace

$$(x - c) = B\sqrt{y^2 + h^2} \tag{A-2}$$

These hyperbolas are indicated as OER and PFQ, respectively, in Fig. 8(a). The perturbation potential at a point $P(x, y, z)$ due to a source distribution in the plane $z = h$ is given by

$$\varphi(x, y, z) = -\iint_{\tau} \frac{f(\xi, \eta)\, d\xi\, d\eta}{\sqrt{(x - \xi)^2 - B^2[(y - \eta)^2 + (z - h)^2]}} \tag{A-3}$$

where the integration is extended over the part of the distribution τ which is upstream of the trace of the fore cone from $P(x, y, z)$ in the plane $z = h$. The equation of this hyperbola, in terms of the coordinates ξ and η, is

$$(x - \xi) = B\sqrt{(y - \eta)^2 + (z - h)^2} \tag{A-4}$$

The elemental perturbation potential $\delta\varphi$ induced by the elemental source distribution considered follows from Eq. (A-3) as

$$\delta\varphi(x, y, z) = -fd\eta \int_0^{\xi_1} \frac{d\xi}{\sqrt{(x - \xi)^2 - B^2[y^2 + (z - h)^2]}} \tag{A-5}$$

where ξ_1 differs according as $P(x, y, z)$ is upstream or downstream of the downstream Mach cone from $B(c, 0, h)$. When $[y^2 + (z - h)^2]$ is non-zero, it is seen that the elemental distribution behaves like a line source whose constant elemental lineal intensity is proportional to $fd\eta$. Therefore, the elemental area of width $d\eta$ may be rotated about its streamwise axis without changing the flow field. If $P(x, y, z)$ is upstream of the Mach cone from $B(c, 0, h)$, then ξ_1 is given by Eq. (A-4), and it follows from Eq. (A-5) that

$$\delta\varphi(x, y, z) = -fd\eta \cosh^{-1} \frac{x}{B\sqrt{y^2 + (z - h)^2}}, \quad [y^2 + (z - h)^2] > 0 \tag{A-6}$$

In Eq. (A-6) the principal value of the inverse function is inferred. By differentiation of Eq. (A-6), the x and z components of the elemental perturbation velocity in the plane $z = 0$ are found to be

$$\delta u(x, y, 0) = -f d\eta / \sqrt{x^2 - B^2(y^2 + h^2)} \quad \text{(A-7)}$$

$$\delta w(x, y, 0) = -f d\eta h x / (y^2 + h^2)\sqrt{x^2 - B^2(y^2 + h^2)}, \quad (y^2 + h^2) > 0 \quad \text{(A-8)}$$

respectively.

We now undertake the derivation from Eqs. (A-7) and (A-8) of several integral relations that serve to implement certain previously discussed calculations and to exhibit some features of the flow field considered. It is convenient in this regard to introduce the oblique coordinates α and β in the plane $z = 0$, the axes of which are inclined by the angle $\tan^{-1}k$ with respect to the y axis as shown in Fig. 8(a). The coordinates α and β are related to the coordinates x and y by the inverse transformation

$$x = (k/\sqrt{1 + k^2})(\alpha + \beta) \quad \text{(A-9)}$$

$$y = (1/\sqrt{1 + k^2})(\beta - \alpha) \quad \text{(A-10)}$$

By substitution of Eqs. (A-9) and (A-10) into Eqs. (A-7) and (A-8) there results

$$\delta u(\alpha, \beta, 0) = -\frac{\sqrt{1 + k^2}\, f d\eta}{B\sqrt{n^2(\alpha + \beta)^2 - (\beta - \alpha)^2 - h^2(1 + k^2)}} \quad \text{(A-11)}$$

$$\delta w(\alpha, \beta, 0) = -\frac{(1 + k^2) nh\, f d\eta (\alpha + \beta)}{[(\beta - \alpha)^2 + h^2(1 + k^2)] \times \sqrt{n^2(\alpha + \beta)^2 - (\beta - \alpha)^2 - h^2(1 + k^2)}} \quad \text{(A-12)}$$

where $n = k/B$. Consider two parallel lines which are inclined with respect to the positive y axis by the angle $\tan^{-1}k$, and which are tangent at points E and F, respectively, to the hyperbolas given by Eqs. (A-1) and (A-2); these lines are identified by EE′ and by DC in Fig. 8(a). From the geometry, the equations of these lines are found to be

$$\alpha_E = (\sqrt{1 + k^2}/2k)\, Bh\sqrt{1 - n^2} \quad \text{(A-13)}$$

$$\alpha_F = (\sqrt{1 + k^2}/2k)(c + Bh\sqrt{1 - n^2}) \quad \text{(A-14)}$$

respectively.

We first evaluate the integral of δu and of δw along a generic line α = const. between the two branches of the hyperbola OER; this line segment is denoted by KJ in Fig. 8(a) and lies in the region CED. That is,

$$\alpha_E < \alpha < \alpha_F \quad \text{(A-15)}$$

From Eq. (A-11),

$$\int_{\beta_K}^{\beta_J} \delta u(\alpha, \beta, 0)\, d\beta = -\frac{\sqrt{1 + k^2}\, f d\eta}{B} \times \int_{\beta_K}^{\beta_J} \frac{d\beta}{\sqrt{n^2(\alpha + \beta)^2 - (\beta - \alpha)^2 - h^2(1 + k^2)}} \quad \text{(A-16)}$$

where β_K and β_J are found by substituting Eqs. (A-9) and (A-10) into Eq. (A-1) and solving the result for β in terms of α:

$$\beta_{K,J} = \frac{(1 + n^2)}{(1 - n^2)}\alpha \mp \frac{1}{(1 - n^2)} \times \sqrt{4n^2\alpha^2 - h^2(1 + k^2)(1 - n^2)} \quad \text{(A-17)}$$

After rearrangement of the radicand, the integral in Eq. (A-16) is readily evaluated by trigonometric substitution. There results

$$(1/\sqrt{1 + k^2})\int_{\beta_K}^{\beta_J} \delta u(\alpha, \beta, 0)\, d\beta = -\pi f d\eta / B\sqrt{1 - n^2} \quad \text{(A-18)}$$

Similarly, from Eq. (A-12),

$$\int_{\beta_K}^{\beta_J} \delta w(\alpha, \beta, 0) d\beta = -(1 + k^2) nhf d\eta \times \int_{\beta_K}^{\beta_J} \frac{(\alpha + \beta) d\beta}{[(\beta - \alpha)^2 + h^2(1 + k^2)] \times \sqrt{n^2(\alpha + \beta^2) - (\beta - \alpha)^2 - h^2(1 + k^2)}} \quad \text{(A-19)}$$

After making the transformation

$$\gamma = (\beta - \alpha)/(\alpha + \beta) \quad \text{(A-20)}$$

the integral in Eq. (A-19) may be evaluated through use of two subsequent trigonometric transformations. There results

$$(1/\sqrt{1 + k^2})\int_{\beta_K}^{\beta_J} \delta w(\alpha, \beta, 0) d\beta = -\pi f d\eta, \qquad h \neq 0 \quad \text{(A-21)}$$

Since $d\beta/\sqrt{1 + k^2} = dy$, Eqs. (A-18) and (A-21) correspond to Eqs. (16) and (17) in the main text. It is significant that the value of each integral is independent of α.

We next evaluate the area integrals of δu and δw over the region CED [see Fig. 8(a)]. Since the elemental area is given by

$$dA = [2k/(1 + k^2)] d\alpha d\beta \quad \text{(A-22)}$$

it follows that

$$\int_{\text{CED}} \delta u\, dA = [2k/(1 + k^2)]\int_{\alpha_E}^{\alpha_F} d\alpha \int_{\beta_K}^{\beta_J} \delta u(\alpha, \beta, 0)\, d\beta \quad \text{(A-23)}$$

The first integral is given by Eq. (A-18); the second integration is trivial. From Eq. (A-23)

$$\int_{\text{CED}} \delta u\, dA = -\pi f\, cd\eta / B\sqrt{1 - n^2} \quad \text{(A-24)}$$

Similarly,

$$\int_{\text{CED}} \delta w\, dA = [2k/(1 + k^2)]\int_{\alpha_E}^{\alpha_F} d\alpha \int_{\beta_K}^{\beta_J} \delta w(\alpha, \beta, 0)\, d\beta \quad \text{(A-25)}$$

With use of Eq. (A-21) there results

$$\int_{\text{CED}} \delta w\, dA = -\pi f\, cd\eta, \qquad h \neq 0 \quad \text{(A-26)}$$

Eqs. (A-24) and (A-26) correspond to Eqs. (12) and (13) in the main text.

We lastly discuss the line integral of induction along a generic line $\alpha_F < \alpha = \text{const.}$ between the branches of the hyperbola OER. This line segment is denoted by NM in Fig. (8a). It is convenient to represent the elemental distribution AB by a semi-infinite elemental source distribution beginning at A and a semi-infinite elemental sink distribution beginning at B. Then the induction due to the former in the entire region downstream of hyperbola OER is given by Eqs. (A-7), (A-8), (A-11), and (A-12). The latter distribution induces a flow in the entire region downstream of the hyperbola PFQ. This flow is also described by Eqs. (A-7), (A-8), (A-11), and (A-12), with f replaced by $-f$, in terms of a second coordinate system whose origin is shifted downstream relative to the first one by a distance c. The complete flow in the region downstream of hyperbola PFQ is then given by superposition. Because the values of the integrals in Eqs. (A-18) and (A-21) are independent of α, it follows that the integral of induction from N′ to M′ due to the semi-infinite sink distribution is equal and opposite to the integral of induction from N to M due to the semi-infinite source distribution. Then the induction due to the elemental distribution AB for all $\alpha > \alpha_F$ is such that

$$\int_{\beta_N}^{\beta_M} \delta u(\alpha, \beta, 0)\, d\beta = 0, \qquad \text{(A-27)}$$

$$\int_{\beta_N}^{\beta_M} \delta w(\alpha, \beta, 0)\, d\beta = 0, \qquad h \neq 0 \qquad \text{(A-28)}$$

Eqs. (A-27) and (A-28) correspond to Eqs. (14) and (15) in the main text.

References

[1] Busemann, A., *Atti del V. Convegno "Volta,"* Rome, Reale Accademia d'Italia, 1935.

[2] Heaslet, M. A., Lomax, H., and Spreiter, J. R., *Linearized Compressible-Flow Theory for Sonic Flight Speeds*, NACA Report 956, 1950.

[3] Whitcomb, R. T., *A Study of the Zero-Lift Drag Rise Characteristics of Wing-Body Combinations Near the Speed of Sound*, NACA RM L52H08, 1952.

[4] Hayes, W. D., *Linearized Supersonic Flow*, North American Aviation Report AL-222, June, 1947.

[5] Jones, R. T., *Theory of Wing-Body Drag at Supersonic Speeds*, NACA RM A53H18a, 1953.

[6] Lomax, H. and Heaslet, M. A., *A Special Method for Finding Body Distortions that Reduce the Wave Drag of Wing and Body Combinations at Supersonic Speeds*, NACA RM A55B16, 1955.

[7] Lomax, H., *The Wave Drag of Arbitrary Configurations in Linearized Flow as Determined by Areas and Forces in Oblique Planes*, NACA RM A55A18, 1955.

[8] Ferri, A., *Elements of Aerodynamics of Supersonic Flows;* The Macmillan Co., New York, 1949.

[9] Ferrari, C., *Campi di Corrente Ipersonora Attorno a Solidi di Rivoluzione*, L'Aerotecnica, Vol. XVII, Fasc. 6, pp. 507–518, 1937.

[10] Ferri, A., *Application of the Method of Characteristics to Supersonic Rotational Flow*, NACA Report 841, 1946.

[11] Sears, W. R., and Tan, H. S., *The Aerodynamics of Supersonic Biplanes*, Quart. of Appl. Math., Vol. IX, No. 1, pp. 67–76, April, 1951.

[12] Bleviss, Z. O., *Some Integrated Properties of Pressure Fields About Supersonic Wings*, Journal of the Aeronautical Sciences, Vol. 20, No. 12, pp. 849–851, Readers' Forum, December, 1953.

[13] Lagerstrom, P. A., Van Dyke, M. D., *General Considerations About Planar and Non-planar Lifting Systems*, Douglas Aircraft Company Report No. SM-13432, June, 1949.

[14] Ferri, A., and Clarke, J. H., *On the Use of Interfering Flow Fields for the Reduction of Drag at Supersonic Speeds*, Polytechnic Institute of Brooklyn, PIBAL Report No. 304, March, 1956.

[15] Evvard, J. C., *Distribution of Wave Drag and Lift in the Vicinity of Wing Tips at Supersonic Speeds*, NACA TN 1382, 1947.

[16] Puckett, A. E., *Supersonic Wave Drag of Thin Airfoils*, Journal of Aeronautical Sciences, Vol. 13, No. 9, pp. 475–484, September 1946.

[17] Ferri, A., *Esperienze su di un Biplano Iperacustico Tipo Busemann*, Atti di Guidonia, No. 37–38, 1940.

[18] Graham, E. W., Lagerstrom, P. A., Beane, B. J., Licher, R. M., and Rodriquez, A. M., *Reduction of Drag Due to Lift at Supersonic Speeds*, Douglas Aircraft Company, WADC Technical Report No. 54-524, Part 2, August, 1954.

Symposium on Computing in the Aircraft Industry

New York University, University Heights Campus, Jan. 31–Feb. 1, 1957

This joint N.Y.U.-IBM symposium, cosponsored by the Society for Industrial and Applied Mathematics and the Institute of the Aeronautical Sciences, will consist of four sessions:

Jan. 31 (9:30 a.m.) "The Aircraft and Its Macrocosm," Chairman, Max Woodbury, New York University.
Jan. 31 (2:00 p.m.) "The Computer and Its Macrocosm," Chairman, Stuart L. Crossman, United Aircraft Corporation.
Feb. 1 (9:30 a.m.) "The Computer and The Aircraft," Chairman, to be announced.
Feb. 1 (2:00 p.m.) "The Computer and Its Mathematics," Chairman, Arnold S. Wolf, IBM Corporation.

It is planned to publish a limited number of proceedings of this symposium. In order to ascertain the number of copies to be printed, will you kindly place your advance order now. The cost of the proceedings will be $8.00. Please make checks payable to N.Y.U.-IBM Symposium and send to Dr. Max Woodbury, New York University, Research Division, 401 West 205 St., New York.

An Experimental Study of the Response of Simple Panels to Intense Acoustic Loading

LESLIE W. LASSITER,* ROBERT W. HESS,* AND HARVEY H. HUBBARD*

Langley Aeronautical Laboratory, NACA

SUMMARY

This paper deals with the measured response of simple panels to intense noise of the type encountered in the vicinity of aircraft power plants. Stress data are presented for panels exposed to noise from a jet engine at levels of approximately 160 db. as well as to nominal levels of discrete and random noise in controlled laboratory tests. Even at noise levels as high as those encountered near jet engines the data are shown to be in general agreement with calculations by the power spectrum procedure suggested by Miles.

Damping is shown to be a particularly significant parameter and is evaluated for various test conditions. Opportunity is taken to discuss the techniques of testing with a high intensity laboratory siren and to present some noise spectra measured near the exhaust of a turbojet engine. Results of an exploratory investigation of fatigue life and crack growth are also presented for various panels which failed under discrete frequency acoustic loading. Fatigue life was noted to decrease markedly for a nominal increase in the noise intensity level.

SYMBOLS

ω	= frequency
ω_0	= damped natural frequency of panel
$\varphi_N(\omega)$	= power spectrum of random noise
$Z(\omega)$	= mechanical impedance of panel
$\varphi_\sigma(\omega)$	= power spectrum of panel stress response
$\overline{\sigma^2}$	= mean square stress
$\sqrt{\overline{\sigma^2}}$	= root mean square stress
$\sigma_{max.}$	= stress amplitude
σ_{st}	= stress under given static load
ΔP	= static pressure differential
δ	= damping ratio, $c/c_{crit.}$
S_0	= stress per unit static pressure
t	= panel thickness
R	= panel radius of curvature
p_1	= root mean square sound pressure at siren fundamental frequency
D	= diameter of engine tailpipe
z	= slant distance from tailpipe (along lines 15° to jet centerline)
d	= radial distance from 15° jet boundary
a	= characteristic panel dimension

INTRODUCTION

FATIGUE DAMAGE to the skin structure of airplanes and missiles due to noise from the power plants is now a serious operating problem. Of particular concern are those failures due to the intense random noise fields near jet engines. There is a need for evaluating the significant parameters involved in the problem in order to permit the design of optimum structures to withstand these fluctuating loads.

The present paper is devoted mainly to a discussion of the response of simple panels to intense random noise inputs. The concepts of generalized harmonic analysis are applied to this latter problem, and the results are compared with experiments for both flat and curved panels. As a matter of interest some sample spectra of the noise near a J-34 turbojet engine with and without afterburner are presented.

There are brief discussions of some exploratory tests of the fatigue of simple riveted panels by means of discrete frequency noise from a laboratory siren. The manner in which these failures occur is illustrated and some indication of how the fatigue life varies with intensity of the input noise is given.

(I) PANEL STRESSES

METHOD OF CALCULATION

The concepts involved in analysis of the problem of panel excitation by random loading are outlined and illustrated in Fig. 1. A random acoustic input or loading which may have a power spectrum such as that shown in the top part of Fig. 1 exists, and it is desired to determine the power spectrum of the stress response which this loading will produce in the panel. The two spectra are related by the transfer characteristic of the panel, which is the square of the admittance or frequency response to a unit-pressure sinusoidal input and in simplified form may be as shown in the middle part of Fig. 1. The power spectrum of the stress response then results from the product at all frequencies of the input spectrum $\varphi_N(\omega)$ and the square of the admittance $|1/Z(\omega)|^2$. If the system is sharply tuned, such that the half-power bandwidth of the panel admittance curve is small relative to that of the loading spectrum, the response $\varphi_\sigma(\omega)$ is essentially resonant and the stress spectrum takes the same form as the admittance curve.

As Miles and others[1, 2] have shown, the response can be calculated in a simple manner if the panel is assumed to behave as a single degree of freedom system which is sharply tuned. Thus, the square of the impedance $|Z(\omega)|^2$ is taken as

$$|Z(\omega)|^2 = \left\{[1 - (\omega/\omega_0)^2]^2 + 4\delta^2 (\omega/\omega_0)^2\right\}/S_0^2 \quad (1)$$

and the input $\varphi_N(\omega_0)$ is taken as the power spectral density at the panel resonant frequency. It should be noted that in this simplified presentation of the problem, the spatial correlation of pressure over the panel area is tacitly assumed to be unity, that is, all parts of

Presented at the Structures Session, Twenty-Fourth Annual Meeting, IAS, New York, January 23–26, 1956.

* Aeronautical Research Scientist.

the panel are assumed to be excited with pressures in the same phase. Where the inputs are of a scale which is not large relative to the panel dimension this condition is not met, and the input loading spectrum must be one in which correlation effects have been included. Such effects, however, will not be considered in the present paper.

The mean square response $\overline{\sigma^2}$, which is a measure of the area under the stress power curve, becomes

$$\overline{\sigma^2} = \pi/4\delta\ \omega_0\ \varphi_N(\omega_0)\ S_0^2 \qquad (2)$$

The mean square stress is thus seen to be dependent upon four parameters, three of which relate to the panel. ω_0 is the damped natural frequency of the panel, S_0 is the stress per unit input pressure under static loading, and δ is the damping in terms of the critical value. The admittance curve of the panel affords a measure of damping, either by its bandwidth $2\delta\omega_0$ at the half-power frequencies, or by the value $(S_0/2\delta)$ at resonance. The input $\varphi_N(\omega_0)$ is the power spectral density at frequency ω_0.

The mean square stress is a useful index of the panel response, but still another characteristic of the response is of interest. This is the time history of stress. Fig. 2 gives a comparison of stress time histories of a given panel for periodic loading and for random loading. For periodic loading, with one Fourier component of the noise near the panel natural frequency, the stress response is essentially sinusoidal at that frequency and the envelope is of constant value.

For random loading Fig. 2 indicates that the response is again essentially sinusoidal, but in this case the envelope is not constant. In fact, it can be shown that the amplitude of a single cycle of the response is a statistical quantity having the so-called Rayleigh probability distribution. This type of response is characteristic of a sharply tuned system randomly excited, and the interval between the beats indicated in Fig. 2 is an indication of the damping of the system.

Experimental Results

The remainder of the present paper will deal with (1) determination of the structural and loading parameters necessary to a calculation of the mean square stress, (2) a comparison of measured stresses with those calculated by Eq. (2), and (3) results of some exploratory fatigue tests of panels under acoustic loading. The panels used in the investigation were of 2024 t3 aluminum alloy, measuring 11 by 13 in. with simulated riveted-edge conditions. The panels were mounted on a rigid plate of 1-in. thickness and this was subsequently bolted to a supporting chamber. Flat panels of thicknesses 0.032 in. and 0.064 in. and curved panels of thickness 0.032 in. are considered. The curved panels consisted of flat stock rolled to a radius of 4 ft.

Panel Characteristics

Static Response—Fig. 3 illustrates the static response of flat and curved panels of 0.032-in. thickness. Static stress is plotted as a function of pressure differential across the panel for loading in both directions. For flat panels the response indicates that for loading in either direction the system is linear over a range of pressure and then becomes nonlinear in the characteristic manner of a system of increasing stiffness with deflection. For curved panels, the static response is dependent upon the direction of loading. For positive pressure on the concave surface the response is similar to that of a flat panel. For negative-pressure loading on the same surface, however, the response curve turns upward, indicating that the nonlinearity involves a decreasing spring stiffness.

Dynamic Response—The dynamic response of the various panels was determined by exciting the panel with periodic noise from a large siren. By holding the acoustic pressure output of the siren constant and varying the frequency, an admittance curve for that pressure level is obtained. Fig. 4 gives sample results of the measured admittances of flat and curved panels of 0.032-in. thickness. Stress amplitude is plotted as a function of frequency for two input pressure levels to the two panels. Although the levels used with the flat and curved panels are not the same, the curves will illustrate the main differences between the two types. At the lowest pressure for each panel the curves are similar and tend toward symmetry about the natural frequency, which is observed to be appreciably higher for the curved panel than for the flat panel. Actually, the curved panel response shown here is for a mode very much like the third of a flat panel (node lines in long direction) and the flat panel response is for the first mode. These were chosen because in each case this particular mode was found to be the primary one excited when the panel was forced by a random input. These are not necessarily typical since the modal response probably depends upon the radius of curvature of the panel and upon the spatial scale of the loading disturbance also, but they are of interest here because of the relation they have to the results obtained under random excitation.

In contrast to this similarity of response of flat and curved panels at low input pressures, the top curves of the Figure illustrate the differences which occur at high levels of excitation. The flat panel assumes a response which is skewed toward higher frequencies, whereas the curved panel response is skewed toward lower frequencies. These two types of response are indications of two types of nonlinearity.[3] For the flat panel the nonlinearity arises from an increasing stiffness with deflection, and for the curved panel at this particular input level the nonlinearity arises from a condition of decreasing stiffness with deflection. At intermediate levels the curved panel also indicates a slight stiffening effect. In practice, the double-valued portions of these skewed curves are nearly impossible to obtain—hence, the half-power frequencies are somewhat a matter of conjecture. For that reason, the determination of damping δ was based on the resonant amplification, using the relation

$$\delta = \sigma_{ST}/2\sigma_{max}$$

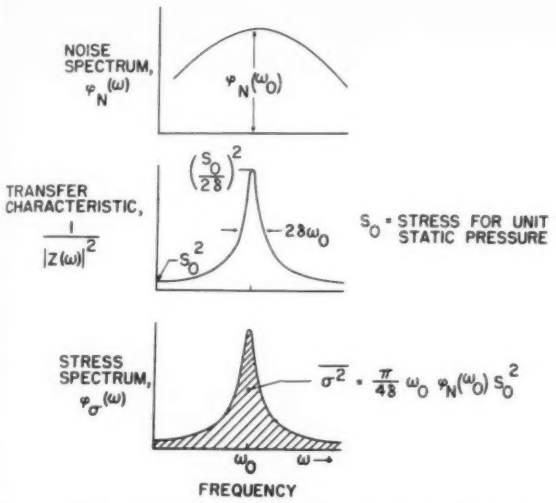

FIG. 1. Concepts of the problem of panel excitation by random noise.

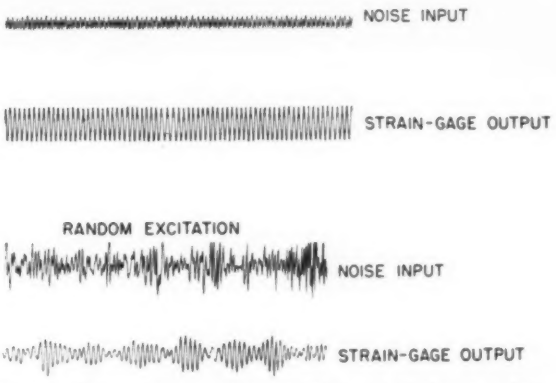

FIG. 2. Stress responses of a panel for periodic input and for random input.

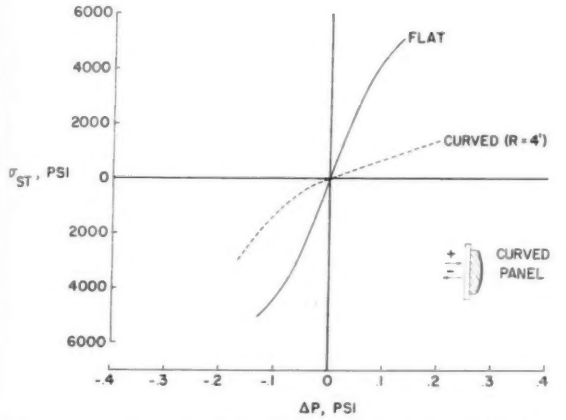

FIG. 3. Static response of flat and curved panels ($t = 0.032$ in.).

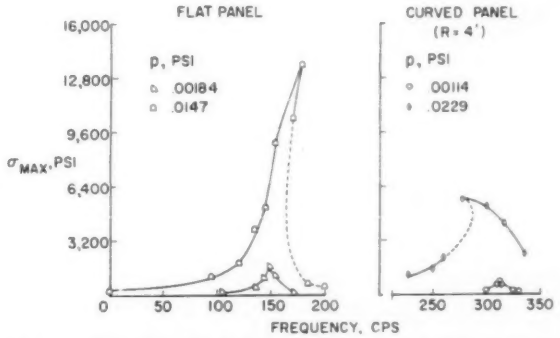

FIG. 4. Sample transfer characteristics for flat and curved panels ($t = 0.032$ in.).

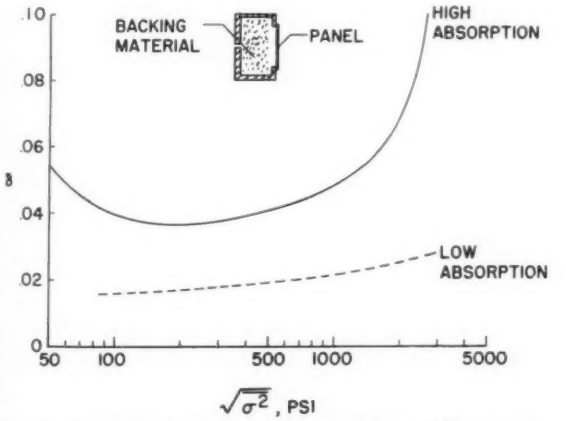

FIG. 5. Variation of damping with stress for two different backing conditions ($t = 0.064$ in.).

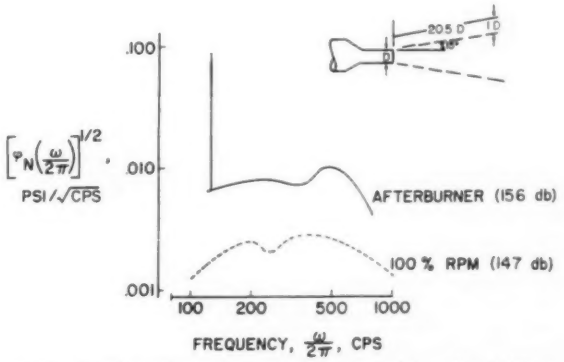

FIG. 6. Sample noise spectra from J-34 turbojet engine ($d/D = 1$, $z/D = 20.5$).

Panel Damping—Fig. 5 illustrates the nature of the damping results obtained from one of the test panels. The Figure gives the variation of damping with stress (or deflection) for a 0.064-in. flat panel for two conditions of acoustic termination on the back side. The top curve is for termination in the mounting chamber of material of high acoustic absorptivity. The lower curve is for termination with a material of appreciably lower absorptivity, and it is seen to indicate damping values of roughly half those of the other case. In neither case does the material actually come in contact with the panel—hence, the difference in damping is taken as evidence of the importance of radiation losses to this type of test mounting. For either case, the damping increases with stress at the higher stresses, but when the termination is highly absorbent the increase is at a much higher rate.

Damping for the curved panel was found to be lower at low stresses and higher at high stresses than the values for the flat panel shown here, thus following a somewhat different variation with stress.

The damping data of this Figure, together with the static stress response and natural frequency from Figs. 3 and 4, respectively, provide the information necessary for a calculation of the mean square stress for a given input noise spectrum, and it thus remains to compare measured values with those calculated. Before proceeding to this, however, it might be well to consider some of the features of a turbojet noise field.

Some Characteristics of the Noise Inputs

The present tests were made with a J-34 engine equipped with afterburner. This is not one of the more powerful engines, but some of the characteristics of its noise field are expected to be more or less typical.

Spectra—Fig. 6 gives sample spectra obtained near the flow boundary for this engine at the 100 per cent r.p.m. condition and for afterburning conditions. Sound pressure is given as the spectrum level value in the units psi/$\sqrt{\text{cps}}$. At 100 per cent r.p.m. the spectrum shape is more or less typical of those obtained heretofore in the near sound field of an engine in that the highest pressures occur in the frequency range 100 cps to 1,000 cps. When the afterburner is cut in, the spectrum level is raised by about 8 to 10 db. as a result of the higher efflux velocity of the jet—root mean square sound pressure varies about as the second power of jet velocity in the near sound field.[4] In addition to this increase, operation of the afterburner introduces a very intense periodic component into the spectrum at 125 cps. This apparently results from an internal resonance of the tailpipe and is not necessarily typical of all afterburners. In the afterburner tests discussed herein the test panel had a resonant frequency of 160 cps and the stress time histories were similar to that of Fig. 2 for random input, thus indicating that the loading was primarily random.

Spatial Variations—The quantity of primary interest from these spectra is the value at the panel natural frequency, that is $[\varphi_N(\omega_0/2\pi)]^{1/2}$. This characteristic of the problem allows a fairly simple means of charting the spacewise variations of sound pressure near the engine, since several pertinent frequencies can be selected and the spatial distribution of pressure at those frequencies plotted. Fig. 7 gives such plots for frequencies of 200 cps, 800 cps, and 1,600 cps. The left-hand plot is a plot of root mean square sound pressure $[\varphi_N(\omega_0/2\pi)]^{1/2}$ as a function of slant distance z/D measured from the tailpipe along a line inclined at the angle of the jet boundary (15°) and displaced radially one diameter from the boundary. The lower frequencies are seen to reach their maximum value at some distance downstream of the tailpipe (11 diameters for 200 cps). At 800 cps the maximum occurs at about 7 diameters and at 1,600 cps the maximum appears to be upstream of 2.5 diameters.

The right-hand plot of Fig. 7 illustrates the relative variation of sound pressure for 200 cps and 1,600 cps, with radial distance d/D from the jet boundary at a slant distance of 8 diameters downstream of the tailpipe. The decrease of pressure with distance from the boundary is rather rapid for 1,600 cps but for 200 cps the decrease is at a comparatively slow rate. The trends illustrated by this Figure are thought to be more or less typical of turbojets in general, although the magnitudes involved are undoubtedly lower than exist near some of the latest model turbojets.

Comparison of Theory and Experiment

The measured stresses to be compared with theory herein were obtained by selecting locations in the turbojet noise field such that a range of input pressures could be obtained. The measurements at the lowest pressures were obtained in the sound field of a 4-in. unheated-air jet.[5] The damping used in a stress calculation for random input can be obtained from Fig. 5 by an iterative process; however, a more direct procedure for obtaining the calculated stress without the necessity of determining the damping as such is available. This involves rewriting Eq. (2) as

$$\sqrt{\overline{\sigma^2}}\,\sqrt{\delta} = [\pi/4\ \omega_0\ \varphi_N\ (\omega_0)\ S_0^2]^{1/2} \qquad (3)$$

Then, based on the damping curve of Fig. 5, the quantity $\sqrt{\overline{\sigma^2}\delta}$ is plotted as a function of $\sqrt{\overline{\sigma^2}}$ as shown in Fig. 8. This allows entry into the ordinate scale with a value computed from the right side of Eq. (3), and the calculated stress is obtained directly from the Figure.

Figs. 9 and 10 give comparisons of measured stresses with values calculated in this manner for flat and curved panels for a range of input pressure $[\varphi_N(\omega_0/2\pi)]^{1/2}$.

Flat Panel—Fig. 9 is for flat panels of thickness 0.032 in. and 0.064 in. The curves represent the calculated stress variations for each panel; the data points represent measured values.

The indications are that the theory is in rather good agreement with experiment throughout the range of the tests for both panels, despite the fact that a markedly nonlinear response is associated with the higher

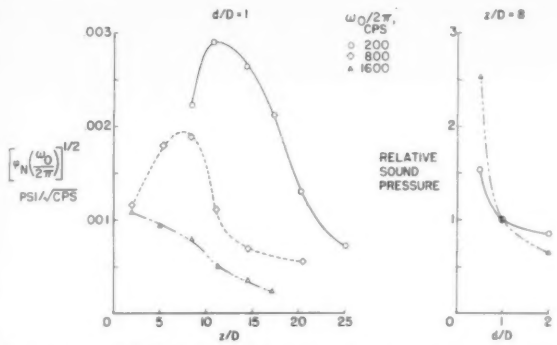

FIG. 7. Spatial distributions of noise at various frequencies for J-34 turbojet engine with afterburner.

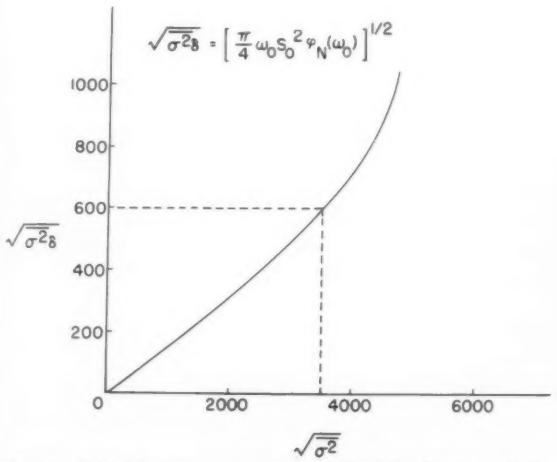

FIG. 8. Relation between stress and damping for one of the 0.064-in. thick panel configurations tested.

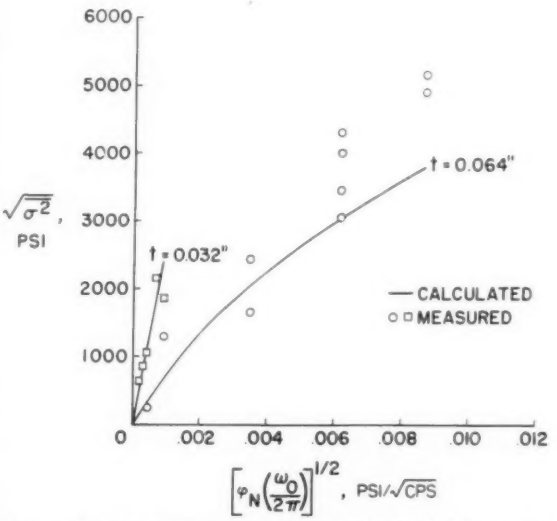

FIG. 9. Comparison of measured and calculated stresses for flat panels of two different thicknesses.

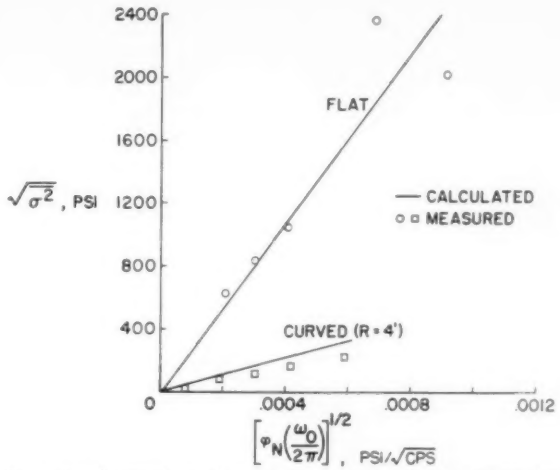

FIG. 10. Comparison of measured and calculated stresses for flat and curved panels (t = 0.032 in.).

FIG. 11. Sample flat panel failure from siren tests (t = 0.032 in.).

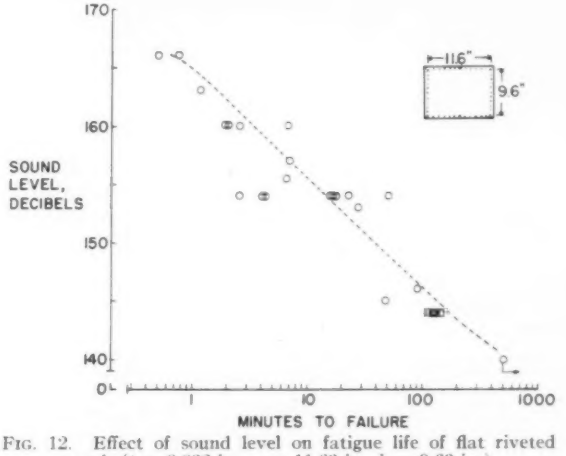

FIG. 12. Effect of sound level on fatigue life of flat riveted panels (t = 0.032 in., a = 11.63 in., b = 9.63 in.).

pressures. It will be noted, however, that the nonlinearities are at least partly accounted for in the empirical values used for the parameters.

It should also be noted that the nonlinearity in Fig. 9 is partly due to the fact that the backing condition for the low-pressure runs differed from those of the turbojet runs, thus yielding different dampings even for the same input pressure. Although the 0.064-in. data indicate that the theory is somewhat unconservative at the higher pressures, similar comparisons for other thicknesses do not always indicate this. Thus the differences appear to be due to experimental scatter or perhaps to a systematic error.

Although the tests with the 0.032-in. panel were limited to the 100 per cent engine condition because of the acoustical resonance of the afterburner, an evaluation of the effect of panel thickness can be made at the lower pressures. If in Eq. (2) the quantity $\omega_0 S_0^2$ is substituted for in terms of panel dimension a and thickness t, there results the proportionality relationship

$$\sqrt{\overline{\sigma^2}} \propto a\ [\varphi_N(\omega_0)]^{1/2}/\delta^{1/2}\ t^{3/2} \qquad (4)$$

which indicates that root mean square stress should vary inversely as thickness to the 3/2 power. Thus it would be expected that a doubling of thickness, as in Fig. 9, would result in a stress reduction of 0.37, as is shown by the two theory curves. The general agreement of experiment and theory in each case appears to confirm the calculated effect of thickness.

Curved Panels—Fig. 10 gives a comparison of stress for panels of given size and thickness (0.032 in.) having different radii of curvature; and it allows evaluation of the theory for the curved panels. The top curve is taken from the preceding Figure for a flat panel ($R = \infty$); the lower curve is the calculated stress for a curved panel of 4-ft. radius. The measured stresses in the latter case are for excitation by the 4-in. air jet only, hence the more limited pressure range. Over this range the theory and experiment are again in rather good agreement. It may be that the agreement for this panel is somewhat fortuitous, since, as previously discussed, the panel responds in a mode much like the third, and the value of S_0 is that for uniform static loading in the nature of a first mode response.

(II) PANEL FATIGUE CHARACTERISTICS

From the results of Figs. 9 and 10, it appears that a power spectrum approach to the stress problem of panels under random excitation affords a usable means of stress prediction. However, it still remains to investigate the fatigue properties of the panels under acoustic excitation.

In view of the differences indicated by Fig. 2 for panel response to periodic and random inputs, it would be expected that for a given panel and mean square stress there would be a difference in fatigue life in the two cases. Thus the specific fatigue properties of a given type of panel should be determined with random loading. This in itself presents serious problems of testing, since the generation of random noise is by nature an inefficient process and to date the best generators are the turbojets themselves. These are not generally available for an extended program of fatigue testing. However, the generation of intense periodic sound with a siren is economical, and it appears that considerable information can be obtained from fatigue testing with a siren. This is particularly true in the investigation of trends, such as was undertaken in the present tests.

Type of Failures

For 0.032-in. flat panels with simulated riveted-edge conditions, Fig. 11 illustrates some characteristics of the failures obtained under periodic acoustic excitation. The regions identified as (1) in the photograph are typical of the first stage of the failures, wherein small cracks originate around rivets where stresses are highest. The time of appearance of such cracks is taken as the fatigue life of the specimen. Further excitation of the panel usually, in a rather short time, results in growth of the cracks around individual rivets until the cracks from adjacent rivets meet and form a split running nearly the length of a side as shown by the region denoted as (2). Once this occurs, the subsequent damage usually takes the form of new cracks extending toward the center of the panel and often growing in such a way as to leave holes in the panel [see region (3)].

Effect of Sound Level on Fatigue Life

Fig. 12 illustrates the importance of the sound level to the problem of fatigue life of a panel. This Figure presents a plot of the sound level in decibels as a function of fatigue life in minutes for flat panels of 0.032-in. thickness. At 140 db. a single sample was tested for over 500 min. without failure. At 154 db. a family of seven panels yielded a mean fatigue life of 14 min. and at 160 db. a family of 5 panels had a mean life of 3 min. At 166 db. two specimens indicated that the life was only of the order of 30 or 40 sec. Thus, it is observed that an increase of the decibel level from 140 db. to 166 db. decreased the fatigue life of these particular panels from a matter of hours to a matter of only a few seconds, or by a factor of roughly 500. Although the data shown in Fig. 12 apply directly only to the particular configuration tested, the trend illustrated by the curve appears to be more or less general.

Concluding Remarks

Consideration has been given to the problem of the response of simple panels to intense acoustic excitation. Application is made of the method of generalized harmonic analysis to the problem of prediction of stresses due to random loading and the results are shown to be in good agreement with measured data. Exploratory

(*Continued on page 80*)

Stagnation Point of a Blunt Body in Hypersonic Flow

TING-YI LI* AND RICHARD E. GEIGER**

Rensselaer Polytechnic Institute and General Electric Company

SUMMARY

The purpose of this paper is to present a method of calculation devised to yield all the important information on the symmetric inviscid hypersonic flow in the stagnation point region of a blunt body. The problem is the same as that considered by Hayes[2, 3] who used a slightly different approach. It is demonstrated that Hayes' results are valid in the stagnation point region and can hence be considered a basis for constructing less restricted solutions.

Equations are presented giving velocity, pressure, detachment distance, and vorticity. The values of shock detachment distance and body pressure coefficient are compared with experimental data for spheres. The pressure comparison shows that the results of Hayes and the theory presented herein represent a better approximation than the Newtonian impact theory for hypersonic Mach Numbers.

In conclusion, the possibility of refinements to this analysis is discussed.

SYMBOLS

A_0, A_1, A_2	= constants of integration, two-dimensional problem
C_0, C_1, C_2	= constants of integration, three-dimensional problem
C_p	= pressure coefficient
f	= velocity function, defined by $u = xf'(y)$
k	= free-stream density divided by density behind bow shock at body axis
K	= body curvature, positive for convex body
p	= pressure
r	= distance between body axis and arbitrary point x, y
R	= radius of curvature, negative in the present analysis
u	= velocity component in x-direction
v	= velocity component in y-direction
x	= curvilinear distance along body surface
y	= distance normal to body surface
α	= flow deflection angle immediately behind shock, relative to free stream
β	= shock angle relative to free stream
δ	= shock layer thickness
δ^*	= shock layer thickness on the axis of symmetry
ν	= kinematic viscosity
ξ	= vorticity number, $(\omega/u_B)\sqrt{\nu x/u_B}$
ρ	= density
ϕ	= angular position on sphere surface, relative to free stream
θ	= body surface slope relative to free stream
ω	= vorticity, $(\partial v/\partial x) - (\partial u/\partial y)$

Subscripts

B	= body
S	= shock
∞	= free stream
2	= immediately behind normal shock

INTRODUCTION

THE PROBLEM of the high-speed flow past a blunt-nosed body has been a subject of considerable research. In this problem the bow shock wave is detached from the body surface. Heybey[1] recently proposed a method of analysis designed particularly for an estimation of the shock detachment distance in the stagnation point region. In his paper Heybey cited many interesting references. In particular, he mentioned that Schwartz suggested that for hypersonic flows the detachment distance should be uniquely dependent upon the density ratio across the shock wave. The important role of the density ratio parameter is even more clearly brought out by the recent investigation of Hayes[2, 3]. Hayes has calculated[2] the symmetric hypersonic flow past a blunt-nosed body, and his results, presumably, can be considered as a first step towards the understanding of the characteristics of such flows. This paper approaches the Hayes' problem in a slightly different manner. The present analysis shows that Hayes' results are valid in the stagnation point region and, hence, can be considered a basis for constructing solutions for other less restricted regions.

An understanding of the inviscid hypersonic flows past blunt bodies is important from a practical point of view. Presumably the inviscid analysis can provide an accurate description of the main stream conditions outside the viscous boundary layer. Analysis of the boundary-layer behavior, then, will provide important design information on skin friction and heat transfer. The heat-transfer rate near the stagnation point of a blunt body, in particular, is important for designers. It is known that this heat-transfer rate depends on the magnitude of the velocity gradient along the body surface.[4, 5] It has also been shown recently that the hypersonic boundary-layer behavior in the presence of a curved bow shock depends upon a "vorticity number."[6]

These considerations clearly point out the importance of an inviscid theory that provides a more or less complete description of the disturbance flow field. This is the main objective of the present study which presents a method of calculation devised to yield all

Presented at the Hypersonics Session, Twenty-Fourth Annual Meeting, IAS, New York, January 23–26, 1956.

* Consultant to Special Defense Projects Department, General Electric Company, and Associate Professor, Department of Aeronautical Engineering, Rensselaer Polytechnic Institute.

** Engineer, Special Defense Projects Department, General Electric Company.

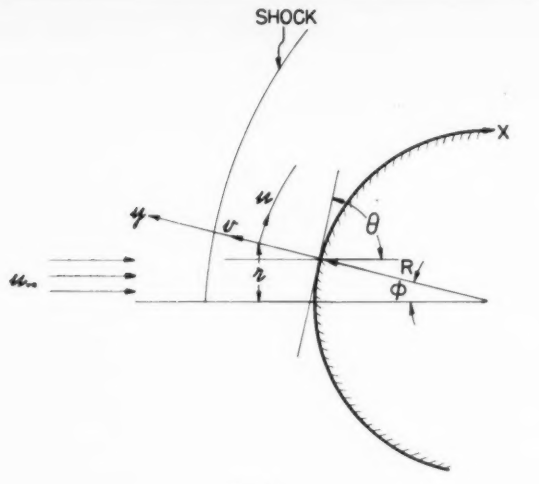

FIG. 1.

the important information on the inviscid hypersonic flow in the stagnation point region.

Hayes' method of small density ratio represents a better approximation than the Newtonian impact theory for finite hypersonic Mach Numbers. This is further substantiated in the present computations as is shown by a comparison of the pressure coefficient on the body surface according to these results with the classical Newtonian value.

Results of the present study are compared with available experimental data, and generally speaking, the comparisons show good agreement. Further refinement of the present analysis is discussed.

ANALYSIS

General Theory

The purpose of the present investigation is to devise a method of computing the steady symmetric inviscid flow field about a body with a blunt nose at hypersonic free-stream Mach Numbers ($M_\infty \gg 1$).

The basic equations of motion governing the flow of an inviscid fluid are as follows:

$$[1/(1 + Ky)]\, u(\partial u/\partial x) + v(\partial u/\partial y) + [K/(1 + Ky)]\, uv + [1/(1 + Ky)]\, (1/\rho)\, (\partial p/\partial x) = 0 \quad (1)$$

$$[1/(1 + Ky)]\, u(\partial v/\partial x) + v(\partial v/\partial y) - [K/(1 + Ky)]\, u^2 + (1/\rho)\, (\partial p/\partial y) = 0 \quad (2)$$

The continuity equation is

$$[1/(1 + Ky)]\, (\partial/\partial x)\, (\rho u) + (\partial/\partial y)\, (\rho v) + [K/(1 + Ky)]\rho v + (i/r)\, \{[\rho u/(1 + Ky)]\, (\partial r/\partial x) + \rho v(\partial r/\partial y)\} = 0 \quad (3)$$

$$i = \begin{cases} 0 \text{ two-dimensional flow} \\ 1 \text{ axially symmetrical flow} \end{cases}$$

In these equations x and y are the axes of an orthogonal curvilinear coordinate system, in which the origin is taken at the nose of the body, x is measured parallel to the body surface, and y is measured normal to the body surface. u and v represent the velocity components in the x and y directions, respectively. (See Fig. 1.)

K (in general, a function of x) represents the local curvature of the body surface:

$$K = -(d\theta/dx) = -(1/R_B) \quad (4)$$

θ is the local inclination of the body surface with respect to free stream, and R_B is the local radius of curvature of the body surface. ρ and p denote, respectively, the density and pressure. r is the distance from an arbitrary point x, y measured normal to the axis of symmetry which is parallel to the free stream.

Eqs. (1) to (3) in their present forms are not amenable to simple mathematical analysis. However, in the nose region they are susceptible to great simplifications, as follows:

(1) Near the stagnation point u/u_∞, $v/u_\infty = 0$ [k]. For hypersonic flow, k—the density ratio across the shock wave—is very small, so that higher order terms like Kuv, Ku^2 can be neglected.

(2) In the disturbed flow region between the shock wave and the body surface—i.e., $0 \leq y \leq \delta$, where δ represents the shock layer thickness—the quantity $Ky = 0[\delta/R_B]$ can be neglected if $\delta/R_B \ll 1$. For the hypersonic flow problem, $\delta/R_B \ll 1$ is, of course, a reasonable estimate.

(3) In the vicinity of the stagnation point, $r \simeq x$. Therefore, for small x, r can be replaced by x in Eq. (3).

(4) As the free-stream Mach Number approaches infinity, the Mach Number immediately behind a normal shock wave, M_2, approaches the quantity $\sqrt{(\gamma - 1)/2\gamma}$. Therefore, the flow field near the stagnation point can be regarded essentially as incompressible.

$$\rho \simeq \rho_2 = \rho_\infty/k \quad (5)$$

For strong shock waves produced by blunt bodies at hypersonic speeds, $k \ll 1$. With these simplifications, the basic equations become

$$u(\partial u/\partial x) + v(\partial v/\partial y) = (-k/\rho_\infty)\, (\partial p/\partial x) \quad (1a)$$

$$u(\partial v/\partial x) + v(\partial v/\partial y) = (-k/\rho_\infty)\, (\partial p/\partial y) \quad (2a)$$

$$i = 0 \qquad (\partial u/\partial x) + (\partial v/\partial y) = 0 \quad (3a)$$

$$i = 1 \qquad [\partial(ux)/\partial x] + [\partial(vx)/\partial y] = 0 \quad (3b)$$

These differential equations must now be solved to yield solutions satisfying appropriate boundary conditions. These are as follows:

The tangency condition at the body surface is

$$y = 0 \qquad v = 0 \quad (6)$$

The shock wave conditions at a point A are:

$$y = \delta \qquad u_A = q_A \cos(\theta - \alpha) \quad (7)$$

$$v_A = -q_A \sin(\theta - \alpha) \quad (8)$$

$$q_A = \sqrt{(ku_\infty \sin\beta)^2 + (u_\infty \cos\beta)^2} \tag{9}$$

$$p_A = p_\infty + \rho_\infty u^2 (1 - k) \sin^2\beta \tag{10}$$

Fig. 2 identifies the quantities appearing in these equations as follows.

α is flow deflection across the shock wave at A, β is the local shock wave angle at A and q_A is the magnitude of the velocity vector after the shock wave at A.

Eqs. (7) and (8) result from considerations of the geometry of the present coordinate system.

Eq. (9) is derived from the conditions of conservation of mass and conservation of momentum along the shock wave direction, while Eq. (10) represents the conservation of momentum normal to the shock wave. Another condition—namely, the stagnation point condition—is simply

$$x = 0 \qquad y = 0 \qquad u = v = 0 \tag{11}$$

Thus, the problem is to seek the solutions of the differential Eqs. (1a), (2a), (3a), or (3b) with the above boundary conditions. This will be carried out for both the two-dimensional and the axially symmetrical flows.

Two-Dimensional Flow

Near the stagnation point, it can be assumed that

$$u = xf'(y) = x(df/dy) \tag{12}$$

Eq. (3a), the continuity equation, is satisfied if

$$v = -f(y) \tag{13}$$

The choice of the particular u form satisfies Eq. (11). It can be justified by the following argument. In general, $u\ (x, y)$ may be expressed for small x as an ascending series of the form

$$u\ (x, y) = a_0 + a_1 x + a_2 x^2 + \ldots$$

where the a's are functions of y. Clearly the symmetry of the problem permits only terms in odd powers of x, and for small x's—i.e., near the stagnation point—third and higher powers of x are unimportant. Therefore, Eq. (12) represents a satisfactory approximation.

The quantity p can be eliminated from Eqs. (1a) and (2a) by cross differentiation. The result is

$$u(\partial\omega/\partial x) + v(\partial\omega/\partial y) = 0 \tag{14}$$

for two-dimensional flow. The vorticity, ω, is expressed by

$$\omega = (\partial v/\partial x) - (\partial u/\partial y)$$

Physically Eq. (14) means that ω remains constant on a streamline. Eqs. (12), (13), and (14) can be combined to yield the total differential equation for $f\ (y)$—namely,

$$f'f'' - ff''' = 0 \tag{15}$$

This third-order ordinary differential equation has the general solution

$$f\ (y) = A_0 \exp\ (A_2 y) + A_1 \exp\ (-A_2 y) \tag{16}$$

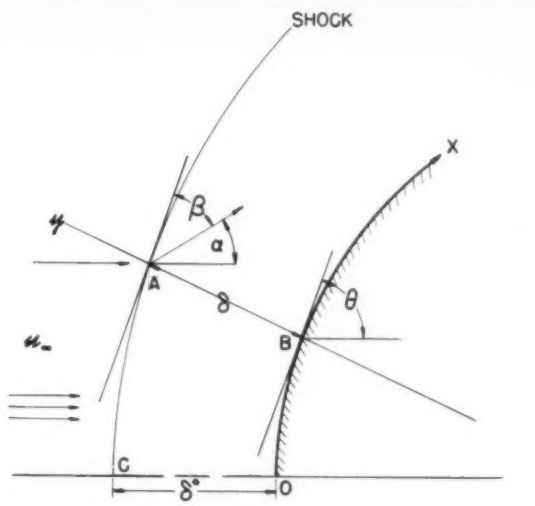

FIG. 2.

where A_0, A_1 and A_2 are integration constants to be determined from the boundary conditions. The tangency condition on the body surface, $y = 0$, yields $A_0 = -A_1$. Thus, Eq. (16) becomes

$$-v = f(y) = 2A_0 \sinh A_2 y \tag{17}$$

From Eq. (12),

$$u = xf' = 2A_0 A_2 x \cosh A_2 y \tag{18}$$

The expression for ω is

$$\omega = -xf'' = -2A_0 A_2^2 x \sinh A_2 y \tag{19}$$

The boundary conditions at the shock wave are

$$2A_0 \sinh A_2\delta = \sqrt{(k\,u_\infty \sin\beta)^2 + (u_\infty \cos\beta)^2} \times \sin\ (\theta - \alpha) \tag{20}$$

$$2A_0 A_2 x \cosh A_2\delta = \sqrt{(ku_\infty \sin\beta)^2 + (u_\infty \cos\beta)^2} \times \cos\ (\theta - \alpha) \tag{21}$$

$$2A_0 A_2^2 x \sinh A_2\delta = \frac{-u_\infty{}^2(1 - k)^2 \sin\beta \cos\beta (d\beta/dx)}{\sqrt{(ku_\infty \sin\beta)^2 + (u_\infty \cos\beta)^2} \sin\ (\theta - \alpha)} \tag{22}$$

Eqs. (20) and (21) follow directly from Eqs. (7) and (8). Eq. (22) can be established easily by using Eqs. (1a) and (2a). Near the stagnation point consider $x_A \to 0$, then $A \to C$ where C is the point behind the normal shock on the axis of symmetry (see Fig. 2). Obviously, when the shock wave conditions are applied near C, the following limiting values must be taken:

$$x \to 0, \quad \alpha \to 0, \quad \theta \to \pi/2, \quad \beta \to \pi/2,$$
$$\cos\ (\theta - \alpha) \to 0, \quad \cos\beta \to 0, \quad \sin\beta \to 1,$$
$$\sin\ (\theta - \alpha) \to 1, \quad \delta \to \delta^*$$

It can easily be shown that to the present order of accuracy

$$\lim_{x\to 0} \frac{\cos\beta}{x} = \left(-\frac{d\beta}{dx}\right)_{x\to 0} = -\frac{1}{R_S}$$

$$\lim_{x\to 0}\frac{\cos(\theta-\alpha)}{x}=\left(-\frac{d\theta}{dx}+\frac{d\alpha}{dx}\right)_{x\to 0}=-\frac{1}{R_B}+\frac{k-1}{kR_S}$$

where R_S and R_B are the radii of curvature of shock and body at the body axis.† When these considerations are applied to the conditions in Eqs. (20)–(22), it is found that

$$2A_0\sinh A_2\delta^*=ku_\infty \tag{20a}$$

$$2A_0A_2\cosh A_2\delta^*=-(u_\infty/R_S) \tag{21a}$$

$$2A_0A_2^2\sinh A_2\delta^*=(1-k)^2\frac{ku_\infty}{(kR_S)^2} \tag{22a}$$

These equations can be solved simultaneously for A_0, A_2 and δ^*. The results are:

$$A_0=ku_\infty\sqrt{k(2-k)}/2(1-k) \tag{23}$$

$$A_2=-(1-k)/kR_S \tag{24}$$

$$\delta^*=[(-kR_S)/(1-k)]\sinh^{-1}[(1-k)/\sqrt{k(2-k)}] \tag{25}$$

Substitution of the results in Eqs. (17) and (18) yields the following velocity profiles in the shock layer:

$$u/u_\infty=(-x/R_S)\sqrt{k(2-k)}\cosh\{(y/\delta^*)\sinh^{-1}[(1-k)/\sqrt{k(2-k)}]\} \tag{26}$$

$$v/u_\infty=-k[\sqrt{k(2-k)}/(1-k)]\sinh\{(y/\delta^*)\sinh^{-1}[(1-k)/\sqrt{k(2-k)}]\} \tag{27}$$

Hayes[2] obtained the results below by a different approach:

$$\delta^*=-(kR/\sqrt{1-2k})\sinh^{-1}\sqrt{(1-2k)/2k}\simeq-[kR/(1-k)]\sinh^{-1}[(1-k)/\sqrt{2k}] \tag{28}$$

$$u/u_\infty=-(x/R)\sqrt{2k}\cosh[(y/\delta^*)\times\cosh^{-1}(1/2k)]\simeq-(x/R)\sqrt{2k}\times\cosh\{(y/\delta^*)\sinh^{-1}[(1-k)/\sqrt{2k}]\} \tag{29}$$

$$v/u_\infty=-k\sqrt{2k/(1-2k)}\sinh[(y/\delta^*)\sinh^{-1}\sqrt{(1-2k)/2k}]\simeq-[k\sqrt{2k}/(1-k)]\times\sinh\{(y/\delta^*)\sinh^{-1}[(1-k)/\sqrt{2k}]\} \tag{30}$$

Obviously, these results are in agreement with the present results as far as the leading terms containing k are concerned.

The expression for surface pressure coefficient is found to be

$$C_p=(2-k)[1-(x/R_S)^2] \tag{31}$$

The general expression for vorticity is

$$\omega=(x/\delta^*)(u_\infty/R_S)\sqrt{k(2-k)}\sinh^{-1}[(1-k)/\sqrt{k(2-k)}]\sinh\{(y/\delta^*)\sinh^{-1}[(1-k)/\sqrt{k(2-k)}]\} \tag{32}$$

which shows that the vorticity vanishes on the surface of the body.

† In the present computations, take $R_B\simeq R_S=R$.

Axially Symmetric Flow

Near the stagnation point the u variation is assumed to be as in Eq. (12). The continuity equation, Eq. (3b), is satisfied if

$$v=-2f(y) \tag{33}$$

When p is eliminated from Eqs. (1a) and (2a) for axially symmetric flow, the resulting equation is

$$u(\partial\omega/\partial x)+v(\partial\omega/\partial y)=(u/x)\omega \tag{34}$$

This equation is the well known law of variation of ω along stream tubes. Combination of Eqs. (12), (31), and (34) yields simply

$$f'''=0 \tag{35}$$

Eq. (35) in turn yields the general solution

$$f(y)=C_0+C_1y+C_2y^2 \tag{36}$$

in which the integration constants C_0, C_1, C_2, must be determined from the boundary conditions. The tangency condition on the body surface implies that $C_0=0$. The shock wave conditions considered near the stagnation point—i.e., $x\to 0$—yield the following equations:

$$C_1\delta^*+C_2\delta^{*2}=(ku_\infty/2) \tag{37}$$

$$C_1+2C_2\delta^*=-(u_\infty/R_S) \tag{38}$$

$$C_2=[(1-k)^2/2][ku_\infty/(kR_S)^2] \tag{39}$$

By substituting C_2 from Eq. (39) into Eqs. (37) and (38) and by solving for C_1 and δ^*, the following equations result:

$$C_1=\mp\sqrt{1-(1-k)^2}\,(u_\infty/R_S) \tag{40}$$

$$\delta^*=\{[-1\pm\sqrt{1-(1-k)^2}]/[(1-k)^2]\}kR_S \tag{41}$$

u, v can now be expressed as follows:

$$\frac{u}{u_\infty}=k\frac{x}{\delta^*}\left[\frac{\pm\sqrt{1-(1-k)^2}-[1-(1-k)^2]}{(1-k)^2}+\frac{2\mp2\sqrt{1-(1-k)^2}-(1-k)^2}{(1-k)^2}\frac{y}{\delta^*}\right] \tag{42}$$

$$\frac{v}{u_\infty}=-2k\frac{y}{\delta^*}\left[\frac{\pm\sqrt{1-(1-k)^2}-[1-(1-k)^2]}{(1-k)^2}+\frac{2\mp2\sqrt{1-(1-k)^2}-(1-k)^2}{2(1-k)^2}\frac{y}{\delta^*}\right] \tag{43}$$

There is the question of the choice of the sign before the radicals in Eqs. (40) to (43). It can be seen that if the "bottom" signs are chosen, Eq. (43) will give a value of v which undergoes a reversal in sign in the range $0<(y/\delta^*)<1$. The physical meaning of such a solution is that there exists a flow reversal in the shock layer near the stagnation point. Since an inviscid theory should not permit a solution with flow reversal, the "top" sign in Eqs. (38) to (43) should be adopted. A comparison with Hayes' work shows again that for $k\ll 1$, the results are in agreement.

The surface pressure coefficient is

$$C_p = (2 - k)\,[1 - (x/R_S)^2] \tag{31}$$

which is the same result as obtained in the two-dimensional case. The vorticity on the body surface does not vanish as in the two-dimensional problem. It can be expressed as

$$\omega = [(-u_\infty)/R_S]\,[-1 + \sqrt{k(2-k)}]\,(x/\delta^*) \tag{44}$$

A comparison of the two-dimensional and three-dimensional shock detachment distances according to the present study is presented in Fig. 3.

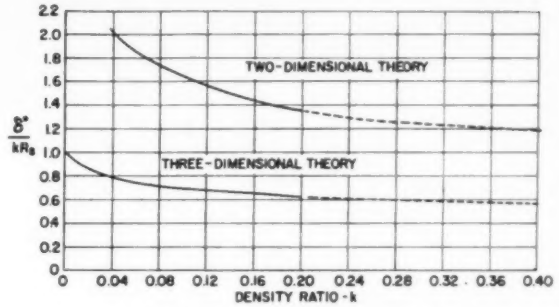

FIG. 3. Theoretical shock detachment distance.

RESULTS

Since primarily three-dimensional shapes are of practical interest, the ensuing discussion and comparisons with experiment treat only the three-dimensional case.

A comparison of experimental values of pressure coefficients on a sphere with those computed in this analysis is presented in Fig. 4 for Mach Numbers 1.97 and 5.8. The agreement is surprisingly good in view of the simplifying assumptions made in the theory. In particular, the values of the density ratio, k, for the test data—0.381 and 0.192, respectively—are certainly not very small compared to 1.0 as was assumed in the theory, yet the correlation is quite good. Moreover, the agreement persists well beyond the theoretical limits of applicability† of the present theory. As would be expected, the agreement is better at the higher Mach Number (smaller k).

Figs. 5a and 5b present a comparison of theoretical and experimental values of shock detachment distance for spheres in air and in monatomic gases, respectively. In both cases the agreement between the theory and test improves with increasing Mach Number (decreasing k). The density ratio, k, in the tests of Figs. 5a and 5b ranges from 0.24 to 0.54 so that the small density ratio assumption of the theory does not, strictly speaking, apply for these data. In view of this, the difference between theory and the experimental measurements is not considered excessive.

Recent experiments on hemispheres reported by Korobkin[7] support the assumption that the u velocity component is directly proportional to distance along the surface of the body. Fig. 6 shows the nondimensionalized velocities measured by Korobkin at four different Mach Numbers in the NOL Aeroballistics Tunnel No. 1. Within the limits of the data, it is seen that the local velocity on the surface is indeed linear up to 45 degrees and deviates from linearity only slightly thereafter.

The velocity gradient at the stagnation point is a quantity of considerable importance in the blunt body heating problem. According to the present analysis the quantity is given by

$$\left.\frac{\partial u}{\partial x}\right|_{\substack{x=0\\y=0}} = -\frac{u_\infty}{R_S}\sqrt{k(2-k)} \tag{45}$$

This estimate is compared with Korobkin's experimental measurements in Fig. 7. The agreement is good, the theory being consistently high by about nine per cent for Mach Numbers ranging from 2.0 to 5.0. Also shown in Fig. 7 are values of

$$\left.\frac{\partial u}{\partial x}\right|_{\substack{x=0\\y=0}} \quad (\text{for } \gamma = 1.4)$$

at Mach Number infinity as predicted by the present analysis and by Lees.[5] The latter two values are practically identical.

The theoretical distribution of velocity and pressures along the axial streamline between the shock and the stagnation point are presented in Figs. 8 and 9, respectively. No experimental data are available for comparison.

In an analysis of the simple shear flow past a flat plate in a viscous fluid,[6] the senior author of the present paper has shown that "vorticity number," rather than the vorticity itself, is an important parameter in studying the effect of vorticity upon the boundary-layer behavior. The vorticity number is essentially the ratio of the vorticity in the free stream to the average vorticity in the boundary layer. It is expressed as

$$\xi = (\omega_B/u_B)\sqrt{\nu x/u_B} = \omega_B/(u_B/\Delta) \tag{46}$$

where

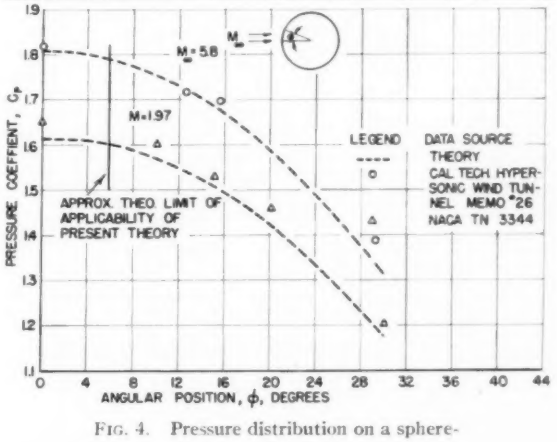

FIG. 4. Pressure distribution on a sphere-

† See Discussion, page 31, on the limits of applicability of the theory.

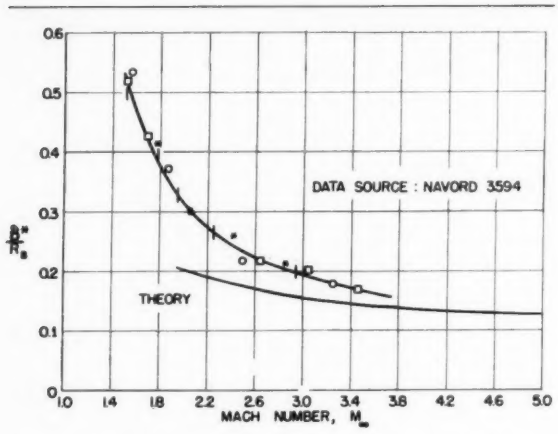

FIG. 5a. Shock detachment distance (spheres tested in air).

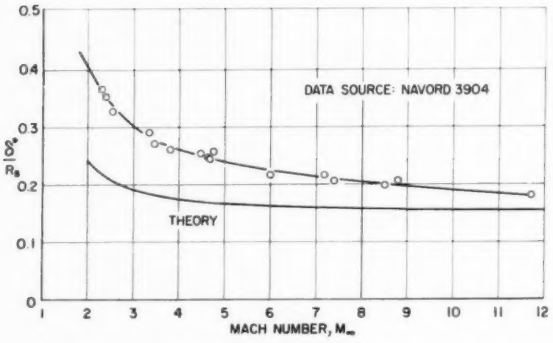

FIG. 5b. Shock detachment distance (sphere tested in monatomic gases).

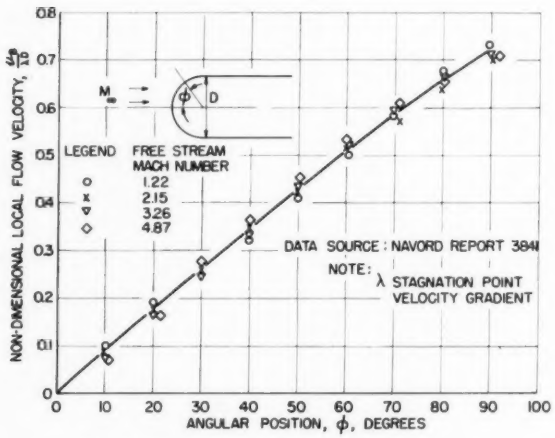

FIG. 6. Velocity distribution on hemispheres.

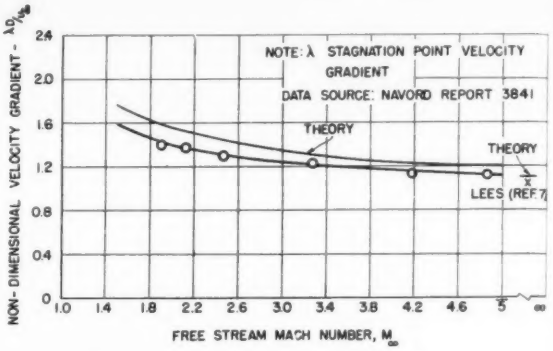

FIG. 7. Stagnation point velocity gradient.

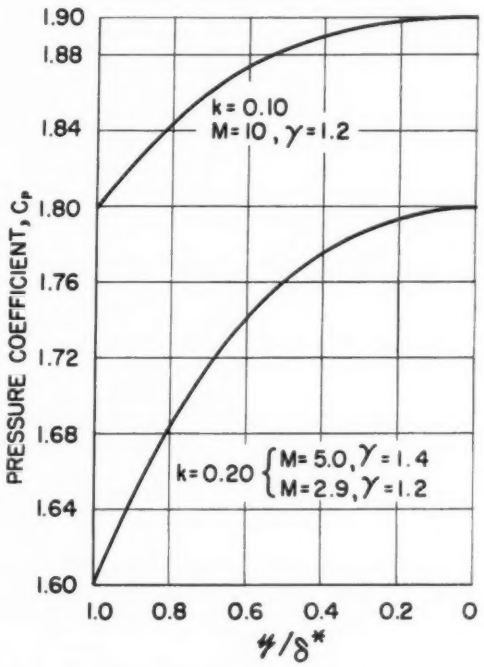

FIG. 8. Pressure distribution along axial streamline.

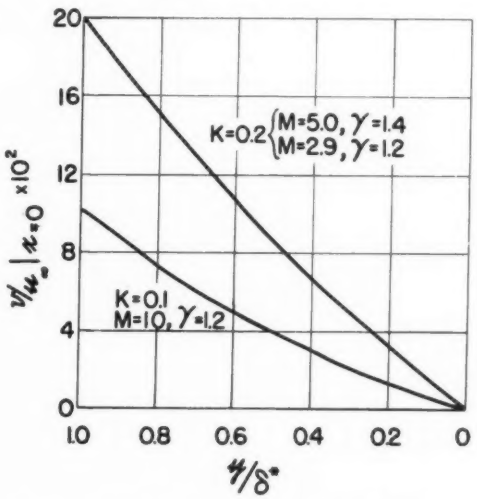

FIG. 9. Velocity distribution along axial streamline.

$\omega = (\partial v/\partial x) - (\partial u/\partial y)$

Δ = boundary-layer thickness near the stagnation point

The vorticity number for spheres has been calculated by the present theory (Fig. 10). Because local velocity on the surface of the spheres varies linearly with x, the vorticity number is constant along the surface. The vorticity number is a function of density ratio and Reynolds Number (based on free-stream velocity, viscosity in the shock layer, and sphere diameter). It is seen that the vorticity effects increase as Mach Number increases. However, on spheres of practical sizes, except in extremely low density flows, the magnitude of ξ remains small. It can therefore be anticipated that the vorticity effect upon the boundary-layer behavior in a blunt-nosed body may also be small.

An estimate of the ratio of boundary-layer thickness to shock layer thickness near the stagnation point expressed in terms of the density ratio and the vorticity number may be obtained from Eq. (46). This ratio is given by

$$\Delta/\delta = 0[\xi\sqrt{2k}]$$

It is less than the vorticity number, which was shown above to be small for spheres of practical sizes in all but extremely low density hypersonic flows. Hence it appears that the boundary-layer thickness is negligible near the nose of the sphere.

Discussion

Two restrictive assumptions made in the present inviscid analysis are (1) $r/x \simeq 1$, and (2) $k = \rho_\infty/\rho$, constant.

The assumption $r/x \simeq 1$ affects only the continuity equation which, for constant curvature and constant density, is

$$(u\partial r/\partial x) + (r\partial u/\partial x) + (1 + Ky) \times \{(v\partial r/\partial y) + (r\partial v/\partial y)\} + Kvr = 0$$

Now
$$r = [1 + Ky]\,|R_B| \sin(x/|R_B|) \qquad (47)$$

hence
$$\partial r/\partial x = [1 + Ky]\cos\phi \qquad (48)$$

and
$$\partial r/\partial y = \sin\phi \qquad (49)$$

To say $r \cong x$ implies that $\partial r/\partial y \simeq 0$ or $\sin\phi \ll 1$ and that $\partial r/\partial x \simeq 1$ or $Ky = 0[\delta/|R_B|] = 0[k] \ll 1$.

Thus, the assumption $r \simeq x$ requires $k \ll 1$ (which is consistent with the explicit use of that assumption elsewhere in the theory) except on or very near the body surface. Moreover the assumption restricts application of the theory to the immediate vicinity of the stagnation point.

Sufficient information concerning high-speed flows about spheres is available to permit an estimate of the extent of the subsonic flow region and, hence, an assessment of the validity of the constant density assumption.

The excellent agreement between the modified Newtonian hypersonic approximation† and experimental pressure measurements on spheres has been pointed out by a number of authors—e.g., Lees,[5] Oliver.[8] Assuming compressible flow, application of the Bernoulli's law readily yields the Mach Number distribution on the sphere surface. The locations of

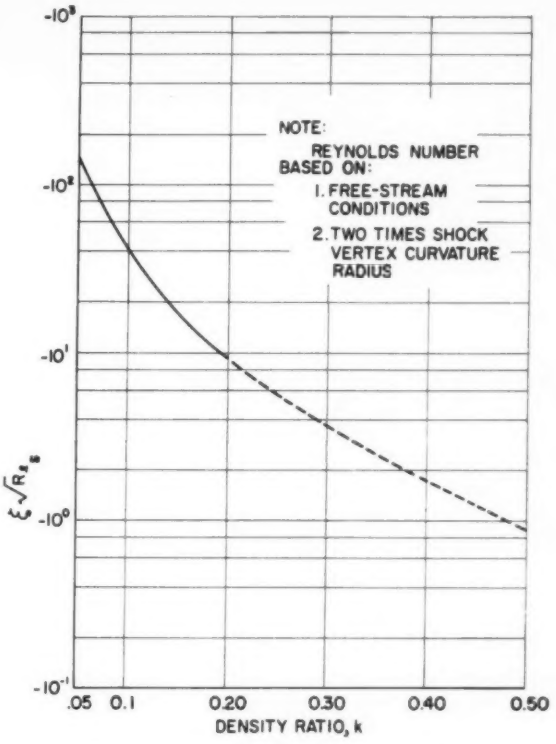

Fig. 10. Vorticity distribution on a sphere.

† The modified Newtonian approximation referred to here alters the simple Newtonian relation for pressure coefficient by replacing the approximate stagnation pressure coefficient of 2.0 with its exact value. This type of modification of the Newtonian impact theory for application to hypersonic blunt bodies has been suggested by a number of investigators on the basis of their experimental measurements.

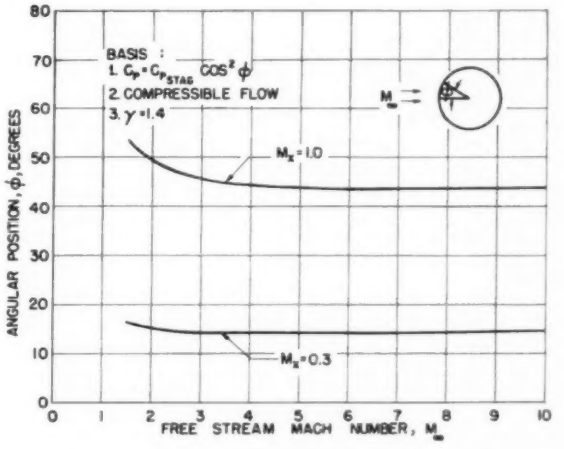

Fig. 11. Extent of incompressible flow on spheres.

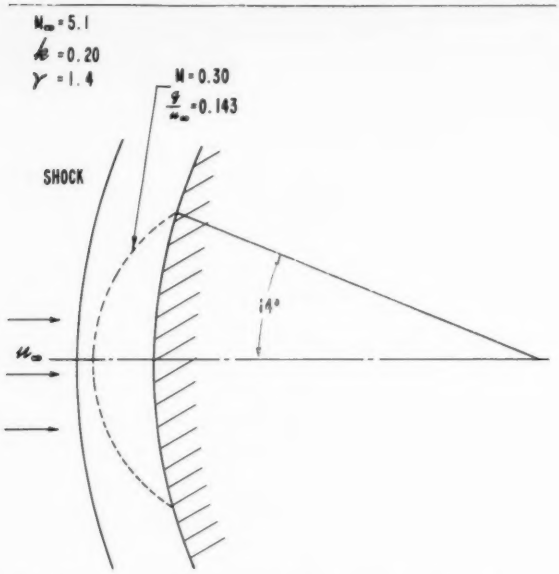

FIG. 12. Approximate extent of incompressible flow region.

the local Mach Number 0.30 and 1.00 points on the sphere were thus calculated for the free-stream Mach Number ranging from 1.5 to 10.0 ($\gamma = 1.4$). The results of the computations are shown in Fig. 11.

Fig. 12 shows a representative contour of constant total velocity for $k = 0.20$. This corresponds to flow past a sphere in ideal air [$\gamma = 1.4$] with a free-stream Mach Number of 5.1. If one considers the three-dimensional Prandtl-Glauert factor, $1/(1 - M^2)$, a fair criterion of the significance of compressibility effects and permits about 9 per cent error, the local Mach Number 0.30 line represents the limit of validity of the constant density assumption for the calculated example.

In view of the relatively severe limitations imposed upon the applicability of the present theory by the assumptions $r \simeq x$ and k constant the excellent agreement with experimental pressure coefficients well beyond the theoretical limits of validity of the theory would seem fortuitous. It is conjectured that perhaps the errors incurred by the various simplifying assumptions† are compensating on the sphere's surface.

It is interesting that the present theory gives pressure coefficients very similar to those given by the Newtonian hypersonic approximation. The present theory gives $C_p = (2 - k)(1 - \phi^2)$, while the simple Newtonian value is $C_p = 2\cos^2\phi$. Within the theoretical range of applicability of the present theory $\phi = \sin\phi$ and hence the pressure coefficient may be written $C_p = (2 - k)\cos^2\phi$. The quantity $(2 - k)$, which is the pressure coefficient at the stagnation point as given by the present theory, is a density ratio correction to the Newtonian approximation‡ resulting from consideration of boundary conditions immediately behind the shock. The present theory has also the apparent advantage that it describes the flow field between the shock and body near the stagnation point while the Newtonian theory yields only surface pressures.

It is noted that the development of the theory of this paper does not depend upon an explicit energy relation. This is an advantage that assumes considerable importance for the hypersonic flow of a real gas about a blunt body. In the present formulation, the theory can be applied to the case of a dissociated or ionized gas when the value of k is correctly estimated, provided the constant density assumption is not invalidated by real gas phenomena. It should be noted that the theory assumes thermodynamic equilibrium; hence, some real gas phenomena, such as relaxation time effects, are not accounted for.

The hypersonic blunt body theory developed herein has the advantage of simplicity but its extent of applicability is limited to the vicinity of the stagnation point. Steps have been initiated to extend the range of applicability of the theory by removing some of the restrictive assumptions.

To provide an understanding of the curvature effects, an attempt is being made to treat the problem with the terms containing K retained in the basic differential equations. The task is being carried out for the case of axially symmetric flows for bodies with a constant K. In this approach it is assumed that $r \simeq (1 + Ky)x$. A preliminary examination of the results obtained to date appears to indicate that the effects of curvature terms are:

(1) To increase the shock detachment distance. Hence, it is anticipated that the agreement between theory and experiment will be improved.

(2) To provide a pressure relief on the body surface. This is in qualitative agreement with the centrifugal force correction to the classical Newtonian impact theory.

The details of this analysis are presently being worked upon. It is anticipated that specific numerical calculations will be made to illustrate quantitatively the effects of curvature.

† $r \simeq x$, k = constant, and $k \ll 1$.

‡ See footnote on page 31.

REFERENCES

[1] Heybey, W. H., *Shock Distances in Front of Symmetrical Bodies*, Navord Report 3594, December, 1953.

[2] Hayes, W. D., *Some Aspects of Hypersonic Flow*, Ramo-Wooldridge Corporation, January, 1955.

[3] Hayes, W. D., *Hypersonic Flow Fields at Small Density Ratio*, Ramo-Wooldridge Corporation, May, 1955.

[4] Reshotko, E., and Cohen, C. B., *Heat Transfer at the Forward Stagnation Point of Blunt Bodies*, NACA TN 3513, 1955.

[5] Lees, Lester, "Hypersonic Flow," *Fifth International Aeronautical Conference* (Proceedings), IAS-RAeS, Los Angeles, June 20–23, 1955; Institute of the Aeronautical Sciences, N.Y., 1956.

[6] Li, Ting-Yi, *Simple Shear Flow Past a Flat Plate in a Compressible Viscous Fluid*, Journal of Aeronautical Sciences, Vol. 22, No. 10, p. 724, October, 1955.

[7] Korobkin, Irving, *Laminar Heat Transfer Characteristics of a Hemisphere for the Mach Number Range 1.9 to 4.9*, Navord Report 3841, 1954.

[8] Oliver, Robert E., *An Experimental Investigation of Flow over Simple Blunt Bodies at a Nominal Mach Number of 5.8*, GALCIT, Hypersonic Wind Tunnel Memo No. 26, June, 1955.

Unsteady Flow Around Thin Wings at High Mach Numbers†

MÅRTEN T. LANDAHL*

Massachusetts Institute of Technology

SUMMARY

The perturbation velocity potential for unsteady flow around thin wings is expanded in a series of M^{-2}, taking into account linear and second-order terms in perturbation velocities. The first terms for the pressure are seen to be in agreement with those predicted by the Hayes-Lighthill piston theory. Additional terms provided by the present theory give improved accuracy for moderately high Mach Numbers and also take into account some effects of three-dimensionality, such as moderate leading-edge sweep and spanwise downwash variations. Comparison with previous solutions suggests that the present theory is sufficiently accurate for practical purposes down to $M = 2$. A calculation performed for the simple case of two-dimensional bending-torsion flutter shows good agreement with results obtained from the exact linearized theory for Mach Numbers above 1.5.

SYMBOLS

a	= distance from mid-chord line to elastic axis (positive aft), divided by b
b	= semichord at wing root
C_p	= pressure coefficient, $(p - p_0)/(1/2)\rho U^2$
C_L	= lift coefficient, $\text{lift}/(1/2)\rho U^2 S$
$g(x, y)$	= function giving the shape of the airfoil
$h(x, y, t)$	= function giving the instantaneous location of the (upper) wing surface
i	= $\sqrt{-1}$
k	= reduced frequency of oscillation $\omega b/U$
$L_1, L_2, \ldots, M_4$	= flutter coefficients as defined in reference 5
M	= free-stream Mach Number
p	= local static pressure
p_0	= free-stream static pressure
r_α	= radius of gyration in pitch, divided by b
s	= Laplace transform variable
S	= wing area
t	= dimensionless time obtained by multiplying by U/b
U	= free-stream velocity
w_0	= downwash on wing in linearized form
x, y, z	= dimensionless Cartesian coordinates obtained by dividing by b
$x = x_t$	= location of pitching axis
x_α	= distance from elastic axis to center of gravity (positive aft), divided by b
α	= angle of attack
γ	= ratio of specific heats
δ	= the larger of the quantities ϵ and λ
ϵ	= thickness ratio of wing
λ	= dimensionless amplitude of time-dependent wing motion
μ	= ratio of wing mass per unit span to the quantity $4\rho b^2$
ρ	= free-stream density
$\phi = \varphi + \psi$	= dimensionless perturbation velocity potential
φ	= first-order potential (in δ)
ψ	= second-order potential
ω	= circular frequency of oscillation
ω_h, ω_α	= circular frequencies of uncoupled vibration in bending and torsion, respectively

Received January 6, 1956.

† This paper is a slightly revised version of OSR Technical Note No. 55-245 carried out under Contract AF 18(600)-961 sponsored by the Office of Scientific Research, United States Air Force.

* Formerly, Senior Research Engineer, Fluid Dynamics Research Group. Now, with the Aeronautical Research Institute of Sweden, Ulfsunda, Sweden.

INTRODUCTION

IN A PAPER by Lighthill,[1] Hayes'[2] piston theory concept was used for calculating the unsteady flow around thin airfoils at high Mach Numbers. Very simple results were obtained which included the effect of nonlinearity. The second-order term was given exactly in the limit of high Mach Numbers, whereas the third-order term, which is influenced by the change in entropy, was only approximately given.

According to Goldsworthy[3] the relative error in piston theory is of order M^{-2}. In Lighthill's result the linear term for the pressure coefficient is of order δM^{-1} and the second-order term of order δ^2. Consequently, the dominating error term must be of order δM^{-3}, since δM is considered small. Naturally, there is no point in retaining the second-order term in Lighthill's expression unless the error is substantially smaller than this term. It follows from the above that this occurs when $M^3 \gg \delta^{-1}$. Thus, a δ of 5 per cent requires $M^3 \gg 20$, which clearly indicates the limited accuracy of piston theory at moderate Mach Numbers. In the present paper, the solution is therefore expanded in powers of M^{-2}, and a few more terms are included than the leading terms constituting piston theory.

METHOD OF SOLUTION

We consider a thin wing, situated mainly along the xy-plane. The undisturbed stream flows along the positive x-axis. Nondimensional coordinates x, y, z, t are used. All lengths are made dimensionless by dividing by the semiroot chord b of the wing. The time is made dimensionless by multiplying by U/b, where U is the free-stream velocity. Then we can set $U = 1$ without loss of generality, and, consequently, the velocity of sound is $1/M$. To second order in perturbation velocities the flow is isentropic and irrotational if viscosity is neglected. Then the perturbation

velocity potential exists and satisfies the following differential equation, omitting third-order terms:

$$(1 - M^2)\phi_{xx} + \phi_{yy} + \phi_{zz} - 2M^2\phi_{xt} - M^2\phi_{tt} = M^2(\gamma - 1)(\phi_t + \phi_x)(\phi_{xx} + \phi_{yy} + \phi_{zz}) + M^2[(\partial/\partial x) + (\partial/\partial t)](\phi_x^2 + \phi_y^2 + \phi_z^2) \quad (1)$$

The position of the upper wing surface is, at every instant, given by

$$z = \delta h(x, y, t) \quad (2)$$

Then we get the following boundary condition on the upper wing surface:

$$\phi_z(x, y, \delta h, t) = (1 + \phi_x)\delta h_x + \phi_y\delta h_y + \delta h_t \quad (3)$$

It is convenient to impose a condition at $z = +0$ instead. Using a Taylor series expansion and neglecting terms of third or higher order, we get

$$\phi_z(+0) = \delta(h_x + h_t) + \delta[h_x\phi_x - h\phi_{zz} + h_y\phi_y]_{z=+0} \quad (4)$$

We also require ϕ and its derivatives to vanish far upstream. For the pressure we have, in isentropic flow,

$$C_P = (2/\gamma M^2)\left(\left\{1 - [(\gamma - 1)/2]M^2(2\phi_x + 2\phi_t + \phi_x^2 + \phi_y^2 + \phi_z^2)\right\}^{\gamma/(\gamma-1)} - 1\right) \quad (5)$$

or, expanding and retaining linear and quadratic terms,

$$C_p = -2(\phi_x + \phi_t) + M^2(\phi_x + \phi_t)^2 - (\phi_x^2 + \phi_y^2 + \phi_z^2) \quad (6)$$

On the wing surface the pressure can be expressed using the values of ϕ and its derivatives on $z = +0$, as follows:

$$C_p = -[2(\phi_x + \phi_t) - M^2(\phi_x + \phi_t)^2 + \phi_x^2 + \phi_y^2 + \phi_z^2 + 2\delta h(\phi_{xz} + \phi_{tz})]_{z=+0} \quad (7)$$

or, making partial use of Eq. (4),

$$C_p = -[2(\phi_x + \phi_t) - M^2(\phi_x + \phi_t)^2 + \phi_x^2 + \phi_y^2]_{z=+0} - 2\delta^2 h[(\partial/\partial x) + (\partial/\partial t)]^2 h - \delta^2(h_x + h_t)^2 \quad (8)$$

To solve the nonlinear equation for ϕ we use an iteration procedure. Putting

$$\phi = \varphi + \psi \quad (9)$$

where $\varphi = 0(\delta)$ and $\psi = 0(\delta^2)$

we get from the above equations

$$(1 - M^2)\varphi_{xx} + \varphi_{yy} + \varphi_{zz} - 2M^2\varphi_{xt} - M^2\varphi_{tt} = 0 \quad (10)$$

$$(1 - M^2)\psi_{xx} + \psi_{yy} + \psi_{zz} - 2M^2\psi_{xt} - M^2\psi_{tt} = M^2(\gamma - 1)(\varphi_x + \varphi_t)(\varphi_{xx} + \varphi_{yy} + \varphi_{zz}) + M^2[(\partial/\partial x) + (\partial/\partial t)](\varphi_x^2 + \varphi_y^2 + \varphi_z^2) \quad (11)$$

$$\varphi_z(+0) = \delta(h_x + h_t) = \delta w_0(x, y, t) \quad (12)$$

$$\psi_z(+0) = \delta(h_x\varphi_x - h\varphi_{zz} + h_y\varphi_y)_{z=+0} \quad (13)$$

$$C_p = -[2(\varphi_x + \varphi_t) + 2(\psi_x + \psi_t) - M^2(\varphi_x + \varphi_t)^2 + \varphi_x^2 + \varphi_y^2]_{z=+0} - 2\delta^2 h[(\partial/\partial x) + (\partial/\partial t)]^2 h - \delta^2(h_x + h_t)^2 \quad (14)$$

By use of an iteration the first term on the right-hand side of Eq. (11) can be somewhat simplified, so that

$$(1 - M^2)\psi_{xx} + \psi_{yy} + \psi_{zz} - 2M^2\psi_{xt} - M^2\psi_{tt} = M^4(\gamma - 1)(\varphi_x + \varphi_t)[(\partial/\partial x) + (\partial/\partial t)]^2\varphi + M^2[(\partial/\partial x) + (\partial/\partial t)](\varphi_x^2 + \varphi_y^2 + \varphi_z^2) \quad (15)$$

To obtain an expansion for high Mach Number we put

$$x_1 = x \qquad y_1 = y$$

$$z_1 = Mz \quad (16)$$

$$t_1 = t - x \quad (17)$$

$$\varphi = (\delta/M)[\varphi_1 + (1/M^2)\varphi_2 + (1/M^4)\varphi_3] + 0(\delta/M^7) \quad (18)$$

$$\psi = \delta^2[\psi_1 + (1/M^2)\psi_2] + 0(\delta^2/M^4) \quad (19)$$

This gives the following sequence of differential equations to solve, with their respective boundary conditions on $z_1 = +0$:

$$-\varphi_{1x_1x_1} + \varphi_{1z_1z_1} = 0 \quad (20)$$

$$\varphi_{1z_1} = w_0 \quad (21)$$

$$-\varphi_{nx_1x_1} + \varphi_{nz_1z_1} = -\left\{[(\partial/\partial x_1) - (\partial/\partial t_1)]^2 + (\partial^2/\partial y_1^2)\right\}\varphi_{n-1} \quad (22)$$

$$\varphi_{nz_1} = 0, \qquad n > 1 \quad (23)$$

$$-\psi_{1x_1x_1} + \psi_{1z_1z_1} = (\gamma - 1)\varphi_{1x_1}\varphi_{1x_1x_1} + 2\varphi_{1z_1}\varphi_{1x_1z_1} \quad (24)$$

$$\psi_{1z_1} = -h\varphi_{1z_1z_1} \quad (25)$$

$$-\psi_{2x_1x_1} + \psi_{2z_1z_1} = (\partial/\partial x)[(\gamma - 1)\varphi_{1x_1}\varphi_{2x_1} + 2\varphi_{1z_1}\varphi_{2z_1}] - \left\{[(\partial/\partial x_1) - (\partial/\partial t_1)]^2 + (\partial^2/\partial y_1^2)\right\}\psi_1 + (\partial/\partial x)[(\varphi_{1x_1} - \varphi_{1t_1})^2 + \varphi_{1y_1}^2] \quad (26)$$

$$\psi_{2z_1} = -h\varphi_{2z_1z_1} + (h_{x_1} - h_{t_1})(\varphi_{1x_1} - \varphi_{1t_1}) + h_{y_1}\varphi_{1y_1} \quad (27)$$

For the solution Van Dyke's method[4] can be directly applied. First, a smoothing is carried out which removes the jump in velocities across the shock. This is achieved by considering a small flexible part attached to the nose of the airfoil so that the relative wind is always parallel to the surface of the nose. The smoothing technique is discussed in detail in reference 4. Then we apply a Laplace transformation in the x_1-direction. We set

$$\mathfrak{L}(\varphi_n) = \bar{\varphi}_n = \int_0^\infty e^{-sx_1}\varphi_n\,dx_1 \quad (28)$$

$$\mathfrak{L}(\psi_n) = \bar{\psi}_n = \int_0^\infty e^{-sx_1}\psi_n\,dx_1 \quad (29)$$

The solution for $\bar{\varphi}_1$ is easily found to be, for $z_1 > 0$,

$$\bar{\varphi}_1 = -(1/s)\bar{w}_0(s, t_1)e^{-sz_1} \quad (30)$$

where

$$\bar{w}_0(s, t_1) = \int_0^\infty e^{-sx_1}w_0(x_1, y_1, t_1 + x_1)\,dx_1 \quad (31)$$

Inversion then gives, by use of standard formulas,

$$\varphi_1 = -\int_0^{x_1-z_1} w_0(\xi_1, y_1, t_1 + \xi_1)\, d\xi_1 \qquad (32)$$

The lower limit can, if desired, be replaced by x_L, where $x_L(y)$ gives the position of the leading edge. For $\bar{\varphi}_2$ we get the following differential equation:

$$-s^2\bar{\varphi}_2 + \bar{\varphi}_{2z_1z_1} = -\{[s - (\partial/\partial t_1)]^2 + (\partial^2/\partial y_1^2)\}\bar{\varphi}_1(s, +0)e^{-sz_1} \qquad (33)$$

The solution is obtained by putting

$$\bar{\varphi}_2 = \bar{A}_2 e^{-sz_1} + \bar{B}_2 z_1 e^{-sz_1} \qquad (34)$$

Inserting this into Eq. (33) and using the boundary condition, Eq. (23), gives

$$\bar{A}_2 = (1/2s^2)\{[s - (\partial/\partial t_1)]^2 + (\partial^2/\partial y_1^2)\}\bar{\varphi}_1(s, +0)$$
$$\bar{B}_2 = (1/2s)\{[s - (\partial/\partial t_1)]^2 + (\partial^2/\partial y_1^2)\}\bar{\varphi}_1(s, +0)$$

or

$$\varphi_2 = \frac{1}{2}\left[\left(\frac{\partial}{\partial x_1} - \frac{\partial}{\partial t_1}\right)^2 + \frac{\partial^2}{\partial y_1^2}\right] \times \int_{x_L}^{x_1-z_1} (x_1 - z_1 - \xi_1)\varphi_1(\xi_1, y_1, +0, t_1)\, d\xi_1 + \frac{1}{2} z_1 \left[\left(\frac{\partial}{\partial x_1} - \frac{\partial}{\partial t_1}\right)^2 + \frac{\partial^2}{\partial y_1^2}\right] \int_{x_L}^{x_1-z_1} (x_1 - z_1 - \xi_1) \times w_0(\xi_1, y_1, t_1 + \xi_1)\, d\xi_1 \qquad (35)$$

By using the result from Eq. (32),

$$\varphi_2 = -\frac{1}{4}\left[\left(\frac{\partial}{\partial x_1} - \frac{\partial}{\partial t_1}\right)^2 + \frac{\partial^2}{\partial y_1^2}\right] \times \int_{x_L}^{x_1-z_1} (x_1 - z_1 - \xi_1)^2 w_0(\xi_1, y_1, t_1 + \xi_1)\, d\xi_1 - \frac{1}{2} z_1 \left[\left(\frac{\partial}{\partial x_1} - \frac{\partial}{\partial t_1}\right)^2 + \frac{\partial^2}{\partial y_1^2}\right] \int_{x_L}^{x_1-z_1} (x_1 - z_1 - \xi_1) \times w_0(\xi_1, y_1, t_1 + \xi_1)\, d\xi_1 \qquad (36)$$

Laplace-transforming the iteration equation for φ_3 gives

$$-s^2\bar{\varphi}_3 + \bar{\varphi}_{3z_1z_1} = -\{[s - (\partial/\partial t_1)]^2 + (\partial^2/\partial y_1^2)\}e^{-sz_1}\bar{\varphi}_2(s, +0) - sz_1\{[s - (\partial/\partial t_1)]^2 + (\partial^2/\partial y_1^2)\}e^{-sz_1}\bar{\varphi}_2(s, +0) \qquad (37)$$

The solution is found by putting

$$\bar{\varphi}_3 = \bar{A}_3 e^{-sz_1} + \bar{B}_3 z_1 e^{-sz_1} + \bar{C}_3 z_1^2 e^{-sz_1} \qquad (38)$$

By substitution, the coefficients are easily found to be

$$\bar{A}_3 = (3/4s^2)\{[s - (\partial/\partial t_1)]^2 + (\partial^2/\partial y_1^2)\}\bar{\varphi}_2(s, +0) \qquad (39)$$

$$\bar{B}_3 = (3/4s)\{[s - (\partial/\partial t_1)]^2 + (\partial^2/\partial y_1^2)\}\bar{\varphi}_2(s, +0) \qquad (40)$$

$$\bar{C}_3 = (1/4)\{[s - (\partial/\partial t_1)]^2 + \partial^2/\partial y_1^2\}\bar{\varphi}_2(s, +0) \qquad (41)$$

In particular, we find by inverting and making use of the above results for φ_2,

$$\varphi_{3x_1}(x_1, +0, t_1) = -\frac{1}{16}\left[\left(\frac{\partial}{\partial x_1} - \frac{\partial}{\partial t_1}\right)^2 + \frac{\partial^2}{\partial y_1^2}\right]^2 \times \int_{x_L}^{x_1} (x_1 - \xi_1)^3 w_0(\xi_1, y_1, t_1 + \xi_1)\, d\xi_1 \qquad (42)$$

For the nonlinear part of the solution we proceed in about the same way and get, after Laplace-transforming Eq. (24),

$$-s^2\bar{\psi}_1 + \bar{\psi}_{1z_1z_1} = (1/2)se^{-sz_1}\mathfrak{L}_t\{[(\gamma - 1)\varphi_{1x_1}^2 + 2\varphi_{1z_1}^2]_{z_1=+0}\} \qquad (43)$$

The solution is obtained, as before, by a proper combination of $z_1e^{-sz_1}$ and e^{-sz_1}. The final result, taking into account the boundary condition, Eq. (25), reads

$$\psi_1 = -\frac{1}{4}\int_{x_L}^{x_1-z_1} [(\gamma - 1)\varphi_{1\xi_1}^2 + 2\varphi_{1z_1}^2]_{z_1=0}\, d\xi_1 - \frac{1}{4} z_1[(\gamma - 1)\varphi_{1x_1}^2 + 2\varphi_{1z_1}^2] + \int_{x_L}^{x_1-z_1} [h\varphi_{1\xi_1\xi_1}]_{z_1=+0}\, d\xi_1 \qquad (44)$$

For ψ_2, the Laplace-transformed right-hand side of Eq. (26) will include terms proportional to e^{-sz_1}, as well as terms containing $z_1e^{-sz_1}$. The solution is then a combination of $z_1^2e^{-sz_1}$, $z_1e^{-sz_1}$ and e^{-sz_1}. After some manipulation we get, for the x_1-derivative on the plane $z_1 = +0$,

$$\psi_{2x_1}(x_1, y_1, +0, t_1) = -\frac{1}{2}(\gamma - 1)\varphi_{1x_1}\varphi_{2x_1} + \frac{3}{4}\left[\left(\frac{\partial}{\partial x_1} - \frac{\partial}{\partial t_1}\right)^2 + \frac{\partial^2}{\partial y_1^2}\right]\int_{x_L}^{x_1} \psi_1\, d\xi_1 + \frac{1}{4}(\gamma + 1) \times \int_{x_L}^{x_1} \varphi_{1z_1}\varphi_{2\xi_1\xi_1}\, d\xi_1 - \frac{1}{2}[(\varphi_{1x_1} - \varphi_{1t_1})^2 + \varphi_{1y_1}^2] - \frac{1}{4}\left[\left(\frac{\partial}{\partial x_1} - \frac{\partial}{\partial t_1}\right)^2 + \frac{\partial^2}{\partial y_1^2}\right]\int_{x_L}^{x_1} (x_1 - \xi_1)\, h\varphi_{1\xi_1\xi_1}\, d\xi_1 + 2h\varphi_{2z_1z_1} - 2(h_{x_1} - h_{t_1})(\varphi_{1x_1} - \varphi_{1t_1}) - 2h_{y_1}\varphi_{1y_1} \qquad (45)$$

Having thus obtained the approximate solutions for the velocity potential, we expand the expression for C_p in the same way,

$$C_p = (\delta/M)[C_{p1}^{(1)} + (1/M^2)C_{p2}^{(1)} + (1/M^4)C_{p3}^{(1)}] + \delta^2[C_{p1}^{(2)} + (1/M^2)C_{p2}^{(2)}] + 0(\delta/M^7) + 0(\delta^2/M^4) \qquad (46)$$

From Eqs. (8), (18), and (19) we get, using the variables t_1, x_1, and z_1,

$$C_{p_n}^{(1)} = -2\varphi_{nx_1} \qquad (47)$$

$$C_{p1}^{(2)} = -2\psi_{1x_1} + \varphi_{1x_1}^2 - w_0^2 - 2hw_{0x_1} \qquad (48)$$

$$C_{p2}^{(2)} = -2\psi_{2x_1} + 2\varphi_{1x_1}\varphi_{2x_1} - (\varphi_{1x_1} - \varphi_{1t_1})^2 - \varphi_{1y_1}^2 \qquad (49)$$

where all derivatives are to be evaluated at $z_1 = +0$. Inserting the results for the expanded potential gives, finally, after a return to the original coordinates,

$$C_{p1}^{(1)} = 2w_0 \qquad (50)$$

$$C_{p2}^{(1)} = D\int_{x_L}^{x}(x-\xi)w_0(\xi)\,d\xi \qquad (51)$$

$$C_{p3}^{(1)} = \frac{1}{8}D^2\int_{x_L}^{x}(x-\xi)^3w_0(\xi)\,d\xi \qquad (52)$$

$$C_{p1}^{(2)} = (1/2)(\gamma+1)w_0^2 \qquad (53)$$

$$C_{p2}^{(2)} = \frac{1}{2}(\gamma+1)w_0D\int_{x_L}^{x}(x-\xi)w_0(\xi)\,d\xi + \frac{1}{8}(3\gamma-5)D\int_{x_L}^{x}(x-\xi)w_0^2(\xi)\,d\xi + \frac{1}{4}(\gamma+1)\int_{x_L}^{x}w_0(\xi)D_1h(\xi)\,d\xi - \frac{1}{4}(\gamma+1)\frac{\partial}{\partial t}\times\int_{x_L}^{x}w_0^2(\xi)\,d\xi + \frac{1}{8}(\gamma+1)w_0^2 - h_x^2 - h_y^2 - \frac{1}{4}(\gamma+1)[h-h(x_L)]D_1h(x_L) - \frac{1}{2}D_1h^2(x_L) + hD_1h(x_L) - 2h_xh_t(x_L) + 2h_yh_y(x_L) \qquad (54)$$

where $D = (\partial^2/\partial x^2) + (\partial^2/\partial y^2)$
$D_1 = (\partial^2/\partial t^2) + (\partial^2/\partial y^2)$
$w_0(\xi) = w_0(\xi, y, t-x+\xi)$
$h(\xi) = h(\xi, y, t-x+\xi)$
$h(x_L) = h(x_L, y, t-x+x_L)$

and the argument of w_0 and h is (x, y, t) if not otherwise stated. After the integrations are carried through the smoothing can be dropped.

Comparisons with Other Results

The above result can be subject to a number of checks. First, it is seen that the first linear term $C_{p1}^{(1)}$ and the first second-order term $C_{p1}^{(2)}$ are, indeed, identical with those obtained from piston theory.

For an infinite swept flat plate, the present theory gives the following lift curve slope:

$$C_{L\alpha} = (4/M) + (2/M^3)(1+\tan^2\Lambda) + (3/2M^5)(1+\tan^2\Lambda)^2 \qquad (55)$$

where Λ is the sweep angle. Eq. (55) is then seen to produce the correct expansion in powers of M^{-2} of linearized swept-wing theory, which gives, for supersonic edges,

$$C_{L\alpha} = 4/\sqrt{M^2-(1+\tan^2\Lambda)} \qquad (56)$$

At $M = 2$ and $\Lambda = 40°$ the error in the approximate formula, Eq. (55), is only about 3 per cent.

For a two-dimensional flat plate oscillating in vertical translation, the force coefficients L_1 and L_2, in the standard American notations,[5] become

$$L_1 = [(1/2M^3) + (3/8M^5)][(\sin 2k)/k] + (3/4M^5)\cos 2k \qquad (57)$$

$$L_2 = (1/kM) + [(1/2M^3) + (3/8M^5)]\times[(\cos 2k)/k] - (3/4M^5)\sin 2k \qquad (58)$$

In Fig. 1 these results are compared with the exact linearized results by Garrick and Rubinow.[5] At $M = 2$, the agreement is quite good for $k < 1$. Even at $M = 5/3$, which cannot be considered a very high Mach Number, the deviation from the exact theory is not too large for, say, $k < 0.7$. The present theory does not work for high reduced frequencies since the iteration introduces on the right-hand side of Eqs. (22) and (26) terms of the relative order k^2M^{-2}, which must be small for the iteration to work. This is, however, not a serious restriction from a flutter point of view since in most practical cases $k < 1$.

For the nonlinear case, a symmetrical airfoil of thickness ratio ϵ oscillating in pitch about the axis $x = x_0$ is considered. In the above formulas, then,

$$\delta h = \epsilon g(x) + \lambda(x-x_0)e^{ikt} \qquad (59)$$

The calculation of the pressure is quite straightforward (although somewhat lengthy for $C_{p2}^{(2)}$), involving only relatively simple integrals like

$$\int_0^x g(\xi)\,(\xi-x_0)\,e^{-ik(x-\xi)}\,d\xi$$

in addition to those like

$$\int_0^x (\xi-x_0)e^{-ik(x-\xi)}\,d\xi$$

appearing in the linearized part. Terms proportional to ϵ^2 and λ^2 drop out when taking the pressure difference across the wing and can, therefore, be omitted in the calculation.

Of particular interest is the coefficient kM_4, which represents the damping moment in pitch. For low values of k, the result simplifies further, to give

$$kM_4 = \left(\frac{1}{3}-\frac{x_0}{4}\right)\left(\frac{4}{M}-\frac{2}{M^3}-\frac{2}{2M^5}\right) - \frac{x_0}{4}(1-x_0)\left(\frac{4}{M}+\frac{2}{M^3}+\frac{3}{2M^5}\right) + \epsilon\left[\frac{1}{2}x_0(\gamma+1)+\frac{5}{4}\frac{x_0}{M^2}(\gamma-1)\right]\int_0^2 g(\xi)\,d\xi - \frac{1}{2}\epsilon\left[\gamma+1+\frac{2}{M^2}(\gamma-1)\right]\int_0^2 \xi g(\xi)\,d\xi \qquad (60)$$

Using this expression, the case of a 6 per cent thick biconvex airfoil with $g = x(2-x)$ is computed for two locations of the pitching axis—namely, at the leading edge ($x_0 = 0$) and at the mid-chord ($x_0 = 1$). Fig. 2 shows that good agreement is obtained with Van Dyke's results[4] for $M > 2$. For the pitching axis located at the leading edge, one notices that the second-order piston theory happens to give results closer to the exact second-order theory than the linearized theory does.

For higher values of k, a single wedge oscillating about its leading edge is treated. For this case, reference 4 gives the second-order lift and moment coefficients for arbitrary frequencies, the expressions being quite complicated. The present theory gives for the force coefficients

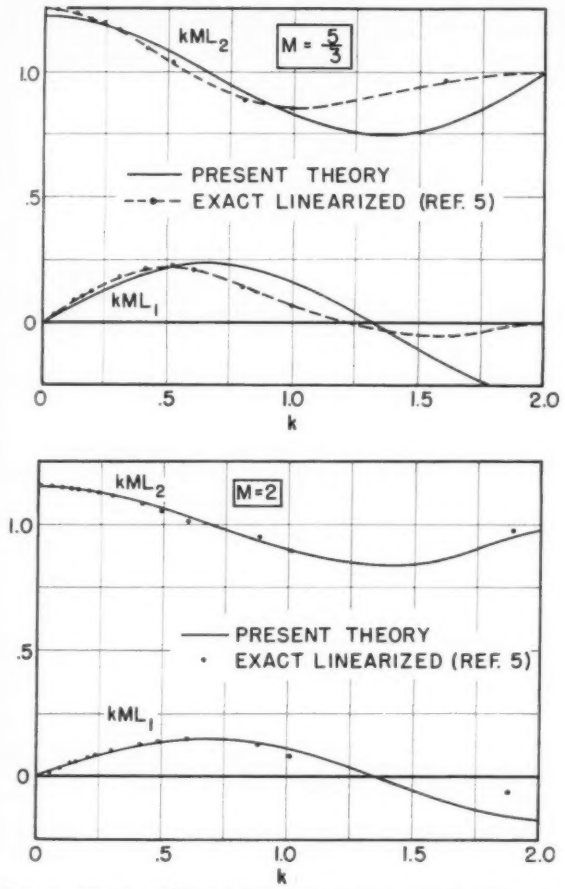

FIG. 1. Force coefficients for a two-dimensional flat plate in plunging oscillations at two supersonic Mach Numbers.

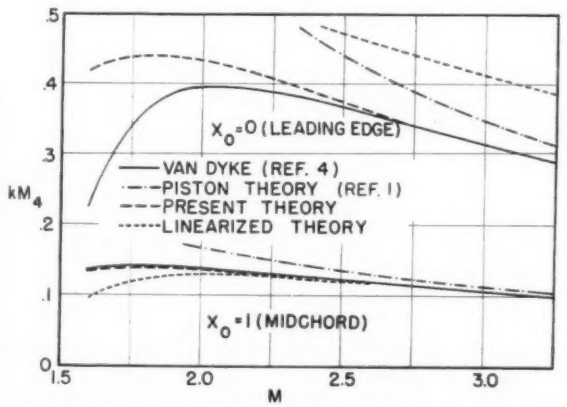

FIG. 2. Damping moment coefficient for a 6 per cent thick biconvex airfoil pitching about its leading edge and about its mid-chord point.

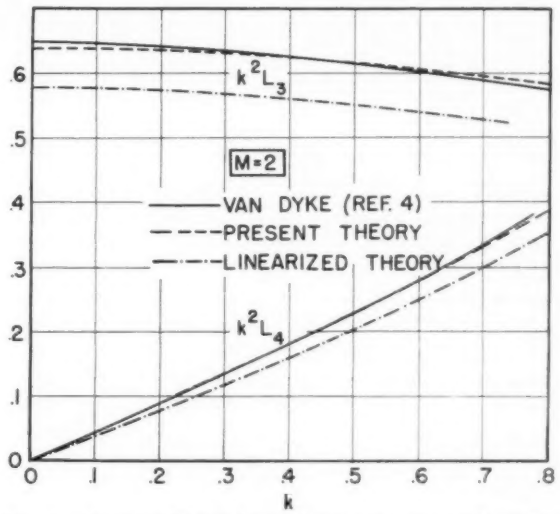

FIG. 3. Force coefficients for a 10 per cent thick single wedge oscillating about its leading edge at $M = 2$.

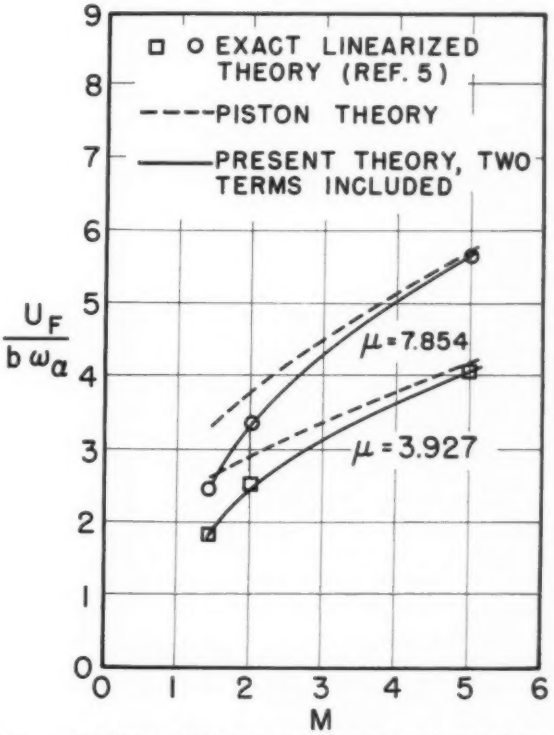

FIG. 4. Bending-torsion flutter speed of a sectional wing of zero thickness with parameters $\omega_h/\omega_\alpha = 0$, $a = 0$, $x_\alpha = 0.2$, $r_\alpha = 1/2$.

$$k^2(L_3 + iL_4) = (1/M)(1 + ik) + (i/4kM^3) \times (e^{-2ik} - 1) + (3/16M^5)[5e^{-2ik} - 1 + (i/k) \times (1 - e^{-2ik})] + (\epsilon/4)(\gamma + 1)(1 + ik) + (\epsilon/8M^2)[\gamma - 3 + ik(\gamma + 1) + (i/2k)(3\gamma - 1)(e^{-2ik} - 1)] \quad (61)$$

As seen in Fig. 3, where $M = 2$ and $\epsilon = 0.10$ are chosen, the agreement with the exact second-order result is quite good in the range of reduced frequencies shown ($k = 0$–0.8).

The present method becomes particularly advantageous for flutter calculations. This is exemplified below for the case of supersonic bending-torsion flutter of a thin wing section. In the exact linearized treatment by Garrick and Rubinow[5] the flutter equations had to be solved by a trial-and-error method, since the reduced frequency and, hence, the aerodynamic forces, were not known beforehand. With the present expansion of the aerodynamic forces, however, the flutter speed can be obtained by iteration in essentially the same manner as the aerodynamic forces. First a solution correct within $0(M^{-2})$ is sought, so that the first-order result in M^{-2}—i.e., piston theory—is used for the aerodynamic forces. In the particular case treated, the following closed form expression is obtained for the flutter speed:[6]

$$\frac{U_F}{b\omega_\alpha} = \sqrt{\frac{(\mu M)^2\{r_\alpha^2[1 + (\omega_h/\omega_\alpha)^2] - X(\omega_h/\omega_\alpha)^2 + (r_\alpha^2/X)(x_\alpha^2 - r_\alpha^2)\}}{\mu M(X_\alpha + a) - (\mu MaX/r_\alpha^2)(\omega_h/\omega_\alpha)^2 - (1/3)}} \quad (62)$$

where

$$X = \frac{r_\alpha^2 + 2x_\alpha a + a^2 + (1/3)}{1 + (1/r_\alpha^2)(\omega_h/\omega_\alpha)^2[a^2 + (1/3)]} = (b\omega_\alpha/U_F)^2(r_\alpha^2/k^2) \quad (63)$$

Using the value of k thus obtained, the correction terms of order M^{-3} in the aerodynamic coefficients are calculated and thence new improved values of U_F and k. This calculation, which is not reproduced here, only involves evaluation of a single radical as in Eqs. (62) and (63) above.

The iteration can then be continued by using the improved value of k and adding the correction term of order M^{-5}. No tables for the aerodynamic coefficients are required, since these are calculated simultaneously with the flutter speed. For the particular case chosen in Fig. 4, it is seen that one iteration already gives results very close to those of Garrick and Rubinow,[5] for $M > 1.5$. For other combinations of the involved parameters, however, two iterations might be required for the lower Mach Number region.

Conclusions

The method presented here for treating the steady or unsteady flow around thin wings for high Mach Numbers can be characterized as an inverse Rayleigh-Janzen method. The leading terms of the expression in M^{-2} are identical with those given by Lighthill's piston theory. Additional terms in the present solution provide extra accuracy, so that it can be used for engineering purposes roughly down to $M = 2$. For very high Mach Numbers the solution is only valid when $\delta^2M^2 \ll 1$, i.e., it cannot be used in the entire hypersonic region. Because of the way the solution is obtained, it is also restricted to low reduced frequencies for which $k^2M^{-2} \ll 1$, although the linear piston theory happens to give the correct result for $k \to \infty$ for all supersonic Mach Numbers, according to Hjelte.[7]

The three-dimensionality of the flow is taken into account in a fairly primitive manner. The method does, however, predict the effect of moderate leading-edge sweep and smooth spanwise variation of downwash. Wing tip effects or the effect of a discontinuous leading-edge slope must, however, be treated by a more complicated method, as shown for the linearized case in reference 6. Fortunately, the influence regions become smaller with increasing Mach Number and, therefore, probably of lesser importance.

The new procedure suggested for flutter calculations, which logically follows from the aerodynamic calculation procedure, represents a substantial saving of labor since both the usual guessing of reduced frequency and the need for tables of the aerodynamic coefficients are eliminated.

A particular flutter example shows the iteration to converge very rapidly so that very few terms usually need be retained in the expressions for the aerodynamic coefficients in order to get good accuracy. Actually, piston theory alone already seems to give fairly good results for $M > 2$.

References

[1] Lighthill, M. J., *Oscillating Airfoils at High Mach Number*, Journal of the Aeronautical Sciences, Vol. 20, No. 6, pp. 402–406, June, 1953.

[2] Hayes, W. D., *Hypersonic Similitude*, Quart. Appl. Math., Vol. 5, p. 105, 1947.

[3] Goldsworthy, F. A., *Two-Dimensional Rotational Flow at High Mach Number Past Thin Aerofoils*, J. Mech. and Appl. Math., Vol. 5, pp. 54–63, 1952.

[4] Van Dyke, M. D., *Supersonic Flow Past Oscillating Airfoils Including Nonlinear Thickness Effects*, NACA Report 1183, 1954.

[5] Garrick, I. E., and Rubinow, S. I., *Flutter and Oscillating Air-Force Calculations for an Airfoil in a Two-dimensional Supersonic Flow*, NACA Report 846, 1946.

[6] Landahl, M., Molio-Christensen, E., and Ashley, H., *Parametric Studies of Viscous and Nonviscous Unsteady Flows*, ARDC Technical Report No. 55-13, April, 1955.

[7] Hjelte, F., *Methods of Calculating Pressure Distributions on Oscillating Wings of Delta Type at Supersonic or Transonic Flow* Swedish KTH AERO TN 39, 1955.

A Simple Method of Matric Structural Analysis

BERTRAM KLEIN*

North American Aviation, Inc.

SUMMARY

A simple method of matric structural analysis is presented which is believed to have certain distinct advantages over existing methods as explained in the text. The possible disadvantages of the method eventually may be minimized as the size and scope of automatic computing equipment are made larger. Certain two- and three-dimensional problems are worked to illustrate the ease and simplicity of the method.

SYMBOLS

A	=	effective cross-sectional area of uniform axial element
$A, B, \ldots H$	=	submatrix
a, b	=	shear panel dimensions
c	=	check number
E, G	=	Young's and shear moduli
h	=	wing depth
k	=	twice the stiffness of an axial element
P	=	axial load in the direction of an axial element
q	=	shear flow
r	=	shear panel aspect ratio
t	=	shear panel gage
u, v, w	=	joint displacements
γ	=	average shear angle of shear panel
δ	=	axial displacement in the direction of an axial element

Subscripts

$0, 1, 2, \ldots, i,$	=	numbering of joints, loads, displacements, and equations
sec	=	secant

INTRODUCTION

WITH THE ADVENT of high-speed computing machines, the door has been opened for the practical use of matric methods in structural analysis. Heretofore, the amount of computational work associated with these methods was considered prohibitive for hand solution. As is true in many fields, the impetus has been given as soon as the calculation part has been found to be realizable. However, the use of matrices in structures is not new. Apparently, one of the first to try these methods was Bayer, back in 1927, in connection with reinforced concrete design. There seems to have been a lull in the Thirties, although matric methods found their way into dynamic and electrical fields.[1–4] The aircraft companies and civil engineers supplied the interest of the structural people for matrices in the Forties.[5–21] The author began applying matrices to structural problems in 1943.[5] The spring matrix approach was pursued. He believed that Southwell's systematic relaxation procedure eventually would be replaced by a matric solution done automatically on some kind of calculating machine. In 1947, Levy laid the groundwork for a matric method based on an energy solution of a redundant structure.[12] This approach has been extended and streamlined by various investigators. (See references 22, 27, 29, 32, 39, and 46.) An interesting discussion of this type of method and the Cross-Southwell (spring matrix) type of method may be found in a recent series of articles by Argyris.[49] In 1950, Heldenfels[25] set up in matrix form a numerical iterative procedure developed by Duberg.[19] Levy later advocated a solution by a growing unit spring matrix type of method.[36] Cox[40] and Williams[41] developed finite difference methods. Various other matric methods have been and are being devised. (This short historical survey is by no means intended to be all-inclusive.)

For several years now the author has been thinking about some way of simplifying the setup procedure in matric structural analysis without subtracting from the generality of the approach. As it turns out, there is such a possibility; but with the simplification there is a penalty in that the size of the matrix is larger than in other methods. Nevertheless, the author feels that as the field of automation expands and progresses, manageable matric size also should grow with time.

THE METHOD

The first step in any method is the idealization of the structure to be analyzed. Only certain semimonocoque structures will be considered here, where it is assumed that the structure is composed of uniform (untapered) structural elements, some taking only axial load and others taking only shear loads in the form of constant shear flows (except for triangular panels). However, other structures and idealizations where members are tapered or take combined loads also may be treated by the method. It should be noted that sometimes a joint of a structure must be considered to be a structural element.

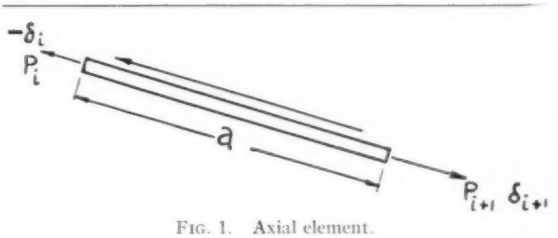

FIG. 1. Axial element.

Received February 6, 1956.

* Senior Engineer—Structures, Missile Development Division.

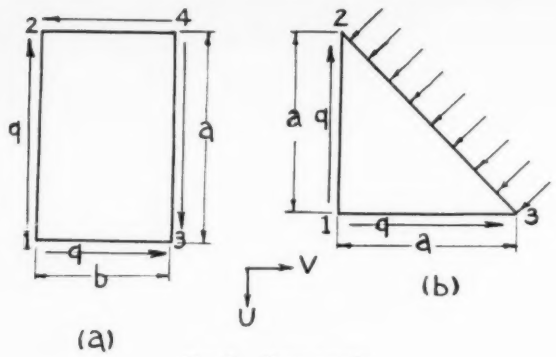

FIG. 2. Shear panels.

The correct solution to a stress distribution problem for an idealized structure is the one in which all structural elements are in equilibrium, all displacements are compatible with the corresponding forces, and all boundary conditions in terms of forces and/or displacements are satisfied. These conditions alone are sufficient for the correct solution. Therefore it is sufficient only to write equations (a) of equilibrium for each structural element (when necessary), (b) of displacement-force compatibility for each structural element (when necessary), and (c) for boundary conditions (when necessary).

For the problems considered here, the unknown quantities are: (a) axial loads acting at the ends of certain axial elements, (b) shear flows (or forces) acting along the edges of certain shear panels, and (c) certain displacements at the corners of these panels. The number of these unknowns must be *identical* with the number of available equations.

For the structures considered here, the nonvanishing numbers in the section of the matrix corresponding to the equilibrium equations are either 1 or -1, since all forces entering such equations are colinear. (See illustrative problems below.) The force-displacement equation for an axial element, such as shown in Fig. 1, is of the form

$$(1/2)\,(P_i + P_{i+1}) = (\delta_{i+1} - \delta_i)\,(E_{sec}A/a) \qquad (1)$$

or

$$(P_i + P_{i+1}) = (\delta_{i+1} - \delta_i)2(E_{sec}A/a) \qquad (1a)$$

which states that the average force in the element is proportional to the elongation of the element. The force-displacement equation for a uniform rectangular shear panel, such as shown in Fig. 2(a), is written

$$qa = G_{sec}t\gamma a = G_{sec}\,t\{(1/2)r[(u_3 + u_4) - (u_1 + u_2)] + (1/2)\,[(v_1 + v_3) - (v_2 + v_4)]\} \qquad (2)$$

where the term in the braces represents the average shear angle in the panel (times a), and where $r = a/b$. For the right isosceles triangle shown in Fig. 2(b), the average shear angle (times a) is

$$a\gamma = -u_1 + u_3 + v_1 - v_2 \qquad (2a)$$

As far as boundary considerations are concerned, in the case of flexible supports equations similar to Eq. (1) may be written; for rigid supports it is a matter of omitting equations and unknowns. Wherever an external load is applied to a joint, that joint must be in equilibrium.

Instead of trying to eliminate unknowns by combining Eqs. (1) and (2) with the equilibrium equations, the method proceeds by entering the original equations into a single square matrix and a RHS (right-hand side) matrix as shown schematically in Fig. 3.

As mentioned previously, submatrix A, in the left-hand corner of Fig. 3, contains only the numbers 1 or -1. The submatrices B and C are weakly populated, the submatrix D is a diagonal matrix, and the submatrix E is heavily populated. The size of the RHS matrix depends on the number of loading conditions that are treated simultaneously. It will be noticed (see illustrative problems below) that each entry in the matrix is a single entry—i.e., it does not consist of sums of numbers. Furthermore, because of the simplicity of the equations, the entries can be written down very rapidly. The simultaneous solution for the unknown forces and displacements may be carried out by any convenient method such as matrix inversion or elimination on an automatic computing machine. Some-

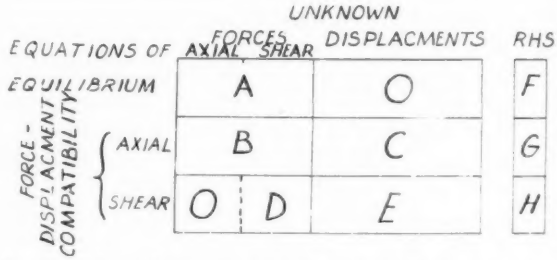

FIG. 3. Schematic representation of the matric formulation of a problem.

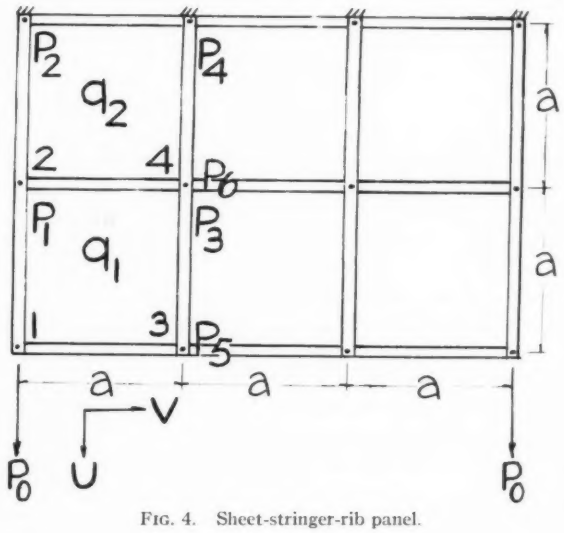

FIG. 4. Sheet-stringer-rib panel.

times it may be of value to rearrange the entries in the matrix for purposes of solution. However, the arrangement shown in Fig. 3 is simplest for formulating the problem. To obtain influence coefficients, it is merely necessary to incorporate the correct RHS and include the necessary equations in the matrix proper. One feature of the method is the ease of treating changes in the structure. If an element is removed from the structure, or one added, it is merely necessary to delete or add certain equations and, consequently, numbers in the matrix; if the size of an element is altered, only one or two numbers need be changed. Since we are working with deflections and, consequently, strains, thermal load terms may be incorporated directly into the RHS matrix. Also, since we are working both with forces and deflections, mixed boundary conditions can be treated.

In recapitulating, it may be stated, as seen by the foregoing development, that nowhere in the method is it necessary to classify certain forces as being redundant and make subsequent "cuts" in the structure; nor is it necessary to write quadratic energy expressions in applying the method. No joints must be "locked," nor elements combined in any way. It is not necessary to consider free bodies of whole cross-sections of the structure. It is not necessary to employ the artifice of dummy loads to obtain deflections at unloaded points.

Several problems are worked below to illustrate the mechanics of the method. The structures considered are of the semimonocoque type discussed earlier.

(1) *Two-Dimensional Shear Lag Problem*

Consider first the plane sheet-stringer-rib panel depicted in Fig. 4. For purposes of simplicity, the structure is assumed to have an axis of symmetry, all axial members are assumed to be identical, all panels to be identical, the loading is taken to be symmetrical, and the structure is assumed to be completely fixed at the supports. The following unknowns are found to exist: 6 axial loads, P_1–P_6; 2 shear flows, q_1 and q_2; and 8 deflections, u_1–u_4 and v_1–v_4, one in each direction at the four corners of the lower left-hand shear panel. Since these unknowns number 16, there must exist 16 equations. These equations consist of 6 axial element equilibrium, 8 axial force-displacement, and 2 shear force-displacement, which may be written as

axial element equilibrium:

(1) $P_0 - P_1 + q_1 a = 0$
(2) $P_1 - P_2 + q_2 a = 0$
(3) $-P_3 - q_1 a = 0$
(4) $P_3 - P_4 - q_2 a = 0$
(5) $P_5 - q_1 a = 0$
(6) $P_6 + q_1 a - q_2 a = 0$

axial force-displacement:

(1) $P_0 + P_1 = (u_1 - u_2)k$
(2) $P_1 + P_2 = u_2 k$
(3) $P_3 = (u_3 - u_4)k$
(4) $P_3 + P_4 = u_4 k$
(5) $P_5 = (v_3 - v_1)k$
(6) $P_6 = (v_4 - v_2)k$
(7) $P_5 = -v_3 k$, $k = 2EA/a$
(8) $P_6 = -v_4 k$

and shear force-displacement:

(1) $(2/Gt)q_1 a = (u_3 + u_4) - (u_1 + u_2) + (v_1 + v_3) - (v_2 + v_4)$

(2) $(2/Gt)q_2 a = (u_4 - u_2) + (v_4 + v_3)$

No boundary condition equations need be written in this problem, since such conditions have been satisfied automatically when the above equations were written. Now let $k = 2EA/a = 1$, and choose A/at so that $2/Gt = 4(E/G)(A/at) = 10$. Let $P_0 = 1$. Then, according to the scheme presented in Fig. 3, the matric formulation of this problem may be written as

$$
\begin{bmatrix}
-1 & 0 & 0 & 0 & 0 & 0 & 1 & 0 & & & & & & & & \\
1 & -1 & 0 & 0 & 0 & 0 & 0 & 1 & & & & & & & & \\
0 & 0 & -1 & 0 & 0 & 0 & 0 & -1 & & & & & & & & \\
0 & 0 & 1 & -1 & 0 & 0 & 0 & -1 & & & & & & & & \\
0 & 0 & 0 & 0 & 1 & 0 & -1 & 0 & & & & & & & & \\
0 & 0 & 0 & 0 & 0 & 1 & 1 & -1 & & & & & & & & \\
1 & 0 & 0 & 0 & 0 & 0 & 0 & 0 & -1 & 1 & 0 & 0 & 0 & 0 & 0 & 0 \\
1 & 1 & 0 & 0 & 0 & 0 & 0 & 0 & 0 & -1 & 0 & 0 & 0 & 0 & 0 & 0 \\
0 & 0 & 1 & 0 & 0 & 0 & 0 & 0 & 0 & 0 & -1 & 1 & 0 & 0 & 0 & 0 \\
0 & 0 & 1 & 1 & 0 & 0 & 0 & 0 & 0 & 0 & -1 & 0 & 0 & 0 & 0 & 0 \\
0 & 0 & 0 & 0 & 1 & 0 & 0 & 0 & 0 & 0 & 0 & 0 & 1 & 0 & -1 & 0 \\
0 & 0 & 0 & 0 & 0 & 1 & 0 & 0 & 0 & 0 & 0 & 0 & 0 & 1 & 0 & -1 \\
0 & 0 & 0 & 0 & 1 & 0 & 0 & 0 & 0 & 0 & 0 & 0 & 0 & 0 & 1 & 0 \\
0 & 0 & 0 & 0 & 0 & 1 & 0 & 0 & 0 & 0 & 0 & 0 & 0 & 0 & 0 & 1 \\
 & & & & & & -10 & 0 & -1 & -1 & 1 & 1 & 1 & -1 & 1 & -1 \\
 & & & & & & 0 & -10 & 0 & -1 & 0 & 1 & 0 & 1 & 0 & 1
\end{bmatrix}
\begin{bmatrix} P_1 \\ P_2 \\ P_3 \\ P_4 \\ P_5 \\ P_6 \\ q_1 a \\ q_2 a \\ u_1 \\ u_2 \\ u_3 \\ u_4 \\ v_1 \\ v_2 \\ v_3 \\ v_4 \end{bmatrix}
=
\begin{bmatrix} -1 \\ 0 \\ 0 \\ 0 \\ 0 \\ 0 \\ -1 \\ 0 \\ 0 \\ 0 \\ 0 \\ 0 \\ 0 \\ 0 \\ 0 \\ 0 \end{bmatrix}
$$

Solution: The unknowns listed below were obtained by matrix inversion on the IBM 701 electronic digital computer. These results appear to represent the physical behavior of this type of structure for the given loading. Also shown are the check RHS terms calculated by substituting the unknowns back into the 16 equations. Total computing time was less than one minute.

P_1 =	0.77377893	u_1 =	3.2030849	c_1 = −1.0000001	c_9 = −0.000000016
P_2 =	0.65552699	u_2 =	1.4293059	c_2 = 0.000000008	c_{10} = −0.000000003
P_3 =	0.22622108	u_3 =	0.79691518	c_3 = 0.000000009	c_{11} = 0.000000002
P_4 =	0.34447301	u_4 =	0.57069409	c_4 = 0.000000003	c_{12} = 0.000000002
P_5 =	−0.22622109	v_1 =	0.45244218	c_5 = −0.000000002	c_{13} = 0.000000005
P_6 =	0.10796915	v_2 =	−0.21593830	c_6 = 0.000000003	c_{14} = 0.000000001
q_1a =	−0.22622108	v_3 =	0.22622109	c_7 = −1.0000002	c_{15} = 0.000000027
q_2a =	−0.11825193	v_4 =	−0.10796915	c_8 = −0.000000016	c_{16} = −0.000000057

Eight significant figures were carried in the computation. The worst check, percentagewise, is that for Eq. 7, which shows an error of 2 in 10^7.

Actual values of deflections may be determined by multiplying the above values by the actual value of $k^{-1} = a/2EA$.

(2) *Two Spar Swept-Wing Analysis*

The next problem considered is the analysis of a three-dimensional structure—i.e., a two spar 45° swept wing with carry-through bay and loaded under symmetric bending as shown in Fig. 5. The wing is assumed to have two planes of symmetry, rib webs as spar webs, identical outer axial members, and identical values of Gt for all shear carrying members. The attachment bulkhead at the wing-fuselage intersection is assumed to be infinitely rigid in its own plane, but free to warp out of its plane, which means that the only motion at this section is axial displacements of the carry-through spar caps. The applied bending moment causes an antisymmetrical state of stress about the horizontal plane of symmetry, so that only the forces and displacement in the top half need be considered as unknown.

In this problem, the unknown quantities are

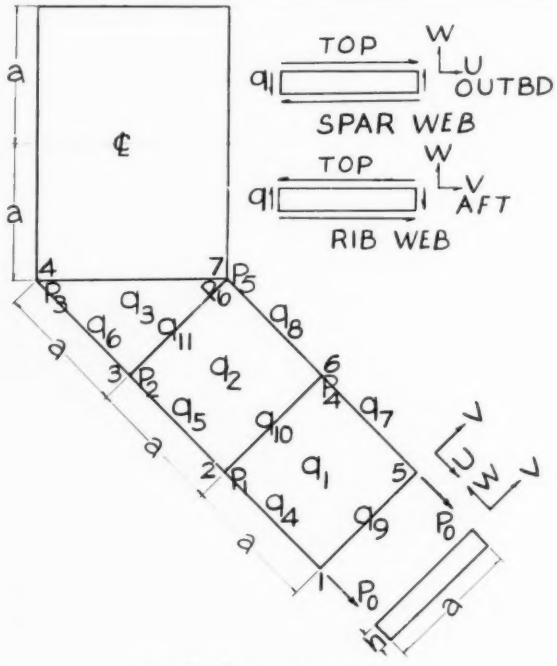
TOP
W
U
OUTBD
SPAR WEB
TOP
W
V
AFT
RIB WEB
a
a
a

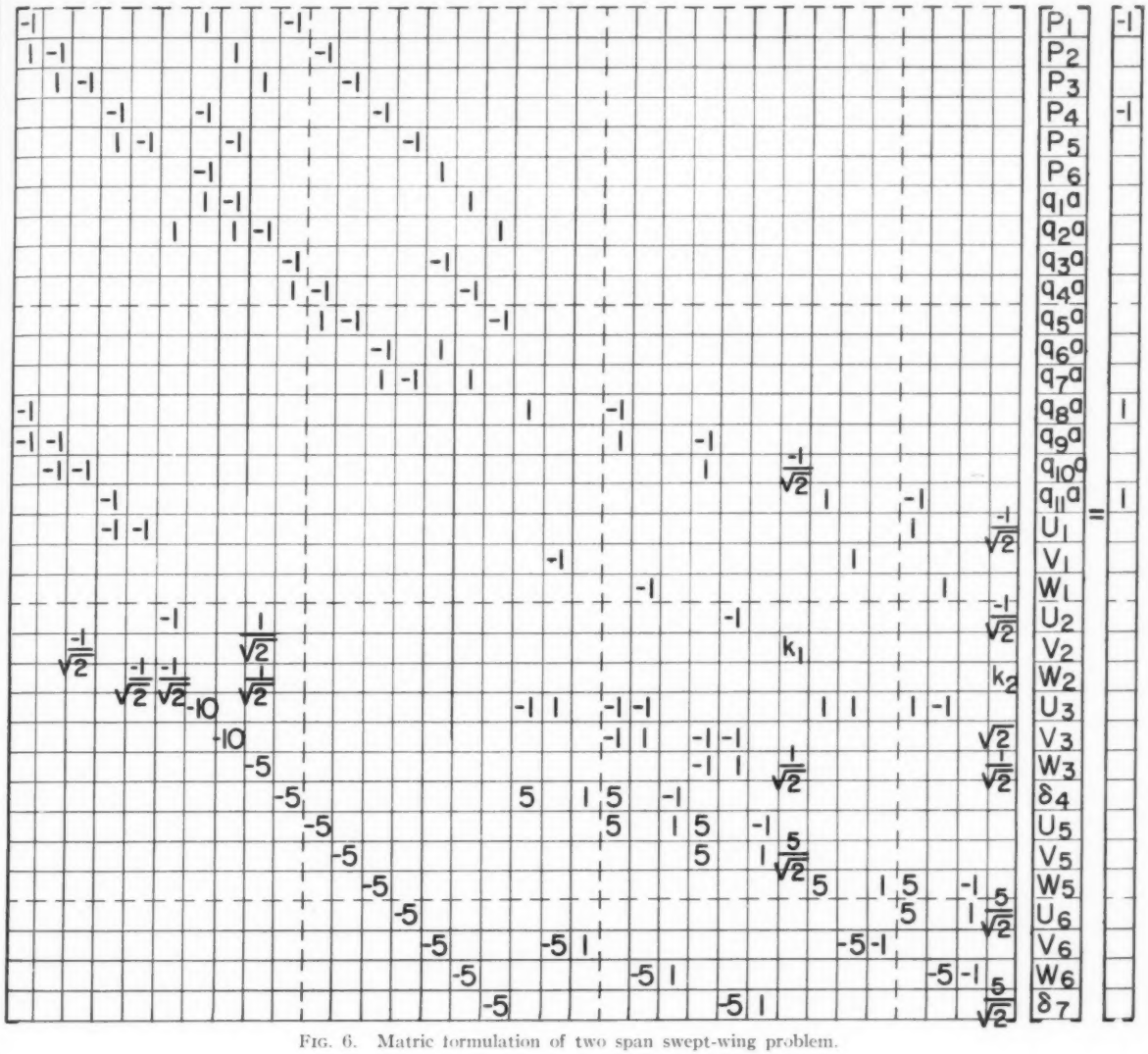

FIG. 6. Matric formulation of two span swept-wing problem.

P_1	= 0.96860242	u_1	= 5.3939165	c_1	= −1.0000004	c_{18}	= −0.000000083
P_2	= 0.76831339	v_1	= −1.2604531	c_2	= −0.000000031	c_{19}	= −0.000000008
P_3	= 0.46004218	w_1	= −79.383929	c_2	= 0.000000040	c_{20}	= −0.000000047
P_4	= 1.0313978	u_2	= 3.4253138	c_3	= −0.99999968	c_{21}	= −0.000000007
P_5	= 1.2316862	v_2	= −1.2118685	c_4	= 0.000000277	c_{22}	= −0.000000007
P_6	= −0.13076514	w_2	= −35.366273	c_5	= 0.000000032	c_{23}	= 0.000000012
q_1a	= −0.015699017	u_3	= 1.6883980	c_6	= 0.000000015	c_{24}	= −0.000000041
q_2a	= −0.10014429	v_3	= −0.97015668	c_7	= −0.000000109	c_{25}	= 0.000000277
q_3a	= −0.21951806	w_3	= −10.298437	c_9	= −0.000000026	c_{26}	= −0.000000130
q_4a	= 0.015699011	δ_4	= 0.65059807	c_{10}	= −0.000000494	c_{27}	= 0.000001222
q_5a	= 0.10014477	u_5	= 5.3954034	c_{11}	= 0.000000396	c_{28}	= −0.000001088
q_6a	= 0.088753112	v_5	= −1.2604531	c_{12}	= 0.000000057	c_{29}	= 0.000000630
q_7a	= −0.015699042	w_5	= −66.700904	c_{13}	= 0.000000177	c_{30}	= −0.000000142
q_8a	= −0.10014448	u_6	= 3.3640058	c_{14}	= 1.0000003	c_{31}	= −0.000000726
q_9a	= −0.015698985	v_6	= −1.2118685	c_{15}	= −0.000000102	c_{32}	= 0.000000459
$q_{10}a$	= −0.0844445261	w_6	= −22.825361	c_{16}	= 0.000000036	c_{33}	= −0.000000836
$q_{11}a$	= 0.011391257	δ_7	= 1.5569381	c_{17}	= 0.99999985	c_{34}	= −0.000000173

Eight significant figures were carried in the calculations, with the worst error in the check RHS being for Eq. 27, 1.222 in 10^6. However, since w_1 and w_2, which appear in this equation, can be accurate only to 6 decimal places, no greater accuracy can be expected when eight significant figures are carried.

(3) *Three Spar Swept-Wing Analysis*

The swept wing of the previous problem is enlarged by adding another spar and adjoining structure, as shown in Fig. 7. All of the basic geometry and gages, and the basic assumptions are the same as those considered in the previous structure, except for the values of $2EA/2a$ for the carry-through spar caps, which are, from forward to aft,

$$k_1 = 0.80109169 \quad k_2 = 0.84206505 \quad k_3 = 0.59764379$$

The matric formulation of this problem, set up according to the same simple procedure used to solve the previous two problems, is shown in Fig. 8. The solution for the 67 unknown quantities is listed below. Calculations were carried out on the IBM 701 machine in about 12 minutes computing time, after some hand computation of an elementary nature had adjusted the form of the matrix to yield a rapid machine solution.

P_1 =	0.9193166	$q_{11}a$ =	−0.04833938	$q_{15}a$ =	−0.0477282	w_2 =	−54.982343	u_8 =	2.0296676
P_2 =	0.7604357	$q_{2}a$ =	−0.10852431	$q_{16}a$ =	−0.1886286	u_3 =	2.3617836	v_8 =	−1.1147309
P_3 =	0.5251984	$q_{3}a$ =	−0.17302184	$q_{17}a$ =	−0.032459	v_3 =	−1.0620915	w_8 =	−12.274127
P_4 =	0.2754757	$q_{4}a$ =	−0.16589635	$q_{18}a$ =	−0.0180123	w_3 =	−23.217530	δ_9 =	0.86083738
P_5 =	1.0012246	$q_{5}a$ =	−0.03173287	$q_{19}a$ =	−0.0118582	u_4 =	1.0761495	u_{10} =	5.84043644
P_6 =	0.8410177	$q_{6}a$ =	−0.13046165	$q_{20}a$ =	−0.02162213	v_4 =	−0.63746158	v_{10} =	−1.5171785
P_7 =	0.5799460	$q_{7}a$ =	−0.25054666	$q_{21}a$ =	−0.0477281	w_4 =	−6.3389383	w_{10} =	−74.408520
P_8 =	1.0794616	$q_{8}a$ =	0.0323430	$q_{22}a$ =	−0.1409010	δ_5 =	0.38958100	u_{11} =	3.7609748
P_9 =	1.3985520	$q_{9}a$ =	0.0503569	$q_{23}a$ =	−0.05713325	u_6 =	5.8731345	v_{11} =	−1.4434195
P_{10} =	−0.0159951	$q_{10}a$ =	0.06221476	u_1 =	5.9608525	v_6 =	−1.5011842	w_{11} =	−26.162823
P_{11} =	−0.0421719	$q_{11}a$ =	0.08383721	v_1 =	−1.4851891	w_6 =	−89.738974	δ_{12} =	1.8143812
P_{12} =	−0.0526394	$q_{12}a$ =	0.01538240	w_1 =	−104.83257	u_7 =	3.8719099		
P_{13} =	0.02875763	$q_{13}a$ =	0.1382701	u_2 =	4.0415359	v_7 =	−1.4012477		
P_{14} =	−0.1155910	$q_{14}a$ =	0.18354615	v_2 =	−1.3590758	w_7 =	−41.090664		

To check the accuracy of these results, one may substitute them back into the original matrix. When this check is made, very small errors are found to exist. Perhaps an even stronger check of the accuracy of the above values is obtained by writing equations of equilibrium of whole cross sections of the structure. For example, consider the equation of equilibrium of a section taken at the rigid rib:

$$P_4 + P_{13} + P_7 + P_{14} + P_9 - 2(q_4a + q_7a) = 3.00000634$$

Since the correct result should be 3, the error here is about 2 in 10^6. Since only eight significant figures were carried in the calculations, this error is entirely satisfactory. The check of vertical equilibrium at this section is:

$$a(q_{11} + q_{20} + q_{14} + q_{23} + q_{16}) = -0.00000062$$

which is an error of 6.2 in 10^7.

Conclusions

The matric method of structural analysis here presented is believed to have the following advantages and disadvantages:

Advantages

(1) simplicity and speed of setup.

(2) yields simultaneously all deflections (and, hence, influence coefficients) and forces *without* the use of (a) quadratic energy expressions, (b) redundant designation and "cutting," (c) locking of joints, (d) combining of elements, (e) free bodies of whole cross sections, and (f) dummy load artifice.

(3) Only one combined matric equation is required, and the entries are but *one* number for each element in the matrix—i.e., no sums of numbers are required.

(4) Removal, addition, or size change of structural elements handled easily.

(5) Thermal loads handled easily.

(6) Mixed boundary conditions handled easily.

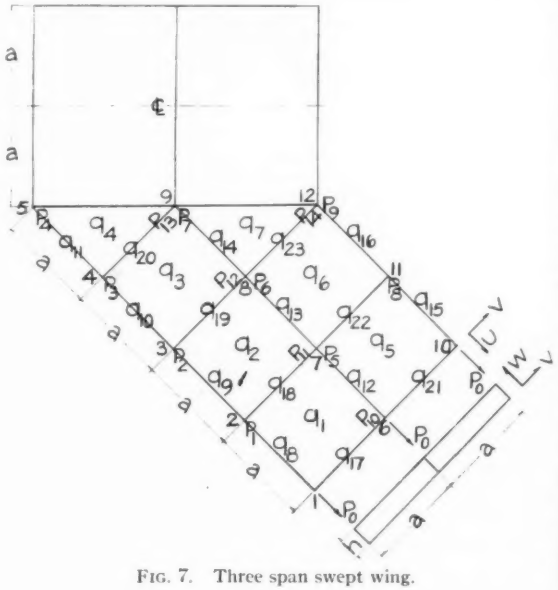

FIG. 7. Three span swept wing.

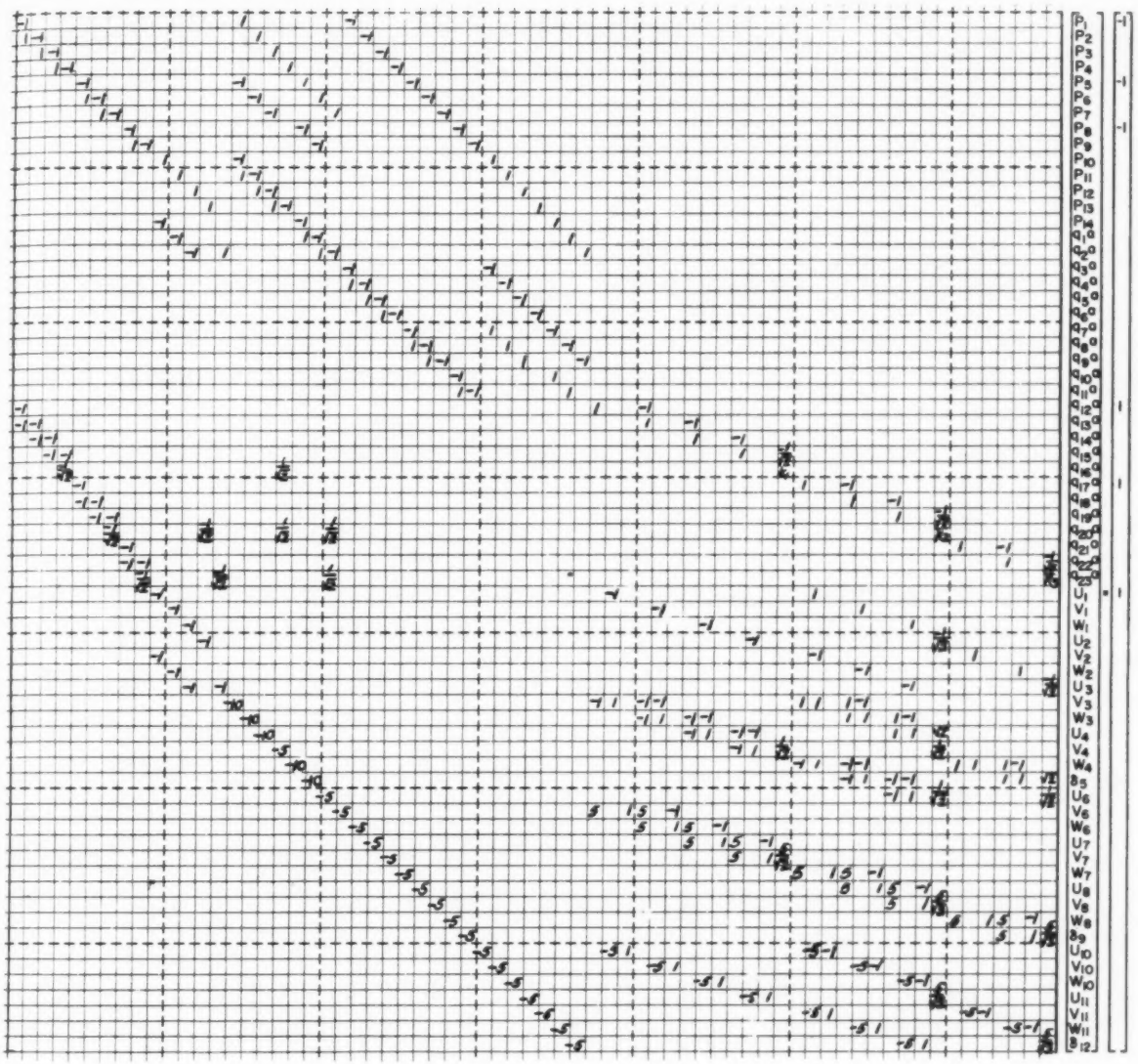

FIG. 8. Matric formulation of three span swept-wing problem.

Disadvantages

(1) Only certain types of structures can be treated conveniently.

(2) Matrix is large.

(3) Matrix is unsymmetric, and the elements in the matrix are not arranged in a fashion which is best suited for solution.

(4) When calculating influence coefficients, extraneous data may have to be calculated.

In conclusion, it should be realized that structures other than the ones treated in the present paper may be analyzed once the basic element equations have been established, such as for skew type panels, tapered spars and panels, curved segments and other multiload carrying members, etc.

REFERENCES

[1] Duncan, W. J., and Collar, A. R., *A Method for the Solution of Oscillation Problems by Matrices*, Phil. Mag. Series 7, Vol. 17, p. 865, 1934.

[2] Brillouin, L., *Les Filtres Electriques et la Theorie des Matrices*, Revue Generale de L'Electricite, pp. 3–16, January 4, 1936.

[3] Pipes, L. A., *Matrices in Engineering*, Electrical Eng., September, 1937.

[4] Kron, G., *Tensor Analysis of Networks*, John Wiley & Sons, Inc., New York, 1939.

[5] Ness, N., *Application of Southwell's Method to the Shear Lag Analysis of a Monocoque Cylinder*, Thesis, Polytechnic Inst. of Brooklyn, October, 1943.

[6] Jensen, V. P., and Dill, D. G., *Matrix Methods of Analysis Applied to Wing Structures*, Douglas Aircraft Co. Report E.S. 6480, January, 1944.

[7] Kempner, J., *Application of a Numerical Procedure to the Stress Analysis of Stringer-Reinforced Panels*, NACA ARR L5C09a(WR L-11), March, 1945.

[8] Hoff, N. J., Libby, P. A., and Klein, B., *Numerical Procedures for the Calculation of the Stresses in Monocoques. III. Calculation of the Bending Moments in Fuselage Frames*, NACA TN 998, April, 1946.

[9] Dunholter, R. J., *Some Fundamental Theorems of Structural Mechanics in Vector Notation*, Journal of Eng. Educ., Vol. 37, No. 3, pp. 207–209, November, 1946.

[10] Boley, B. A., *Numerical Methods in the Calculation of Elastic Instability*, Journal of the Aeronautical Sciences, Vol. 14, No. 6, pp. 337–348, January, 1947.

[11] Morris, J., *On the Nature of Least Work Equations in Structures*, Journal of the Royal Aero. Soc., Vol. 51, No. 435, pp. 327–333, March, 1947.

[12] Levy, S., *Computation of Influence Coefficients for Aircraft Structures with Discontinuities and Sweepback*, Journal of the Aeronautical Sciences, Vol. 14, No. 10, pp. 547–560, October, 1947.

[13] Benscoter, S. U., *Orthogonal Functions Used in the Solution of Linear Difference Problems*, Trans. ASME, Vol. 68, pp. A 281–283, December, 1946.

[14] Bisch, P. E., *Determination of Stress Distribution and Rigidity of Multicell Box Structures by a General Method of Individual Panels*, North American Aviation Report no. N.A. 48-310, March, 1948.

[15] Pei-ping, Chen, *Matrix Analysis of Pin-Connected Structures*, Proc. Amer. Soc. Civ. Engrs., Vol. 73, pp. 1475–1482, December, 1947.

[16] Benscoter, S. U., *The Partitioning of Matrices in Structural Analysis*, Journal of Appl. Mechs., Vol. 15, No. 4, pp. 303–307, December, 1948.

[17] Benscoter, S. U., and Gossard, M. L., *Matrix Methods for Calculating Cantilever Beam Deflections*, NACA TT 1827, March, 1949.

[18] Watts, G. W., and Burrows, W. R., *The Basic Elastic Theory of Vessel Heads under Internal Pressure*, Journal of Appl. Mechs., Vol. 16, pp. 55–73, March, 1949.

[19] Duberg, J. E., *A Numerical Procedure for the Analysis of Stiffened Shells*, Journal of the Aeronautical Sciences, Vol. 16, No. 8, pp. 451–462, August, 1949.

[20] Gutshall, W. D., *Practical Inversion of Matrices of High Order*, Proceedings of the Computation Seminar, IBM, pp. 171–173, December, 1949.

[21] Thomson, W. T., *Matrix Solution of the n-Section Column*, Journal of the Aeronautical Sciences, Vol. 16, No. 10, pp. 623–624, October, 1949.

[22] Falkenheiner, H., *Le Calcul Systématique des Caracteristiques Élastiques des Systèmes Hyperstatiques*, La Recherche Aeronautique, No. 17, France, September–October, 1950.

[23] Ortega, M. G., *Space Structures*, Rev. Cienapli, Vol. 4, Nos. 2, 3; pp. 97–116, 209–226; March–April–May–June, 1950.

[24] Heldenfels, R. R., Zender, G. W., and Libove, C., *Stress and Distortion Analysis of a Swept Box Beam Having Bulkheads Perpendicular to the Spars*, NACA TN 2232, November, 1950.

[25] Heldenfels, R. R., *A Numerical Method for the Stress Analysis of Stiffened Shell Structures under Non-Uniform Temperature Distributions*, NACA TR 1043, 1951.

[26] Pöschl, T., *On an Application of Matrix Calculus to the Theory of Frames*, Ing.-Arch., Vol. 19, No. 1, pp. 69–74, 1951.

[27] Langefors, B., *Structural Analysis of Sweptback Wings by Matrix Transformation*, SAAB Airc. Co., Linköping T.N. 3, 1951.

[28] Lewis, S. R., *The Evaluation of Matrix Elements for the Analysis of Sweptback Wing Structures by the Method of Oblique Coordinates*, Coll. Aero. Cranfield Rep. 44, April, 1951.

[29] Lang, A. L., and Bisplinghoff, R. L., *Some Results of Sweptback Wing Structural Studies*, Journal of the Aeronautical Sciences, Vol. 18, No. 11, pp. 705–717, November, 1951.

[30] Bateman, E. H., *Elastic Stress Analysis of Multi-bay Single-storey Frameworks*, Engineering, Vol. 172, Nos. 4482–3; pp. 772–774, 804–806; December, 1951.

[31] Langefors, B., *Analysis of Elastic Structures by Matrix Transformation with Special Regard to Semimonocoque Structures*, Journal of the Aeronautical Sciences, Vol. 19, No. 7, pp. 451–458, July, 1952.

[32] Wehle, L. B., and Lansing, W., *A Method for Reducing the Analysis of Complex Redundant Structures to a Routine Procedure*, Journal of the Aeronautical Sciences, Vol. 19, No. 10, pp. 677–684, October, 1952.

[33] Skopinski, T. H., Aiken, W. S., Jr., and Huston, W. B., *Calibration of Strain-Gage Installations in Aircraft Structures for the Measurement of Flight Loads*, NACA RM L52G31, October, 1952.

[34] Brock, J. E., *Matrix Method for Flexibility Analysis of Piping Systems*, Journal of Appl. Mechs., Trans. ASME, Vol. 74, pp. 501–516, December, 1952.

[35] Wilder, T. W., III, *An Analysis of Statically Indeterminate Trusses having Members Stressed Beyond the Proportional Limit*, NACA TN 2886, February, 1953.

[36] Levy, S., *Structural Analysis and Influence Coefficients for Delta Wings*, Journal of the Aeronautical Sciences, Vol. 20, No. 7, pp. 449–454, July, 1953.

[37] MacNeal, R. H., *Application of the Compensation Theorem to the Modification of Redundant Structures*, Journal of the Aeronautical Sciences, Vol. 20, No. 10, pp. 726–727, October, 1953.

[38] Schuerch, H. U., *Delta Wing Design Analysis*, presented at the SAE National Aeronautical Meeting, Los Angeles, September 29–October 3, 1953.

[39] Denke, P. H., *Matric Structural Analysis*, presented at the Second National Conference of Applied Mechanics, Ann Arbor, Mich., June, 1954.

[40] Cox, H. L., and Denke, P. H., *Stability and Free Vibration of Nonuniform Beams Continuous Across Flexible Supports*, Journal of the Aeronautical Sciences, Vol. 21, No. 8, pp. 572–573, August, 1954.

[41] Williams, D., *A General Method (Depending on the Aid of a Digital Computer) for Deriving the Structural Influence Coefficients of Aeroplane Wings*, Farnborough Report no. Structures 168, November, 1954.

[42] Williams, D., *Development in the Structural Approach to Aero-Elastic Problems*, Aircraft Eng., Vol. 26, No. 307, pp. 303–307, September, 1954.

[43] Denke, P. H., *Matric Solution of Certain Non-Linear Problems in Structural Analysis*, IAS Preprint no. 507, presented at the 23rd Annual Meeting, IAS, New York, January, 1955.

[44] Denke, P. H., and Boldt, I. V., *General Digital Computer Program for Static Stress Analysis*, Western Computer Conference, Los Angeles, March 2–3, 1955.

[45] Sanders, J. L., and Stein, M., *Deflection Analysis of Low-Aspect Ratio Wings*, NACA TN, to be published.

[46] Kaplan, A., *Systematic Method for the Strain Energy Analysis of Multicell Beams*, Northrop Aircraft Report no. NAI-54-721, October 15, 1954.

[47] Kron, G., *Solving Highly Complex Elastic Structures in Easy Stages*, Journal of Appl. Mechs., Vol. 22, No. 2, pp. 235–244, June, 1955.

[48] Hoskin, B. C., and Rodok, J. R. M., *The Root Section of a Swept Wing—A Problem of Plane Elasticity*, Journal of Appl. Mechs., Vol. 22, No. 3, pp. 337–347, 1955.

[49] Argyris, J. H., *Energy Theorems and Structural Analysis*, Aircraft Eng., Vol. 27, No. 313, pp. 80–94, March, 1955.

[50] Brock, J. E., *Matrix Analysis of Flexible Filaments*, pp. 285–289, Proceedings of the First U. S. National Congress of Applied Mechanics, Ann Arbor Press, Ann Arbor, Mich., 1951.

[51] Gossard, M. L., Seide, P., and Roberts, W. M., *Thermal Buckling of Plates*, NACA TN 2771, August, 1952.

An Experimental Investigation of Leading-Edge Shock-Wave - Boundary-Layer Interaction at Mach 5.8†

JAMES M. KENDALL, JR.*
California Institute of Technology

Summary

The boundary layer on a slender body tends to be very thick at hypersonic speeds. It interacts with the external flow by producing larger flow deflections near the leading edge than those due to the body alone. The increased shock strength affects the boundary-layer growth. The flow around the boundary layer gives rise to an induced pressure with a negative gradient which thins the boundary layer and increases the skin friction with respect to the zero pressure gradient value.

Experiments on a flat plate with a sharp leading edge ($Re_t < 100$) have been performed in the GALCIT 5- by 5-in. Mach 5.8 hypersonic wind tunnel. The induced pressure was measured by means of orifices in the plate surface. Profiles of Mach Number, velocity, mass flow, pressure, and momentum deficiency were calculated from impact pressure surveys normal to the plate surface made at various distances from the leading edge.

The results are as follows. (1) The induced pressures are 25 per cent higher than the weak interaction theory. (2) The boundary layer and the external flow are distinctly separate for Re_x as low as 6,000. (3) The shock wave location is in good agreement with that predicted by the Friedrichs theory for a body shape equivalent to the observed boundary-layer displacement thickness. (4) Expansion waves reflected from the shock are weak. (5) The average skin-friction coefficient tends toward and nearly matches the zero pressure gradient value downstream, but increases to approximately twice that value as the leading edge is approached.

Symbols

a = speed of sound
C = constant in viscosity relation $\mu/\mu_\infty = C\,T/T_\infty$
C_f = local skin-friction coefficient
C_F = average skin-friction coefficient
K = similarity parameter $M\theta$
l = mean free path
M = Mach Number
p = static pressure
$\vec{q}$ = velocity
Re = Reynolds Number per in.
Re_x = Reynolds Number based on x
S = entropy
t = leading-edge thickness
T = static temperature
u = velocity in x-direction
v = velocity in y-direction
x = distance from leading edge
y = distance normal to plate surface
γ = ratio of specific heats
δ = boundary-layer thickness
δ^* = boundary-layer displacement thickness
θ = flow deflection angle
θ' = momentum deficiency $(\rho u/\rho_\infty u_\infty)\,[1 - (u/u_\infty)] - (1/\gamma M_\infty^2)\,[(p/p_\infty) - 1]$
μ = viscosity
ν = kinematic viscosity
ρ = density
χ = interaction parameter $M^3\sqrt{C}/\sqrt{Re_x}$
$\vec{\omega}$ = vorticity $v_x - u_y$

Subscripts

e = outside boundary-layer edge
s = refers to shock-wave location
w = value at wall
0 = isentropic stagnation value
∞ = undisturbed stream

Introduction

THE KINETIC ENERGY of a hypersonic flow may be indefinitely larger than its thermal energy. Thus, when kinetic energy is converted into heat, small changes in speed such as occur in the inviscid flow field about a slender body are reflected as proportionally large changes in temperature, while at a stagnation point or in an uncooled boundary layer the temperature may rise to many times the free-stream value. These large temperature variations serve to distinguish hypersonic flows from supersonic ones with respect to both nonviscous and viscous effects. For example: (1) small velocity perturbations make such large changes in the local speed of sound that the linearized equations of motion of a supersonic flow are accurate only when the parameter $M\theta$ is everywhere much less than unity; (2) when the Mach Number of a flow with fixed static temperature becomes high enough, imperfect gas effects, including dissociation and ionization, will occur because the temperatures become large; (3) the low density of the fluid within the compressible boundary layer enhances the possibility of slip-flow; and (4) the thickness of the hypersonic laminar boundary layer tends to increase like M^2 for a given Reynolds Number, and may be so great that considerable interaction with the free stream results. This phenomenon is the subject of the present experimental investigation.

So-called shock-wave - boundary-layer interaction occurs at supersonic speeds when the rapid growth of the boundary-layer displacement thickness near the leading edge produces an effective thickening of the body. The resulting disturbance to the oncoming stream adds an induced pressure with a negative gradient to the

Presented at the Hypersonics Session, Twenty-Fourth Annual Meeting, IAS, New York, January 23–26, 1956.

† The work discussed in this paper was carried out under the sponsorship and with the financial support of the Office, Chief of Ordnance, and the Office of Ordnance Research, U.S. Army.

* Research Assistant.

inviscid pressure. The induced pressure has a tendency to thin the boundary layer and increase the local skin friction. Simultaneously, the shock wave emanating from the leading edge must increase in strength to account for the added flow deflection, so that streamlines crossing it carry increased values of vorticity and entropy. In this regard, even for bodies which are slender in the usual sense, the leading-edge thickness is a parameter of great importance because of its strong influence on the shock strength. The streamlines crossing the shock travel very large distances downstream before entering the boundary layer because the relative mass flow in the boundary layer is very small for hypersonic flow. On blunt bodies the pressure induced by interaction is generally insignificant because the boundary layer is kept thin by the high pressures and gradients of the inviscid flow, but on sharp-nosed slender bodies the induced pressure may amount to several times the inviscid pressure.

Several theoretical studies of this problem, principally for a flat plate with an infinitely sharp leading edge, have been made by Bertram,[1] Kuo,[2] Lees[3, 4] Lees and Probstein,[5] Li and Nagamatsu,[6] Maslen,[7] and Shen.[8] These theories have followed two general approaches. Shen[8] and Li and Nagamatsu[6] have applied the Kármán momentum integral technique to the boundary-layer equations in the entire region between the plate surface and the shock wave, not recognizing a boundary layer edge. The other solutions have considered the shock wave and boundary layer as separate, and have calculated the inviscid flow over a body represented by the boundary-layer displacement thickness using the concepts of hypersonic similarity and certain approximations. Much of this work is succinctly reviewed in references 9 and 10. Experiments have been performed by Baldwin,[11] Bertram,[12] and Hammitt and Bogdonoff.[9, 13] These have been mainly concerned with the measurement of the induced pressure, although an optical determination of the shock wave location has been included in reference 13.

It is found that, in general, the theory does not accurately predict the measured induced pressure distribution. As an extreme example, the induced pressures measured in the helium tunnel[9] are about $2^1/_2$ times those expected from the theory. Therefore, it appears that the theoretical fluid-mechanical model is either deficient in some respect, or is inconsistent with the physical model, especially with regard to the blunt leading edge. These discrepancies have prompted the present experiment. The aim of this experiment has been to measure and map the flow field for the case where the leading edge is so sharp as to be of vanishing importance.

It will be of interest to interpret some of the experimental results in connection with those theories which treat the shock wave and boundary layer as distinct. Therefore, some of the concepts involved will be discussed and certain significant parameters deduced by means of order of magnitude estimates.

There exist two regions of flow behind the leading-edge shock wave—one near the body surface where viscous or boundary-layer effects predominate because high temperatures cause the viscosity to be large and the density to be small, and an external one where the density is large and the viscosity small so that dynamic forces predominate. The mass flow deficiency of the hot layer is balanced by an excess mass flow in the cool layer. These regions are distinguished very clearly for the laminar hypersonic boundary layer with no interaction, but near the leading edge where interaction occurs, such a separation of predominating effects is subject to restrictions arising from the boundary-layer equations. In references 3 and 6 it has been shown that the Prandtl boundary-layer equations remain valid in the presence of interaction as long as $(\delta/x)^2 \ll 1$. This restriction essentially demands that the pressure variation across the thickness of the boundary layer be small.

Two characteristics of the flow outside the boundary layer are particularly important. (1) The flow is practically inviscid. A comparison of the kinematic viscosity here with that in the boundary layer by means of the linear viscosity relation $\mu/\mu_\infty = C\ T/T_\infty$ gives

$$\nu_e/\bar{\nu} = [1/C(\bar{T}/T_e)^2] \sim (1/CM_e^4) \ll 1$$

where the bars denote average values in the boundary layer. Also, the shear introduced by the curvature of the leading-edge shock is much smaller than in the boundary layer. (2) The expansion waves of the flow over the convex boundary-layer edge which are incident upon the leading-edge shock are practically absorbed there and, thus, serve to weaken it. For example, according to reference 14, the reflected strength of a wave is less than four per cent at Mach 10 for flow deflections under 40 degrees. It follows from these two characteristics that the flow in this region approximates a simple wave state, so that there exists a relation between the pressure and the flow deflection at every point.

This pressure-angle approximation divides interaction into the categories of weak and strong. For the weak case, the values of $K = M\theta$ are small enough so that the pressure is proportional to θ, corresponding in two dimensions to the first term of the tangent-wedge formula for $K \ll 1$,

$$(p/p_\infty) - 1 = \gamma K + [\gamma(1+\gamma)/4]\,K^2 + \ldots$$

(See reference 10.) The parameter upon which the induced pressure depends may then be deduced. The mass flow in the boundary layer is

$$m = \rho_e u_e(\delta - \delta^*)$$

and

$$dm/dx = \rho_e u_e[(d\delta/dx) - \theta]$$

These give

$$\theta = (d\delta^*/dx) - [(\delta - \delta^*)/\rho_e u_e]\,[d(\rho_e u_e)/dx]$$

On a flat plate, the boundary layer grows like

$$\delta^2 \sim (\bar{\mu}x/\bar{\rho}u_\infty) = [(\bar{\mu}/\mu_\infty)/(\bar{\rho}/\rho_\infty)] \cdot (\mu_\infty x/\rho_\infty u_\infty)$$

where $\bar{\mu}\ \mu_\infty$ and $\bar{\rho}/\rho_\infty$ take into account the viscous heating. Using the linear viscosity law, and taking $\bar{\rho}\ \rho_\infty$ to be $T_\infty/\bar{T}$,

$$\delta \sim (M^2\sqrt{C}/\sqrt{Re_x})\,x$$

If θ is taken to be $d\delta^*/dx$, the induced pressure becomes

$$(p/p_\infty) - 1 = \gamma M(d\delta^*/dx) \sim (M^3\sqrt{C}/\sqrt{Re_x}) \equiv \bar{\chi}$$

In the strong interaction case, K is large and the pressure varies more nearly like θ^2, as in the tangent wedge formula

$$(p/p_\infty) - 1 = [\gamma(\gamma+1)/4]K^2 + \gamma K\{1 + [(\gamma+1)/4]^2K^2\}^{1/2}$$

The same estimate of the boundary-layer growth may be made by taking

$$\bar{\rho}/\rho_\infty = (T_\infty/\bar{T})\cdot(p/p_\infty) \qquad \text{and} \qquad p/p_\infty \sim M^2(\delta/x)^2$$

Then

$$p/p_\infty \sim M^3\sqrt{C}/\sqrt{Re_x}$$

and

$$\delta \sim (\sqrt{M}C^{1/4}/Re_x^{1/4})x$$

The restriction for the Prandtl boundary-layer equations to hold becomes

$$\bar{\chi}/M^2 \ll 1$$

The occurrence of slip-flow is most probable near the leading edge where the shear is highest, and in the boundary layer where the mean free path, l, is largest. It is assumed that the no-slip condition is satisfied if

$$l(du/dy) \ll u_\infty$$

This restriction is to be applied to the strong interaction region. In the free stream, $\mu_\infty \sim \rho_\infty l_\infty a_\infty$. In the boundary layer $l \sim 1/\rho$ so that

$$l/l_\infty = Tp_\infty/pT_\infty \sim \sqrt{Re_x}/M\sqrt{C}$$

du/dy is taken to be u_∞/δ, or may be obtained from the theoretical expression for C_f. The restriction becomes

$$(\delta/x)/M = 1/\sqrt{M}\,Re_x^{1/4}C^{3/4} \ll 1$$

For a fixed Reynolds Number, this is more easily satisfied as the Mach Number increases because l decreases faster than the shear increases. In the weak interaction region, the restriction is

$$(\delta/x)/M = M/\sqrt{C}\,\sqrt{Re_x} \ll 1$$

Description of the Experiment

Model and Equipment

The experiment was performed in the GALCIT 5- by 5-in. Mach 5.8 hypersonic wind tunnel, which is of the closed-circuit continuously operating type. All tests were made under steady-state conditions. Ahead of the nozzle the air stream was heated to 225°F. to prevent air condensation. The supply pressure ranged between 25 and 95 psia, depending on the test-section Reynolds Number per inch desired. Extensive facilities are provided for filtering and drying the air. More complete descriptions of the tunnel and its associated instrumentation are to be found in references 15 and 16.

The high carbon steel flat plate model shown in Fig. 1 was 7 in. long, 5 in. wide, and 3/8 in. thick. The bottom of the leading edge was beveled 15°. By comparison with a reference under a high-power microscope, the leading-edge thickness was estimated to be 0.0002 in., except at a few places where it was as large as 0.0005 in. For the measurement of the pressure induced by the growth of the boundary layer, there were 10 orifices in the top surface between x = 0.050 and 4.00 in. spaced approximately equidistantly in the scale $1/\sqrt{x}$. The plate was located in a region of the test section where the static pressure was constant to within 2 per cent, and was aligned with the measured flow direction. The flow was regarded as two-dimensional.

Three impact pressure probes with frontal heights 0.0025 in. (seen in Fig. 1), 0.005 in., and 0.010 in. were used in surveys of the flow field about the plate. The tips of the probes were made from stainless steel hypodermic tubing by flattening one end and honing to proper shape. These tips were soldered into off-set holders.

The plate surface pressures were measured by means of a 32-tube vacuum referenced silicone oil manometer. The tubes were read directly to 0.1 mm. The impact pressures were read on a vacuum referenced mercury micromanometer to 0.1 mm.

Test Program

The plate surface pressures were measured several times at each of three supply pressures.

Two preliminary tests concerning impact pressure probes were made. First, because a flow deflection of up to 10° behind the leading-edge shock was expected, a test of probe sensitivity to angle of attack was made. As the angle of attack of the 0.0025-in. probe was increased from zero, it read 0.1 per cent lower at 3°, 0.5 per cent lower at 6°, and 1.2 per cent lower at 9°. Accordingly, during surveys the probe was maintained at about 4° with respect to the free stream so that the angle of attack error should have been small at every point of measurement. Second, it is well known that when an impact probe being used in boundary-layer measurements is not small compared to the boundary-layer thickness, considerable disturbance to the boundary layer results. Fig. 2 shows the resulting change in the impact pressure profile normal to the plate surface as the size of the probe is increased. The largest of the three probes caused the boundary layer to thicken and to show a pressure bump at its outer edge characteristic of probe interference. This is tentatively explained as follows: the static pressure in the vicinity of the probe is increased by the presence of the probe, separating the low dynamic pressure region of the boundary layer for some distance upstream. The resulting deflection of the flow is equivalent to a thickening of the boundary layer, and at the same time

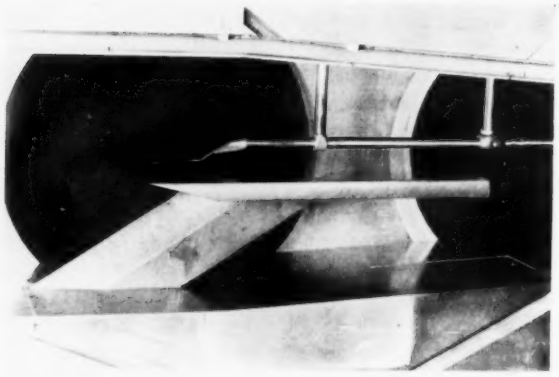

FIG. 1 FLAT PLATE MODEL

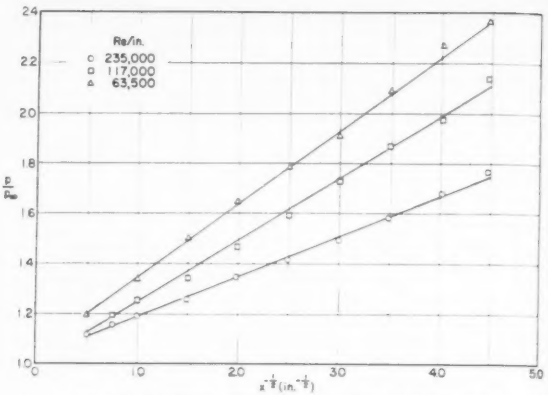

FIG. 5 INDUCED PRESSURE ON A FLAT PLATE AT M=5.8

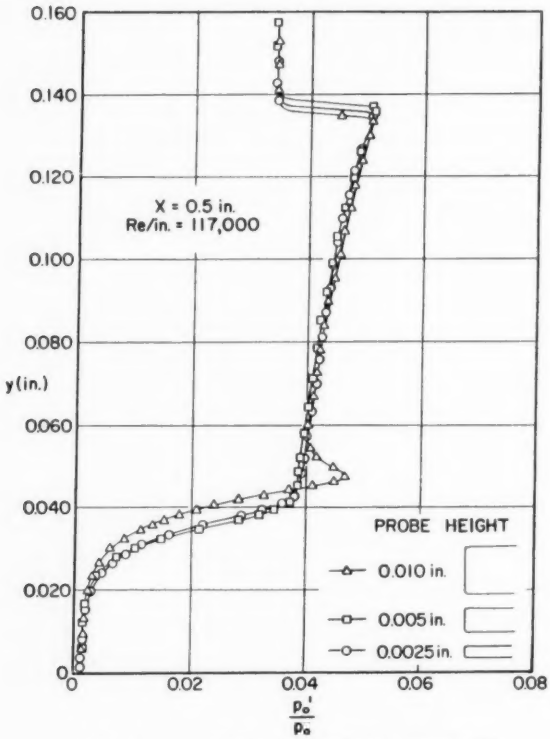

FIG. 2 IMPACT PRESSURE PROFILES

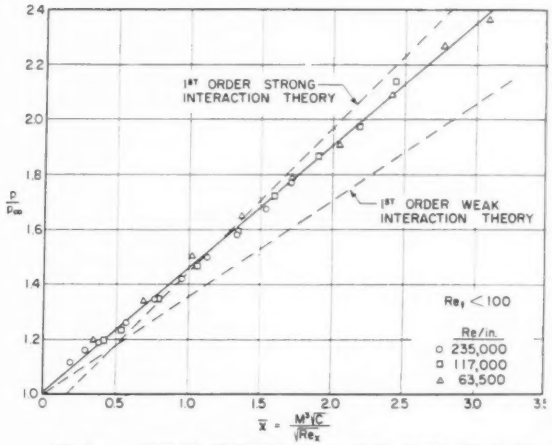

FIG. 6 INDUCED PRESSURE ON A FLAT PLATE AT M=5.8

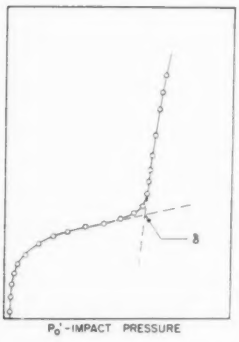

FIG. 3 DEFINITION OF δ

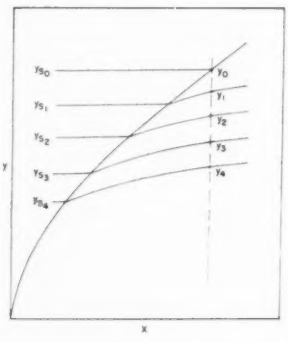

FIG. 4 STREAMLINE PATHS

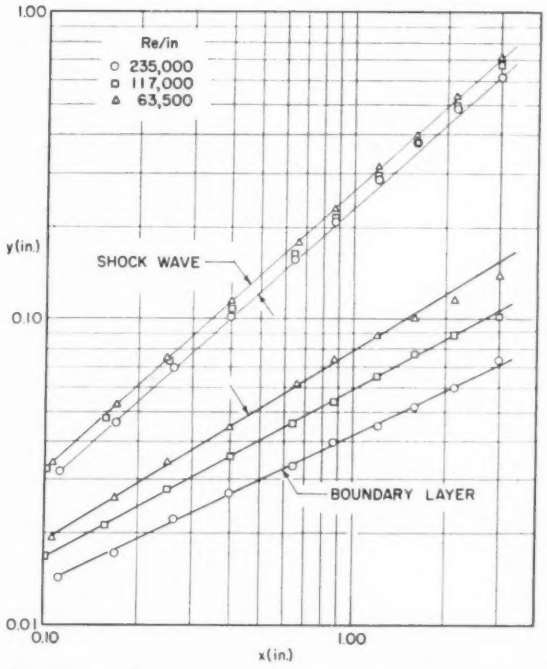

LOCATION OF SHOCK WAVE AND BOUNDARY LAYER EDGE AT M=5.8
FIG. 7

increases the efficiency of the shock system in front of the probe, so that it may read higher pressures.

A detailed examination of the flow over the flat plate was undertaken by measuring the impact pressure profiles normal to the plate surface at 10 stations between $x = 0.1$ and 3.00 in. for each of three supply pressures. The forward limit, $x = 0.1$ in., was imposed by the boundary layer being so thin that even the 0.0025-in. probe caused excessive interference.

Data Reduction

It was desired to present the induced pressure data as p/p_∞ versus $\bar{\chi}$ in accordance with the interaction theory. p was given by the pressure orifice readings, and p_∞ was taken as the empty-tunnel pressure at the point in space corresponding to each orifice location. The values of M_∞, calculated from the impact pressure ahead of the leading edge shock, were 5.66, 5.79, and 5.80, respectively, for the low, medium, and high Reynolds Number conditions. The viscosities used in calculating the Reynolds Numbers and

$$C = \mu_w T_\infty / \mu_\infty T_w$$

were determined from the Sutherland formula. For the present case, $C = 0.90$.

The location of the boundary-layer edge, δ, and the shock wave, y_s, were taken from the impact pressure profiles. The artificial definition of δ shown in Fig. 3 is not subject to the usual ambiguity. y_s was taken to be that distance above the plate where the impact pressure reached its maximum value.

Using the impact pressures and an independently determined estimate of either the total pressure—the pressure recovered by an isentropic compression to zero speed—or the static pressure at the same points in space, the following quantities were computed for the intermediate Reynolds Number condition: Mach Number, velocity, mass flow, momentum deficiency, and either static or total pressure, whichever was not estimated. Isoenergetic flow was assumed.

Outside the boundary layer, the total pressure along a streamline was estimated by determining where that streamline crossed the shock wave by consideration of the mass flow. The measured strength of the shock along its length then determined the total pressure. The details are as follows. (1) The impact pressure ratio across a shock gives an accurate measure of its strength. From the impact pressure profiles a plot of total pressure ratio across the shock as a function of the shock location, y_s, was made. (2) In Fig. 4, several streamlines are shown crossing a curved shock. The y_n's represent the points at which the impact pressure was measured, and the y_{s_n}'s were sought. If $\overline{\rho u}$ is the average mass flow between y_0 and y_1, then by continuity,

$$y_{s_1} = y_{s_0} - (\overline{\rho u}/\rho_\infty u_\infty)(y_0 - y_1)$$

(3) u was taken to be the speed of the flow with negligible error because the inclination of the flow was small. For a first approximation, $\overline{\rho u}$ was taken equal to the value of ρu at y_0, which was known from the oblique shock relations, and an approximation to y_{s_1} was obtained. (4) The total pressure ratio for this value of y_{s_1} and the impact pressure at y_1 were used to compute ρu at y_1. (5) An improved estimate of $\overline{\rho u}$ was made, and the process repeated until a consistent value of y_{s_1} was obtained. (6) By similar means, y_{s_2} was computed using y_{s_1}, and so on until the streamline being computed crossed the leading-edge shock at a value of y_s lower than for which there was information about the shock strength. (7) The other quantities listed above were computed with the aid of the compressible flow tables.

Using the static pressures thus calculated and the measured plate surface pressure, the static pressure was estimated for the remainder of the flow field. The calculations were continued using the impact and static pressures.

θ', the "momentum" deficiency, has the interpretation of being one-half the contribution of a stream tube to the total drag of a body. θ' is defined by

$$(\rho u/\rho_\infty u_\infty)[1 - (u/u_\infty)] - (1/\gamma M_\infty^2)[(p/p_\infty) - 1]$$

For the present case, the average drag coefficient at any x-station is given by

$$C_F = (2/x)\int_0^{y_s} \theta'\, dy$$

Outside the boundary layer, θ' is proportional to the mass flow times the entropy rise through the shock wave and, hence, for weak shocks, vanishes like $(M_n^2 - 1)^3$, where M_n is the component of M_∞ normal to the shock.

The mass flow profiles were integrated with respect to y by means of a mechanical integrator, and several streamlines were traced by locating points of equal value of the integral at each x-station. Several Mach lines were traced by a simple quadrature of the sum of the local Mach angle and streamline inclination.

Discussion of the Accuracy

The plate surface pressures were measured with less than 1 per cent error. The scatter of any one orifice reading was occasionally as high as 3 per cent, but the repeatability of the best straight line in a plot of p/p_∞ versus $1/\sqrt{x}$ was within 2 per cent. The viscosity used in calculating the Reynolds Numbers and C was known to within 5 per cent, and M_∞ was known to 0.2 per cent, so that $\bar{\chi}$ is accurate to within 6 per cent.

In the boundary layer, the flow quantity profiles reflect errors due to (1) impact probe location, (2) probe error—low Reynolds number effects, etc., (3) estimated static pressure error, and (4) assumption of isoenergetic flow. Near the plate surface, errors (2) and (4) are expected to produce large errors in each of the profiles. These errors may, however, be circumvented to some extent by estimating values which are consistent with u/u_∞ being zero at the plate surface and nearly linear in y. At the value of y where $u/u_\infty \doteq 0.5$, u/u_∞, $\rho u/\rho_\infty u_\infty$, M, and $p_0/p_{0\infty}$ may be somewhat affected by errors (2), (3), and (4), but θ', which reaches

approximately its maximum there, is relatively unaffected. In the outer boundary layer and in the remainder of the region where the calculations were based on the estimated static pressure, U/U_∞, $\rho u/\rho_\infty u_\infty$, and M are reasonably accurate, but θ' is not reliable because of its dependence on $[1 - (u/u_\infty)]$. Since this region extends over at most one-third of y_s, and because θ' is small compared to its maximum, the error contributed to the integral of θ' is small. In the range of y where the calculations were based on the estimated total pressure, all quantities are believed to be nearly as accurate as the measured impact pressures.

One check of the overall accuracy is given by how well the mass flow profiles satisfy the continuity relation

$$(1/y_s)\int_0^{y_s} (\rho u/\rho_\infty u_\infty)\, dy = 1$$

The value of the integral was 0.97 at $x = 0.157$ in., and was between 0.98 and 1.00 for all other stations. It is felt that the integrals of θ' are probably accurate to within 5 per cent.

Results and Discussion

Induced Pressures

The induced pressure ratios are shown versus $1/\sqrt{x}$ in Fig. 5, and versus the interaction parameter $\bar{\chi}$ in Fig. 6. In these Figures, the leading edge lies to the right, the trailing edge to the left. Because the Mach Number was nearly constant, the present experiment offers no justification for the use of the interaction parameter other than permitting a direct comparison with theory. However, the correlation was improved by including the slight variations of Mach Number. Also shown in the latter figure are the first-order weak and strong interaction theory results,

$$p/p_\infty = 1 + 0.35\bar{\chi} \quad \text{and} \quad p/p_\infty = 0.92 + 0.52\bar{\chi}$$

(See reference 10.) The data are seen to differ from the expected results in two ways—the weak interaction theory should be adequate for $\bar{\chi} < 1$, but the data lie 25 per cent higher; and the data are strikingly linear, failing to show any second-order variations or any transition between weak and strong forms.

The discrepancy between the data and the weak interaction theory might be due to one of the following causes.

(1) The finite leading-edge size in the experiment. This possibility is to be dismissed for two reasons. First, in measuring the induced pressures on a flat plate, Bertram[12] has found that the variation in the plate surface pressure as the leading-edge thickness, t, is changed is approximately equal to the corresponding variation of the theoretically calculated pressure of an inviscid flow over a blunt wedge-plate body. In the present experiment, the first pressure orifice was 250 leading-edge thicknesses downstream, and according to Bertram's calculation the leading edge makes a negligible contribution to the measured pressures. Second, no systematic change in the slope of the curves of p/p_∞ versus $\bar{\chi}$ is observed although Re_t has varied by a factor of four.

(2) An inaccuracy of the pressure-angle approximation used in the theory. This will be checked by comparing the tangent-wedge pressure with the measured pressure along a streamline.

(3) An inaccuracy in the theoretical boundary-layer growth. This will be checked by comparison with the experimentally determined boundary-layer thickness.

(4) Error resulting from the neglect of the second term of the expression

$$\theta = (d\delta^*/dx) - [(\delta - \delta^*)/\rho_e u_e]\,[d(\rho_e u_e)/dx]$$

Taking

$$p/p_\infty = 1 + 0.45\bar{\chi}$$

$$(1/\rho_e u_e)\,[d(\rho_e u_e)/dx] = (1/\gamma p_e)\,(dp_e/dx)$$

$$\delta^* = 0.75\delta \sim \sqrt{x}$$

the ratio of the second term to the first becomes

$$r = (0.11\bar{\chi})/(1 + 0.45\bar{\chi})$$

The flow deflection is underestimated by about 7 per cent for $\bar{\chi} = 1$ and by 14 per cent for $\bar{\chi} = 3$.

(5) A pressure variation across the boundary-layer thickness. The flow quantity profiles support this possibility.

Boundary-Layer Growth

The impact pressure surveys were found to define a boundary-layer edge very distinctly for even the lowest Re_x, about 6,000, where the probe frontal height was 15 per cent of δ. These data are presented in Fig. 7. The straight lines faired through them are proportional to $x^{0.49}$, $x^{0.55}$, and $x^{0.61}$, respectively, for the high, medium, and low Reynolds Number per inch conditions. In Fig. 8, these data are presented as δ/x versus $M^2\sqrt{C}/\sqrt{Re_x}$ in accordance with theory. The satisfactory correlation is not surprising in view of the good correlation of the induced pressures. The thinning of the boundary layer near the leading edge by the induced pressure is clearly seen, and suggests that δ/x does not exceed some maximum value, in contrast to the infinite value predicted by a simple power law. Thus the requirement $(\delta/x)^2 \ll 1$ for the Prandtl boundary-layer equations to hold may be satisfied.

The boundary-layer displacement thickness, δ^*, as defined by

$$\int_0^\delta \rho u\, dy = \rho_e u_e(\delta - \delta^*)$$

may be written

$$\frac{\delta^*}{\delta} = 1 - \frac{1}{\delta}\,\frac{\rho_\infty u_\infty}{\rho_e u_e}\int_0^\delta \frac{\rho u}{\rho_\infty u_\infty}\, dy$$

This quantity has been evaluated from the mass flow profiles (which are to be discussed) and is approxi-

mately 0.75. According to Fig. 8, the displacement thickness for large Reynolds Numbers may then be written

$$\delta^*/x = 0.50(M^2\sqrt{C}/\sqrt{Re_x})$$

The value used in the first-order weak interaction theory is

$$\delta^*/x = 0.48(M^2\sqrt{C}/\sqrt{Re_x})$$

The method of Cohen and Reshotko[17] for calculating the laminar boundary layer with arbitrary pressure gradient was used to predict a boundary-layer thickness for the case $Re/\text{in.} = 117{,}000$. Taking the observed value of δ at $x = 0.100$ in. as the starting point of the calculation in order to avoid making assumptions about the flow conditions very near the leading edge, and using the measured plate surface pressures, the resulting boundary-layer growth was found to agree with the experimental values to within 5 per cent up to $x = 3$ in.

Shock-Wave Location and Strength

The shock location, y_s, is given for three Reynolds Numbers in Fig. 7. When these data are presented as Re_y versus Re_x, as in Fig. 9, it is found that they may be empirically represented as $Re_y \sim Re_x^{0.90}$. It is interesting to note that in the Princeton helium tunnel at Mach Numbers of the order of 14, the shock shape for a flat plate with $Re_t = 119$ may be expressed as $Re_y \sim Re_x^{0.88}$ (see reference 13).

However, it is perhaps more appropriate to present these data in another way. The shock-wave location on a body equivalent to the observed parabolic boundary-layer shape

$$\delta^* = 0.50(M^2\sqrt{C}/\sqrt{Re})\sqrt{x}$$

has been calculated according to the Friedrichs theory, as outlined in reference 18, pp. 397–402. In this method, the flow behind the shock is considered to be a simple wave, and the equation of a Mach line may be written

$$y - x\tan[(1/\beta) + \theta] = Y(\theta)$$

where $\beta = \sqrt{M_\infty^2 - 1}$. Along the shock, dy/dx obtained from this expression must be set equal to $\tan[\eta(\theta)]$, giving the linear differential equation

$$\{\tan[(1/\beta) + \theta] - \tan[\eta(\theta)]\}(dx/d\theta) + x(d/d\theta)\tan[(1/\beta) + \theta] = -Y'(\theta)$$

To the first order one has

$$\tan[(1/\beta) + \theta] = (1/\beta) + 2A\theta$$

$$\tan[\eta(\theta)] = (1/\beta) + A\theta$$

where

$$A = [(\gamma + 1)/4](M_\infty^4/\beta^4)$$

Integration gives

$$x_s = \frac{1}{A\theta^2}\int_{\theta_0}^{\theta} \theta\, dY(\theta)$$

where $\theta_0 = \theta$ at $x = 0$. Together with the equation of the Mach lines, this expression gives a parametric representation of the shock shape. Taking $\theta = d\delta^*/dx$, one obtains for the present case

$$Re[y_s - (x/\beta)] = 3.13Re_x^{2/3}$$

This result is shown in Fig. 10, and the experimental data are seen to compare favorably with the theoretical prediction.

In Fig. 11, the flow deflection behind the shock wave is given for the intermediate value of Re in. This measure of the shock strength has been determined from the impact pressure ratio across the shock and is considered to be quite accurate. The same quantity has been calculated from the empirical relation $y_s \sim x^{0.88}$, which represents the best fit of the shock location for this value of $Re/\text{in.}$ The agreement is seen to be rather poor.

As a check, the reverse procedure was followed. The shock-wave angle determined from the impact pressure ratio was integrated by a simple quadrature, starting from the observed shock location at $x = 0.1$ in. The shock location determined by this means was virtually identical with that measured. It is to be concluded that the determination of the strength of a weak shock by differentiation of its measured location is a matter requiring some care.

Flow Quantity Profiles

Certain interesting features of the flow field are disclosed by the profiles of the calculated flow quantities at the various x-stations. One such set of profiles is shown in Fig. 12. For example, the velocity in the viscous region appears to retain the form usual for the laminar compressible boundary layer, while in the external region the velocity is near the free-stream value, and the mass flow ratio is larger than unity. The extent to which there exist separate viscous and nonviscous regions does not diminish in the profiles nearer the leading edge. In contrast to the usual viscous flow over a flat plate, the momentum deficiency does not vanish outside the boundary-layer edge, but extends to the shock because of the wave drag of the boundary layer.

A substantial pressure gradient in the y-direction due to the streamline curvature occurs in the inviscid flow region. The mass flow, Mach Number, velocity, and momentum deficiency show variations which are consistent. Above a certain value of y the velocity and Mach Number decrease with increasing y because of the increasing static pressure and slowly varying total pressure, while the momentum deficiency increases due to the increasing mass flow. Below this value of y these quantities show the opposite variation because the total pressure change with y is rapid.

A measure of the vorticity outside the boundary-layer edge is afforded by the total pressure profiles. Crocco's theorem is

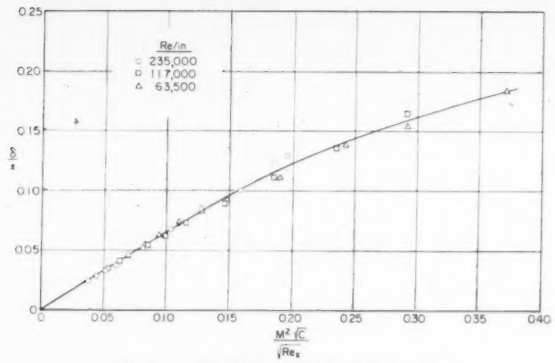

FIG. 8 BOUNDARY LAYER THICKNESS AT M = 5.8

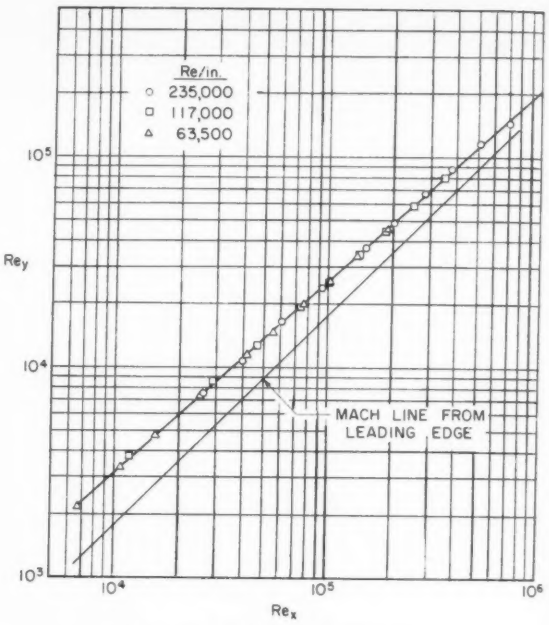

FIG. 9 LOCATION OF SHOCK WAVE

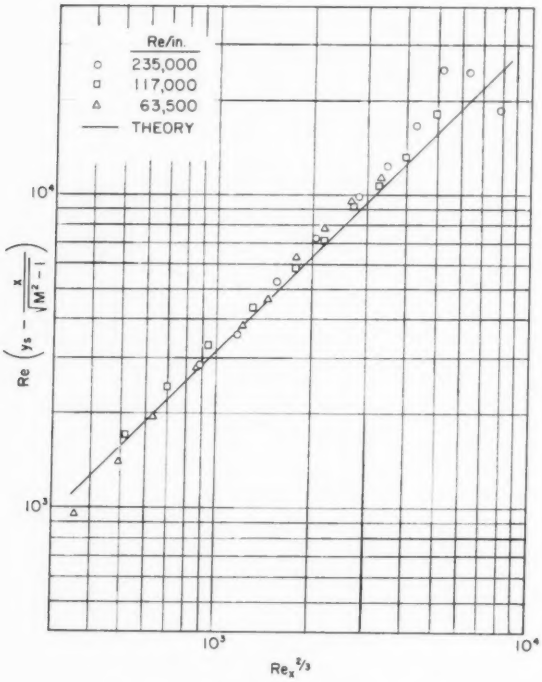

FIG. 10 LOCATION OF SHOCK WAVE

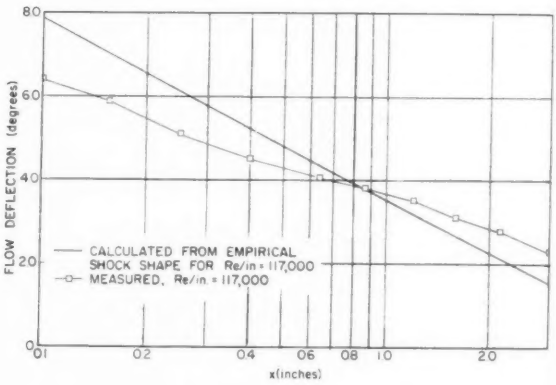

FIG. 11 FLOW DEFLECTION BEHIND LEADING EDGE SHOCK WAVE

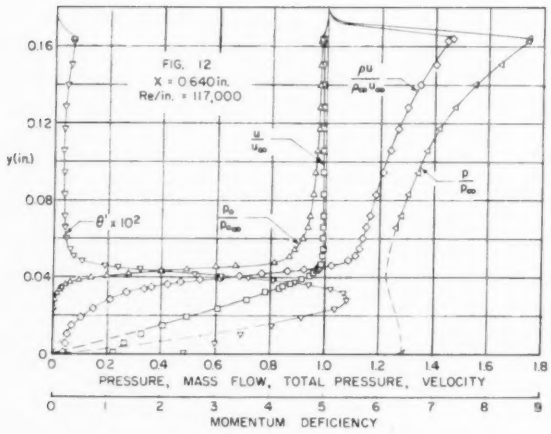

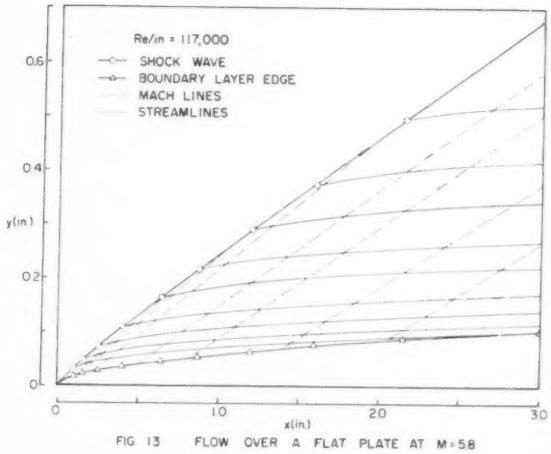

FIG. 13 FLOW OVER A FLAT PLATE AT M = 5.8

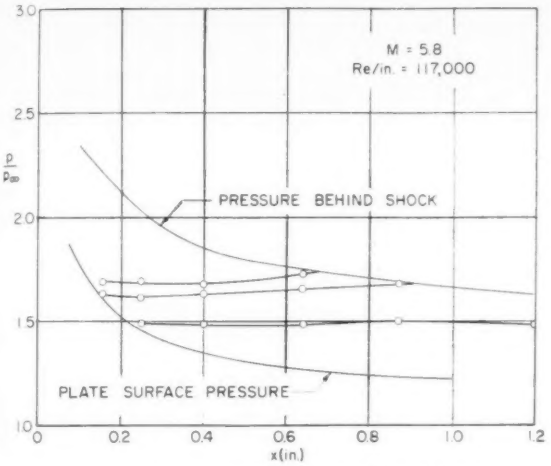

FIG. 14 PRESSURE ALONG MACH LINES

$$\vec{q} \times \omega = -T\nabla S$$

where $\vec{q}$ is the velocity, ω the vorticity $v_x - u_y$, T the temperature, and ∇S the entropy gradient. The entropy may be written

$$S - S_\infty = C_p \ln (p_{0\infty}/p_0)^{(\gamma-1)/\gamma}$$

and its gradient is approximately

$$\nabla S \doteq dS/dy = [(\gamma - 1)/\gamma]\, C_p (d/dy)\, [(p_{0\infty} - p_0)/p_0] = R(d/dy)\,(\Delta p_0/p_0)$$

The vorticity at the plate surface is nearly $\vec{\omega}_w = u_e/\delta$, so that

$$\vec{\omega}/\vec{\omega}_w = (\delta RT/u_e^2)\,(d/dy)\,(\Delta p_0/p_0) = (\delta/\gamma M_e^2)\,(d/dy)\,(\Delta p_0/p_0)$$

At $x = 0.25$ in., for example $\vec{\omega}/\vec{\omega}_w = 0.1$ outside the boundary-layer edge, but is only 0.005 near the shock. The rate of shearing strain $v_x + u_y$ near the shock will be approximately $2u_y < 0$ since $\vec{\omega} \doteq 0$.

Some anomalies remain to be considered. (1) The behaviors of each of the flow quantity profiles near $y = 0$ reflect the errors suffered by an impact probe at low Reynolds Numbers. (2) The profiles at $x = 0.157$ and 0.250 in. (not shown) show the effects of impact probe interference near $y = \delta$. (3) According to the profiles at $x = 0.64$ in. and aft, the pressure is about 5 per cent higher in the boundary layer than in the nearby external region. Although such an effect has not been explained, no reason to discount this result has been found.

Flow Field

Fig. 13 gives an experimentally determined representation of the complete flow field. It is seen that the streamlines cross the shock quite far ahead of where they enter the boundary layer, and the Mach lines intersect the shock at very small angles, so that the rather slow decay of the shock strength, corresponding to its $x^{0.90}$ shape, is accounted for. The boundary-layer growth in the first 0.1 in. determines the shock strength up to about $x = 0.7$ in.

In Fig. 14 the static pressure along each of the three most forward Mach lines of Fig. 13 shows only a slight increase with x. Apparently the expansion waves incident upon the shock are reflected as very weak compression waves. The flow deflection along the first Mach line is calculated to be 4.36° at $x = 0.157$ in. and 4.25° at $x = 0.64$ in. This Mach line is nearly straight, having an inclination of 15.40° at $x = 0.157$ in. and 15.21° at $x = 0.64$ in. The other Mach lines show smaller variations along their lengths.

The static pressure along the streamline shown crossing the shock at $x = 0.1$ in. in Fig. 13 has been calculated from the local streamline inclination by means of the tangent-wedge approximation and compared with the pressures taken from the calculated profiles. The results are shown in Fig. 15.

Total Drag

Near the leading edge the shear is expected to be higher than the zero pressure gradient value because the boundary layer is thinned by, and $\partial u/\partial y$ at $y = 0$ increased by, the negative induced pressure gradient. The velocity profiles are not considered to be sufficiently accurate near $y = 0$ to permit a direct calculation of the local skin friction. Instead, the average skin-friction coefficient, C_F, has been obtained from the θ' profiles and is shown in Fig. 16. The drag of the

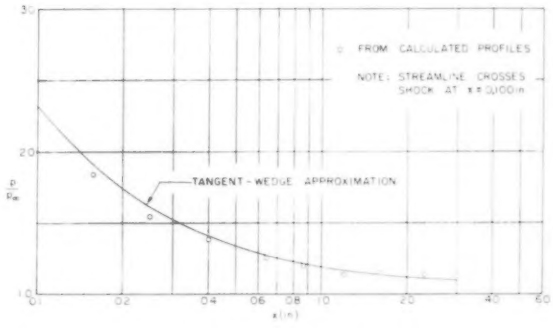

FIG. 15 STATIC PRESSURE ALONG A STREAMLINE

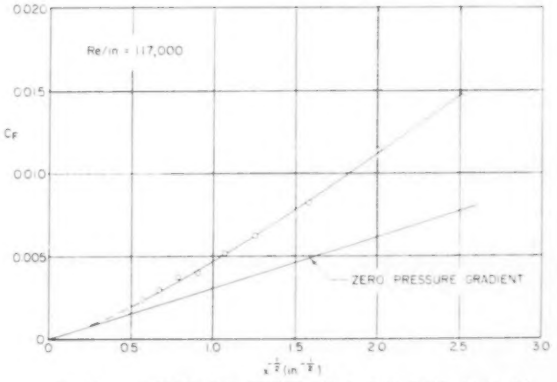

FIG. 16 AVERAGE SKIN FRICTION ON A FLAT PLATE AT M = 5.8

leading edge, approximated as the impact pressure times half the leading-edge thickness, is about 7 per cent of the measured C_F at $x = 0.157$ in., and is less at succeeding stations. Eimer[15] has measured the local skin friction on a flat plate in the same tunnel, and the average skin friction corresponding to his result is shown for comparison. His measurements were made by means of a floating element balance located sufficiently far from the leading edge that interaction effects may be neglected.

Maslen[7] has given a theoretical expression for the local skin friction of the form

$$C_f \sqrt{Re_x} = f(M) + [g(M)/\sqrt{Re_x}]$$

It is not directly integrable to give C_F. Instead, the experimental value of C_F at $x = 3$ in. was taken, and its variation ahead of this station computed from Maslen's result according to the expression

$$C_F = (1/x) \int_0^x C_f \, dx = (3/x) C_{F_3} - (1/x) \int_x^3 C_f \, dx$$

The values of C_F thus determined agreed with the experimental results to within 2 per cent.

Summary of Results

The following results have been found. The induced pressures are linear in $M^3\sqrt{C}/\sqrt{Re_x}$ and are about 25 per cent higher than the first-order weak interaction theory.

The boundary-layer edge is well defined for Re_x at least as small as 6,000. The flow outside the edge is inviscid, but vorticity is present.

Away from the leading edge, the boundary-layer thickness is in agreement with the zero pressure gradient theory, but is thinner near the leading edge.

The shock-wave location may be represented by $Re[y_s - (x/\beta)] \sim Re_x^{2/3}$ and is in good agreement with the theoretical shock location for a parabolic body.

The paths of the Mach lines indicate that the shock location ahead of $x = 0.7$ in. is determined by the boundary-layer growth ahead of $x = 0.1$ in. The Mach lines are so nearly parallel to the shock that the strength of the shock along its length decays slowly.

The static pressure and flow deflection are nearly constant along the length of a Mach line, indicating that waves reflected from the shock are weak.

The average skin-friction coefficient tends toward and nearly matches the zero pressure gradient value downstream, but increases to approximately twice that value as the leading edge is approached.

Conclusions

An experiment intended to indicate the behavior of the interaction of the viscid and inviscid flow regions near the leading edge of a flat plate has been performed without consideration of any theory for the case where the leading-edge thickness is negligibly small and at a moderately hypersonic Mach Number. The case where the leading-edge thickness is an important parameter has been discussed in reference 13.

The experiment yields a picture of the flow which is consistent with the weak interaction theory of Lees,[10] with the exception that the induced pressures are somewhat higher. The external flow field is well described by simple wave theory since entropy gradients are small and hence waves reflected from the shock are weak. The boundary-layer growth is just what one expects from the observed pressure distribution.

References

[1] Bertram, M. H., *An Approximate Method for Determining the Displacement Effects and Viscous Drag of Laminar Boundary Layers in Two-Dimensional Hypersonic Flow*, NACA TN 2773, 1953.

[2] Kuo, Y. H., *Viscous Flow Along a Flat Plate Moving at High Supersonic Speeds*, Journal of the Aeronautical Sciences, Vol. 23, No. 2, pp. 125–136, February, 1956.

[3] Lees, L., *On the Boundary-Layer Equations in Hypersonic Flow and Their Approximate Solutions*, Journal of the Aeronautical Sciences, Vol. 20, No. 2, pp. 143–145, February, 1953.

[4] Lees, L., *Influence of the Leading-Edge Shock Wave on the Laminar Boundary Layer at Hypersonic Speeds*, GALCIT Technical Report No. 1, July 15, 1954.

[5] Lees, L., and Probstein, R. F., *Hypersonic Viscous Flow Over a Flat Plate*, Princeton University, Aeronautical Engineering Laboratory Report No. 195, April 20, 1952.

[6] Li, Ting-Yi, and Nagamatsu, H., *Shock-Wave Effects on the Laminar Skin Friction of an Insulated Flat Plate at Hypersonic Speeds*, Journal of the Aeronautical Sciences, Vol. 20, No. 5, pp. 345–355, May, 1953.

[7] Maslen, S. H., *Second Approximation to Laminar Compressible Boundary Layer on Flat Plate in Slip-Flow*, NACA TN 2818, 1952.

[8] Shen, S. F., *An Estimate of Viscosity Effect on the Hypersonic Flow Over an Insulated Wedge*, J. Math. and Physics (M.I.T.), Vol. 31, No. 3, pp. 192–205, October, 1952.

[9] Hammitt, A. G., and Bogdonoff, S. M., *A Study of Flow About Simple Bodies at Mach Numbers from 11 to 15*, WADC Technical Report 54-257, October, 1954.

[10] Lees, L., *Hypersonic Flow*, Institute of the Aeronautical Sciences, Preprint No. 554, June, 1955.

[11] Baldwin, L. C., *Viscous Effects on Static Pressure Distribution for a Slender Cone at a Nominal Mach Number of 5.8*, GALCIT Memorandum No. 28, June, 1955.

[12] Bertram, M. H., *Viscous and Leading-Edge Thickness Effects on the Pressures on the Surface of a Flat Plate in Hypersonic Flow*, Journal of the Aeronautical Sciences, Vol. 21, No. 6, pp. 430–431, June, 1954.

[13] Hammitt, A. G., Vas, I. E., and Bogdonoff, S. M., *Leading Edge Effects on the Flow Over a Flat Plate at Hypersonic Speeds*, Princeton University, Aeronautical Engineering Laboratory Report No. 326, September, 1955.

[14] Eggers, A. J., Jr., and Syvertson, C. A., *Inviscid Flow About Airfoils at High Supersonic Speeds*, NACA TN 2646, 1952.

[15] Eimer, M., and Nagamatsu, H., *Direct Measurement of Laminar Skin Friction at Hypersonic Speeds*, GALCIT Memorandum No. 16, July, 1953.

[16] Baloga, P. E., and Nagamatsu, H. T., *Instrumentation of GALCIT Hypersonic Wind Tunnels*, GALCIT Memorandum No. 29, July, 1955.

[17] Cohen, C. B., and Reshotko, E., *The Compressible Laminar Boundary Layer with Heat Transfer and Arbitrary Pressure Gradient*, NACA TN 3326, April, 1955.

[18] Sears, W. R., (Ed.), *High Speed Aerodynamics and Jet Propulsion, Vol. VI*, Princeton University Press, Princeton, New Jersey, 1954.

An Investigation of Effects of Certain Types of Structural Nonlinearities on Wing and Control Surface Flutter

DONALD S. WOOLSTON,* HARRY L. RUNYAN,* AND ROBERT E. ANDREWS*

Langley Aeronautical Laboratory, NACA

SUMMARY

This paper presents some effects of nonlinear structural terms on the flutter of a wing capable of bending and twisting and, also, of a system including a control surface. Several type of nonlinearities in the stiffness are investigated, including free play, a hysteresis loop, and cubic variations. These are introduced in the torsional degree of freedom of the wing and in the aileron stiffness in the three degree of freedom system. Calculations have been made on an analog computer. A wind-tunnel investigation of one case having free play in the torsional degree of freedom has been made, and good correlation between theory and experiment is shown.

The results indicate that the stability of a nonlinear system is highly dependent on the magnitude of initial displacements of the system from equilibrium. It is shown that in many cases the flutter speed is decreased by increasing the initial disturbance. The results also indicate that when a nonlinear system becomes unstable its flutter may become self-limited.

SYMBOLS

a = coordinate of pitch axis measured from midchord, referred to semichord b, positive for pitch axis behind midchord

b = wing semichord, ft.

c = coordinate of aileron hinge measured from midchord, referred to semichord b

h = displacement of system in vertical translation

α = angular displacement of wing in torsion

β = angular rotation of control surface about hinge

h_0, α_0, β_0 = initial displacements in degrees of freedom h, α, and β, respectively

H = height of hysteresis box

I_α = moment of inertia of wing or wing-control surface about a per unit span length

I_β = moment of inertia of control surface about c per unit span length

K_α, $\bar{K}_\alpha$ = spring constants in equation of cubic spring

m = mass of wing or wing-aileron system per unit span length

M = moment

r_α = radius of gyration of wing or wing-control surface system referred to a, $\sqrt{I_\alpha/mb^2}$

r_β = reduced radius of gyration of aileron referred to c, $\sqrt{I_\beta/mb^2}$

R/R_{lin} = ratio of amplitude of response of system with nonlinearity present to amplitude of response of linear system

S_α = static moment of wing or wing-control surface system per unit span length referred to a

S_β = static moment of control surface per unit span length referred to c

V = velocity of main stream

V_{lin} = flutter velocity of linear system

V_0 = flutter velocity of linear system for control surface frequency $\omega_\beta = 0$

x_α = location of center of gravity of wing or wing-control surface system referred to a, S_α/mb

x_β = reduced location of center of gravity of control surface referred to c, S_β/mb

δ = angular free play in torsion or control surface rotation

κ = wing-mass air-density ratio $m/\pi\rho b^2$

ρ = mass density of air

ω = circular frequency of driving force (see Fig. 2)

ω_h = natural circular frequency of wing in vertical translation

ω_α = natural circular frequency of torsional vibrations about a

ω_β = natural circular frequency of torsional vibrations of control surface about c

Presented at the Aeroelasticity Session, Twenty-Fourth Annual Meeting, IAS, New York, January 23–26, 1956.

* Aeronautical Research Scientist.

INTRODUCTION

ALMOST ALL PROBLEMS in mechanics contain some elements of nonlinearity. For the most part, however, the great fund of knowledge now available to the physical scientist or engineer has been made on the grounds of linear approximations of the governing equations. In many cases, the approximations introduced by linearization are quite valid, and the results are sufficiently accurate for their purposes. On the other hand, the introduction of nonlinearities into a problem may not only change the linearized solution but may even introduce certain new types of phenomena which are not even indicated by the linear theory.

In the aeronautical field, the demand for faster and still faster airplanes has resulted in the absolute necessity for the more accurate prediction of the various airplane characteristics than has been required in the past. It has become necessary to examine very closely the new problems which have arisen in order to ensure that no important nonlinear effects are being neglected. Also it becomes necessary to re-examine and recast some of the more classical problems in the light of the possible effects of nonlinearities which have not been studied in the past.

The purpose of this paper is to examine some effects of the introduction of several types of nonlinear terms into the classical two and three degree of freedom flutter problem.

In considering the flutter problem, three types of forces are involved—namely, inertia, damping, and

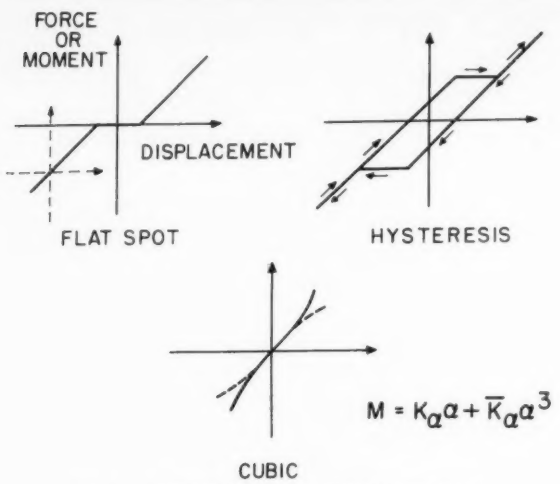

FIG. 1. Types of nonlinear springs investigated.

elastic. Each of these forces may arise from either the aerodynamics of the problem or from the structure. Nonlinearities may arise from the aerodynamics, for instance, from the effect of airfoil thickness, or from flow separation or breakdown. The structural side of the problem may also give rise to nonlinearities in the inertial, damping, and elastic forces, some examples of which will be indicated later. This paper is concerned essentially with structural nonlinearities and constitutes an extension of the work done in reference 1, in that a third degree of freedom, a control surface, has been added to the bending-torsion degrees which were studied in reference 1.

In examining the literature on nonlinear vibrations it was soon evident that only the single degree of freedom cases had received extensive treatment and that the state of the art had not progressed to the point of handling analytically more than one degree of freedom. It was therefore decided to study the problem on an analog computer. The type of analog used in the analysis involved the principle of the electronic differential analyzer, wherein successive integrations of voltages are performed by the use of feedback amplifiers.

In order to gain an understanding of some effects of nonlinearities, the physical systems to be dealt with have been intentionally limited to simple ones. The flutter characteristics of two configurations will be examined; one, a wing, or all-movable control, free to translate and pitch about some spanwise axis, and the other, a wing-control surface system with freedoms in translation and pitch of the wing and rotation of the control about its hinge. Both systems are treated as two-dimensional, and, in the flutter calculations, incompressible indicial air forces are used.

With regard to the nonlinear springs to be considered, little is known of the exact nature and magnitude of nonlinearities which exist in actual aircraft. In the study to be discussed, the nonlinearities, too, have been kept simple in form and were selected as representative of types which might occur.

TYPES OF NONLINEAR SPRINGS INVESTIGATED

The types of nonlinear springs considered are illustrated in Fig. 1 and are represented by plots of the force or moment required to produce a given displacement. Shown at the left of the Figure is a flat spot type of nonlinearity which represents free play in the hinge or linkage of a control system. The effects of free play will be considered for two different conditions: in one, the equilibrium condition will be taken as in the center of the free play, as shown by the solid lines in the sketch; in the other condition, a preload will be assumed to act on the system so that the equilibrium position lies at some point on the linear arm, as shown by the dashed lines.

The second nonlinearity to be dealt with is a type of hysteresis, shown at the right of the Figure. As force or moment is increased, displacement varies linearly until a point is reached at which a jump occurs, after which the system is again linear. On the return path, a corresponding jump occurs at another value of the force. A nonlinearity of this type may occur in the case of a control surface with free play if friction exists at some point in the linkage. In the case of a wing, this type of nonlinearity might represent the effect of rivet slip.

The third type of nonlinearity treated has been termed a cubic spring, where the force exerted depends on the usual linear power of the displacement and, in addition, on a term containing the cube of the displacement. This can be considered either as a hard spring, which becomes stiffer as displacement increases, as shown by the solid line, or as a soft spring, which becomes weaker as displacement increases, as shown by the dashed line. In the case of a control surface, a hard-spring effect might be associated with power controls. In the case of a structure, a hardening effect is found when a thin wing, or perhaps a propeller, is subjected to increasing amplitudes of torsion. A soft-spring effect may be associated with panel buckling.

EFFECTS OF NONLINEAR SPRINGS ON AIRCRAFT FLUTTER

The three types of nonlinear springs illustrated in Fig. 1 have been considered in flutter investigations conducted on the analog computer. For the case of free play, experimental wind-tunnel results have also been obtained for a two degree of freedom system. The free play nonlinearity is considered first.

Effects of Free Play

Before actually presenting flutter results showing effects of free play, it is instructive and of interest to examine the zero air-speed vibration characteristics of a simple single degree of freedom system with this type of nonlinearity.

Vibration Characteristics of a System with Free Play—A usual preliminary step in the flutter investigation of an aircraft is a ground vibration survey to determine natural frequencies and modes of oscillation. Such a

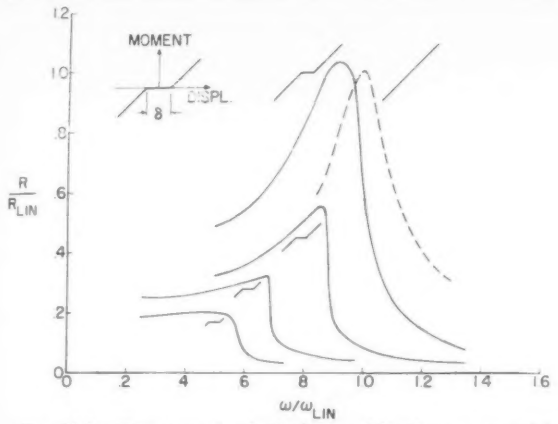

FIG. 2(a). Response of a single degree of freedom system with free play in the spring restoring force—free play constant, driving force variable.

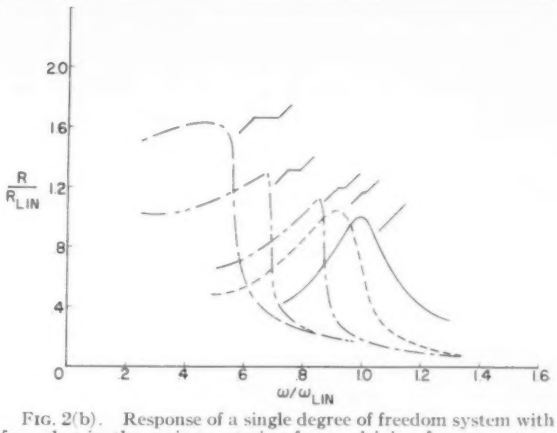

FIG. 2(b). Response of a single degree of freedom system with free play in the spring restoring force—driving force constant, free play variable.

survey is generally conducted by measuring amplitudes of the response of a structure to a sinusoidal forcing function over a wide range of frequencies. The results of such a vibration survey of a single degree of freedom system with free play are shown in Fig. 2. In obtaining these results a small amount of structural damping was included.

Results are shown in Fig. 2(a) in the form of an amplitude ratio R/R_{lin} of the response of the system with free play to the response of the linear system—that is, the same system with zero free play—against the frequency ratio ω/ω_{lin}, of the frequency of the driving force to the natural frequency of the linear system. The response curve for the linear system with damping present is shown by the dashed line. The solid curves show results obtained with a constant amount of free play but with successively smaller amplitudes of the driving force. For the curve with maximum response amplitude, the driving force was the same as that used with the linear system. To obtain the remaining curves, the driving force was successively reduced to 1/2, 1/4, and 1/8 of this value. With each reduction in driving force, the amplitude of the oscillation relative to the region of free play is reduced and the response peak occurs at a lower value of the frequency. In addition, for the lower driving forces, the response curve is flattened. Since the shape of the response curve is frequently used to measure structural damping, it is seen that the value obtained in this example would be highly dependent on the amount of driving force. Thus, both natural frequency and damping would be difficult to determine.

In Fig. 2(b) these results are presented in another form, representing the effect of a variation in free play with the amplitude of the driving force held constant. Results are shown for the linear case, for an amount of free play δ, and for successively greater amounts of free play of 2δ, 4δ, and 8δ. With each increase in the amount of free play in the system the effective spring constant is reduced and the amplitude of the response is increased. This indicates that in an actual aircraft, if the amount of free play increases with increasing flight time, the effective spring constant will be reduced. It is of interest to note in this connection that the response amplitude and effective spring constant for a given amount of free play and a given driving force can be approximately determined by consideration of the work performed per cycle and comparison with the work performed per cycle in an equivalent linear system. It will be shown, however, that the effects of free play on the flutter characteristics of a system will not necessarily be predicted by considering the equivalent linear system. The effects of free play on flutter are considered next for a two degree of freedom system.

Flutter of a Two Degree of Freedom System with Free Play—For this case both experimental wind-tunnel results and analog results, which were given in reference 1, will be compared again in order to establish the accuracy of the analog results. In Fig. 3 the configuration used in the wind-tunnel tests is shown.

The sketch represents a two-dimensional model which is free to oscillate in pitch and translation. The pitching degree of freedom is provided by a bearing-supported shaft. This system, in turn, is suspended between a pair of leaf springs on either side of the test section, so that the entire mechanism is free to translate.

In translation the system is linear. The nonlinearity is introduced in the torsional degree of freedom as shown in the detail sketch. A leaf spring is clamped to

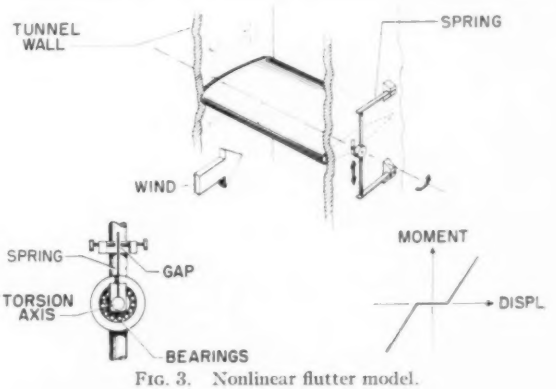

FIG. 3. Nonlinear flutter model.

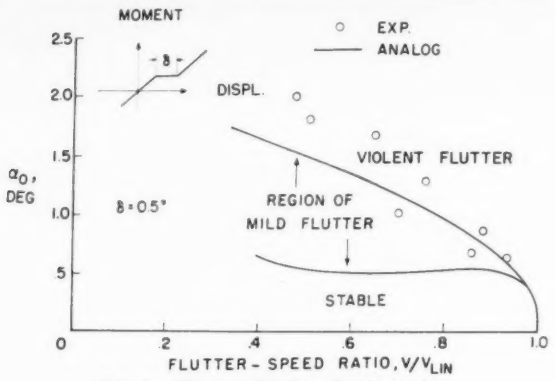

FIG. 4. Flutter with free play in torsion.

the end of the torsion axis and its free end extends upward between two setscrews. The gap between the screws can be closed completely to give a linear torsion spring, or opened to provide any desired amount of angular free play, giving the spring characteristic shown at the right of the Figure. Physical properties of the system are given in Table 1.

Flutter results obtained both in the wind tunnel and by analog calculations are given in Fig. 4. In this example a preload acted on the system so that at equilibrium the model was not centered in the flat spot, but rather at some point on the linear curve of the spring diagram.

Flutter results are shown on the lower part of the Figure. In obtaining these results, the system was given an initial torsional displacement α_0 and suddenly released. In the Figure α_0 is plotted as ordinate against a flutter speed ratio V/V_{lin}, where V_{lin} is the flutter speed of the system without free play. At each velocity the value of α_0 was increased until the model became unstable. Throughout the test the amount of free play δ was kept constant at 0.5.°

Analog results are shown by the solid curves, the circles show experimental points. It is seen that flutter occurred well below the flutter speed of the linear system and that three distinct regions were found—a stable region, a region of mild flutter, and a region of violent flutter.

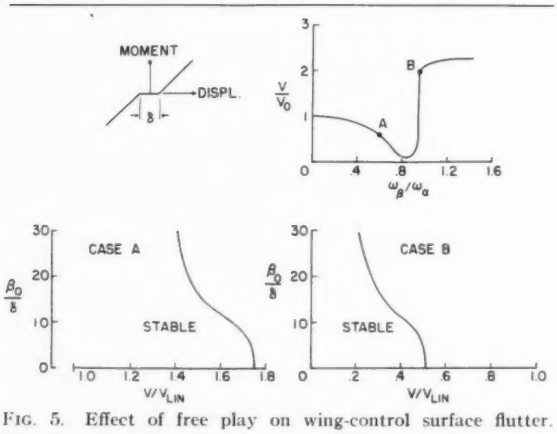

FIG. 5. Effect of free play on wing-control surface flutter.

TABLE 1

PROPERTIES OF SYSTEMS

Parameter	Two Degrees of Freedom		Three Degrees of Freedom
	Free play	Cubic spring	
a	−0.406	−0.54	−0.2
x_α	0.042	0.052	0
r_α^2	0.1603	0.24	0.5
ω_h, rad./sec.	58.94	94.25	81.7
ω_α, rad./sec.	81.24	125.66	136.0
ω_β, rad./sec.	...	...	variable
c	...	...	0.6
x_β	...	...	0
r_β^2	...	...	0.002
$1/\kappa$	156.405	79.724	12.0
b, ft.	0.5	0.5	2.375

Because of the presence of the preload, the system oscillated on the linear arm of the spring for small initial displacements and, at velocities below V_{lin}, was stable. For slightly larger displacements the oscillations entered the region of free play so that the effective torsional stiffness was reduced. In this example a decrease in torsional stiffness was destabilizing and a limited amplitude flutter occurred. (This limited amplitude flutter was found both experimentally and on the analog. Experimental points for this mild flutter are not shown.)

As initial displacements were increased still further the oscillations covered more and more of the region of free play. A further destabilizing reduction in stiffness occurred, and the flutter oscillations became violent. Both experimental and analog results for the violent flutter are shown.

The results indicate good agreement between experiment and the analog. They also show that, with preload acting on a system with free play, for small initial displacements the system will act as a linear system.

In the next example a three degree of freedom system (wing with control surface) will be treated. First, the effects of free play without preload will be considered.

Wing-Control Surface Flutter with Free Play; Zero Preload—Results for a wing-control surface with free play and zero preload are given in Fig. 5. At the upper right of the Figure flutter characteristics of the corresponding system without free play are shown. This linear case is one of those treated by Theodorsen and Garrick in reference 2. Properties of the system are included in Table 1.

Results for the linear system are shown in the form of a flutter speed ratio V/V_0 against the ratio $\omega_\beta/\omega_\alpha$, of control surface frequency to wing torsional frequency. In the ordinate V_0 is the flutter speed for control surface frequency $\omega_\beta = 0$. It is seen that, as the ratio $\omega_\beta/\omega_\alpha$ increases from zero to about 0.8, the flutter speed rapidly decreases. With further increases in the frequency ratio the flutter speed increases sharply.

To examine the effects of free play in the control surface, two cases were studied: in one, Case A, the frequency ratio $\omega_\beta/\omega_\alpha$ in the absence of free play was 0.6; in the other, Case B, $\omega_\beta/\omega_\alpha$ for zero free play was 0.95. It is noted in the linear system that, in Case A, the flutter speed for $\omega_\beta = 0$ is above that for $\omega_\beta/\omega_\alpha = 0.6$, while,

for Case B, the flutter speed for $\omega_\beta = 0$ is about half of the speed for $\omega_\beta/\omega_\alpha = 0.95$.

Flutter results for Cases A and B with free play are shown at the bottom of Fig. 5. Results are presented in the form of a ratio β_0/δ, of initial angular displacement of the control surface to the angular free play, against the flutter speed ratio V/V_{lin}. In the two sets of results the value of V_{lin} used is the linear flutter speed appropriate to the case being treated. The amount of free play δ was kept constant.

In the results for Case A, the effects of free play seem to be beneficial in that, for small displacements, flutter is first encountered well above the flutter speed of the corresponding linear system. When the initial displacements are increased, the flutter boundary shifts to lower values of the ratio V/V_{lin}. For Case B, the presence of free play is detrimental. For small values of β_0/δ flutter is encountered at about 1/2 of the flutter speed of the corresponding linear system. Again, the flutter boundary moves to lower speeds with increasing initial displacements.

Actually, results for the two cases are quite similar. In the absence of any preload the control surface is initially floating in the region of free play, and, for small displacements, the oscillations are confined within this region where the effective value of ω_β is zero. For both cases, therefore, flutter occurs first at the same velocity V_0, the flutter speed of the linear system at $\omega_\beta = 0$. It is recalled that this velocity is above V_{lin} for Case A and below V_{lin} for Case B.

As the initial displacements and the resulting flutter amplitudes are increased, the oscillations extend beyond the region of free play a proportionate amount, and the effective value of ω_β is increased. In the linear system an increase in ω_β means a reduction in flutter speed, so that in both Cases A and B the flutter boundary shifts to lower speeds. If sufficiently high initial displacements could be attained, the flutter boundaries in the two cases would become asymptotic to the respective linear flutter speeds.

Wing-Control Surface Flutter with Free Play; Preload Included—Results for Case A of the system just considered are given in Fig. 6, with a preload added to the control surface spring. For ease of reference, the curve showing variation of flutter speed with $\omega_\beta/\omega_\alpha$ for the linear system is included at the upper left. It is recalled that Case A corresponds to a value of $\omega_\beta/\omega_\alpha = 0.6$ in a system without free play.

Results for this case with fixed amounts of free play, δ, and preload are shown at the lower left of the Figure. Results are again given in the form of β_0/δ, the ratio of initial displacement to free play, against the flutter speed ratio V/V_{lin}.

With preload on the spring the system is stable only at velocities below the flutter speed of the corresponding linear system. For values of V/V_{lin} between 1.0 and 1.3 a region of limited amplitude flutter occurs. At higher values of V/V_{lin} the flutter is divergent. This is a result quite different from that found for Case A in Fig. 5, where no preload was considered and where the system was flutter-free at velocities well above V_{lin}.

When preload is applied the control surface oscillates about a point on the linear arm of the spring diagram. For small amplitude oscillations the system is linear and, therefore, flutters at $V = V_{lin}$. If, at the linear flutter speed, the flutter oscillation grows into the region of free play, the effective value of ω_β is reduced. This means that the flutter speed is raised, as shown by the flutter curve for the linear system. Without an increase in velocity, the flutter amplitude is therefore limited. Through the range of values of V/V_{lin} up to 1.3 the flutter amplitude increases and takes in more and more of the free play. The effective ω_β is therefore continually dropping and the flutter speed increasing so that the flutter amplitude remains limited. Finally, at values of V/V_{lin} greater than 1.3, the control surface oscillates completely through the free play and onto the upper linear arm of the spring diagram. The effective value of ω_β is immediately increased, the flutter speed is decreased, and the flutter oscillation becomes divergent.

It should be pointed out that, if Case B had been considered, divergent flutter would probably have been encountered immediately at the value of V_{lin} for Case B. This system lies on the side of the flutter valley for which any reduction in ω_β is accompanied by a sharp reduction in flutter speed.

It is interesting to note that, in performing flutter studies on the analog computer, the flutter amplitudes in each of the degrees of freedom can be continuously recorded. A plot of the variation with velocity of α/δ (the ratio of torsional displacement to the amount of free play) and β/δ (the ratio of control surface rotation to angular free play) in the region of limited amplitude flutter is shown at the lower right of the Figure. The value of β/δ at $V/V_{lin} = 1.3$ is that for which the control surface oscillates completely through the free play.

In the next examples to be considered, some effects of hysteresis are examined.

Effects of Hysteresis

If, in addition to the free play just discussed, some source of static friction exists in the system, the hys-

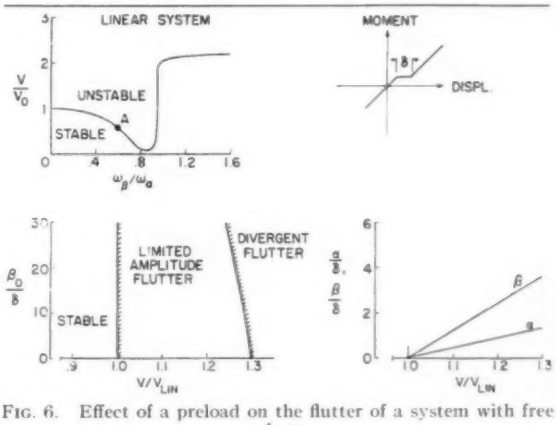

FIG. 6. Effect of a preload on the flutter of a system with free play.

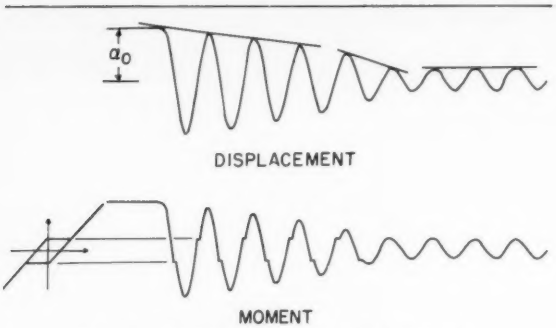

FIG. 7. Response of a system with hysteresis.

teresis type of nonlinearity described earlier is encountered. Before considering the flutter results, the response of a single degree of freedom system with hysteresis is examined, as was done in the case of free play.

Response of a System with Hysteresis—Fig. 7 represents the response of a system with hysteresis after release from an initial displacement at zero air speed. The upper trace shows the displacement of the system; the lower trace shows the corresponding variation in the moment. The indentations on the lower trace occur when the system passes through the flat spots of the hysteresis box.

In the upper trace the lines drawn tangent to the peaks indicate the rate of decay of the oscillation and show that the damping in the hysteresis system varies with amplitude. At high amplitudes the rate of decay is relatively small. As the amplitude decreases the damping is considerably greater. For very small amplitudes the system oscillates on a line through the center of the box with a linear spring constant. When the amplitude of the oscillation is less than the height of the box the structural damping is zero.

The second effect of the hysteresis on the structural properties of the system amounts to the free play effect of introducing an effectively weaker spring. At amplitudes of oscillation for which the system passes completely through the hysteresis box the frequency of oscillation is less than the frequency at low amplitudes where the system is linear.

Flutter Results with Hysteresis—The effects of this type of hysteresis on the flutter of a wing-control surface system are shown in Fig. 8. Again, the nonlinearity has been introduced in the control surface spring. The variation of flutter speed with frequency ratio for the same system without hysteresis is included for reference. The nonlinearity is again considered in a system corresponding to Case A ($\omega_\beta/\omega_\alpha = 0.6$).

In this example it was desirable to excite the system in the translation, or h, degree of freedom. The analog results are therefore presented in the form of a ratio, h_0/δ, of the initial displacement to the width of the hysteresis box, against the flutter speed ratio V/V_{lin}. (In this example, for $\delta = 1.0°$, a value of the ordinate $h_0/\delta = 10$ corresponds to an initial displacement in translation equal to approximately 1/15 of a chord length.)

Results are shown for two values of the ratio, H/δ, of height to width of the hysteresis box. In the two cases the height, H, is held constant. The Figure at the lower left applies to a relatively narrow hysteresis box for which $H/\delta = 2$. Flutter occurs first at the flutter speed of the corresponding linear system. For values of V/V_{lin} up to 1.7 and for fairly high initial displacements the flutter is of limited amplitude. For higher velocities and displacements the flutter is divergent.

No flutter occurs below $V/V_{lin} = 1.0$ since, for small displacements, the system oscillates on a linear path through the center of the box. For higher displacements, at speeds below V_{lin}, hysteresis damping effects enter, and the free play lowers the spring constant, combining to give a higher flutter speed. The interaction of these two effects is also responsible for the region of limited amplitude flutter. For high displacements and for values of V/V_{lin} above 1.7, the oscillation extends well beyond the hysteresis region. The damping is reduced and the effective value of ω_β increases so that the flutter speed is lowered and the flutter becomes divergent.

Results for a wider hysteresis box, $H/\delta = 1$, are shown at the lower right of the Figure. The results are similar to those just discussed, except that the limited amplitude flutter extends to much higher values of V/V_{lin}. This is probably due to the fact that the wider hysteresis loop introduces a greater amount of damping and that the increased amount of free play produces a lower effective value of ω_β.

Flutter Results with the Cubic Spring

The final type of nonlinearity to be considered is the cubic spring. In Fig. 9, analog results are given for a cubic spring in the torsional degree of freedom of a system free to translate and pitch. Physical properties of the system treated in this case are included in Table 1.

For this case, the relation between moment and displacement was assumed to be $M = 140.5\alpha \pm 400\alpha^3$, where M is the moment in foot-pounds and α the torsional displacement in radians. The coefficient of the linear term in α represents the spring constant in foot-pounds per radian of the linear system.

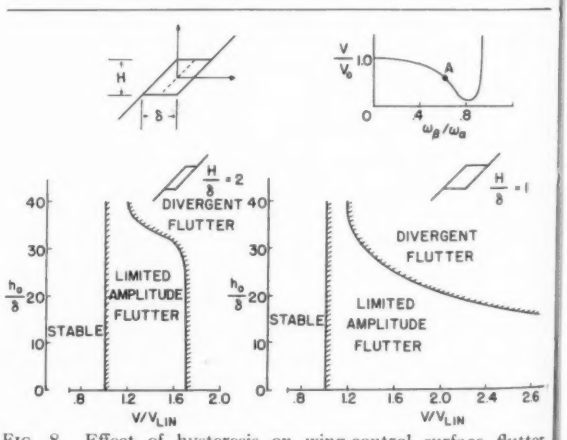

FIG. 8. Effect of hysteresis on wing-control surface flutter.

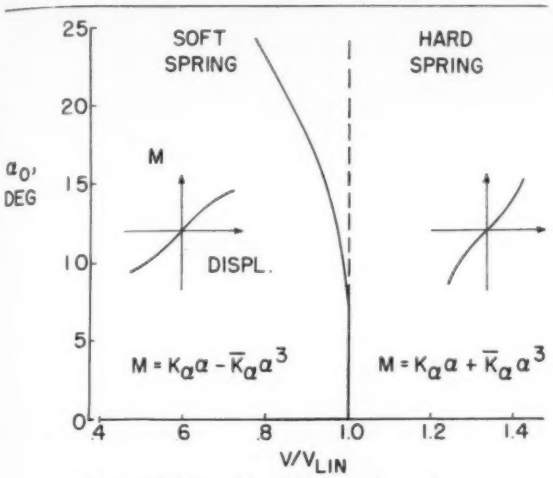

FIG. 9. Flutter with cubic spring in torsion.

Results for this case are presented in the form of the initial angular displacement α_0 (in degrees) against the velocity ratio V/V_{lin}. Both hard and soft cubic springs were considered. Flutter boundaries are shown by the solid curve for the soft spring and by the dashed line for the hard spring. In both cases the flutter region lies to the right of the boundary. In this example, a reduction in torsional stiffness in the linear system was destabilizing.

For the hard spring, the flutter boundary is a straight line at the flutter speed of the linear system. The soft spring in this case had a destabilizing effect, in that flutter could be induced below the flutter speed of the linear system by making the initial displacement sufficiently large. For the system treated here, however, the deviation from V_{lin} occurs only at fairly high initial displacements. A similar result was noted when a cubic spring was introduced in the control surface of the three degree of freedom system.

In concluding the discussion of the cubic spring it is also of interest to consider the flutter amplitudes associated with the results shown here. For the soft spring the flutter oscillation was highly divergent at any velocity above that of the flutter boundary. With the hard spring in the system, however, the flutter amplitude is self-limited. In general, it appears that the effects produced by a cubic spring depend on the effects of a variation in stiffness in the linear system.

CONCLUDING REMARKS

This paper is concerned with a study of some effects of simplified nonlinear structural terms on the classical flutter of two and three degree of freedom systems. The results were obtained by the use of an electronic differential analyzer type of analog computing machine, which is well suited to the study of problems of this type.

The form of the nonlinearities encountered on actual aircraft structures is in general not very well known and is an area worthy of further research. In the absence of more definite information, three relatively simple characteristic types of structural nonlinearities were chosen and studied—namely, free play, hysteresis, and a cubic spring.

As would be expected for nonlinear systems, the results are highly dependent on the amplitude of the initial disturbance. In many cases the flutter speed was lowered as the initial disturbance was increased. Some of the inconsistencies with regard to flutter speed which have appeared between airplanes of the same type may be due to differences in the excitations experienced by the different airplanes. In addition, variations in the extent of the nonlinearities in the different planes may be significant. Variations in the amount of free play, for example, have been shown to greatly change the effective stiffness.

The existence of a preload on the nonlinear system has been shown to have a very marked effect on the flutter speed. In actual practice, the amount of preload on a control surface would depend on the control surface deflection. Thus, the flutter speed could be a function of the amount of control surface deflection.

The importance of proper initial design and subsequent careful maintenance cannot be overemphasized. In one of the cases presented here, the flutter speed was reduced by a factor of two when free play was introduced into the system. However, the flutter was of a very mild nature and limited in amplitude. On the other hand, the existence of this mild limited-amplitude flutter could result in wear of certain parts, and a more severe flutter could be encountered later in the life of the airplane.

The results of this investigation show that nonlinear effects can influence the flutter speed significantly and suggest that structural nonlinearities may often be responsible for some of the inconsistencies which have occurred in the past, particularly with regard to control surface flutter.

REFERENCES

[1] Woolston, Donald S., Runyan, Harry L., and Byrdsong, Thomas A., *Some Effects of System Nonlinearities in the Problem of Aircraft Flutter*, NACA TN 3539, 1955.

[2] Theodorsen, Theodore, and Garrick, I. E., *Flutter Calculations in Three Degrees of Freedom*, NACA Report 741, 1942.

Readers' Forum

BRIEF REPORTS of investigations in the aeronautical sciences and discussions of papers published in the JOURNAL are presented in this special department. Entries must be restricted to a maximum of 1,300 words or the equivalent of one JOURNAL page including formulas and illustrations. Publication is completed as soon as possible after receipt of the material. The Editorial Committee does not hold itself responsible for the opinions expressed by the correspondents.

Contents

On the Evaluation of Two Functions Occurring in Maslen and Moore's Theory of Strong Transverse Waves in a Circular Cylinder ..... HENRY E. FETTIS 64

Supersonic Flow Past an Oscillating Cascade With Supersonic Leading-Edge Locus ..... FRANK LANE 65

The Warping of Triangular Wings for Minimum Drag at Supersonic Speeds ..... DORIS COHEN 67

Comments on "Analysis of a Rolling Pull-Out Maneuver" ..... W. J. G. PINSKER 68

Mathematical Analysis and Analog Simulation of Atmospheric Turbulence Gust Velocities ..... JULIUS S. BENDAT 69

Further Comments on "Supersonic Diffuser Instability" ..... CHARLES L. DAILEY 70

Erratum—"Note on the Unsteady Heat Regenerator" ..... R. E. MEYER AND T. A. D'EWS THOMSON 71

On a Third Mode of Longitudinal Control-Fixed Oscillation ..... BERNARD ETKIN 71

The Effect of an Arbitrary Distribution of Surface Temperatures on Heat Transfer in the Compressible Laminar Boundary Layer ..... CRAIG M. SCHMIDT AND ARNOLD J. HANAWALT 73

A Note on Missile Launching ..... TELFORD W. OSWALD 74

On Aeroelastic Solutions ..... WILLIAM J. GAUGH AND JOSEPH K. SLAP 76

Displacement Thickness of the Unsteady Boundary Layer ..... FRANKLIN K. MOORE AND SIMON OSTRACH 77

On Some Concepts of Nonlinear Oscillation Theory ..... K. KLOTTER 78

The Shear Flow Along a Flat Plate With Uniform Suction ..... TAKEO SAKURAI 79

Donnell's Equation for Thin Shells ..... HERBERT BECKER 79

On the Evaluation of Two Functions Occurring in Maslen and Moore's Theory of Strong Transverse Waves in a Circular Cylinder

Henry E. Fettis

Aeronautical Research Laboratory, Wright Air Development Center, ARDC, Wright-Patterson AFB, Ohio

July 23, 1956

IT IS THE PURPOSE of this note to derive simple expressions for the functions $f(\alpha)$ and $g(\alpha)$[1] defined by the equations

$$(d^2f/d\alpha^2) + (1/\alpha)\,(df/d\alpha) + 4[1 - (n^2/\alpha^2)]f = J_n^2(\alpha) \quad (1)$$

$$(d^2g/d\alpha^2) + (1/\alpha)\,(dg/d\alpha) + 4g = J_n^2(\alpha) \quad (2)$$

subject to the conditions

$$f = g = 0 \qquad \text{at } \alpha = 0$$

$$df/d\alpha = dg/d\alpha = 0 \qquad \text{at } \alpha = \beta$$

Particular integrals of these equations are

$$\bar{f}_n = \frac{1}{4\pi}\int_0^\pi \frac{J_{2n}(2\alpha\cos\theta) - J_{2n}(2\alpha)}{\sin^2\theta}\,d\theta \quad (3)$$

$$\bar{g}_n = \frac{(-)^n}{4\pi}\int_0^\pi \frac{J_0(2\alpha\cos\theta) - J_0(2\alpha)}{\sin^2\theta}\cos(2n\theta)\,d\theta \quad (4)$$

That Eqs. (3) and (4) are solutions of Eqs. (1) and (2) is readily verified by direct substitution after making use of the relation[2]

$$J_n^2(\alpha) = \frac{1}{\pi}\int_0^\pi J_{2n}(2\alpha\cos\theta)\,d\theta \quad (5)$$

in Eq. (1) and the relation

$$(-)^n J_n^2(\alpha) = \frac{1}{\pi}\int_0^\pi J_0(2\alpha\cos\theta)\cos(2n\theta)\,d\theta \quad (6)$$

in Eq. (2).

Eqs. (3) and (4) may also be derived directly by applying Lagrange's method of variation of parameters to Eqs. (1) and (2), inserting the integral representation [Eqs. (5) and (6)], and carrying out the integrations with the aid of Lommel's Formula:[3]

$$\int^x xJ_p(\alpha x)J_p(\beta x)\,dx = \left[\frac{x}{\alpha^2 - \beta^2}\right][\alpha J_p(\alpha x)J_{p-1}(\beta x) - \beta J_{p-1}(\alpha x)J_p(\beta x)] \quad (7)$$

Expressions for Eqs. (3) and (4) which are suitable for numerical calculation may be obtained as Neumann series,[4] starting with the expansion

$$J_{2n}(2\alpha\cos\theta) = J_n^2(\alpha) + 2\sum_{r=1}^{\infty} J_{n+r}(\alpha)J_{n-r}(\alpha)\cos(2r\theta) \quad (8)$$

which, when inserted in Eqs. (3) and (4), gives

$$\bar{f}_n = -\frac{1}{2\pi}\sum_{r=1}^{\infty} J_{n+r}(\alpha)\,J_{n-r}(\alpha)\int_0^\pi \frac{1 - \cos 2r\theta}{\sin^2\theta}\,d\theta \quad (9)$$

$$\bar{g}_n = -\frac{1}{2\pi}\sum_{r=1}^{\infty} J_r(\alpha)J_{-r}(\alpha)\int_0^{\pi}\frac{1-\cos 2r\theta}{\sin^2\theta}\cos 2n\theta\, d\theta \quad (10)$$

and, since (see Appendix)

$$\left.\begin{aligned}\int_0^{\pi}\frac{1-\cos 2r\theta}{\sin^2\theta}\cos 2n\theta\, d\theta &= 0 \qquad \text{if } r \le n\\ &= 2\pi(r-n) \qquad \text{if } r \ge n\end{aligned}\right\} \quad (11)$$

the final series become

$$\bar{f}_n = -\sum_{r=1}^{\infty} r\,J_{n+r}(\alpha)J_{n-r}(\alpha) \quad (12)$$

$$\bar{g}_n = -\sum_{r=1}^{\infty} r(-)^r\,J_{n+r}{}^2(\alpha) \quad (13)$$

These series are absolutely and uniformly convergent for all values of n and α,[5] and, because of the availability of extensive tables of Bessel functions, provide a very rapid means of obtaining numerical values.

Since the functions $\bar{f}$ and $\bar{g}$ satisfy $\bar{f}(0) = \bar{g}(0) = 0$, the complete solution is obtained as

$$f = AJ_{2n}(2\alpha) + \bar{f}_n$$
$$g = BJ_0(2\alpha) + \bar{g}_n$$

where A and B are determined from the conditions $f'(\beta) = g'(\beta) = 0$, and f and g are found by differentiating Eqs. (12) and (13).

Appendix

Evaluation of $\int_0^{\pi}\frac{1-\cos 2r\vartheta}{\sin^2\theta}\cos 2n\theta\, d\theta$.

$$\int_0^{\pi}\frac{1-\cos 2r\vartheta}{\sin^2\theta}\cos 2n\theta\, d\theta = \frac{1}{2}\int_0^{\pi}\frac{1-\cos 2r\theta}{1-\cos\theta}\cos 2n\theta + \frac{1}{2}\int_0^{\pi}\frac{1-\cos 2r\theta}{1+\cos\theta}\cos 2n\theta\, d\theta$$
$$= \int_0^{\pi}\frac{1-\cos 2r\theta}{1-\cos\theta}\cos 2n\theta\, d\theta$$

From the known relation (see reference 6, formula 860.1),

$$\int_0^{\pi}\frac{\cos m\theta}{1+a^2+2a\cos\theta}d\theta = \frac{\pi a^m}{1-a^2},$$
$$m \text{ an integer } \ge 0,\ |a| < 1$$

we find

$$\int_0^{\pi}\frac{1-\cos m\theta}{1-\cos\theta}\,d\theta = 2\lim_{a\to 1}\left[\pi\frac{(1-a^m)}{1-a^2}\right]$$
$$= m\pi, \qquad m \ge 0$$

Thus

$$\int_0^{\pi}\frac{1-\cos 2r\theta}{1-\cos\theta}\cos 2n\theta\, d\theta = \frac{1}{2}\int_0^{\pi}\frac{1-\cos 2(n+r)\theta}{1-\cos\theta}d\theta + \frac{1}{2}\int_0^{\pi}\frac{1-\cos 2(n-r)\theta}{1-\cos\theta}d\theta - \int_0^{\pi}\frac{1-\cos 2n\theta}{1-\cos\theta}d\theta$$
$$= \pi\left[(n+r) + |(n-r)| - 2n\right]$$

and therefore

$$\int_0^{\pi}\frac{1-\cos 2r\theta}{\sin^2\theta}\cos 2n\theta\, d\theta = \begin{cases}0 & \text{if } r \le n\\ 2\pi(r-n) & \text{if } r \ge n\end{cases}$$

References

[1] Maslen, Stephen H., and Moore, Franklin K., *On Strong Transverse Waves Without Shocks in a Circular Cylinder*, Journal of the Aeronautical Sciences, Vol. 23, No. 6, pp. 583–593, June, 1956.

[2] Watson, G. N., *Bessel Functions*, Art. 2-6; The Macmillan Co., New York, 1952.

[3] *Ibid.*, Art. 5-11.

[4] *Ibid.*, Chapter 16.

[5] *Ibid.*, Art. 16-2.

[6] Dwight, H. B., *Tables of Integrals and Other Mathematical Data*, The Macmillan Co., New York, 1947.

Supersonic Flow Past an Oscillating Cascade with Supersonic Leading-Edge Locus

Frank Lane

Research Associate Professor of Aeronautical Engineering, Daniel Guggenheim School of Aeronautics, New York University, New York

August 3, 1956

The Laplace transform method utilized by John Miles[1] in treating the wind-tunnel wall interference problem for the oscillating wing in supersonic flow may, by a slight extension, be employed in the study of oscillatory supersonic air forces on two-dimensional cascades having nonzero stagger and arbitrary interblade phase-lag angle, provided the locus of blade leading edges is not swept behind the Mach lines. The condition of subsonic leading-edge locus (leading-edge locus swept behind the Mach lines), with its attendant nonvanishing disturbance existing infinitely far upstream of every blade, would require Fourier rather than Laplace transform and subsequent formulation of the problem as an integral equation in much the same fashion as utilized by Miles in the subsonic wind-tunnel interference case. The apparently restrictive assumption of identical blade modes and amplitudes but with equal phase lag between adjacent blades has been shown by Lane[2] to be completely general with respect to the flutter problem, the ultimate determination of the critical interblade phase-lag angle constituting one part of the solution of the blade-row critical flutter condition.

The cascade geometry is as shown in Fig. 1. Symbols are the same as those used by Miles, lengths being scaled with respect to blade chord c, and the additional variable $2x_1$ represents dimensionless stagger distance while σ represents interblade phase angle, each blade leading the blade below it by σ. The dimensionless length $2y_1$ now represents blade (normal) gap distance rather than tunnel height.

The boundary-value problem is formulated for the strip domain shown shaded in Fig. 1. Under the system-mode shape characterized by the phase angle σ, conditions at $y = 2y_1{}^+$ are identical to $e^{i\sigma}$ times those at $y = 0^+$ at a point shifted a distance $2x_1$ to the left. This connection provides sufficient data for a complete formulation and solution of the problem. The restriction to supersonic leading-edge locus ensures the vanishing of all disturbances upstream of all blade leading edges and hence for $x < 0$ in the shaded strip of Fig. 1. This permits use of Laplace transform and leads to Miles' equation [Eq. (3.2)] in the transform $\bar{\varphi}(s, y)$ of the dimensionless disturbance potential, $\varphi(x, y)$.

$$\bar{\varphi}_{yy} - \lambda^2\bar{\varphi} = 0 \quad (1)$$

where $\lambda^2 = B^2[(s + i\kappa M)^2 + \kappa^2]$

In accordance with Miles, the dimensionless downwash is given by $\alpha(x)e^{i\omega t}$, $\bar{\alpha}(s)$ being the transform of $\bar{\alpha}(x)$. The boundary

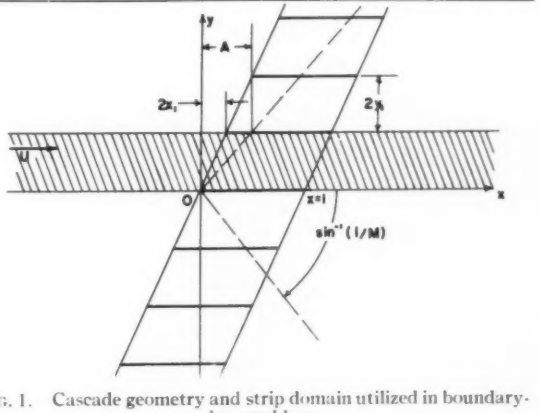

Fig. 1. Cascade geometry and strip domain utilized in boundary-value problem.

conditions are

$$\left.\begin{aligned} -\varphi_y\ (x,\ 0) &= \alpha(x) \\ -\varphi_y\ (x,\ 2y_1) &= e^{i\sigma}\alpha\ (x - 2x_1) \end{aligned}\right\} \tag{2}$$

In terms of $\bar{\varphi}(s, y)$, the conditions of Eqs. (2) become

$$\left.\begin{aligned} -\bar{\varphi}_y(s,\ 0) &= \bar{\alpha}(s) \\ -\bar{\varphi}_y(s,\ 2y_1) &= e^{(i\sigma - 2x_1 s)}\bar{\alpha}\ (s) \end{aligned}\right\} \tag{3}$$

The solution of Eq. (1) subject to the boundary conditions of Eqs. (3) is

$$\bar{\varphi}(s,\ y) = -\frac{\bar{\alpha}(s)}{\lambda}\,\frac{e^{(i\sigma - 2x_1 s)}\cosh \lambda y - \cosh \lambda(y - 2y_1)}{\sinh 2\lambda y_1} \tag{4}$$

This reduces to Miles' result for the case of wall interference upon letting $\sigma = \pi, x_1 = 0$. By convolution,

$$\varphi(x,\ y) = \int_0^x \alpha(\zeta) g(x - \zeta,\ y)\ d\zeta$$

where

$$g(x,\ y) = L^{-1}\left\{\lambda^{-1}\left[\frac{\cosh \lambda(y - 2y_1) - e^{(i\sigma - 2x_1 s)}\cosh \lambda y}{\sinh 2\lambda y_1}\right]\right\} \tag{5}$$

Using the exponential expansion of csch $2\lambda y_1$ and, for simplicity, letting

$$e^{(i\sigma - 2x_1 s)} = e^{[i\sigma - 2x_1\,(s + i\kappa M)]}\ e^{2ix_1\kappa M} \tag{6}$$

and utilizing the fact that

$$L^{-1}\ [e^{-2x_1 s}\bar{f}(s)] = f(x - 2x_1)1\ (x - 2x_1) \tag{7}$$

there results, letting $\epsilon_n = 1 \quad n = 0$

$$= 2 \quad n > 0$$

$$g\ (x,\ 0^+) = B^{-1}\ e^{-i\kappa Mx}\left\{\sum_{n=0}^{\infty}\epsilon_n\ J_0\left\{\kappa\sqrt{x^2 - B^2(4ny_1)^2}\right\}1\ (x - B\ 4ny_1) - 2e^{i(\sigma + 2x_1\kappa M)}\ \times\right.$$

$$\left.\sum_{n=0}^{\infty} J_0\left\{\kappa\sqrt{(x - 2x_1)^2 - B^2(2y_1 + 4ny_1)^2}\right\}\ 1[x - 2x_1 - B(2y_1 + 4ny_1)]\right\} \tag{8}$$

$$g\ (x,\ 2y_1^-) = B^{-1}e^{-i\kappa Mx}\left\{2\sum_{n=0}^{\infty} J_0\left\{\kappa\sqrt{x^2 - B^2(2y_1 + 4ny_1)^2}\right\}\ 1\ [x - B(2y_1 + 4ny_1)] -\right.$$

$$\left. e^{i(\sigma + 2x_1\kappa M)}\sum_{n=0}^{\infty}\epsilon_n J_0\left\{\kappa\sqrt{(x - 2x_1)^2 - B^2(4ny_1)^2}\right\}\ 1\ (x - 2x_1 - B\ 4ny_1)\right\} \tag{9}$$

These expressions, substituted into Eq. (5), give the dimensionless disturbance potential amplitude $\varphi(x, y)$ at $y = 0^+$ and $y = 2y_1^-$. This then provides sufficient data to compute oscillatory pressure-jump amplitude.

As a consequence of the interblade phase-lag condition, the pressure jump across the lower blade of the shaded strip of Fig. 1 is given

$$\left.\begin{aligned} p(x,\ 0^-,\ t) - p(x,\ 0^+,\ t) &= e^{i\omega t}\left\{e^{-i\sigma}\ p(x + 2x_1,\ 2y_1^-) - p\ (x,\ 0^+)\right\} \\ &= 2\rho_0 U^2\gamma(x)e^{i\omega t} \end{aligned}\right\} \tag{10}$$

the latter relation serving to define $\gamma(x)$ in accordance with Miles' notation. The linearized expression for pressure then gives

$$\gamma(x) = -(1/2)\ [(\partial/\partial x) + ik]\ \left\{e^{-i\sigma}\varphi(x + 2x_1,\ 2y_1^-) - \varphi(x,\ 0^+)\right\} \tag{11}$$

where it should be noted that the k utilized is that of reference 1, based on chord, and is twice the usual k based on semichord. Thus there results

$$\gamma(x) = \frac{-B^{-1}}{2}\left(\frac{\partial}{\partial x} + ik\right)\left\{e^{-i\sigma}\int_0^{x + 2x_1}\alpha(\zeta)e^{-i\kappa M(x + 2x_1 - \zeta)}\left[2\sum_{n=0}^{\infty} J_0\left\{\kappa\sqrt{(x + 2x_1 - \zeta)^2 - (2By_1)^2\ (1 + 2n)^2}\right\}\ \times\right.\right.$$

$$1[x + 2x_1 - \zeta - 2By_1\ (1 + 2n)] - e^{i(\sigma + 2x_1\kappa M)}\sum_{n=0}^{\infty}\epsilon_n J_0\left\{\kappa\sqrt{(x - \zeta)^2 - (4Bny_1)^2}\right\}\ 1(x - \zeta - 4Bny_1)\Big]\,d\zeta -$$

$$\int_0^x \alpha(\zeta)e^{-i\kappa M\ (x - \zeta)}\left[\sum_{n=0}^{\infty}\epsilon_n J_0\left\{\kappa\sqrt{(x - \zeta)^2 - (4Bny_1)^2}\right\}\ 1(x - \zeta - 4Bny_1) -\right.$$

$$\left.\left. 2e^{i(\sigma + 2\kappa x_1 M)}\sum_{n=0}^{\infty} J_0\left\{\kappa\sqrt{(x - \zeta - 2x_1)^2 - (2By_1)^2\ (1 + 2n)^2}\right\}\ 1[x - \zeta - 2x_1 - 2By_1(1 + 2n)]\right]d\zeta\right\} \tag{12}$$

The presence of the unit step functions and the supersonic leading-edge locus condition serve to cut off all contributions to the first integral for values of ζ greater than x, thereby permitting replacement of the upper limit $(x + 2x_1)$ by x. Under this replacement, the two series involving the ϵ_n become identical, and Eq. (12) may be simplified to the form

$$\gamma(x) = -B^{-1}\left(\frac{\partial}{\partial x} + ik\right)\left\{\int_0^x \alpha(\zeta)e^{-i\kappa M(x - \zeta)}\left[e^{-i\Omega}\sum_{n=0}^{\infty} J_0\left\{\kappa\sqrt{(x + 2x_1 - \zeta)^2 - (1 + 2n)^2A^2}\right\}\ 1[x + 2x_1 - \zeta -\right.\right.$$

$$(1 + 2n)A] + e^{i\Omega}\sum_{n=0}^{\infty} J_0\left\{\kappa\sqrt{(x - 2x_1 - \zeta)^2 - A^2(1 + 2n)^2}\right\}1\ [x - 2x_1 - \zeta - (1 + 2n)A] -$$

$$\left.\left.\sum_{n=0}^{\infty}\epsilon_n\ J_0\left\{\kappa\sqrt{(x - \zeta)^2 - 4n^2A^2}\right\}\ 1(x - \zeta - 2nA)\right]d\zeta\right\} \tag{13}$$

wherein Ω and A are defined, respectively, as

$$\Omega = \sigma + 2\kappa Mx_1 \qquad A = 2By_1$$

In performing the $\partial/\partial x$ operation, in the step involving differentiation of the integrand, derivatives of the unit step functions are to be considered as unit delta functions. The presence of the step function serves to cut off all series after a finite number of terms.

References

[1] Miles, John W., *The Compressible Flow Past an Oscillating Airfoil in a Wind Tunnel*, Journal of the Aeronautical Sciences, Vol. 23, No. 7, pp. 671–678, July, 1956.

[2] Lane, Frank, *System Mode Shapes in the Flutter of Compressor Blade Rows*, Journal of the Aeronautical Sciences, Vol. 23, No. 1, pp. 54–66, January, 1956.

The Warping of Triangular Wings for Minimum Drag at Supersonic Speeds

Doris Cohen
Aeronautical Research Scientist, Ames Aeronautical Laboratory, NACA, Moffett Field, Calif.
August 6, 1956

S. H. TSIEN[1] has investigated the minimum drag due to lift to be obtained with triangular wings of conical shape and loading. Lower drag may be obtained, however, if the restriction to conical form is removed. Using higher order homogeneous solutions[2, 3] already available,[4, 5, 6] the drag of laterally symmetrical triangular wings having camber and twist developable in the form of the double power series

$$\alpha(x, y) = \sum_r \sum_s A_{rs} x^r |y|^s \qquad \left.\begin{matrix} r \\ s \end{matrix}\right\} \geq 0 \qquad (1)$$

has been computed for $M = \sqrt{2}$, with the following results (Fig. 1):

Whereas—by optimizing a five-term series of a purely conical family—less than 1 per cent reduction in C_D/C_L^2 from the flat-plate value was achieved[1] for wings with $m = 0.5$ and 0.8, and 8.1 per cent when $m = 1$, gains of 8.2, 6.1, and 8.9 per cent, respectively, can be obtained at these same values of m by using approximately the same number of terms ($r + s \leq 2$) of the type given in Eq. (1). With additional terms ($r + s = 3$), the gain when $m = 1$ can be increased to 9.6 per cent. (The figures cited, from both reference 1 and the present work, include the full theoretical benefit of leading-edge suction.)

The shapes derived (Fig. 2) have generally negative camber when the wing lies entirely within the Mach cone from the apex, except for a reversal of the curvature in the vicinity of the rear third of the root section. As the leading edge approaches the Mach cone, the region of positive camber spreads spanwise and then forward so that, when $m = 1.2$, the indicated camber is for the most part positive. As in other investigations of the problem of drag reduction (e.g., reference 7), washout of the angle of attack toward the tips is consistently indicated, particularly for the wider wings.

It may be noted that the shape for $m = 0.3$ differs considerably near the leading edge from that of a low-drag wing of the same sweep derived by Tucker.[8] The reason for the difference is that the present calculations have as their basis a set of assumed shapes, each of which, like the flat plate, causes infinite velocities around the leading edge, resulting in a suction force acting in opposition to the drag. (On airfoils of finite thickness, an equal force results from the very high velocities around the nose acting on the small but finite frontal area of the section.) In Tucker's example, the *loading* is stipulated and in such a way as to preclude any such leading-edge singularities. A substitute for the leading-edge suction is therefore obtained by bending the surface downward into the stream.*

The low value of drag indicated by the present theoretical calculations can be approached in practice only if it is possible to maintain the type of unseparated flow assumed in the analysis The indicated decrease of angle of attack and pressure toward the tips is, of course, beneficial from the standpoint of preventing flow separation. Nevertheless, it seems that a certain amount of downward camber should be introduced in the immediate vicinity of the leading edge. A highly localized modification could be used to prevent flow separation while permitting the overall lift and drag to remain as calculated.

The shapes shown in Fig. 2 were all derived by combining six terms of Eq. (1)—that is,

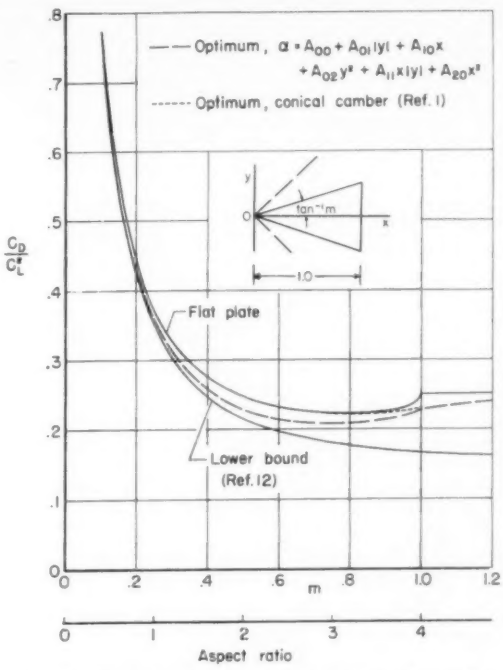
Optimum, $\alpha = A_{00} + A_{01}|y| + A_{10}x + A_{02}y^2 + A_{11}x|y| + A_{20}x^2$
Optimum, conical camber (Ref. 1)
Flat plate
Lower bound (Ref. 12)
C_D/C_L^2
m
Aspect ratio

FIG. 1. Drag due to lift, triangular wings, $M = \sqrt{2}$.

$$\alpha(x, y) = A_{00} + A_{01}|y| + A_{10}x + A_{02}y^2 + A_{11}x|y| + A_{20}x^2 \qquad (2)$$

As previously indicated, the gains obtained by increasing the number of terms to ten ($r + s \leq 3$) were not very great (of the order of 1 per cent), and, in the case of narrow wings, there was little change in shape.

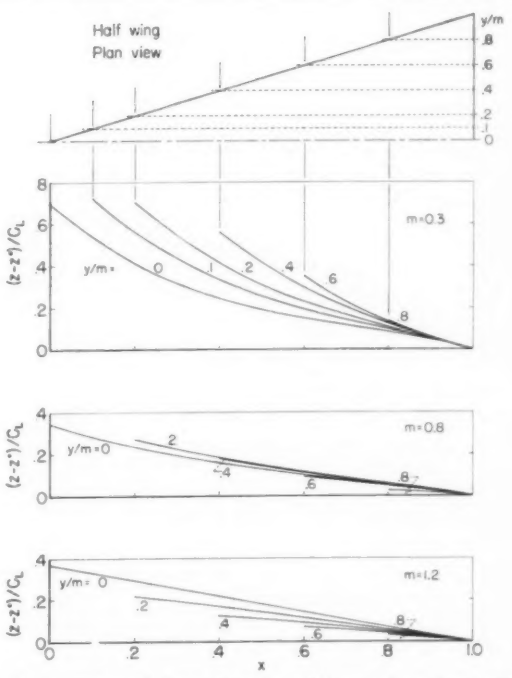

FIG. 2. Shape of the surface for minimum drag due to lift, $M = \sqrt{2}$. (z^* is the elevation of the trailing edge and may vary along the span.)

* It should be noted, however, that the value of the drag computed by Tucker in his example is lower than the minimum possible value later calculated by Grant[9] for all wings having loadings of the same form. Grant's values, in fact, are essentially those for the flat plate with leading-edge suction.

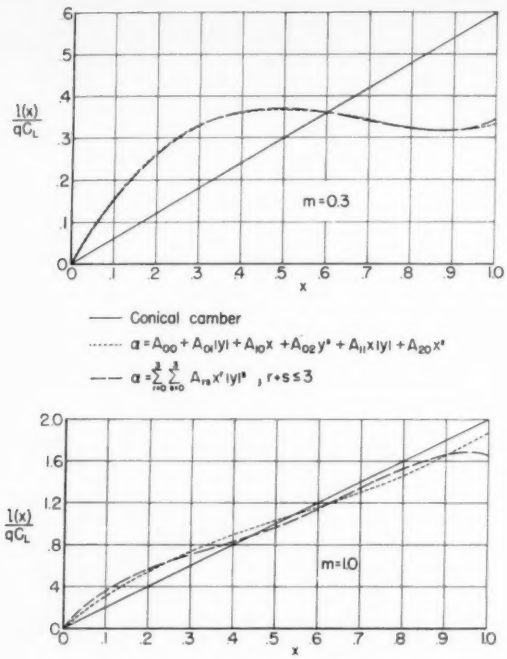

FIG. 3. Lengthwise loading for minimum drag.

The lengthwise loading

$$l(x) = 2\int_0^{mx} \Delta p(x, y)dy \qquad (3)$$

is plotted for two values of m in Fig. 3. Simple incidence in the case of a flat plate or any conical camber, as in Tsien's investigation, will result in a triangular lengthwise loading. The optimum loading appears to be fuller over the forward portion of the wing, falling off toward the rear on the narrower wing. Only on the narrow wing is any considerable tendency seen toward the elliptical lengthwise load which is optimum in the limiting case of an infinitely slender wing.[10] If the wing is of finite span, the drag depends on the load distribution as it appears in certain other projections as well.[11] The lower bound shown in Fig. 1 is derived[12] by assuming the impossible condition that all such projected loadings, as well as the span loading, are elliptical over the entire projected length of the wing. The condition is hardest to approach in the case of the wide delta wing, and the minimum drag is consequently farthest from approaching the lower bound at that end of the aspect ratio range. At the lower end, however, ($m < 0.5$, $A < 2$) the lower bound is very nearly attained in the present calculations, explaining the apparent stationary state of the $m = 0.3$ solution.

REFERENCES

[1] Tsien, S. H., *The Supersonic Conical Wing of Minimum Drag*, Journal of the Aeronautical Sciences, Vol. 22, No. 12, pp. 805–817, 843, December, 1955.

[2] Germain, P., *La Théorie des Mouvements Homogènes et son Application au Calcul de Certaines Ailes Delta en Régime Supersonique*, La Recherche Aéronautique, No. 7, pp. 3–16, January-February, 1949.

[3] Lomax, Harvard, and Heaslet, Max. A., *Generalized Conical-Flow Fields in Supersonic Wing Theory*, NACA TN 2497, 1951.

[4] Zienkiewicz, H. K., *A Note on Generalised Conical Fields with Applications to Lift of Twisted and Cambered Delta Wings with Subsonic Leading Edges*, English Electric Co. Ltd., Luton; Navigational Project Division, Report No. I.A.t.050, August 26, 1953.

[5] Lance, G. N., *The Lift of Twisted and Cambered Wings in Supersonic Flow*, Aero. Quart., Vol. VI, Part 2, pp. 149–163, May, 1955.

[6] Lance, G. N., *Tables of Pressure Fields Over Swept Wings with Supersonic Leading Edges for Use in Aero-Elastic Theory*, Hawker Aircraft Ltd., Design Dept. Report No. 1189, December, 1953.

[7] Beane, Beverly, *Examples of Drag Reduction for Delta Wings*, Douglas Aircraft Co., Inc., Report SM-14447, January 12, 1953.

[8] Tucker, Warren A., *A Method for the Design of Sweptback Wings Warped to Produce Specified Flight Characteristics at Supersonic Speeds*, NACA RM L51F08, 1951.

[9] Grant, Frederick C., *The Proper Combination of Lift Loadings for Least Drag on a Supersonic Wing*, NACA TN 3533, 1955.

[10] Jones, Robert T., *The Minimum Drag of Thin Wings in Frictionless Flow*, Journal of the Aeronautical Sciences, Vol. 18, No. 2, pp. 75–81, February, 1951.

[11] Jones, Robert T., *Theoretical Determination of the Minimum Drag of Airfoils at Supersonic Speeds*, Journal of the Aeronautical Sciences, Vol. 19, No. 12, pp. 813–822, December, 1952.

[12] Jones, Robert T., *Minimum Wave Drag for Arbitrary Arrangements of Wings and Bodies*, NACA TN 3530, 1956.

Comments on "Analysis of a Rolling Pull-Out Maneuver"[1]

W. J. G. Pinsker
Royal Aircraft Establishment, Bedford, England

August 6, 1956

THE COMPUTATION OF fin loads in rolling pull-out maneuvers suggested by W. J. Oakes and P. T. Holliday[1] is clearly a substantial improvement on the crude estimates derived so far. However, the method again makes an arbitrary assumption—that of constant angle of attack. This assumption offers no substantial simplification of the computation nor can it be justified from piloting considerations, and the results may be still fairly inaccurate.

In violent maneuvers, such as the rolling pull-out, pilots cannot be expected to discriminate more than the approximate position of the aircraft with reference to the horizon. Any success he may occasionally have in relieving normal or, for that matter, lateral loads by coordinated control movements can only be purely accidental. If, in fact, such action were feasible, the need for predicting such loads would be largely nonexistent. Mr. Oakes and Mr. Holliday argue now that, although constant elevator constitutes the more probable case, the incidence variations resulting from constant elevator have little influence on the magnitude of the final peak amplitude in vertical tail load—i.e., on sideslip. This is certainly not generally true as the stability of the lateral and longitudinal motion of a rolling aircraft is dramatically altered by the free interplay of inertial cross coupling between pitch and yaw. In fact, W. H. Phillips[2] has shown that either of these motions may become divergent at certain critical rolling velocities. Even before this condition is reached, the damping of one of the two oscillations is reduced, and the frequencies are substantially altered. Taking the typical case of an aircraft on which the period of the directional oscillation is longer than the period of the high-frequency pitching oscillation, the lateral oscillation in rolling will increase in period and lose damping, and the inverse will happen to the longitudinal oscillation. As a consequence, in a rolling pull out the first peak in sideslip will be delayed and the pitching response speeded up so that large changes in incidence occur before sideslip has developed a peak value and will, of course, then have had sufficient time to influence the lateral motion. Also the second peak in β may be considerably in excess of the first peak so that it cannot be considered safe to discontinue the computation until the aircraft has settled back to a steady-flight condition. In fact, the maximum load is very likely to occur after the cessation of the aileron application, as can be seen from two typical examples of fully simulated rolling maneuvers in Figs. 1 and 2.

To predict aircraft motions of such complex nature from any simplified computations requires very scrupulous justification. On the other hand, to represent the full pitching-moment equation and angle of attack as variable in the analysis would increase computational labor by not more than 20 per cent, and the gain would be an incomparable increase in reliability. As most designers will have electronic simulators available for this work, simplifications of the type proposed by Mr. Oakes and Mr. Holliday seem hardly worth considering.

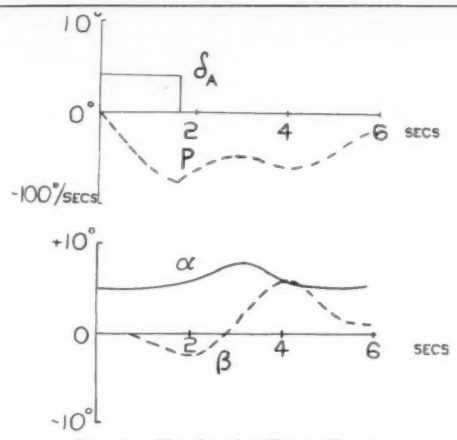

FIG. 1. Simulated rolling pull out.

On the other hand, for fast maneuvers, gravity has been found to have relatively little effect on the motion, and it is suggested that the gravity components may be omitted with very little loss in accuracy. This will facilitate electronic simulation in particular, where the representation of the trigonometric functions would be exceedingly difficult.

Using principal inertia axes instead of stability axes and dropping minor aerodynamic terms, an adequate solution may be obtained by solving the equations

$$\dot{\alpha} = Q - P\beta + (q_d S/mU_0)C_{z\alpha}\alpha$$

$$\dot{\beta} = -R + P\alpha + (q_d S/mU_0)C_{y\beta}\beta$$

$$\dot{Q} = PR[(I_z - I_x)/I_y] + (q_d Sl/I_y) \times [C_{m\alpha}\alpha + C_{mq}(Ql/U_0) + C_{m\dot{\alpha}}(\dot{\alpha}l/U_0)]$$

$$\dot{R} = PQ[(I_x - I_y)/I_z] + (q_d Sb/I_z)[C_{n\beta}\beta + C_{np} \times (Pb/2U_0) + C_{nr}(Rb/2U_0) + C_{n\delta_A}\delta_A]$$

$$\dot{P} = (q_d Sb/I_x)[C_{l_p}(Pb/2U_0) + C_{l\beta}\beta + C_{l\delta_A}\delta_A]$$

using the initial conditions that, at $t = 0$,

$$P = \dot{P} = \beta = \dot{\beta} = \dot{Q} = \dot{R} = \dot{\alpha} = 0$$

$\alpha = \alpha_0 =$ initial incidence of the principal inertia axis

$R = R_0 = (g/U_0) \sin \phi_0$

$Q = Q_0 = (g/U_0)(n - \cos \phi_0)$

$\phi_0 = \cos^{-1}(1/n)$

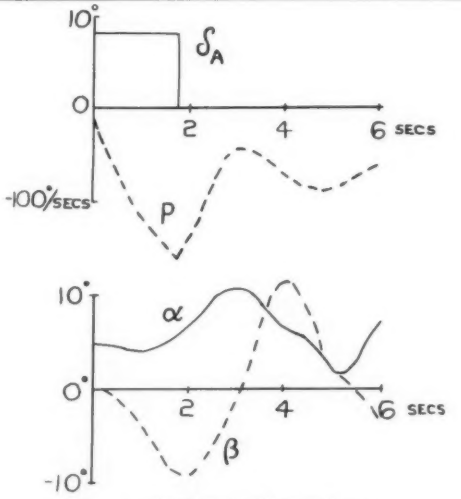

FIG. 2. Simulated rolling pull out.

REFERENCES

[1] Oakes, W. J., and Holliday, P. T., *Analysis of a Rolling Pull-Out Maneuver*, Journal of the Aeronautical Sciences, Vol. 23, No. 6, pp. 517–529, June, 1956.

[2] Phillips, W. H., *Effect of Steady Rolling on Longitudinal and Directional Stability*, NACA TN 1627, June, 1948.

Mathematical Analysis and Analog Simulation of Atmospheric Turbulence Gust Velocities

Julius S. Bendat

Control Systems Division, The Ramo-Wooldridge Corporation, Los Angeles

August 9, 1956

INTRODUCTION

AVAILABLE MEASUREMENTS of atmospheric turbulence gust velocities by Clementson,[1] Douglas Aircraft Company, Inc., personnel,[2] NACA personnel,[3] Summers,[4] and Chilton[5] indicate that, over a considerable range of frequencies, the power spectral density function $G(\omega)$ may be represented by a c/ω^2 type of curve. For lower frequencies, $G(\omega)$ is more complicated, approaching a constant value as ω approaches zero.[6]

ANALYSIS

A power spectral density function which is able to explain much of the observed results in a continuous way is given by one whose related autocorrelation function $R(\tau)$ has a simple damped exponential-cosine form,

$$R(\tau) = Ae^{-k|\tau|} \cos c\tau \qquad A \geq 0, \quad k > 0, \quad c \geq 0 \qquad (1)$$

where A has units of power—e.g., (ft./sec.)^2, c has units of rad./sec., and k has units of sec.$^{-1}$ (see Fig. 1).

The corresponding power spectral density function is

$$\left.\begin{aligned} G(\omega) &= \frac{2}{\pi}\int_0^\infty R(\tau) \cos \omega\tau \, d\tau \\ &= [2Ak/\pi]\,\{[\omega^2 + (k^2 + c^2)]/[\omega^4 + 2(k^2 - c^2)\omega^2 + (k^2 + c^2)^2]\} \end{aligned}\right\} \qquad (2)$$

Note that for small ω

$$G(\omega) \sim 2Ak/[\pi(k^2 + c^2)] = \text{constant} \qquad (3)$$

while for large ω

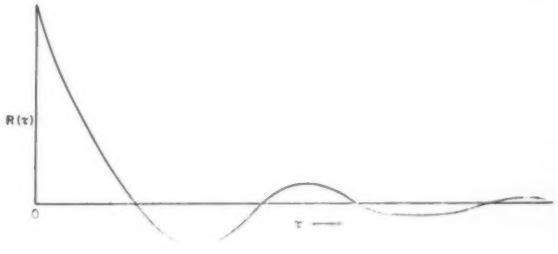

FIG. 1. Autocorrelation function.

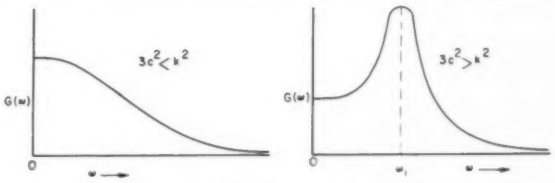

FIG. 2. Individual power spectra.

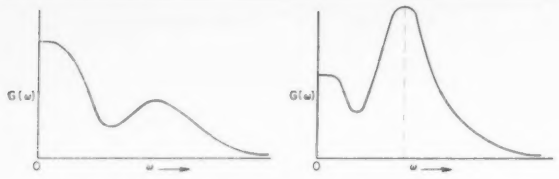

FIG. 3. Typical composite power spectra.

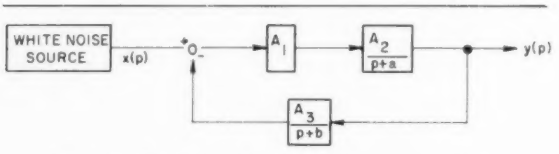

FIG. 4. Generator of gust velocity power spectra.

$$G(\omega) \sim c/\omega^2 \quad \text{where} \quad c = 2Ak/\pi \tag{4}$$

If $3c^2 < k^2$, no maximum of $G(\omega)$ occurs, and $G(\omega)$ decreases monotonically to zero as ω approaches infinity. If $3c^2 > k^2$, a single maximum occurs at

$$\omega_1 = [-(k^2 + c^2) + 2c(k^2 + c^2)^{1/2}]^{1/2} \tag{5}$$

with $G(\omega_1) > G(0)$ (see Fig. 2). The combination of two of these situations together, using different sets of parameters, will generate many composite curves (see Fig. 3). Power spectra curves, as pictured in Figs. 2 and 3, compare favorably with much observed data in references 1–6. Similar power spectra curves have been observed in radar fading and error records.[7]

Analog Simulation

A method for generating input turbulence gust velocity power spectra, of the continuous form discussed above, will now be developed. Consider white noise possessing a constant power spectral density function of N—i.e., $G_n(\omega) = N$. If this white noise is passed through a linear constant parameter system, with frequency response function $Y(j\omega)$, then the output power spectral density function is

$$G_0(\omega) = N\,|\,Y(j\omega)\,|^2 \tag{6}$$

where $|\,Y(j\omega)\,|^2$ = square of the absolute value of $Y(j\omega)$.

The desired power spectral density function has the form shown in Eq. (2). Equivalence between Eqs. (2) and (6) occurs if one constructs a system with transfer function, $Y(p) = Y(j\omega)$ where $p = j\omega$, given by

$$Y(p) = [2Ak/N\pi]^{1/2}\,\{[p + (k^2 + c^2)^{1/2}]/[p^2 + 2kp + (k^2 + c^2)]\} \tag{7}$$

$Y(p)$ and also $Y^{-1}(p)$ are physically realizable since no poles or zeros lie in the right half of the complex p-plane. A simple mechanization for $Y(p)$ is shown in the feedback circuit of Fig. 4 which has the transfer function

$$Y(p) = y(p)/x(p) = [A_1A_2(p + b)]/[p^2 + (a + b)p + (ab + A_1A_2A_3)] \tag{8}$$

With one parameter in the design arbitrary [since there are five adjustable parameters (A_1, A_2, A_3, a, b), while only four constants are specified in Eq. (9)—namely (A, k, c, N)], equivalence between Eqs. (7) and (8) results by setting

$$\left.\begin{aligned} A_1A_2 &= [2Ak/N\pi]^{1/2} & b &= (k^2 + c^2)^{1/2} \\ a + b &= 2k & ab + A_1A_2A_3 &= k^2 + c^2 \end{aligned}\right\} \tag{9}$$

In the special case where $c \ll k$, the desired transfer function [Eq. (7)] takes the approximate form

$$Y(p) = [2Ak/N\pi]^{1/2}[1/(p + k)] \tag{10}$$

Combinations of such circuits in parallel will generate composite power spectra like those shown in Fig. 3.

References

[1] Clementson, G. C., *An Investigation of the Power Spectral Density of Atmospheric Turbulence*, Report No. 6445-T-31, Instrumentation Laboratory, Massachusetts Institute of Technology, May, 1950.

[2] Connor, R. J., Hawk, J., and Levy, C., *Dynamic Analysis for the C-47 Airplane Gust Alleviation System*, Report No. SM-14456, Douglas Aircraft Company, Inc., July, 1952.

[3] Press, H., and Houbolt, J. C., *Some Applications of Generalized Harmonic Analysis to Gust Loads on Airplanes*, Journal of the Aeronautical Sciences, Vol. 22, No. 1, pp. 17–26, January, 1955.

[4] Summers, R. A., *A Statistical Description of Large-Scale Atmospheric Turbulence*, Report No. T-55, Instrumentation Laboratory, Massachusetts Institute of Technology, May, 1954.

[5] Chilton, R. G., *Some Measurements of Atmospheric Turbulence Obtained from Flow-Direction Vanes Mounted on an Airplane*, NACA TN 3313, November, 1954.

[6] Press, H., Meadows, M. T., and Hadlock, I., *Estimates of Probability Distribution of Root-Mean-Square Gust Velocity of Atmospheric Turbulence from Operational Gust-Load Data by Random-Process Theory*, NACA TN 3362, p. 17, March, 1955.

[7] James, H. M., Nichols, N. B., and Phillips, R. S., *Theory of Servomechanisms*, Radiation Laboratory Series, Vol. 25, Chap. 6, pp. 282, 296; McGraw-Hill Book Company, Inc., New York, 1947.

Further Comments on "Supersonic Diffuser Instability"

Charles L. Dailey

Engineering Center, University of Southern California, Los Angeles

August 13, 1956

R. L. TRIMPI[1] has taken exception to the writer's omission[2] of reference to NACA work on supersonic inlet instability performed by Trimpi, Ferri, Nucci, Sterbentz, Evvard, and Davids. Although this work was available in an unclassified form early in 1955, as Trimpi observes, it was, unfortunately, not available when the writer's article was submitted (October, 1954). Security regulations also precluded mention of several other papers on the subject by authors at many universities and aircraft and engine companies in this country and in England, including work done by the writer as early as 1947.

Since the NACA reports mentioned by Trimpi are now unclassified and readily available, the reader can explore the various opinions expressed therein as thoroughly as he wishes. The specific references to Trimpi's views on buzz and to points in reference 2 are sufficiently pointed to require some discussion

It is observed, first, that Trimpi's theoretical formulation of the problem is physically unconvincing. He represents a supersonic diffuser as a one-dimensional duct of variable cross-sectional area. This is a customary approximation, valid as long as the flow is stationary up to the inlet. However, when the subcritical shock is in front of the inlet, during the buzz cycle, the cone surface boundary layer of a conical spike diffuser interacts with the moving shock to produce a separation strong enough to by-pass the inlet entirely. At this moment, air, which has already entered the inlet, reverses and spills out around the cowl lip. As this continues and the high-pressure air stored in the plenum chamber empties out, a relatively high-frequency oscillation of the expelled shock is observed, due apparently to the by-passed air flowing obliquely over the sharp cowl lip. These points have been observed and described in detail in reference 2 and are regarded as part of the basic explanation of the buzz phenomenon. They clearly cannot be explained by use of a one-dimensional theory.

To avoid this difficulty in his calculation, Trimpi simply uses experimentally determined pressures for the part of the cycle in which the shock is expelled and the characteristic relations of constant area channel flow for the "fill-up" phase of the cycle. In this way, he uses the experimental "answer" to fill in the interval over which his theory is not valid and employs the theory of constant-area channel flow where it does apply to calculate a

fairly accurate variation of pressure with time as the plenum chamber fills up due to the excess mass inflow in the supercritical phase of the cycle.

It is important to distinguish two things here: (1) his use of the measured pressure-time history when the shock is expelled is artificial in terms of his one-dimensional theory; (2) his use of the one-dimensional theory to describe the pressure-time history after the artificial starting condition has been imposed in the fill-up phase of the relaxation cycle is sound. Trimpi's models had sufficiently long plenum chambers that the simple constant-area theory could be used. For more realistic cases, the tedious method of step-by-step construction would have to be employed.

It should be mentioned that the writer was aware of Trimpi's work at the time reference 2 was written, although reference to it could not be made at that time because of security regulations. In fact, the reference on page 748 of reference 2 to the use of the characteristic method for the fill-up phase was made with Trimpi's excellent result in mind. As mentioned there, it was not felt that the additional accuracy afforded by this method was necessary in establishing the essential relaxation aspect of the buzz cycle.

It is the writer's impression that Trimpi's work is an unusual mixture of good analytical judgment and inaccurate physical description. For example, the statements[1] concerning (1) the thought that a buzz cycle can be generated by the spontaneous "outward" motion of a shock in a one-dimensional channel and (2) that the subsequent wave patterns can result in reflected compressions which, by the simple mechanism of reflection, are somehow able to pump the plenum chamber back up to its initial pressure are not entirely convincing.

For the first point to be true, Trimpi's one-dimensional channel would have to have a pulsing area in the oncoming "free" stream which would permit it to adjust to the instantaneous mass flow required when it reached the inlet. In fact, the stream tube would have to pulse through negative values to permit outflow of air which enters the inlet just before the buzz cycle starts. It is not clear what laws of nature would have to be invoked to permit such a behavior. It is difficult to find a meaning for the second point mentioned above in view of Trimpi's apparent insistence that the pressure rise in the plenum chamber is not due to the excess supercritical mass inflow over the outflow corresponding to a subcritical exit throttle setting—i.e., a relaxation phenomenon. This same point appears again in the discussion of the exit throttle effect on frequency. He apparently does not recognize that the excess inflow during fill-up increases as the exit flow decreases with a decreasing throttle area.

One point which Trimpi misses completely is that buzz consists of a sequence of individual relaxation cycles. Although they occur at almost periodic intervals for average mass flows below the transition point, the individual nature of the cycles and the random time interval between cycles is clearly demonstrated for operation very near the transition point. This is mentioned on page 737 of reference 2 and is shown in Fig. 9 of that reference. It is obvious from this consideration alone that the theory of duct resonance employed by Trimpi is qualitatively incorrect. As mentioned above, the only validity it has is in prediction of the pressure-time history of the fill-up phase of the buzz cycle.

Trimpi objects to the writer's omission of upstream traveling compression waves in his consideration of the possibility that plenum-chamber separation might cause inlet instability. It was not intended that those qualitative considerations serve any purpose other than to show that plenum-chamber effects must be unimportant and that attention must be focused on the inlet region to find the cause of instability. It is interesting that Trimpi attaches such importance to this point immediately after mentioning an instability theory of his own concerning conditions in "the supersonic diffuser and immediate neighboring subsonic diffuser" and also mentions work of Ferri and Nucci concerning "the initial rate of subsonic diffusion," which seems to indicate that he also feels the inlet region is important with respect to stability.

Trimpi also objects to the writer's statement that instability is a result of choking of the inlet flow. Experimental work at the U.S.C. Engineering Center currently being conducted by A. C. Brown, recently of the Bristol Aeroplane Company, and the writer under a research contract supported by the Office of Scientific Research is shedding light on this aspect of the instability problem. This work is broader than that of reference 2 in that it includes the ramp and scoop type as well as the spike type. It is unclassified, and the results will be published soon.

References

[1] Trimpi, R. L., *Comments on "Supersonic Diffuser Instability,"* Journal of the Aeronautical Sciences, Readers' Forum, Vol. 23, No. 6, pp. 611, 612, June, 1956.

[2] Dailey, C. L., *Supersonic Diffuser Instability*, Journal of the Aeronautical Sciences, Vol. 22, No. 11, pp. 733–749, November, 1955.

Erratum—"Note on the Unsteady Heat Regenerator"*

R. E. Meyer and T. A. d'Ews Thomson
Department of Aeronautics, University of Sydney, Sydney, Australia
September 18, 1956

THE AUTHORS are indebted to H. Riedel for drawing their attention to an error in Eq. (2). The correct equation is

$$(hs\ \partial T/\partial t) + [c_p\ \partial(\rho T)/\partial t] + [c_p\ \partial(\rho u T)/\partial x] = 0$$

and leads to the result that there is no compressibility correction to the total mass of gas available at the outlet at constant temperature when the pressure is kept constant.

* Meyer, R. E., and d'Ews Thomson, T. A., Readers' Forum, Journal of the Aeronautical Sciences, Vol. 22, No. 5, p. 337, May, 1955.

On a Third Mode of Longitudinal Control-Fixed Oscillation

Bernard Etkin
Research Associate and Associate Professor of Aeronautical Engineering, Institute of Aerophysics, University of Toronto, Toronto, Canada
August 14, 1956

Symbols

T	=	period
t_{half}	=	time to damp to half amplitude
u	=	speed perturbation
α	=	angle of attack perturbation
θ	=	angle of pitch perturbation
C_{m_α}	=	static stability derivative, $\partial C_m/\partial\alpha$

Discussion

THE SHORT-PERIOD and phugoid modes of longitudinal oscillation of airplanes have been known for a long time. These are characteristic of aircraft over a wide range of configuration and flight variables. If the variations in u, θ, and α be depicted by rotating vectors, these modes appear typically as in Figs. 1 and 2. Fig. 1 shows the phugoid mode. The important characteristics are the phase difference of about 90° between u and θ and the nearly zero value of the α perturbation. The short-period mode, shown in Fig. 2, is characterized by the nearly zero value of the speed variation.

Some recent calculations have revealed what appears to be a new mode of oscillation, fundamentally different from the two classical ones. The appearance of this mode is best shown by a

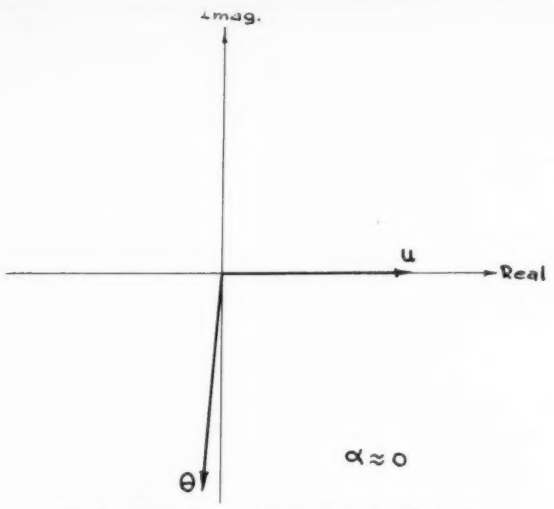

FIG. 1. Typical vector diagram of phugoid mode.

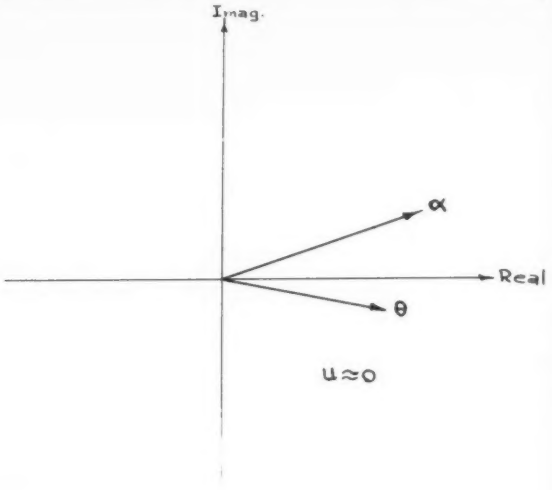

FIG. 2. Typical vector diagram of short-period mode.

plot of the loci of the roots of the stability quartic for varying c.g. position. Such a plot is illustrated (not to scale) in Fig. 3.

The calculations described were for a conventional configuration with typical values of the stability derivatives—gross weight $W = 100{,}000$ lbs., altitude = 30,000 ft., speed = 500 m.p.h.

For forward c.g. positions, the conjugate roots giving the short-period mode are at D,D^1, and those giving the phugoid are at E,E^1. As the c.g. moves aft, these roots approach the axis of reals at A and B. Point A corresponds to a c.g. position 1 per cent of the M.A.C. ahead of the stick-fixed neutral point, and point B corresponds to the c.g. almost on the neutral point. As the c.g. moves still farther aft, the complex roots disappear and are replaced by pairs of real roots as shown. Of the four real roots, three are negative, corresponding to subsidences, and one, on the branch BG, is positive, indicating a static instability.

One branch of the locus coming from A and a second branch coming from B meet at C. This is at a c.g. position between 2 and 3 per cent aft of the neutral point. From C there springs a new pair of complex branches, CF and CF^1, which define a third oscillatory mode, essentially different from the phugoid and short-period. Analysis of this mode with the c.g. 3 per cent aft of the neutral point has shown it to be of long period and heavily damped:

$$T = 76.5 \text{ sec.}$$
$$t_{half} = 0.65 \text{ sec.}$$

(For more aft c.g. positions, the damping decreases rapidly.) The vector diagram of Fig. 4 shows the relationships among the variables in this mode. It is seen to be entirely different from those of Figs. 1 and 2; in particular, all three degrees of freedom are significantly excited. No two degree of freedom approximation to this mode is possible.

In a sense, the mode is a "cross" between the phugoid and short-period. Its period is comparable to that of the phugoid, but the number of cycles to damp is characteristic of the short-period mode. The long period is responsible for the significant

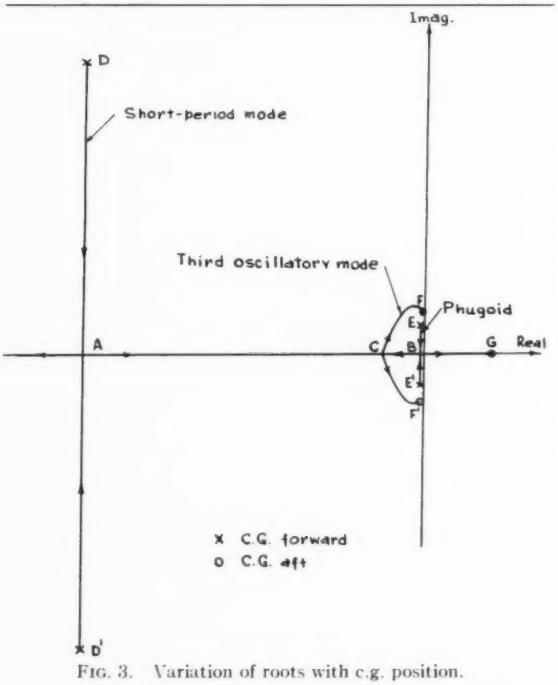

FIG. 3. Variation of roots with c.g. position.

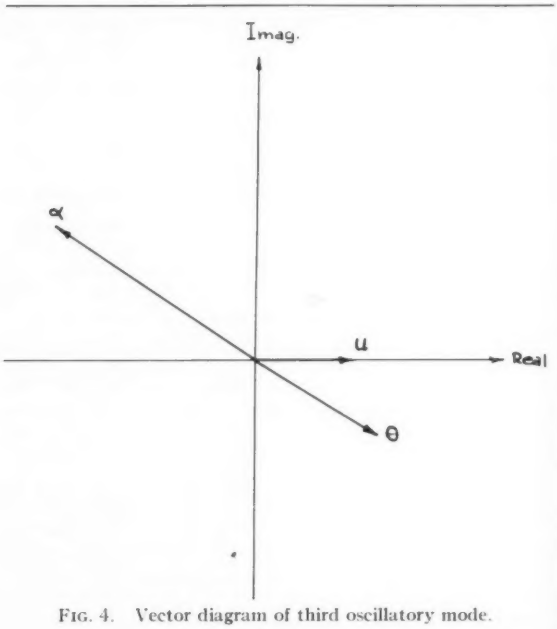

FIG. 4. Vector diagram of third oscillatory mode.

speed changes, and the positive $C_{m\alpha}$ which exists with the c.g. aft of the neutral point is the cause of the large variations in α.

One of the problems of airplane design is to determine the permissible aft limit of the c.g. The solution of this problem requires an understanding of the behavior of the airplane for unstable as well as for stable positions of the c.g. This is particularly so when the air-frame dynamics are neutrally stable, or even unstable, and acceptable flying qualities are provided by an automatic pilot. The investigation reported here throws additional light on the dynamic behavior when the c.g. is aft of the neutral point.

The Effect of an Arbitrary Distribution of Surface Temperatures on Heat Transfer in the Compressible Laminar Boundary Layer

Craig M. Schmidt and Arnold J. Hanawalt
Aerodynamics Engineers, Bell Aircraft Corporation, Buffalo, N.Y.
September 2, 1956

IT IS THE PURPOSE of this note to discuss the effect of a realistic wall-temperature distribution on the heat-transfer coefficient. The examples that have been chosen by Chapman and Rubesin[1] and by Lighthill[2] point out a very marked change in the heat-transfer coefficient. However, it is felt that these examples are not very realistic for many high-speed flight conditions. Generally, in supersonic or hypersonic flight, the leading-edge temperature is below the recovery or adiabatic wall temperature, and the wall-temperature profile is such that it is steep at the leading edge and becomes more flat as the trailing edge is approached.

The following consists of four examples that tend to point out the degree of accuracy attained by the constant wall-temperature theory. The first assumes a cubic wall-temperature variation and is analyzed by the theory of Chapman and Rubesin. Since this theory is limited to a power series expression for the wall temperature, the remaining three examples use the theory of Lighthill, modified to include compressibility effects. Equilibrium temperatures are calculated for two flight conditions while, for the last case, the wall temperature is assumed to vary as the square root of the distance. These examples tend to point out that, for many design purposes, it is not necessary to use the more complex variable wall-temperature theory.

For the first example, using the method of Chapman and Rubesin and their notation, let us consider the following, which is representative of the temperatures associated with high-speed, high-altitude flight.

$$T_\infty = 400°\text{R.} \qquad T_e = 6{,}000°\text{R.}$$

$$t(x^*) = T_w^* - T_e^* = T_e^*(-0.667 - 0.646x^* + 0.792\,x^{*2} - 0.3125\,x^{*3})$$

$$\bar{T}_w^* = 2.94 \qquad C = 0.758$$

The ratio of variable wall temperature q and h to their counterparts for a constant wall temperature are given in the following equations:

$$q/\bar{q} = h/\bar{h} = C_{w/C}\left\{\frac{1 - [T_w^*(0,0)/T_e^*]}{1 - (T_w^*/T_e^*)} - \frac{1}{Y'(0)} \times \frac{a_1 Y'(1)x^* + a_2 Y'(2)x^{*2} + a_3 Y'(3)X^{*3}}{1 - (T_w^*/T_e^*)}\right\}$$

The results of these computations are shown in Fig. 1. It can be seen that the variation of $h/\bar{h}$ is not particularly large, showing a decrease (from the constant wall-temperature theory) at the leading edge of 16 per cent and a maximum increase of about 12 per cent occurring at about $x^* = 0.6$.

Introducing a higher degree polynominal than in the previous example in order to obtain a steeper gradient at the leading edge followed by a relatively constant temperature shows the effect of

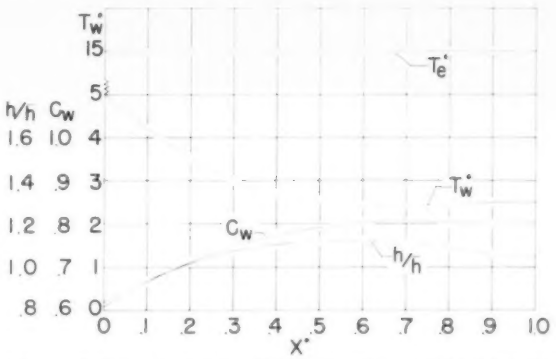

FIG. 1. Effect of variable wall temperature on the heat-transfer characteristics.

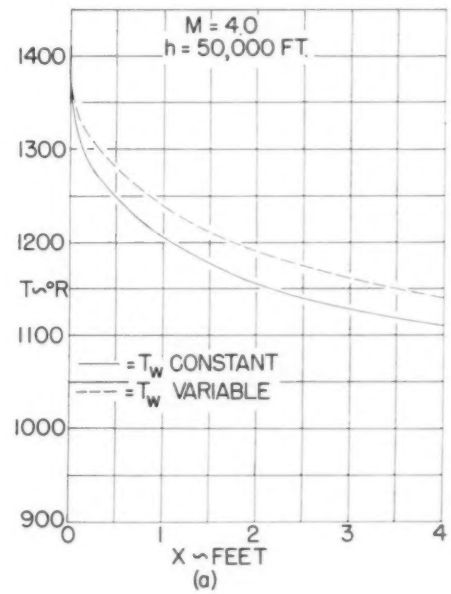

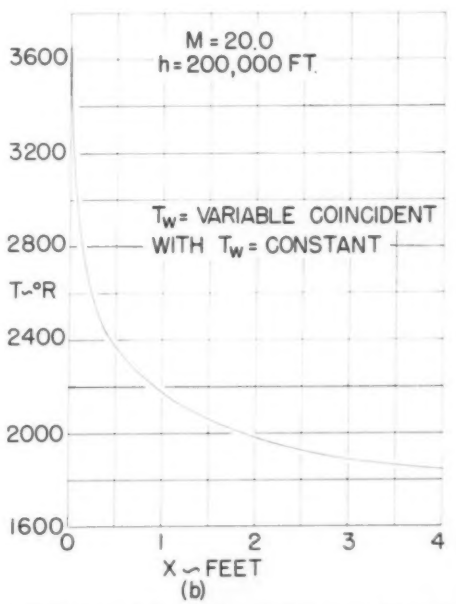

FIG. 2. Effect of variable wall temperature on radiation equilibrium temperatures.

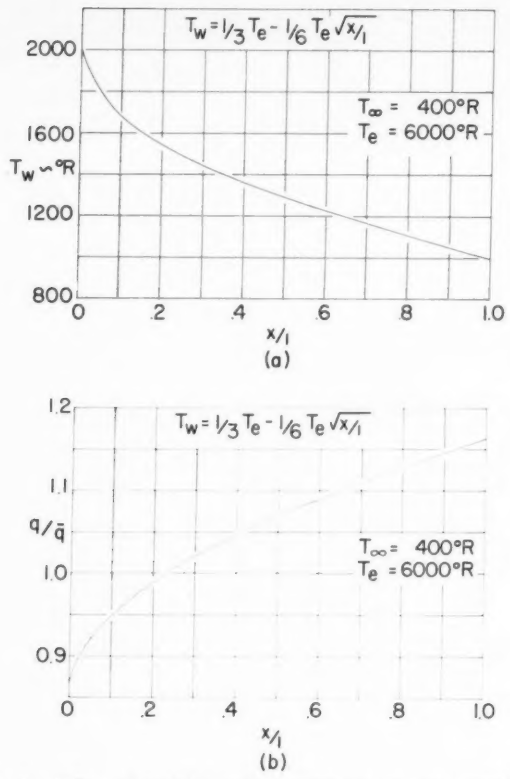

FIG. 3. Effect of variable wall temperature on heat-transfer characteristics for square-root variation of T_w.

the temperature gradient on the heat-transfer coefficient to be even smaller. This also is generally what has been found using Lighthill's method, and illustrations of this are listed below.

Lighthill[2] has shown the effect of variable wall temperature on equilibrium temperatures (i.e., convective heat in equals radiative heat out) to be very significant for the several examples chosen. However, the physical assumptions used in this comparison are inconsistent—namely, that the surface conductivity for the variable wall-temperature case was zero and for the constant wall-temperature case was infinite. If the conductivity is assumed to be zero for both cases, then the results are much different than what Lighthill has shown, as can be seen for the two examples shown in Fig. 2. These two examples show that the simpler constant wall-temperature theory is accurate to within 3 per cent for the calculation of equilibrium temperature.

Lighthill also states that his theory agrees to within 3 per cent with the more exact theory of Chapman and Rubesin. This is only true if his expression for heat transfer is altered by the multiplicative factor $C_w/\sqrt{C}$ (notation of reference 1) to account for the evaluation of the physical properties of the air. The addition of this factor, however, invalidates Lighthill's analytic solution for the equilibrium temperatures and necessitates the use of an iteration method of solution. However, since $C_w/\sqrt{C}$ is quite close to 1.0 and since it enters approximately to the 1/4 power for the equilibrium temperatures, the results shown in Fig. 2 are felt to be essentially correct.

As an additional example of the effect of variable wall temperature on heat transfer, the following case was examined:

$$T_w = (1/3)T_e - (1/6)T_e\sqrt{X^*},\ T_\infty = 400°\text{R.},\ T_e = 6{,}000°\text{R.}$$

This is felt to be somewhat representative of accelerating or quasi-steady-state flight at high speeds. The results are shown in Fig. 3. A maximum of 16 per cent increase over constant wall temperature theory is observed. As the leading-edge wall temperature approaches T_e, this increase becomes larger and may reach a value of 50 per cent for a square-root variation of T_w. However, $T_w = T_e$ at the leading edge is not felt to be very realistic except possibly for low supersonic speeds.

Examples given by Chapman and Rubesin and by Lighthill tend to overemphasize the importance of variable wall temperature on heat transfer while more realistic examples show the heat flux to be less dependent on the space history of the wall temperature. In a good many design cases, the use of the simple constant wall-temperature theory would introduce errors no greater than about 10 to 20 per cent. As far as equilibrium temperatures are concerned, the error would be much less than this. However, in some cases such as wind-tunnel tests where the temperature levels are much different than that experienced in free flight or in local areas of large temperature gradients (e.g., ends of fuel tanks), the variable wall temperature would be much more important.

REFERENCES

[1] Chapman, D. R., and Rubesin, M. W., *Temperature and Velocity Profiles in the Compressible Laminar Boundary Layer with Arbitrary Distribution of Surface Temperature*, Journal of the Aeronautical Sciences, Vol. 16, No. 9, pp. 547–565, September, 1949.

[2] Lighthill, M. J., *Contributions to the Theory of Heat Transfer Through a Laminar Boundary Layer*, Proc. Royal Society, Series A, Vol. 202, No. 1070, pp. 359–377, August, 1950.

A Note on Missile Launching

Telford W. Oswald
Engineering Staff Assistant, Hughes Aircraft Co., Culver City, Calif.

August 21, 1956

IN A RECENT PAPER,[1] a method of computing launching trajectories for the case of a missile whose natural frequency is proportional to velocity has been presented. In practice, such missiles are characterized by small changes in inertia and stability margin. The following analysis extends the method to account for large changes in inertia and stability margin such as occur with a solid-propellent-rocket-powered missile launched at subsonic speeds and accelerated to supersonic speeds. Such missiles experience simultaneously a forward shift of the center of gravity, an aft shift of center of pressure, together with large changes in the lift curve slope.

The outlined method provides an approximate solution which is readily obtained by quadrature. It affords a large time saving

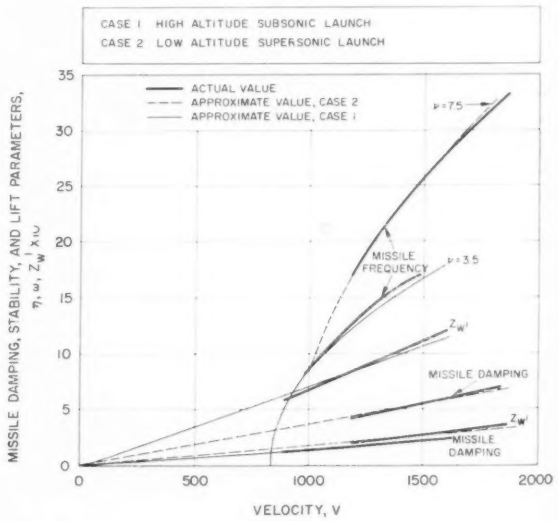

FIG. 1.

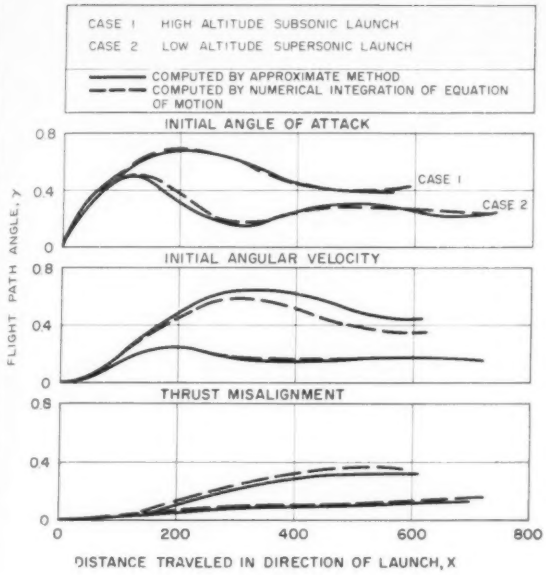

FIG. 2.

over the method of numerical integration of the differential equations of motion and avoids the troublesome question of convergence. It applies equally well to missiles which are unstable at launch, providing the stability increases with velocity. Typical examples are presented compared with "exact" numerical integrations. These indicate that the method provides a very good approximation.

The longitudinal equations of motion (short-period oscillation) are referred to a set of principal body axes. The longitudinal motion is assumed to be a uniform acceleration. The damping derivatives are assumed to be proportional to velocity, and the frequency in pitch is approximated by the expression

$$\omega_n^2 = \omega_{n_0}^2 U^2 - (A^2/U^2) \tag{1}$$

The validity of these latter two assumptions is shown in Fig. 1.

Under these conditions the equations of motion are combined into one second-order linear differential equation for the angle of attack. (See reference 1 for derivation.) With the distance along the flight path, x, as independent variable, the equation is written

$$\alpha'' + [(1/x) + 2\eta_0]\alpha' + \{\omega_{n_0}^2 + (\eta_0/x) - [(a^2 + A^2)/4a^2x^2]\}\alpha = F(U)/2ax \tag{2}$$

where

α = angle of attack $= w/U$
ω_n = $\sqrt{-UM_w' + Z_w'M_q'}$ = pitch frequency
$F(U)$ = forcing function

Letting $\alpha = y \exp(-\eta_0 x)$ and $\xi = \omega_0 x$, Eq. (2) becomes

$$\frac{d^2y}{d\xi^2} + \frac{1}{\xi}\frac{dy}{d\xi} + \left[1 - \frac{1 + (A^2/a^2)}{4\xi^2}\right] y = \frac{F[U(\xi)]}{2a\omega_0\xi} \exp\left(\frac{\eta_0}{\omega_0}\right)\xi \tag{3}$$

The homogeneous equation obtained from Eq. (3) is Bessel's equation of order ν where

$$\nu = (1/2)\sqrt{1 + (A^2/a^2)} \tag{4}$$

The complete solution to Eq. (3) in the case that ν is not an integer* is given by

$$y = C_1 J_\nu(\xi) + C_2 J_{-\nu}(\xi) + I(\xi) \tag{5}$$

where the particular solution, $I(\xi)$, may be obtained by the method of variation of parameters.

* If ν is an integer, $J_{-\nu}$ must be replaced by Y_ν (Bessel function of the second kind).

The solution for the angle of attack for the case of launching with a finite velocity U_1 is given by

$$\alpha(\xi) = \exp(-\zeta_0\xi)\,[C_1 J_\nu(\xi) + C_2 J_{-\nu}(\xi)] + I(\xi, \xi_1) \tag{6}$$

where $\xi_1 = \omega_0 U_1^2/2a$ is the value of ξ at the launch speed U_1, and C_1 and C_2 are constants to be evaluated from the initial conditions:

$$y(\xi_1) = \exp(\zeta_0\xi_1)\alpha_1 = C_1 J_\nu(\xi_1) + C_2 J_{-\nu}(\xi_1) \tag{7}$$

$$y'(\xi_1) = \exp(\zeta_0\xi_1)\left\{(q_1/\omega_1) - [(a/U_1) - Z_{w_1}'] \times (\alpha_1/\omega_1) + (Z_1'/\omega_1 U_1) + \xi_0\alpha_1\right\} = C_1 J'(\xi_1) + C_2 J_{-\nu}'(\xi_1) \tag{8}$$

and $I(\xi, \xi_1)$ is determined from the equation

$$I(\xi, \xi_1) = \exp(-\zeta_0\xi)\left[J_\nu(\xi)\int_{\xi_1}^{\xi} \frac{J_{-\nu}(\xi)\,\pi\xi}{2\sin\nu\pi} f(\xi)d\xi - J_{-\nu}(\xi)\int_{\xi_1}^{\xi} \frac{J(\xi)\,\pi\xi}{2\sin\nu\pi} f(\xi)d\xi\right] \tag{9}$$

where

$$f(\xi) = [\exp(\zeta_0\xi)/2a\omega_0\xi]\,\{(M_T/I_y) + [M(\delta)/I_y] - \{[Z(\delta)/m] + [(T\sin\epsilon)/m] + g\cos\Theta_1\}[M_{q_0} + (\omega_0/2\xi)]\} \tag{10}$$

Since it is assumed that $U = at = \sqrt{2a\,\xi/\omega_0}$ where a is constant, the forcing function, $f(\xi)$, can be determined as a function of

$$\xi = \omega_0 x = \omega_0 U^2/2a \tag{11}$$

In this form the equation provides for any integrable forcing function, and, by means of numerical integration, Eq. (9) can be evaluated. Combining this with Eq. (6), the angle of attack as a function of ξ is known. With the angle of attack determined, the flight-path tangent can be determined from the equation

$$\gamma = \int_{\xi_1}^{\xi}\left(\frac{\alpha(\xi)}{2\xi} - \frac{Z_{w_0}}{\omega_0}\alpha(\xi)\right)d\xi - Z(\delta)_0\frac{\xi - \xi_1}{\omega_0} \tag{12}$$

The trajectory can then be determined from the equations

$$h = \frac{1}{\omega_0}\int_{\xi_1}^{\xi} \sin\gamma\, d\xi \tag{13}$$

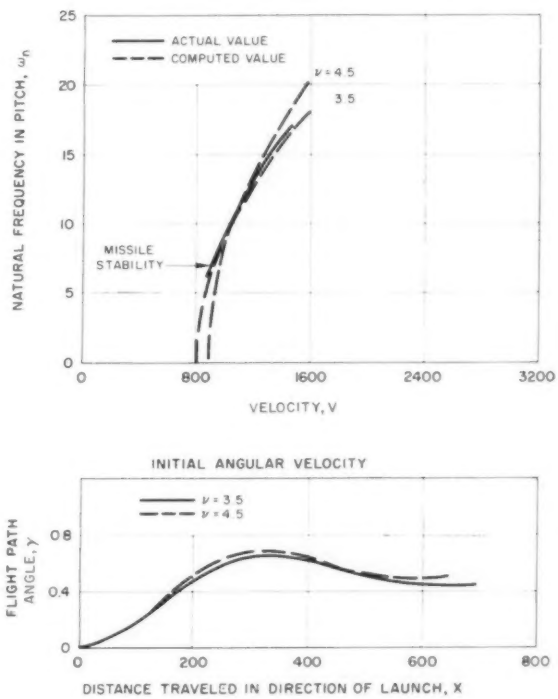

FIG. 3.

$$d = \frac{1}{\omega_0} \int_{\xi_1}^{\xi} \cos \gamma \, d\xi \tag{14}$$

In applying this method of calculation it is first necessary to determine ν from Eq. (4), after approximating the missile stability by Eq. (1). In doing this, it is suggested that the value of $\nu = n + (1/2)$, where n is an integer, be selected and the corresponding values of A computed from Eq. (4) and those of ω_{n_0} from Eq. (1). Use of this value is permissible since the Bessel functions are continuous functions of the order ν. It is desirable because the Bessel function of order $\pm n + (1/2)$ are tabulated in references 2 and 3.

Typical launch cases for a representative missile have been computed, and the accuracy of the basic approximations is shown in Fig. 1. The results are presented in Fig. 2 in the form of flight-path angle versus distance for a subsonic launch at high altitude (case 1) and a supersonic launch at low altitude (case 2). These results are compared with those obtained from a step-by-step integration of the differential equations of motion.

In order to indicate how sensitive the method is to the accuracy of the approximation, the solution for an initial angular velocity is computed using two different approximations to the stability velocity relation. These two approximations and the results are shown in Fig. 3.

References

[1] Oswald, T. W., *Dynamic Behavior During Accelerating Flight with Particular Application to Missile Launching*, Journal of the Aeronautical Sciences, Vol. 23, No. 8, pp. 781–791, August, 1956.

[2] Jahnke and Emde, *Tables of Functions*, Fourth Edition, Dover Publications, New York, 1945.

[3] *Tables of Spherical Bessel Functions*, Vol. I, Prepared by the Mathematical Tables Project of National Bureau of Standards; Columbia University Press, New York, 1947.

On Aeroelastic Solutions

William J. Gaugh* and Joseph K. Slap**
Northrop Aircraft, Inc., Hawthorne, Calif.
August 27, 1956

Reference 1 discusses a procedure for estimating aeroelastic effects on aircraft lateral stability and control. This paper is one of a number in the literature which, more or less rigorously, derive short-cut methods for aeroelasticity calculations. Certain remarks pertinent to such methods might be warranted at this time.

In these procedures, simplifying assumptions must, of course, be made. Among the more common are aerodynamic strip theory,[2] variation of stiffness parameters with fourth-power of the chord,[3] and known shape of the deflection modes.[2, 4] These assumptions usually lead to equations which permit isolation of the parameters being varied in the preliminary design study. Thus, the effect of varying one or more of the parameters can be analyzed. Although the trends predicted are usually correct and of value, the basic air-load and stiffness assumptions introduce a lack of confidence in the accuracy of the estimated aeroelastic effects for any one particular model or condition. It is therefore expedient to use the "quick-and-dirty" approach for getting the design into "the right ball park" but not for fixing on a precise configuration.

The advent of high-speed electronic calculators has provided a valuable tool for detailed engineering work. This is particularly true in quasi-stationary aeroelasticity. Once a method of solution has been selected, it can be programed for automatic calculation. If air-load and stiffness influence coefficient matrices are used, their size should definitely be variable in the computer program. By allowing the number of span stations to be specified, the designer can obtain solutions, at minimum cost, which are consistent with his estimate of the air-load and stiffness accuracies at the particular design stage. For example, if a large number of configurations or conditions is to be perused and only crude estimates of wing stiffnesses are available, then perhaps as few as five semispan stations should be considered. In an advanced design, this number may be 20. For the smaller matrices, more than 60 conditions have been calculated† during an 8-hour night shift. It is suggested that, for a few of these cases, 10- or 20-point solutions be computed in order to estimate the effect of loosely spacing the span stations. As a rule of thumb, doubling the number of stations approximately triples the computing time. With the above in mind it is now proposed that, in the preliminary phase, the range of possible configurations be narrowed by use of approximation techniques, such as are recommended by references 2–4. The optimum preliminary design should then be chosen using a precise theory set up for high-speed calculation. As stated previously, a significant amount of computing time can be saved here by use of fewer calculation points than would be warranted in advanced design stages.

If a configuration exhibits small aeroelastic effects, then a rough estimate will probably not have serious consequences. But if severe losses, such as 50 per cent of C_{L_α} or near-reversal of C_{l_β} are contemplated, then it is essential that the utmost confidence in the analysis be guaranteed.

Almost always, an approximate method is compared with a more refined one for justification purposes. Frequently, however, as in reference 1, the comparison is made using either an extremely simple configuration or one having a high stiffness level. In either case, fair to good agreement can be expected. But extrapolation of the same technique to complex or moderately flexible models should be executed with caution. Substantiation of approximating assumptions must be made via a wide variety of examples. If this is not done, the limitations must be stated precisely in order to avoid misuse.

In reference 1, for example, all limitations of the theory are not apparent. It is perhaps illuminating to investigate these. Eq. (2) of that reference expresses the wing tip twist angle as an infinite series of twists:

$$\epsilon = \epsilon_1 + \epsilon_2 + \epsilon_3 + \ldots \tag{2}$$

where ϵ_1 is the twist due to the initially applied loads and each successive ϵ_{i+1} is caused by the loads resulting from ϵ_i. Eq. (4) of the reference assumes that the ratio of successive twist angles is a constant:

$$\epsilon_2/\epsilon_1 = \epsilon_3/\epsilon_2 = \epsilon_4/\epsilon_3 = \ldots = -k \tag{4}$$

The conclusion is then drawn that

$$\epsilon = \epsilon_1/(1 + k) \tag{5}$$

The author neglects to discuss k other than to state "for conventional wings with sweptback elastic axes this term is usually positive and of order unity so that an error in $1/(1 + k)$ is small compared to an error in k." Actually, k is of prime importance and is equal to the ratio $-(q/q_{div})$, where q is the flight dynamic pressure and q_{div} is the divergence dynamic pressure. If $k \leq -1$, then not only is Eq. (5) invalid but the series in Eq. (2) does not converge and the wing in fact diverges physically. Eq. (5), however, gives a finite answer for ϵ even when $q > q_{div} > 0$. It is precisely here, in obtaining an unconsciously incorrect result, that the danger lies in applying an equation without a clear exposition of its limitations. If $k \geq 1$, then the wing is physically stable, but Eq. (5) cannot represent Eq. (2) for certain formulations of the problem since the series again diverges. That is, the operator which yields ϵ_{i+1} from ϵ_i must have certain properties in order for Eq. (5) to hold if $q \geq |q_{div}|$, $q_{div} < 0$. This can impose a severe restriction because, even if q_{div} were a mathematical

* Aerodynamics Engineering Specialist.

** Group Engineer, Electronic Computing and Numerical Analysis, Fluid Dynamics Department.

† These figures apply for the IBM Type 776 Electronic Calculator, using a matrix formulation of the theory of reference 5 as outlined in reference 6.

limit on q, it would by no means be a physical limit for a highly swept wing. This series convergence problem is discussed in more detail in reference 5. It is adequate here to emphasize that the foundation of a simplified theory may be invalidated by restrictions not uncovered because of insufficient study. Reference 1 unfortunately selected only a nondivergent unswept wing for correlation purposes. Consequently, the inherent limitations were not encountered.

References

[1] Rodden, William P., *An Aeroelastic Parameter for Estimation of the Effects of Flexibility on the Lateral Stability and Control of Aircraft*, Journal of the Aeronautical Sciences, Vol. 23, No. 7, pp. 660–662, July, 1956.

[2] Miles, John W., *A Formulation of the Aeroelastic Problem for a Swept Wing*, Journal of the Aeronautical Sciences, Vol. 16, No. 8, pp. 477–490, August, 1949.

[3] Diederich, Franklin W., *The Calculation of the Aerodynamic Loading of Flexible Wings of Arbitrary Plan Form and Stiffness*, NACA TN 1876, 1949.

[4] Hedgepeth, John M., Waner, Paul G., and Kell, Robert J., *A Simplified Method for Calculating Aeroelastic Effects on the Roll of Aircraft*, NACA TN 3370, 1955.

[5] Gaugh, William J., and Slap, Joseph K., *Determination of Elastic Wing Aerodynamic Parameters*, Journal of the Aeronautical Sciences, Vol. 19, No. 3, pp. 173–182, March, 1952.

[6] Ernest, A. W., *A Matrix Method for Computing Aeroelastic Effects*, Northrop Aircraft Report No. NAI-56-249, March, 1956.

Displacement Thickness of the Unsteady Boundary Layer

Franklin K. Moore* and Simon Ostrach**

Cornell Aeronautical Laboratory, Inc., and Lewis Flight Propulsion Laboratory, NACA, Respectively

August 29, 1956

THE PURPOSE of this note is to extend a previous result[1] for the displacement effect of a three-dimensional boundary layer to apply to the unsteady boundary layer and to apply the result to certain flows for which unsteady boundary-layer solutions are available.

The general definition of displacement thickness may be stated as follows: At the outer limit of the boundary layer (say at $y = h$, where y is measured normal to the surface) a certain distribution of normal velocity v appears owing to the displacement effect exerted by the boundary layer; if the flow were entirely nonviscous, the same distribution of v at $y = h$ could be produced by the presence of an impermeable surface $y = \Delta(x, z, t)$, where x, z are coordinates in the surface. This fictitious displacement surface $y = \Delta$ is useful for determining the effect of the boundary layer on the outer flow. It is required to determine $\Delta(x, z, t)$ in terms of the boundary-layer profiles which are presumed to be known.

In the fictitious nonviscous flow (subscript $o.f.$), we have the boundary condition at the displacement surface

$$(v_{o.f.})_\Delta = \boldsymbol{q}_1 \cdot \operatorname{grad} \Delta + \partial\Delta/\partial t \tag{1}$$

Consequently, at $y = h$, if the boundary layer is thin,

$$(v_{o.f.})_h = \boldsymbol{q}_1 \cdot \operatorname{grad} \Delta + \partial\Delta/\partial t + (h - \Delta)(\partial v_{o.f.}/\partial y)_0 \tag{2}$$

where $\boldsymbol{q}$ is the projection of the velocity vector on the surface and subscripts 1 and 0 denote evaluation at the outer edge of the boundary layer and the surface, respectively.

In the boundary layer (subscript $b.l.$), continuity requires that

$$\partial(\rho v_{b.l.})/\partial y = -\partial\rho/\partial t - \nabla\cdot(\rho_1 \boldsymbol{q}_1) \tag{3}$$

Integrating, one finds, after rearrangement of terms,

$$\rho_1(v_{b.l.})_h = -h[\partial\rho_1/\partial t + \nabla\cdot(\rho_1\boldsymbol{q}_1)] + \nabla\cdot\int_0^h (\rho_1\boldsymbol{q}_1 - \rho\boldsymbol{q})\,dy + \frac{\partial}{\partial t}\int_0^h (\rho_1 - \rho)\,dy \tag{4}$$

Continuity also requires that

$$\rho_1(\partial v_{o.f.}/\partial y)_0 = -[\partial\rho_1/\partial t + \nabla\cdot(\rho_1\boldsymbol{q}_1)] \tag{5}$$

Now, in order that the displacement effect of the surface Δ in the nonviscous flow be the same as that actually produced by the boundary layer, one must impose the condition

$$(v_{o.f.})_h = (v_{b.l.})_h \tag{6}$$

Eqs. (2), (4), and (5), when substituted in Eq. (6), yield, after simplification,

$$\Delta\cdot\left[\rho_1\boldsymbol{q}_1\Delta - \int_0^\infty (\rho_1\boldsymbol{q}_1 - \rho\boldsymbol{q})\,dy\right] + \frac{\partial}{\partial t}\left[\rho_1\Delta - \int_0^\infty (\rho_1 - \rho)dy\right] = 0 \tag{7}$$

wherein h is taken to be infinite for purposes of integration across the boundary layer.

Eq. (7) is the defining relation for the displacement surface of a three-dimensional unsteady boundary layer. For steady flow, the second term of Eq. (7) is zero, and the previous result[1] remains; and, further, if the boundary layer is two-dimensional, the appropriate solution of Eq. (7) is

$$\Delta = \delta^* \equiv \int_0^\infty \left(1 - \frac{\rho q}{\rho_1 q_1}\right) dy \tag{8}$$

which is the usual two-dimensional result.

The second term of Eq. (7) relates to the piston-like effect of aerodynamic heating discussed, for example, by Van Dyke.[2] Van Dyke considered the case of a doubly infinite flat plate suddenly set in motion at a sufficiently high Mach Number so that pressure waves are generated by the boundary-layer growth. For this problem, the boundary layer depends only on y. Thus, the first term of Eq. (7) vanishes, and a suitable solution is

$$\Delta = \int_0^\infty \left(1 - \frac{\rho}{\rho_1}\right) dy \tag{9}$$

which may be evaluated from Van Dyke's solution for the profile of ρ/ρ_1 to yield

$$\Delta = \sqrt{2\nu_1 t/\pi}\,(\gamma - 1)M^2 \tag{10}$$

where ν is kinematic viscosity, M is Mach number, and γ is the ratio of specific heats. Eq. (10) conforms to van Dyke's result[2] when interpreted as a displacement thickness effect.

Other unsteady solutions to which Eq. (7) may be simply applied are available[3–5]—namely, those for the compressible laminar boundary layer of a semi-infinite insulated or isothermal flat plate in nearly quasi-steady flow. The solutions were obtained as expansions in the various time derivatives of a differentiable but otherwise arbitrary flight velocity $U(t)$.

Insulated Plate—The required quantities for the insulated plate are[3, 4]

$$\delta^* = \int_0^\infty \left(1 - \frac{\rho q}{\rho_1 q_1}\right) dy = (1.721)\sqrt{\frac{xC\nu_1}{U}}\left\{1 + (0.645)(\gamma - 1)M^2 - (0.592)[1 + (2.938)(\gamma - 1)M^2] \times (xU'/U^2) + (0.694)[1 + (2.702)(\gamma - 1)M^2](x^2U''/U^3) - (0.445)[1 - (1.361)(\gamma - 1)M^2](xU'/U^2)^2 + \ldots\right\} \tag{11}$$

$$\int_0^\infty \left(1 - \frac{\rho}{\rho_1}\right) dy = (\gamma - 1)M^2\sqrt{\frac{xC\nu_1}{U}}\left\{(1.110) - (2.992) \times (xU''/U^2) + (3.229)(x^2U'''/U^3) + (1.042)(xU''/U^2)^2 + \ldots\right\} \tag{12}$$

where x is measured aft from the leading edge and C is a constant required to adjust an assumed linear viscosity relation.

If it is assumed that the solution for Δ has the same form as that of Eq. (11), with different numerical coefficients, then substitution of Eqs. (11) and (12) into Eq. (7) and collection of like terms yields the following result for Δ:

* Head, Aerodynamic Research Department.

** Chief, Applied Mechanics Branch.

$$\Delta = \delta^* + 0.5735\sqrt{xC\nu_1/U}\,\{[1 + 2.579\,(\gamma - 1)M^2] \times (xU'/U^2) + 0.310\,[1 - (3.322)\,(\gamma - 1)M^2]\,(x^2U''/U^3) - 0.776\,[1 + (2.056)\,(\gamma - 1)M^2]\,(xU'/U^2)^2 + \ldots\} \quad (13)$$

Eq. (13) is written in such a way that the significant differences between the true displacement thickness Δ and the thickness δ^* defined in the usual way by Eq. (8) are immediately evident.

Isothermal Plate—For the isothermal plate,[4, 5]

$$\delta^* = 1.721\sqrt{\frac{xC\nu_1}{U}}\left\{1 + 0.167\,(\gamma - 1)M^2 + 1.126\left(\frac{\theta_w - \theta_1}{\theta_1}\right) - 0.592\left[1 + 0.436\,(\gamma - 1)M^2 - 0.0869\left(\frac{\theta_w - \theta_1}{\theta_1}\right)\right]\frac{xU'}{U^2} + 0.694\left[1 + 0.259\,(\gamma - 1)M^2 + 0.529\left(\frac{\theta_w - \theta_1}{\theta_1}\right)\right]\frac{x^2U''}{U^3} - 0.445\left[1 - 0.0280\,(\gamma - 1)M^2 + 0.128\left(\frac{\theta_w - \theta_1}{\theta_1}\right)\right] \times \left(\frac{xU'}{U^2}\right)^2 + \ldots\right\} \quad (14)$$

where θ denotes temperature and the subscript w denotes surface conditions, and

$$\int_0^\infty \left(1 - \frac{\rho}{\rho_1}\right) dy = \sqrt{\frac{xC\nu_1}{U}}\,\{(\gamma - 1)M^2\,[0.288 - 0.444\,(xU''/U^2) + 0.3095\,(xU'''/U^3) + 0.0713(xU''/U^2)^2] + 2\,[(\theta_w - \theta_1)/\theta_1]\,[0.969 + 0.0443\,(xU''/U^2) + 0.316(xU'''/U^3) - 0.163(xU''/U^2)^2] + \ldots\} \quad (15)$$

Substitution of Eqs. (14) and (15) into Eq. (7) yields the displacement surface for the unsteady motion of an isothermal plate:

$$\Delta = \delta^* + 0.5735\sqrt{xC\nu_1/U}\,\{[1 + 0.669\,(\gamma - 1)M^2] \times (xU''/U^2) + 0.310\,[1 - 0.863\,(\gamma - 1)M^2]\,(xU'''/U^3) - 0.776\,[1 - 0.0644\,(\gamma - 1)M^2]\,(xU'/U^2)^2 + \ldots\} \quad (16)$$

Eq. (16) shows that the difference between Δ and δ^* for an isothermal plate does not depend on wall temperature.

References

[1] Moore, Franklin K., *Displacement Effect of a Three-Dimensional Boundary Layer*, NACA Rep. 1124, 1953 (formerly NACA TN 2722, 1952).

[2] Van Dyke, Milton D., *Impulsive Motion of an Infinite Plate in a Viscous Compressible Fluid*, Zeitschr. Angew. Math. u. Phys. Vol. 3, No. 5, pp. 343–353, 1952.

[3] Moore, Franklin K., *Unsteady Laminar Boundary-Layer Flow*, NACA TN 2471, 1951.

[4] Moore, Franklin K., and Ostrach, Simon, *Average Properties of Compressible Laminar Boundary Layer on Flat Plate with Unsteady Flight Velocity*, NACA TN 3886, 1956.

[5] Ostrach, Simon, *Compressible Laminar Boundary Layer and Heat Transfer for Unsteady Motions of a Flat Plate*, NACA TN 3569, 1955.

On Some Concepts of Nonlinear Oscillation Theory

K. Klotter

Professor of Engineering Mechanics, Stanford University, Stanford, Calif.

August 30, 1956

In a recent paper in this Journal,[1] F. H. Clauser has set himself the task of promoting an understanding of nonlinear phenomena by presenting them "in terms of fundamental and well-understood concepts." He may be credited with having accomplished his difficult task, in general, very well; some of the remarks in the paper are truly elucidating.

In a field which is still in rapid evolution and where concepts in many instances have not yet been formulated to complete satisfaction, any author of an expository paper is burdened with the two responsibilities of (a) helping such an evolution and (b) not doing anything which endangers that process. The writer feels that in a few cases the author of the paper quoted violated stipulation (b) because of either improper generalization or confusing terminology.

Three items will be singled out for discussion:

(1) The phenomenon of the sudden changes in the amplitudes of forced oscillations (Fig. 24 of the paper), the so-called "jump phenomenon," is linked to and called "hysteresis" by the author as unfortunately has been done by other authors before. The similarity between a true hysteresis loop (e.g., in a displacement-force plane for elastic hysteresis or in a B-H-plane for magnetic hysteresis) and the "loop" in an amplitude-frequency plane is purely superficial, however, because (a) the latter lacks the essential property of a true hysteresis loop (as defined in any field of physics) that the loop area represents the energy dissipated; (b) in response diagrams (of the amplitude-frequency plane) even if jumps do occur they need not necessarily lead to closed "loops"—e.g., in the case of an undamped system; (c) physical hysteresis curves, on the other hand, do not show any sudden changes—i.e., jumps—at all. Hence, the term "hysteresis" ought to be carefully avoided in describing the jump phenomenon. Conversely, using it certainly does not help to clarify the concepts.

(2) Clauser uses the important terms "autonomous" and "nonautonomous" in strict contrast to the established usage. He starts from the generally accepted criterion (which he does not cite literally but rather in a paraphrased form) that if the independent variable t does not appear explicitly in the differential equation, the system is called autonomous, and that if t does appear explicitly, the system is called nonautonomous. Then, however, Clauser goes on to apply the criterion to the *left*-hand side of the differential equation exclusively. Consequently, he calls all systems autonomous except those which have varying coefficients. Cases where a driving function appears on the right-hand side of the equation he calls "stimulated autonomous systems," as contrasted with "isolated autonomous systems" if there is no driving term.

This being a matter of definitions, the issue, of course, cannot be decided logically. However, new definitions or usages should not be introduced without this fact being mentioned openly and without giving excellent reasons for the departure from generally accepted terminology.

Even judging Clauser's terminology on its own merits, one would have to raise objections to calling "isolated" a system like the one described by van der Pol's differential equation

$$\ddot{x} - \epsilon\dot{x}(1 - \alpha^2x) + k^2x = 0$$

because there is a continuous exchange of energy; mechanical energy has to be fed into the system repeatedly (periodically in steady state). Hence, energy-wise at least, the system certainly is not "isolated."

(3) The writer maintains that a departure from recently introduced terminology is necessary in order to comply with a much older and very well established one.

Everybody, engineer or not, calls a spring hard if its spring constant (slope of the force-deflection curve) is large and soft if the spring constant is small. In 1938 M. Rauscher[2] started a usage where a spring is called hard if the slope of the force-deflection curve is increasing and soft if that slope is decreasing. This usage, unfortunately, has spread, and it has been adopted by Clauser, although it conflicts with the much older terminology and hence is bound to create confusion. The writer wants to repeat here his earlier suggestions[3,4] of resolving the difficulty by retaining the words "hard" and "soft" for describing the slope (of the force-deflection curve) and by using the words "hardening" and "softening" for describing the change in slope.

REFERENCES

[1] Clauser, F. H., *The Behavior of Nonlinear Systems*, Journal of the Aeronautical Sciences, Vol. 23, No. 5, pp. 411–434, May, 1956.

[2] Rauscher, M., *Steady Oscillations of Systems with Nonlinear and Unsymmetrical Elasticity*, J. Appl. Mech., p. A-169, December, 1938.

[3] Klotter, K., *Steady State Vibrations in Systems Having Arbitrary Restoring and Arbitrary Damping Forces*, Proc. Symposium on Nonlinear Circuit Analysis, pp. 234–257; Polytechnic Institute of Brooklyn, New York, 1953.

[4] Klotter, K., *Analysis of a Nonlinear Dynamic Vibration Absorber*, Discussion Remark, J. Appl. Mech. Vol. 22, No. 5, pp. 299–301, September 1954.

The Shear Flow Along a Flat Plate With Uniform Suction

Takeo Sakurai

Department of Physics, Faculty of Science, University of Tokyo, Tokyo, Japan

September 5, 1956

RECENTLY, several authors[1–4] have investigated the boundary layer in a shear flow. In this note, an exact solution of the Navier-Stokes equations will be presented, which represents the boundary layer along an infinite flat plate with uniform suction situated in a shear flow.

Let the x-axis and y-axis be taken parallel and perpendicular to the plate, respectively. If the flow condition is assumed to be steady and independent of the x-coordinate, then the Navier-Stokes equations and the equation of continuity for incompressible fluid become

$$v(du/dy) = -(1/\rho)(\partial p/\partial x) + \nu(d^2u/dy^2) \tag{1}$$

$$v(dv/dy) = -(1/\rho)(\partial p/\partial y) + \nu(d^2v/dy^2) \tag{2}$$

$$dv/dy = 0 \tag{3}$$

where (u, v) are the velocity components, p is the pressure, ρ is the density, and ν is the kinematic viscosity.

Eq. (3) gives

$$v = \text{const.} = v_0 \tag{4}$$

Hence, Eqs. (1) and (2) become

$$\partial p/\partial x = \rho[\nu(d^2u/dy^2) - v_0(du/dy)] \tag{5}$$

$$\partial p/\partial y = 0 \tag{6}$$

respectively. From Eq. (6), p is found to be a function of x only, while Eq. (5) shows that $\partial p/\partial x$ is a function of y only. Therefore $\partial p/\partial x$ should be a constant (α, say). Thus,

$$p = \alpha x + \text{const.} \tag{7}$$

and Eq. (5) reduces to

$$\nu(d^2u/dy^2) - v_0(du/dy) = \alpha/\rho \tag{8}$$

The solution of Eq. (8), subject to the appropriate boundary condition,

$$u = 0 \quad \text{at} \quad y = 0 \tag{9}$$

is easily found to be

$$u = \omega_\infty y + U_0 - U_0 \exp(v_0 y/\nu) \tag{10}$$

where U_0 is an arbitrary constant and

$$\omega_\infty = -\alpha/\rho v_0 \tag{11}$$

If it is assumed that

$$v_0 < 0 \tag{12}$$

so that there is a uniform suction along the plate, then the last term of Eq. (10) shows the exponential decay as y increases—namely,

$$u \to \omega_\infty y + U_0 \qquad \text{as } y \to \infty \tag{13}$$

This indicates that the above obtained solution corresponds to the boundary layer over a flat plate in a shear flow defined by

$$U = U_0 + \omega_\infty y \tag{14}$$

the thickness of the boundary layer being of order of $0(\nu/v_0)$.

It is interesting to note that the solution [Eq. (10)] can be constructed by simply superposing the shear flow and the usual suction flow[5]; this is because of the linearity of the basic equations, Eqs. (1), (2), and (3). Also, it is to be noted that the pressure gradient α, the vorticity ω_∞, and the suction velocity v_0 are related to each other by Eq. (11). Accordingly, if the usual boundary condition, $u \to U_0$ as $y \to \infty$, instead of Eq. (12) is assumed, then the solution reduces to the usual suction flow with no pressure gradient.

Finally, it should be emphasized that the boundary-layer nature appears only in the case of suction $v_0 < 0$. Indeed, if $v_0 > 0$, the solution [Eq. (10)] represents an exponentially diverging velocity as $y \to \infty$, and if $v_0 = 0$—i.e., no suction is assumed—Eq. (10), subject to the boundary condition of Eq. (9), has only the plane Poiseuille flow as its solution:

$$u = (\alpha/2\rho\nu)y^2 + \beta y, \qquad \beta = \text{const.}$$

In conclusion, the writer would like to express his cordial thanks to Prof. Isao Imai for his continual guidance and encouragement. The writer is also indebted to Dr. Hidenori Hasimoto for his invaluable advice and discussions in the course of this investigation.

REFERENCES

[1] Ferri, A., and Libby, P. A., *Note on an Interaction between the Boundary Layer and the Inviscid Flow*, Readers' Forum, Journal of the Aeronautical Sciences, Vol. 21, No. 2, p. 130, February, 1954.

[2] Li, T. Y., *Simple Shear Flow past a Flat Plate in an Incompressible Fluid of Small Viscosity*, Readers' Forum, Journal of the Aeronautical Sciences, Vol. 22, No. 9, pp. 651, 652, September, 1955.

[3] Li, T. Y., *Simple Shear Flow past a Flat Plate in a Compressible Viscous Fluid*, Readers' Forum, Journal of the Aeronautical Sciences, Vol. 22, No. 10, pp. 724, 725, October, 1955.

[4] Yen, K. T., *Approximate Solutions of the Incompressible Laminar Boundary-Layer Equations for a Flat Plate in a Shear Flow*, Readers' Forum, Journal of the Aeronautical Sciences, Vol. 22, No. 10, pp. 728–730, October, 1955.

[5] Schlichting, H., *Boundary Layer Theory*, p. 231; Pergamon Press, London, 1955.

Donnell's Equation for Thin Shells

Herbert Becker

Engineering Scientist, Research Division, College of Engineering, New York University, New York

October 3, 1956

DONNELL'S EQUATION, originally derived for buckling of a circular cylinder under torsional loading[1] has yielded useful results in a large variety of load applications for cylinder problems. This note contains a discussion of an equation in the Donnell form which has application to thin shells of constant thickness. This equation is applicable to plates and cylinders over the entire surface and may be applied, with certain limitations, to more general shells. The equation has been used herein to determine the classical expression for the buckling stress of a sphere under uniform external pressure.

In this analysis, orthogonal curvilinear coordinates, x and y, are used in the manner described by Reissner.[2] This permits writing the metric relation for a thin shell in the form

$$(ds)^2 = \alpha_1^2(d\xi_1)^2 + \alpha_2^2(d\xi_2)^2 \tag{1}$$

where

$$\left.\begin{aligned} ds &= \text{arc length} \\ \alpha_1 d\xi_1 &= dx \\ \alpha_2 d\xi_2 &= dy \end{aligned}\right\} \tag{2}$$

The stress-strain-displacement and curvature-displacement relations are

$$\left.\begin{aligned}
\epsilon_x &= (1/\alpha_1)(\partial u/\partial\xi_1) + (v/\alpha_1\alpha_2)(\partial\alpha_1/\partial\xi_2) + (w/R_x) = (\sigma_x/E) - \nu(\sigma_y/E)\\
\epsilon_y &= (1/\alpha_2)(\partial v/\partial\xi_2) + (u/\alpha_1\alpha_2)(\partial\alpha_2/\partial\xi_1) + (w/R_y) = (\sigma_y/E) - \nu(\sigma_x/E)\\
\gamma &= (\alpha_2/\alpha_1)(\partial/\partial\xi_1)(v/\alpha_2) + (\alpha_1/\alpha_2)(\partial/\partial\xi_2)(u/\alpha_1) = \tau/G\\
\chi_x &= (1/\alpha_1)(\partial/\partial\xi_1)[(u/R_x) + (1/\alpha_1)(\partial w/\partial\xi_1)] + (1/\alpha_1\alpha_2)[(v/R_y) + (1/\alpha_2)(\partial w/\partial\xi_2)](\partial\alpha_1/\partial\xi_2)\\
\chi_y &= (1/\alpha_2)(\partial/\partial\xi_2)[(v/R_y) + (1/\alpha_2)(\partial w/\partial\xi_2)] + (1/\alpha_1\alpha_2)[(u/R_x) + (1/\alpha_1)(\partial w/\partial\xi_1)](\partial\alpha_2/\partial\xi_1)\\
\chi_{xy} &= (1/2)\{(\alpha_2/\alpha_1)(\partial/\partial\xi_1)[(v/\alpha_2R_y) + (1/\alpha_2^2)(\partial w/\partial\xi_2)] + (\alpha_1/\alpha_2)(\partial/\partial\xi_2)[(u/\alpha_1R_x) + (1/\alpha_1^2)(\partial w/\partial\xi_1)]\}
\end{aligned}\right\} \quad (3)$$

The ensuing development will be restricted to surfaces with constant but not necessarily equal radii of curvature for which

$$(1/\alpha_1)(\partial\alpha_1/\partial\xi_1) = (1/\alpha_2)(\partial\alpha_1/\partial\xi_2) = (1/\alpha_1)(\partial\alpha_2/\partial\xi_1) = (1/\alpha_2)(\partial\alpha_2/\partial\xi_2) = 0 \quad (4)$$

Utilizing Eqs. (2), this permits writing the first three of Eqs. (3) in the form

$$\left.\begin{aligned}
\epsilon_x &= (\partial u/\partial x) + (w/R_x) = (\sigma_x/E) - \nu(\sigma_y/E)\\
\epsilon_y &= (\partial v/\partial y) + (w/R_y) = (\sigma_y/E) - \nu(\sigma_x/E)\\
\gamma &= (\partial u/\partial y) + (\partial v/\partial x) = \tau/G
\end{aligned}\right\} \quad (5)$$

When these are employed in deriving the compatibility equation for the stresses in a small plate-like element at the origin, it is found that (using the Airy stress function, F)

$$(1/E)\nabla^4F = (\partial^2/\partial x^2)(w/R_y) + (\partial^2/\partial y^2)(w/R_x) \quad (6)$$

If Donnell's simplification for cylinders,

$$v/R_y \ll (1/\alpha_2)(\partial w/\partial\xi_2)$$

is extended to shells,

$$u/R_y \ll (1/\alpha_1)(\partial w/\partial\xi_1), \quad v/R_y \ll (1/\alpha_2)(\partial w/\partial\xi_2) \quad (7)$$

then the curvature relations of Eqs. (3) will lead to the following equilibrium equation for transverse forces acting on the plate-like element:

$$D\nabla^4w + t[\sigma_x(\partial^2w/\partial x^2) + 2\tau(\partial^2w/\partial x\partial y) + \sigma_y(\partial^2w/\partial y^2) + (1/R_x)(\partial^2F/\partial y^2) + (1/R_y)(\partial^2F/\partial x^2)] + p = 0 \quad (8)$$

A form of Donnell's equation may be obtained by eliminating F between Eqs. (6) and (8):

$$D\nabla^8w + t\nabla^4[\sigma_x(\partial^2w/\partial x^2) + 2\tau(\partial^2w/\partial x\partial y) + \sigma_y(\partial^2w/\partial y^2)] + \nabla^4p + (Et/R_xR_y)\{R_y[(\partial^4/\partial y^4)(w/R_x) + (\partial^4/\partial x^2\partial y^2)(w/R_y)] + R_x[(\partial^4/\partial x^4)(w/R_y) + (\partial^4/\partial x^2\partial y^2)(w/R_x)]\} = 0 \quad (9)$$

This equation is applicable to plates and cylinders. For other surfaces, such as a sphere, it is restricted to a small region in the neighborhood of the origin of coordinates. Consequently, it may be limited for purposes of stress analysis. However, for determination of buckling stresses, which generally involve small regions of a shell, it could have useful application.

When R_y is chosen at a constant value, R, and R_x is equal to αR (α = arbitrary constant), then Eq. (9) reduces to

$$D\nabla^8w + t\nabla^4[\sigma_x(\partial^2w/\partial x^2) + 2\tau(\partial^2w/\partial x\partial y) + \sigma_y(\partial^2w/\partial y^2)] + \nabla^4p + (Et/R^2)[(\partial^2/\partial x^2) + (1/\alpha)(\partial^2/\partial y^2)]^2(w) = 0 \quad (10)$$

When $\alpha = \infty$, Eq. (9) reduces to Donnell's equation for a cylinder, and, when $\alpha = 1$, the expression for a sphere is obtained:

$$\nabla^4\{D\nabla^4w + t[\sigma_x(\partial^2w/\partial x^2) + 2\tau(\partial^2w/\partial x\partial y) + \sigma_y(\partial^2w/\partial y^2)] + p + (Etw/R^2)\} = 0 \quad (11)$$

As an illustration of the simplicity gained through the use of Eq. (11), it is employed to find the classical buckling stress for a thin-walled spherical shell under uniform external pressure. The solution to Eq. (11) is assumed to be

$$w = w_0 \sin mx \sin my \quad (12)$$

in which the buckle wave lengths are required to be small relative to R. Since $\sigma_x = \sigma_y = \sigma\,(= pR/2t)$, it is found that

$$\sigma = 2(m^2D/t) + [E/(2m^2R^2)] \quad (13)$$

Minimization with respect to m leads to the well-known classical result

$$\sigma_{cr} = [3(1 - \nu^2)]^{-1/2}(Et/R) \quad (14)$$

References

[1] Donnell, L. H., *Stability of Thin-Walled Tubes Under Torsion*, NACA TR 479, 1933.

[2] Reissner, E., *A New Derivation of the Equations for the Deformation of Elastic Shells*, Am. J. Math., Vol. 63, No. 1, pp. 177–184, January, 1941.

. . . Response of Simple Panels to Intense Acoustic Loading

(*Continued from page 24*)

laboratory siren studies have shown the fatigue life to be markedly shortened for these panels by a nominal increase in the noise intensity level.

References

[1] Miles, John W., *On Structural Fatigue Under Random Loading*, Journal of the Aeronautical Sciences, Vol. 21, No. 11, November, 1954, pp. 753–762.

[2] Liepmann, H. W., *On the Application of Statistical Concepts to the Buffeting Problem*, Journal of the Aeronautical Sciences, Vol. 19, No. 12, pp. 793–810, December, 1952.

[3] Den Hartog, J. P., *Mechanical Vibrations*, pp. 378–411; McGraw-Hill Book Company, Inc., New York, 1940.

[4] Lassiter, L. W., and Hubbard, H. H., *The Near Noise Field of Static Jets and Some Model Studies of Devices for Noise Reduction*, NACA TN 3187, July, 1954.

[5] Hess, R. W., Lassiter, L. W., and Hubbard, H. H., *A Study of the Response of Panels to Random Acoustic Excitation*, NACA RM L55E13c, July 15, 1955.

(3)

For other
gion in the
quently, it
wever, for
olve small

s equal to

$\partial y^2)] +$
$= 0$ (10)

tion for a
obtained:

$/\partial y^2)] +$
$= 0$ (11)

the use of
stress for a
pressure.

(12)

ıll relative

(13)

n classical

(14)

sion, NACA

formation of
y, 1941.

l Sciences,

378–411;

ise Field of
Reduction,

., A Study
on, NACA